

UNIVERSITY OF OKLAHOMA

GRADUATE COLLEGE

NUMERICAL SIMULATIONS OF WELLBORE CEMENT SHEATH MICROANNULI
LEAKAGE IN GULF OF MEXICO WELLS

A DISSERTATION

SUBMITTED TO THE GRADUATE FACULTY

in partial fulfilment of the requirements for the

Degree of

DOCTOR OF PHILOSOPHY

By

JARRETT WISE
Norman, Oklahoma
2021

NUMERICAL SIMULATIONS OF WELLBORE CEMENT SHEATH MICROANNULI
LEAKAGE IN GULF OF MEXICO WELLS

A DISSERTATION APPROVED FOR THE
MEWBOURNE SCHOOL OF PETROLEUM AND GEOLOGICAL ENGINEERING

BY THE COMMITTEE CONSISTING OF

Dr. Runar Nygaard, Chair

Dr. Saeed Salehi

Dr. Hamidreza Karami

Dr. Harold Stalford

© Copyright by JARRETT WISE 2021
All Rights Reserved.

Acknowledgement

First I would like to thank my advisor Dr. Runar Nygaard for accepting me as a graduate student at OSU and bringing me to OU. He has been an amazing academic advisor but also a mentor and a friend. I have enjoyed grabbing lunches and talking about life over the last four years all while beating him in March Madness brackets.

In addition, I would like to thank my committee members, Dr. Saeed Salehi for all his valuable time and the conversations we have had, Dr. Hamidreza Karami for discussing career paths and helping with fluid flow derivations, and Dr. Harold Stalford for his valuable feedback and support. I would also like to thank Nils Opedal from SINTEF for the collaborations and some of the experimental data used in this work, and the research group from NORCE for the experimental data, feedback, and collaborations on two publications. I would also like to thank the graduate students who have helped with feedback, editing (ACED), good times, and technical discussions.

Lastly, I would like to thank my family back home and my Norman family at Paradigm for their love, support, and encouragement through this process. The many years of school and numerous destinations along the way couldn't have been done without their support.

Table of Contents

Acknowledgement	iv
Table of Contents	v
List of Tables	ix
List of Figures	xii
Abstract	xxiii
Chapter 1: Introduction	1
Chapter 2: Critical Literature Review	4
2.1 Well Construction	4
2.2 Well Operations	15
Wellbore leakage	17
2.3 Cement Secondary Failure Mechanisms	18
Modeling of Leakage	27
2.4 Circular Flow	27
2.5 Annular Flow	30
2.6 Slot Flow	31
Prediction of Fluid Leakage	33
2.7 Lab Leakage Prediction	33
2.8 Field Leakage Prediction	45
2.9 Analytical Methods	49

2.10 Numerical Methods.....	54
Summary of Previous Work.....	62
Chapter 3: Field Description.....	64
Gulf of Mexico.....	64
Eugene Island OPD.....	66
3.1 Three Representative Wells	70
3.2 Formation Properties.....	71
High Island OPD.....	73
3.3 Case Study Well.....	75
3.4 Formation Properties.....	77
Chapter 4: Methodology	82
Derivation of Real Gas Fluid Flow	82
4.1 Comparison of Fluid Flow Models	89
Staged Poro-Elastic FEA Stress Continuum Model	91
Staged Poro-Elastic FEA Fracture Model.....	94
Continuous Leakage Pathway Models.....	96
Numerical Experiments Performed.....	100
4.2 Verification of Models	100
4.3 GoM Parametric Study	109
4.4 GoM Continuous Leakage Path Model.....	111

4.5 Case Study Well.....	114
Chapter 5: Results	121
5.1 Fluid Flow Model Comparison.....	121
5.2 Verification of Models	123
5.3 GoM Parametric Study	133
5.4 GoM Continuous Leakage Path.....	147
5.5 Case Study Well.....	148
Chapter 6: Discussions.....	170
Effect of Modeling Gas versus Water.....	170
Effect of Shrinkage	171
Effect of Confinement.....	172
Effect of Traction Separation Law	175
Implications of Wellbore Leakage in the Gulf of Mexico.....	177
Chapter 7: Conclusions, Recommendations, and Future Work	181
Conclusions and Recommendations	181
Future Work	183
Nomenclature	184
References	187
Appendix A: Basic Rock Mechanics	196
Appendix B: Wellbore Abandonment Requirements	202

Appendix C: Parallel Plate Capillary Pressure	204
Appendix D: Case Well Data.....	205
Appendix E: Numerical Model Details.....	236
Appendix F: Compressibility Factor Method Verification.....	239
Appendix G: Riemann Sum Verification.....	242
Appendix H: Mesh Sensitivity Analysis.....	245
Appendix I: Staged Poro-Elastic FEA Stress Continuum Model Results	248
Appendix J: Rock Formation Failure Mechanism	259
Appendix K: Finite Element Model Theory	261
Appendix L: Fanning Friction Factor from Bernoulli's Equation	264
Appendix M: Biography	268

List of Tables

Table 2.1: Hydraulic and shear bond strengths from Carter and Evans (1964) with at different curing ages.	22
Table 2.2: Summary of the Aas et al. (2016) experiments used for the FEA model verification.	36
Table 2.3: Experimentally measured pressure drops and equivalent microannuli gaps for both expanding and conventional cement in Aas et al. (2016) experiments.....	37
Table 3.1: Cement database for Class H and Class G cements.	79
Table 4.1: Values for the synthetic wellbore to compare the analytical equations derived in this work with the Hagen-Poiseulle flow equation.....	91
Table 4.2: Dimensions and mechanical properties used in the FEA model.	103
Table 4.3: Linear correlations for the initial pressure versus the microannuli gap for the test cement types with respect to their eccentricity. Note the intercept is the shrinkage induced gap.	108
Table 4.4: Base case input parameters for the three wells in the Eugene Island OPD and the source of their values.....	110
Table 4.5: Summary of the two High Island Well logs for the rock mechanical properties.	117
Table 4.6: Parameters for the case well (API# 427094116400) in the High Island OPD and the source of their value(s).....	118
Table 4.7: High and low values for the parametric study. These values apply for all three well depth parameters.	119
Table 5.1: Comparison of the six analytical equations for the synthetic well. Note that Hagen-Poiseulle flow was determined for both water and gas. Equation 4.15 resulted in the highest flow rate while Equation 4.34 did not have a flow rate.	122

Table 5.2: Corresponding Reynold’s numbers (<i>NRe</i>) for the fluid flow models for the synthetic wellbore. All eight fluid flow models are in the laminar flow regime (<i>NRe</i> ≤ 2, 100).	123
Table 5.3: Maximum percent difference (% Diff.) of the variation between the real and ideal gas flow.	125
Table 5.4: Corresponding maximum Reynold’s numbers (<i>NRe</i>) for the cement mixtures SF120, SF66, and SF120EA. The Reynold’s numbers are all in the laminar flow regime.....	127
Table 5.5: Effective stress percent difference of the FEA stress continuum and fracture model from the analytical solution for the casing, cement, and rock formation.	128
Table 5.6: Calculated pressure drops and simulated microannuli gaps for both expanding and conventional cement in comparison to the experimentally measured pressure drops and equivalent microannuli gaps.	130
Table 5.7: Representation that the simulated pressure drops can mimic the experimental data by altering either the shrinkage or the fluid friction factor in the simulations.	133
Table 5.8: Base case wellbores comparison between the stress continuum model (stress model) and the fracture model for the shallow, medium, and deep depth wellbores. The gray shaded cells represent tensile failure in the stress continuum model whereas the orange shaded cell represents tensile failure in the fracture model resulting in a microannuli gap width of 13.6 μm.....	135
Table 5.9: Microannuli gap initiation reduction changes for ΔP and ΔT including nanometer (nm) gap and micrometer (μm) gap initiation Δ ’s.....	151
Table 5.10: Gap magnitudes created by change in wellbore parameters for a 29% ΔP and ΔT . These parameters cause gaps to occur when the base case wellbore did not have gaps at 29% ΔP and ΔT	155

Table 5.11: Parameters that caused the microannuli gap magnitudes to be eliminated (0 μm) with a 44% ΔP and ΔT 156

Table 5.12: Wellbore parameters sorted based off their percent change of the maximum gap width (%MGW) from the base gap magnitude. 1st Order Parameters are critical in the development of the gap width magnitude at the casing/cement interface. 2nd Order Parameters have minor effect, and 3rd Order Parameters have little to no effect on the development of the gap widths. 158

Table 5.13: Comparison of the three flow paths for the volume of the leakage path for an ideal and real gas with and without the effect of gravity. The constant gap method produces the largest flow rate while the FEA gap method produces the smallest flow rate..... 168

Table 5.14: Comparison of the literature methods for calculating cumulative leakage for the case study well in comparison with the method presented in this work. The effect of using the FEA predicted microannuli along with analyzing a real gas with the effect of gravity reduces the total flow rate from the case study well. 169

List of Figures

Figure 2.1: Schematic of a wellbore orientated such that the borehole is parallel to the overburden stress (σ_v). The principal stresses are represented with respect to Cartesian coordinates.	6
Figure 2.2: Illustration showing the magnitude of hoop stress around a wellbore.	8
Figure 2.3: Kirsch analytical solution of the effective hoop and radial stress from the wellbore versus the distance away from the wellbore.	9
Figure 2.4: Example drilling fluid weight window with corresponding casing design from GoM well API 427094116400.	11
Figure 2.5: Schematic of uniform, radial, and axial cement shrinkage. Uniform volumetric shrinkage assumes the same percent change in volume of both the radial and axial direction. Radial volumetric shrinkage assumes only volumetric shrinkage in the radial direction. Axial volumetric shrinkage assumes only volumetric shrinkage in the axial direction.	15
Figure 2.6: Primary and secondary leakage pathways in the near wellbore region. Picture from Weideman (2014).	18
Figure 2.7 A: Failure mechanisms within the cement sheath showing inner and outer debonding, radial cracks, and shear cracks. B: Failure mechanism within the cement sheath showing diskings.	19
Figure 2.8: Schematic of the three bond strengths: tensile, shear, and hydraulic.	20
Figure 2.9: Mode I debonding (top) with the corresponding traction separation law (bottom). ..	24
Figure 2.10: Traction separation law (CZM) showing extrinsic (solid line) versus intrinsic (dotted line) behavior.	25
Figure 2.11: A) Example of a load versus time data acquired in bond test experiments. B) Analyzed experimental data in terms of stress versus displacement data.	26

Figure 2.12: Velocity profile in a circular pipe with laminar flow.....	29
Figure 2.13: Slot flow dimensions used in the derivation of Equation 2.49.....	32
Figure 2.14: Experimental data from Corina et al. (2019) showing the flow rate through the cement plug given the differential pressure (ΔP) with the neat cement at 66 °C (SF66), neat cement at 120 °C (SF120), and neat cement plus expanding agent at 120 °C (SF120EA).....	34
Figure 2.15: Cut test assembly showing complete cement displacement between the casing and tubing. Figure modified from Aas et al. (2016).....	36
Figure 2.16: Microannuli (w) versus flow rate for the three test cases from Corina et al. (2019) analyzed using the methodology from Corina et al. (2020).....	39
Figure 2.17: Microannuli (w) versus pressure differential (ΔP) for the three test cases from Corina et al. (2019) analyzed using the methodology from Corina et al. (2020).	40
Figure 2.18: Results of experiments from Skorpa and Vrålstad (2018) used in the CFD simulations. A) representation of flow path through connected cracks within the cement sheath. B) debonding channel between the cement and formation (as shown by dashed box). C) partial microannuli between the cement and casing. D) a uniform microannuli at the casing/cement interface as predicted by equivalent microannuli analyses. Figure from Skorpa and Vrålstad (2018).....	43
Figure 2.19: Schematic of the CO ₂ production well located in the Dakota Sandstone formation used in Crow et al. (2010). The different formation strata depths, cement depths, true vertical depths (TVD), and wellbore dimensions are shown. Figure from Crow et al. (2010).	46
Figure 2.20: Wellbore Sketch showing generalized radii of the three bodies used in the analytical stress distributions equations.	50
Figure 2.21: Schematic showing the fracturing fluid flow (q), fracture width (w), pressures surrounding the fracture (P_{pt}, P_{pb}), and the leak-off velocities (v_t, v_b).	58

Figure 3.1: The Outer Continental Shelf (OCS) of the Gulf of Mexico showing the three planning areas: the Western Planning Area, the Central Planning Area, and the Eastern Planning Area.

Figure from www.boem.gov..... 65

Figure 3.2: The distribution of wells in the Outer Continental Shelf (OCS) in the Gulf of Mexico.

Note: TA = temporarily abandoned, PA = permanently abandoned, COM = borehole completed, ST = sidetracked wellbore, and Other = various wellbore statuses for wellbores in the planning stage. 66

Figure 3.3: The distribution of wells from the Eugene Island OPD before and after removing 2,127 wells that had a status of CNL, ST, and AST. 67

Figure 3.4: Total depth distribution of the wells in the Eugene Island OPD including the distribution of their respective status codes of Completed (COM), Temporarily Abandoned (TA), or Permanently Abandoned (PA). 68

Figure 3.5: Spud date distribution of the wells in the Eugene Island OPD including the distribution of their respective status codes of COM, TA, or PA. 68

Figure 3.6: Water depth distribution of the wells in the Eugene Island OPD including the distribution of their respective status codes of COM, TA, or PA. 69

Figure 3.7: Schematic of the shallow well (left), medium well (centered), and deep well (right). Included are the depths of the casing strings, dimensions of the casings, number of casing strings, and the approximate location of the perforations. 71

Figure 3.8: Finkbeiner et al. (1996) data overburden stress (σ_v) with respect to depth. A linear approximation was determined such that the overburden stress can be determined for any depth in the Eugene Island OPD. 72

Figure 3.9: The distribution of wells from the High Island OPD before and after removing 1,055 wells that did not have a status of TA, COM, or PA. 74

Figure 3.10: Total Depth (TD) distribution of the number of wells in the High Island OPD with the distribution of their respective status codes of completed (COM), temporarily abandoned (TA), or permanently abandoned (PA) with an average being 2,541 m (8,336 ft.). Raw data from BSEE (2019). 74

Figure 3.11: High Island well API 427094116400 casing size and depths along with pore pressure and drilling fluid weight gradients in standard units. 76

Figure 3.12: High Island well API 427094116400 casing size and depths along with pore pressure and drilling fluid weight gradients in metric units. 77

Figure 4.1: Velocity profile in a circular pipe with Hagen-Poiseuille flow. Where, R is the radius of the pipe, $P1$ and $P2$ are the inlet and outlet pressures, respectively, V is the velocity, Q is the volumetric flow rate, and Δx and L are the length. 83

Figure 4.2 A) FEA 3D model schematic with dimensions and far-field stresses for the medium well case study. B) 2D schematic of the medium well wellbore with dimensions and internal casing pressure. 92

Figure 4.3 A) Cutaway of the well model showing the three different materials included in the near wellbore region with casing (green), cement (gray), and rock formation (brown) and the finite element grid pattern for the materials. B) 3D view of the finite element gridded model consisting of a total of 18,384 elements. 93

Figure 4.4: Illustration of the segmented discrete method used to model the wellbore from the simulation depth to the top of cement depth (TOC). 97

Figure 4.5: Finite element gridded eccentric tubing configuration (left) and concentric tubing configuration (right) showing the casing (gray), cement sheath with initial pressure location (blue), tubing (green), and cement plug (brown). 102

Figure 4.6: Sensitivity analysis showing the pressure drop (ΔP) versus number of segments relationship used for the explicitly coupled FEA model with the frictional pressure equation (4.54). 1,000 segments was determined to be sufficient for both casing lengths. 105

Figure 4.7: Maximum and minimum initial pressure versus microannuli gap with corresponding average linear correlation for conventional cement with eccentric configuration. Note that for no pressure applied to system, there is not a microannuli gap..... 106

Figure 4.8: Maximum and minimum initial pressure versus microannuli gap with corresponding average linear correlation for conventional cement with concentric configuration. 107

Figure 4.9: Maximum and minimum initial pressure versus microannuli gap with corresponding average linear correlation for expanding cement with eccentric configuration..... 107

Figure 4.10: Maximum and minimum initial pressure versus microannuli gap with corresponding average linear correlation for expanding cement with concentric configuration. 108

Figure 4.11: Pore pressure (long dash), *ICP* (solid line), and microannuli pressure (short dash) with respect to depth for the shallow GoM well (A), medium GoM well (B), and deep GoM well (C). The pore pressure and microannuli pressure start at the same magnitude but decrease with depth at different rates due to the density difference between a water/brine (pore pressure) and a gas (microannuli pressure). 112

Figure 4.12: Model input parameters for mud weight (*MW*), cement stress, minimum (σ_h) and maximum (σ_H) horizontal stress, and overburden stress (σ_v) with respect to depth for the shallow well (A), medium well (B), and deep well (C). 114

Figure 5.1: Microannuli (w) versus flow rate for the developed real and ideal gas flow equations (Equation 4.15 and Equation 4.31, respectively) using experimental data from Corina et al. (2019). The difference between the real and ideal gas flow equations is a maximum of 0.04%, 0.25%, and 0.50% for SF120, SF66, and SF120EA, respectively..... 124

Figure 5.2: Microannuli (w) versus pressure differential (ΔP) for the developed real and ideal gas flow equations (Equation 4.15 and Equation 4.31, respectively) using experimental data from Corina et al. (2019). The difference between the real and ideal gas flow equations is a maximum of 0.04%, 0.25%, and 0.50% for SF120, SF66, and SF120EA, respectively. 124

Figure 5.3: Microannuli (w) versus flow rate for the developed ideal gas flow equation (Equation 4.15) and the Darcy flow equation used in conjunction with the cubic law (Equation 2.54). The maximum percent difference between Equation 4.15 and Equation 2.54 is 1.5% for SF120, 25.3% for SF66, and 55.7% for SF120EA..... 126

Figure 5.4: Microannuli (w) versus pressure differential (ΔP) for the developed ideal gas flow equation (Equation 4.15) and the Darcy flow equation used in conjunction with the cubic law (Equation 2.54). The maximum percent difference between Equation 4.15 and Equation 2.54 is 1.5% for SF120, 25.3% for SF66, and 55.7% for SF120EA. 126

Figure 5.5: FEA stress continuum and fracture model compared to the analytical solution showing less than 2.6% variation of the casing hoop and radial stress, less than 1.4% variation of the cement hoop and radial stress, and less than 7.2% variation of the rock formation hoop and radial stress for the medium well in the Eugene Island OPD. 128

Figure 5.6: Sensitivity analysis of the cement mechanical parameters with respect to the percent change in resulting microannuli. The base microannuli is 13.6 μm . Cement Young's modulus (E)

has a nonlinear effect on microannuli percent change whereas cement Poisson’s ratio (**PR**) appears to have a linear effect. 131

Figure 5.7: 0.5x magnified directional deformation of the eccentric expanding cement model. Note the pressure induced microannuli gap is continuous throughout the circumference of the cement sheath. 132

Figure 5.8: Mohr-Coulomb shear failure envelope of the cement sheath for the shallow (black), medium (orange), and deep (blue) wells. All three wells are not close to shear failure or cement tensile failure. 137

Figure 5.9: Graphical results of the base case stress values shown in Table 5.8 for the shallow, medium, and deep wells for the fracture model. The shear stresses are depicted on the left and the minimum principal stresses are depicted on the right. 138

Figure 5.10: Results of the parametric study with the continuum stress model ranking the parameters with the largest impact on stress development for the shallow well. The cement pore pressure (**Pp**), cement stress, and internal casing pressure have the most effect on the effective cement stress for the shallow well stress continuum model. 140

Figure 5.11: Results of the parametric study with the fracture model ranking the parameters with the largest impact on stress development for the shallow well. The cement pore pressure (**Pp**), cement stress, and internal casing pressure have the most effect on the effective cement stress for the shallow well fracture model. 141

Figure 5.12: Results of the parametric study with the continuum stress model ranking the parameters with the largest impact on stress development for the medium well. The cement pore pressure (**Pp**), cement stress, and internal casing pressure have the most effect on the effective cement stress for the medium well stress continuum model. 142

Figure 5.13: Results of the parametric study with the fracture model ranking the parameters with the largest impact on stress development for the medium well. The cement pore pressure (***Pp***), cement stress, and internal casing pressure have the most effect on the effective cement stress for the medium well fracture model. 143

Figure 5.14: Results of the parametric study with the continuum stress model ranking the parameters with the largest impact on stress development for the deep well. The cement pore pressure (***Pp***), cement stress, and internal casing pressure have the most effect on the effective cement stress for the deep well stress continuum model. 144

Figure 5.15: Results of the parametric study with the fracture model ranking the parameters with the largest impact on stress development for the deep well. The cement pore pressure (***Pp***), cement stress, and internal casing pressure have the most effect on the effective cement stress for the deepwell fracture model..... 145

Figure 5.16: Continuous leakage pathways for the shallow well (black), medium well (blue), and deep well (orange) in the Eugene Island OPD. The solid line is the water induced microannuli while the dashed line is the gas induced microannuli. The water induced microannuli do not propagate up the wellbore whereas the gas induced microannuli propagate up the wellbore for the medium and deep wells..... 147

Figure 5.17: Microannuli magnitude versus reduction in pressure (**ΔP**) and temperature (**ΔT**) at the casing/cement interface. Micron (μm) sized microannuli initiate at **$\Delta P = 43.3\%$** and **$\Delta T = 42.5\%$** 149

Figure 5.18: **ΔP** and **ΔT** and their respective microannuli sizes at the cement/rock interface. Note that the max size of the microannuli are two orders of magnitude smaller than the microannuli at the casing/cement interface..... 150

Figure 5.19: Parametric analysis of the maximum and minimum variables tested for change in wellbore pressures (ΔP) of 29%, 44%, 50%, and 67%. Variances in the hole size and casing thickness have the largest change in resulting gap magnitudes..... 153

Figure 5.20: Parametric analysis of the maximum and minimum variables tested for change in wellbore temperatures (ΔT) of 29%, 44%, 50%, and 67%. None of the wellbore parameters change gap magnitude as significantly as hole size and casing thickness do for change in pressures (ΔP).
..... 154

Figure 5.21: Heat map showing the gap magnitudes resulting from a combination of ΔP and ΔT . A positive Δ indicates a reduction while a negative Δ is an increase. Note in the legend that nanometer (nm) sized gaps are indicated (0.001 μm) along with micron (μm) sized gaps. The results of this heat map are indicative of a 31.12 cm (12.25”) hole size with 24.45 cm (9.625”) P-110EC casing at a depth of 1,920 m (6,300 ft.). 160

Figure 5.22: Heat map showing the gap magnitudes resulting from a combination of ΔP and ΔT . A positive Δ indicates a reduction while a negative Δ is an increase. Note in the legend that nanometer (nm) sized gaps are indicated (0.001 μm) along with micron (μm) sized gaps. The results of this heat map are indicative of a 31.12 cm (12.25”) hole size with 24.45 cm (9.625”) P-110EC casing at a depth of 1,595 m (5,233 ft.). 161

Figure 5.23: Heat map showing the gap magnitudes resulting from a combination of ΔP and ΔT . A positive Δ indicates a reduction while a negative Δ is an increase. Note in the legend that nanometer (nm) sized gaps are indicated (0.001 μm) along with micron (μm) sized gaps. The results of this heat map are indicative of a 31.12 cm (12.25”) hole size with 24.45 cm (9.625”) P-110EC casing at a depth of 1,270 m (4,167 ft.). 162

Figure 5.24: Heat map showing the gap magnitudes resulting from a combination of ΔP and ΔT . A positive Δ indicates a reduction while a negative Δ is an increase. Note in the legend that nanometer (nm) sized gaps are indicated (0.001 μm) along with micron (μm) sized gaps. The results of this heat map are indicative of a 31.12 cm (12.25”) hole size with 24.45 cm (9.625”) P-110EC casing at a depth of 945 m (3,100 ft.). 163

Figure 5.25: Cement/casing interface microannuli size from the simulation depth to the top of cement (TOC) depth for pore pressure induced (water) microannuli (fracture) and gas induced microannuli (fracture). The water induced microannuli propagates up the wellbore for 365 m before it does not form. The gas induced microannuli propagates up the entire cement sheath to the TOC depth..... 165

Figure 5.26: Microannuli width (w) with respect to depth for the FEA model (orange long dash), a constant microannuli (red solid line), and a microannuli with tortuosity (gray short dash). The FEA model microannuli starts off at 23.2 μm and ends at 641.5 μm . The constant microannuli method stays at 23.2 μm from the simulation depth to TOC. The tortuosity method has an average microannuli of 23.2 μm with a Gaussian distribution of 4.64 μm standard deviation..... 167

Figure 6.1: Sensitivity plot for normalized cement Young’s modulus (E) versus the percent change in microannuli gap width. Medium well (Section 4.3) and case study well (Section 4.5) have confining stresses while P&A model (Section 4.2.3) has no confinement. The model confinement reverse the effect Young’s modulus has on gap width. 173

Figure 6.2: Sensitivity plot for normalized cement Poisson’s ratio (PR) versus the percent change in microannuli gap width. The medium well (Section 4.3) and case study well (Section 4.5) have confining stresses while the P&A model (Section 4.2.3) has no confinement. The cement Poisson’s ratio has less than 5% effect on the microannuli gap with and without confinement. 174

Figure 6.3: Flow chart for identifying if a well is at risk for microannuli and for leakage pathways to the environment based on cement shrinkage, reductions of pressure and/or temperature, and a gas source. The flow chart can either be used for wellbores in the planning stage or previously completed..... 178

Abstract

The Gulf of Mexico (GoM) is home to more than 50,000 oil and gas wells with approximately 30,000 wells that are plugged and abandoned leading to concerns of oil and gas leakage where currently, little to no monitoring is performed. The cement used when completing and eventually plugging wells are subject to harsh conditions leading to failure of the cement due to debonding of the cement to the formation and/or casing, shrinkage of the cement, and chemical degradation in the cement. Due to the complicated mechanical and chemical nature of cement, researchers have turned to numerical simulations to model cement failure and predict potential leakage rates. However, the numerical models in previous studies either predict leakage mechanisms but fail to provide comprehensive quantification of the fracture magnitudes. Or the models assume a fracture value and quantify leakage assuming water as the leaking fluid.

The goal of this study is to determine if leakage is occurring through the cement sheath in GoM wells. This study develops a realistic finite element analysis (FEA) model coupled with fluid flow to determine if hydraulic propagation occurs providing a continuous leakage pathway. An analytical gas flow model is developed and used in conjunction with the FEA fracture volume to provide accurate fluid leakage rates within the pathways.

The results of this work show that FEA models coupled with fluid flow can accurately quantify microannuli magnitude and predict if the microannuli propagate up the wellbore to the environment. The fluid flow models show that assuming wellbore water leakage versus gas leakage has an order of magnitude difference in leakage rates, cement shrinkage occurs in conventional cements causing continuous leakage pathways, and cement additives that change the mechanical properties of the cement are not required to achieve wellbore integrity.

Chapter 1: Introduction

Wellbore leakage can occur throughout every stage of a wells life. The construction of the well only accounts for a small portion of a wells life, thus wellbore leakage is most likely to occur after drilling and completion once the casing and cement are present (Fourmaintraux et al. 2005; Zhang and Bachu 2010; Feng et al. 2017). This leakage is known to contribute to oil and gas well blowouts, resulting in a complete loss of wellbore integrity (Khodami et al. 2021). Wellbore leakage is often observed as surface casing pressure (SCP), surface casing vent flow (SCVF), or gas migration (GM) (Nelson and Guillot 2006; Wolterbeek et al. 2021).

Migration of wellbore fluids can contaminate aquifers or potentially even reach the surface environment (Watson and Bachu 2007). For example, in Alberta, Canada, approximately 4.6% of the 440,000 wells have SCVF (Bachu and Watson 2006; Natural Resources Canada 2019). Data taken from wells in Pennsylvania showed that between 2000 and 2012, approximately 1.9% of 41,381 wells had integrity issues (Ingraffea et al. 2014). Kang et al. (2014) measured surface methane emissions on 19 plugged and abandoned (P&A) wells and determined that more than half of the wells exhibited leakage. Kell (2011) investigated wells in Texas and Ohio and noted that out of 250,000 wells, 211 had leakage into groundwater due to integrity failure. All of these wells are onshore and relatively easy to access. However, the question arises about offshore wellbore integrity? According to the regulatory agencies, the Bureau of Ocean Energy Management (BOEM) and the Bureau of Safety and Environmental Enforcement (BSEE), the Gulf of Mexico has over 54,000 wells. Assuming that offshore wells follow similar trends as onshore wells, significant leakage could be occurring in the Gulf of Mexico.

Before a well can be permanently P&A'ed, it has to meet current standards designated by specific regulatory agencies for the region/country to prevent leakage. For instance, cement bond

logs (CBL) showing intact cement sheath are required before P&A procedures can occur according to 30 CFR 250, Subpart Q, Decommissioning Activities, Section §250.1715 for the Gulf of Mexico (2011). A limitation of CBL's are that they cannot detect gas-filled microannuli gaps or quantify the gap sizes (De Andrade et al. 2019). This is a problem because cement sheath microannuli is a likely pathway for fluid migration (Bois et al. 2011; Vrålstad et al. 2018). To better understand how microannuli gaps form and what influences the size of such gaps, various modeling approaches have been implemented in the past. An in depth overview of different models are shown in Chapter 2.

The various models have shown the likely leakage mechanisms and locations of leakage, but have failed to provide comprehensive quantification of the microannuli widths. Many models assume a microannuli (or permeability) value (Ford et al. 2017; Lavrov and Torsaeter 2018; Moeinkia et al. 2018). Other models have treated wellbore leakage as a hydraulic fracturing process assuming water to be the fluid causing fracturing and leakage (Zielonka et al. 2014; Feng et al. 2017; Jiang et al. 2020). The water assumption makes the numerical approximation simple, but could be unrealistic if gas is the fracturing fluid.

The objective of this dissertation is to determine if leakage is occurring through the cement sheath in Gulf of Mexico wells. The deliverables of this work are to develop a realistic FEA model coupled with fluid flow to determine if hydraulic propagation is occurring providing a continuous leakage pathway and to predict accurate fluid leakage rates within the leakage pathways.

In the following chapters, a critical literature review is presented in Chapter 2. Chapter 3 will describe the Gulf of Mexico, the study location for a representative analysis, and the location for the case study well. The fluid flow models, the finite element analysis (FEA) models, and the associated parameters used within the models will be discussed in Chapter 4. Chapter 5 will present

the model verifications and comparisons along with the Gulf of Mexico representative analysis and the case study well. The discussion of the results is in Chapter 6 followed by the conclusions and future work in Chapter 7.

Chapter 2: Critical Literature Review

An oil and gas well's life cycle can be broken down into three main phases: construction, operation, and abandonment. The following sections give a brief overview of all three phases and how they can contribute to potential leakage. It is important to note that this is not a complete set of rules and regulations for designing, operating, and abandoning a wellbore. This section serves as a brief overview.

2.1 Well Construction

Wellbores are designed with steel casing and cement to prevent leakage and maintain wellbore integrity and support the wellbore wall made up by the surrounding rock formation. The cement is placed in the annulus between the casing and the formation (known as the cement sheath) when a well is completed and serves dual purposes: the cement is responsible to hold and support the casing in place and to provide zonal isolation between formation fluids of different zones (Smith 1984; Smith 1987; Nelson 1990). The annulus between the casing and the borehole can be cemented from the bottom of a casing string to the surface but other times, wells are only partially cemented through hydrocarbon or freshwater zones to provide zonal isolation. Therefore, the integrity of the cement is critical in preventing leakage. To ensure integrity a thorough understanding of the rock formation casing and cement sheath is required.

Rock Formation

When a wellbore is drilled, the drilling fluid ensures stable wellbore walls (Bourgoyne et al. 1986)¹. The removal of the rock and replacement of a fluid column causes the in-situ stresses

¹This section (and an in depth overview of rock mechanics discussed in Appendix A) stem from work presented in Jaeger et al. (2007) and Fjaer et al. (2008). This section assumes the reader understands the concept of principal stresses, radial stress, hoop stress, effective stress, and tensile stress.

in the rock to be altered around the wellbore. Since the wellbore fluid pressure is different in magnitude and acting isotropically on the cylindrical wellbore wall instead of a combination of orthogonal stresses, a stress concentration is created around the wellbore. There are two types of stress categories:

- The far field stress field in the rock (i.e. in-situ stresses)
- The stress concentration around the wellbore

The Kirsch (1898) equations describe the concentration of stresses for a circular hole in an infinite linear elastic plate with a uniform tension within the solid and were later modified to include anisotropic horizontal stresses and the wellbore fluid pressure (Hiramatsu and Oka 1968; Bradley 1979).

For the wells in this dissertation, the wellbores are oriented vertically and are parallel to the overburden stress. This assumption simplifies the Kirsch equations as illustrated in Figure 2.1. The following Equations, 2.1-2.5, describe the stress concentrations around the wellbore in terms of the hoop stress (σ_θ), radial stress (σ_r), vertical stress (σ_v or σ_z), and shear stresses ($\tau_{r\theta}$, $\tau_{\theta z}$, and τ_{rz}) given the far field stresses (σ_v , σ_H , and σ_h) are known.

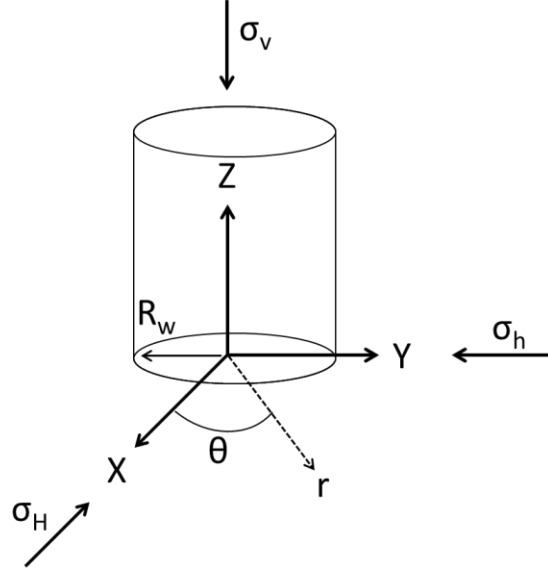


Figure 2.1: Schematic of a wellbore orientated such that the borehole is parallel to the overburden stress (σ_v). The principal stresses are represented with respect to Cartesian coordinates.

$$\sigma_r = \frac{\sigma_H + \sigma_h}{2} \left(1 - \frac{R_w^2}{r^2}\right) + \frac{\sigma_H - \sigma_h}{2} \left(1 + 3 \frac{R_w^4}{r^4} - 4 \frac{R_w^2}{r^2}\right) \cos 2\theta + P_w \frac{R_w^2}{r^2} \quad 2.1$$

$$\sigma_\theta = \frac{\sigma_H + \sigma_h}{2} \left(1 + \frac{R_w^2}{r^2}\right) - \frac{\sigma_H - \sigma_h}{2} \left(1 + 3 \frac{R_w^4}{r^4}\right) \cos 2\theta - P_w \frac{R_w^2}{r^2} \quad 2.2$$

$$\sigma_z = \sigma_v - 2\nu(\sigma_H - \sigma_h) \frac{R_w^2}{r^2} \cos 2\theta \quad 2.3$$

$$\tau_{r\theta} = -\frac{\sigma_H - \sigma_h}{2} \left(1 - 3 \frac{R_w^4}{r^4} + 2 \frac{R_w^2}{r^2}\right) \sin 2\theta \quad 2.4$$

$$\tau_{rz} = \tau_{\theta z} = 0 \quad 2.5$$

At the borehole wall (with a borehole pressure, P_w):

$$\sigma_r = P_w \quad 2.6$$

$$\sigma_{\theta} = \sigma_H + \sigma_h - 2(\sigma_H - \sigma_h)\cos 2\theta - P_w \quad 2.7$$

$$\sigma_z = \sigma_v - 2\nu(\sigma_H - \sigma_h)\cos 2\theta \quad 2.8$$

$$\tau_{r\theta} = \tau_{\theta z} = \tau_{rz} = 0 \quad 2.9$$

Equation 2.7 indicates that the maximum and minimum hoop stresses at the wellbore wall will occur at:

$$\sigma_{\theta,max} = 3\sigma_H - \sigma_h - P_w \quad 2.10$$

$$\sigma_{\theta,min} = 3\sigma_h - \sigma_H - P_w \quad 2.11$$

in which the maximum hoop stress occurs in the direction of the minimum horizontal stress ($\sigma = 90^\circ$) and the minimum hoop stress occurs in the direction of the maximum horizontal stress ($\sigma = 0^\circ$) as shown in Figure 2.2.

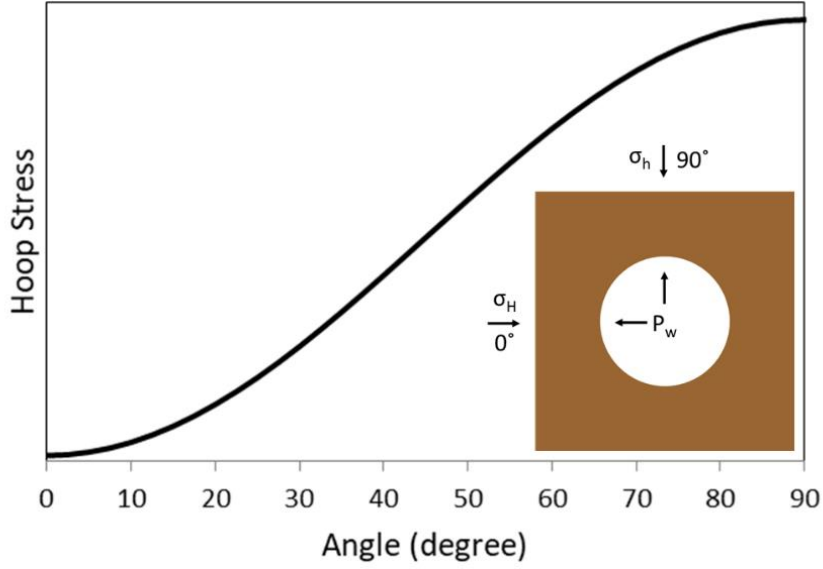


Figure 2.2: Illustration showing the magnitude of hoop stress around a wellbore.

Equations 2.1-2.4 can be converted to effective stress by including initial pore pressure (P_p).

$$\sigma'_r = \frac{\sigma_H + \sigma_h}{2} \left(1 - \frac{R_w^2}{r^2}\right) + \frac{\sigma_H - \sigma_h}{2} \left(1 + 3 \frac{R_w^4}{r^4} - 4 \frac{R_w^2}{r^2}\right) \cos 2\theta + (P_w - P_p) \frac{R_w^2}{r^2} \quad 2.12$$

$$\sigma'_\theta = \frac{\sigma_H + \sigma_h}{2} \left(1 + \frac{R_w^2}{r^2}\right) - \frac{\sigma_H - \sigma_h}{2} \left(1 + 3 \frac{R_w^4}{r^4}\right) \cos 2\theta - (P_w - P_p) \frac{R_w^2}{r^2} \quad 2.13$$

$$\sigma'_z = \sigma_v - 2\nu(\sigma_H - \sigma_h) \frac{R_w^2}{r^2} \cos 2\theta - P_p \quad 2.14$$

$$\tau'_{r\theta} = -\frac{\sigma_H - \sigma_h}{2} \left(1 - 3 \frac{R_w^4}{r^4} + 2 \frac{R_w^2}{r^2}\right) \sin 2\theta - P_p \quad 2.15$$

And Equations 2.6-2.8 and ultimately Equations 2.10 and 2.11, respectively:

$$\sigma'_r = P_w - P_p \quad 2.16$$

$$\sigma'_{\theta} = \sigma_H + \sigma_h - 2(\sigma_H - \sigma_h)\cos 2\theta - P_w - P_p \quad 2.17$$

$$\sigma'_z = \sigma_v - 2\nu(\sigma_H - \sigma_h)\cos 2\theta - P_p \quad 2.18$$

With a max and min of:

$$\sigma'_{\theta,max} = 3\sigma_H - \sigma_h - P_w - P_p \quad 2.19$$

$$\sigma'_{\theta,min} = 3\sigma_h - \sigma_H - P_w - P_p \quad 2.20$$

According to the Kirsch analytical equations for anisotropic poro-elastic material with a pressurized open hole, the plot of the effective hoop and radial stresses versus the ratio of the position, r , to the wellbore radius, R_w , shows that the stress concentrations around the open hole dissipate into the in-situ stresses, as illustrated in Figure 2.3.

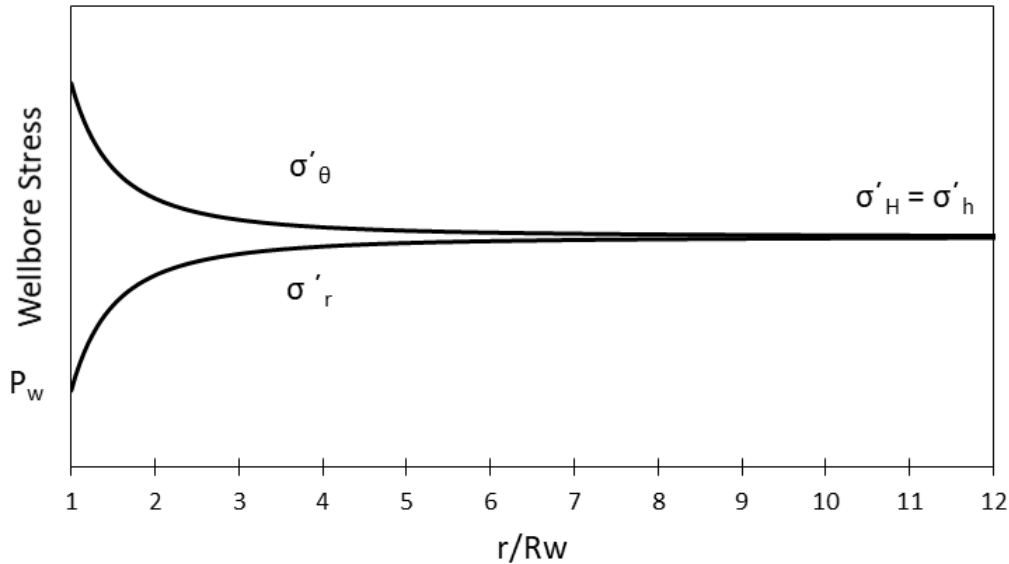


Figure 2.3: Kirsch analytical solution of the effective hoop and radial stress from the wellbore versus the distance away from the wellbore.

Steel Casing

The steel casing serves several important functions within the wellbore. It prevents collapse of the borehole, isolates unwanted rock formations from fluid fracturing, and hydraulically isolates wellbore fluids from rock formations and in-situ formation fluids (Bourgoyne et al. 1986). Wellbores are drilled like an inverse telescope. The largest sections are drilled in the shallowest depths while the smallest sections are in the deepest depths such that the deeper casings all fit within the next shallowest one. The design of the steel casing is based off the mud weight window.

An example of a drilling fluid weight window with a corresponding casing design is shown in Figure 2.4. The drilling fluid weight window ranges from the formation pore pressure to the formation fracture pressure. If the drilling fluid weight is below the pore pressure, the rock formations experience breakouts. If the drilling fluid weight is above the fracture pressure, the borehole will be fractured. As shown in Figure 2.4, the pore pressure and fracture pressure change with depth. A constant drilling fluid weight that works at 1,000 m will cause wellbore stability issues at 2,500 m. Therefore, the casing is used to isolate shallower formations such that the wellbore will be stable, and the correct drilling fluid weight can be used for deeper formations.

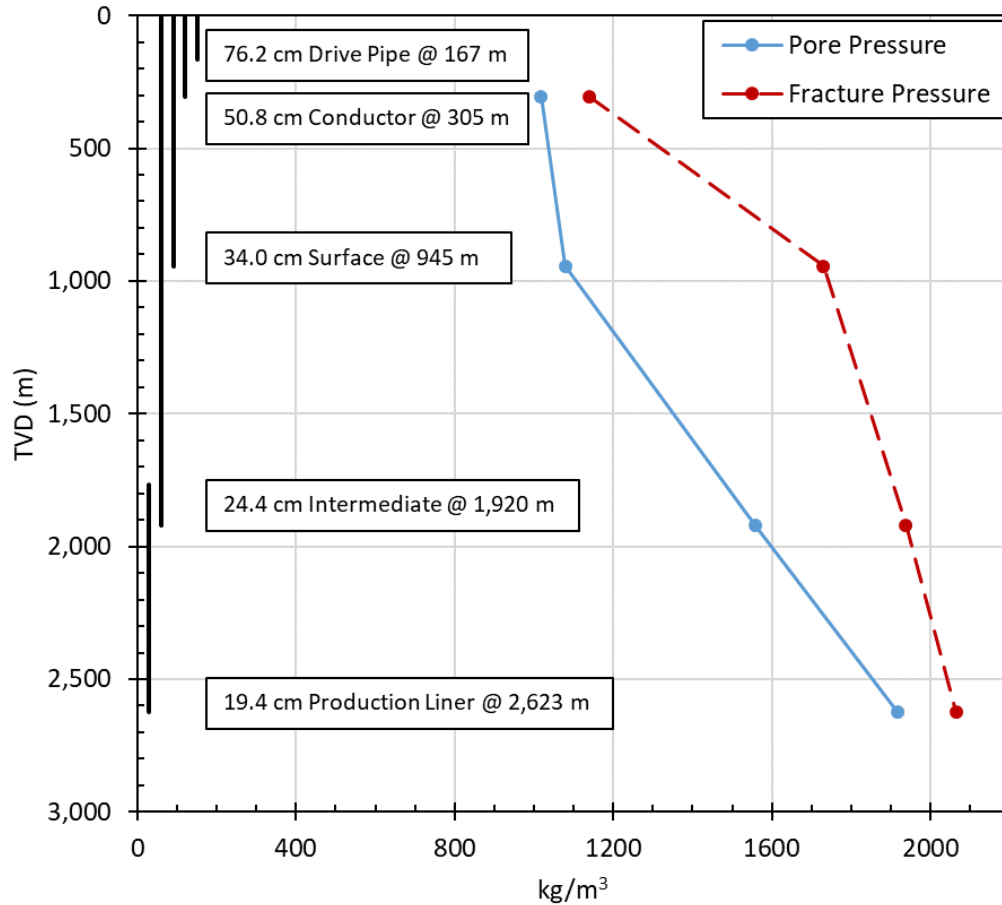


Figure 2.4: Example drilling fluid weight window with corresponding casing design from GoM well API 427094116400.

The casing is designed to withstand three types of loads: burst, collapse, and tensile loads (API 2015). Burst loads are the maximum pressure inside the casing and are determined by the drilling fluid weight/fracture fluid pressure. Collapse loads are the maximum load the casing can sustain from the outside. Tensile loads are the maximum axial load the casing allows.

Cement Sheath

The annular cement sheath is used to hold the casing in place, to provide stability and zonal isolation between formation fluids (Smith 1984; Smith 1987; Nelson 1990). Cement involves a complicated chemical and thermal process that involves two phases: when the cement is a slurry (liquid), and when the cement is a paste (solid) (Vu et al. 2018; Bois et al. 2019). The cement undergoes the liquid to solid transition through cement hydration. The following subsections

discuss the placement of the cement slurry, hydration, shrinkage, and a brief discussion of different additives.

2.1.1 Wellbore Cementing Procedures and Materials

Primary cementing is placing cement within the annular space between the casing and the formation (Nelson 1990). The outer cement sheath has a dual purpose; it supports the casing and provides zonal isolation between formation fluids of different zones (Smith 1984; Smith 1987; Nelson 1990). Cement also acts as a hydraulic seal in annuli between casings or between the casing and the formation. This seal needs to be in full contact between the two interfaces to prevent flow conduits from forming, thus preventing leakage through the cement sheath. The formation of flow conduits requires additional cementing operations, which are likely to be costly, time-consuming, and may damage the wellbore.

The basic process for performing a primary cement job uses a two-plug method after drilling a well section to the desired depth and casing is inserted into the hole while the drilling fluid remains in the hole (Smith 1987). The primary cement job's objective is to displace drilling fluid and replace it with the cement slurry. For the common two-plug cementing method, two mechanical plugs are used to isolate the cement slurry as it is pumped through the casing and prevent it from coming in contact with the drilling fluid. One plug is placed between the cement slurry and drilling fluid while the other follows the cement slurry and prevents any displacement fluids from coming in contact with the slurry. If the cement slurry and drilling fluid/displacement fluids get mixed, the cement slurry will become contaminated, and the mechanical and/or chemical properties may change, potentially leading to undesired effects or the creation of flow paths. Enough cement slurry is pumped such that the annular column is filled from the bottom of the casing to past any production/freshwater zones. The cement slurry may be pumped such that it fills

the annular space from the bottom of the casing string to the surface depending on the stability and depth of the wellbore. In many wellbores, the annular cement job is cemented partially to the surface, referenced as the top of cement (TOC), per regulatory bodies such as API Standard 65-2 (2010). Once the slurry is pumped to the desired locations, the well is left shut-in to allow the cement to hydrate and harden.

Cement Hydration

Portland cement powder when mixed with water evolves with time to produce a solid material referred to as cement paste. Portland cement is initially made from the mixing of raw materials (such as lime, silica, and alumina) and heated to 1,500 °C to form clinker composed mainly of Alite, Belite, Aluminite, and Ferrite (Bensted and Barnes 2002). The clinker is ground down to specific particle sizes and the resulting product is Portland cement (Bensted and Barnes 2002).

The anhydrous compounds within Portland cement, when mixed with water, starts a complex chemical process (i.e. cement hydration) that initially reacts quickly (minutes) and takes a long time to fully react (months to years) (Bensted and Barnes 2002). Hydration of Portland cement creates four main components: remaining anhydrous grains (un-hydrated clinker), high-density calcium silicate hydrate (CSH), low-density CSH (which is composed of Ettringite and other impurities), and portlandite (which is hardened calcium hydroxide) (Bensted and Barnes 2002). Cement hydration results in intergranular and intragranular porosity. The intergranular porosity is due to the volume of the end products (cement hydration products and water) being smaller than the volume of the initial reactants (Portland cement powder and water). The pores within the CSH grains initially go to the cavitation pressure of the liquid within the cement once hydration is complete (Ghabezloo et al. 2008; Saint-Marc et al. 2008; Bois et al. 2012). Cavitation

pressure is defined as the pressure at which a liquid transitions to a gas (i.e. vaporization pressure) (Piau et al. 1995). Bois et al. (2012) developed a model that shows how the cement sheath pore pressure goes to the cavitation pressure once hydration is complete and equalizes with the surrounding rock formation such that the two pressures are equivalent. This means that the pore pressure on hydrated cement is equal to the vaporization pressure of the water solution, but if the hardened cement has access to outside pressure, which would be available in a permeable rock formation (rock pore pressure), the pressures will “equalize” resulting in the cement pore pressure becoming equal with the surrounding pressure. The time required for the cement pore pressure being equal to the surrounding rock formation pore pressure is dependent on the permeability of the cement and rock formation. Low permeability systems will require longer time periods for the pressure to equalize (if at all) while high permeability systems will equalize quicker.

Shrinkage

Shrinkage is defined as the dimensional change (volumetric change) in cements after placement (API 10B-5 2010). Cement shrinkage can be thought of as external and/or internal shrinkage. External shrinkage can result in debonding and microannuli formation between the cement sheath and the casing and/or rock formation interface while internal shrinkage can result in tensile cracks resulting in increased permeability (Reddy et al. 2007; API Standard 65-Part 2 2010).

From a geometric standpoint, there are three forms of external shrinkage possible: uniform volumetric, radial volumetric, or axial volumetric. A schematic of shrinkage of a cement plug is shown in Figure 2.5.

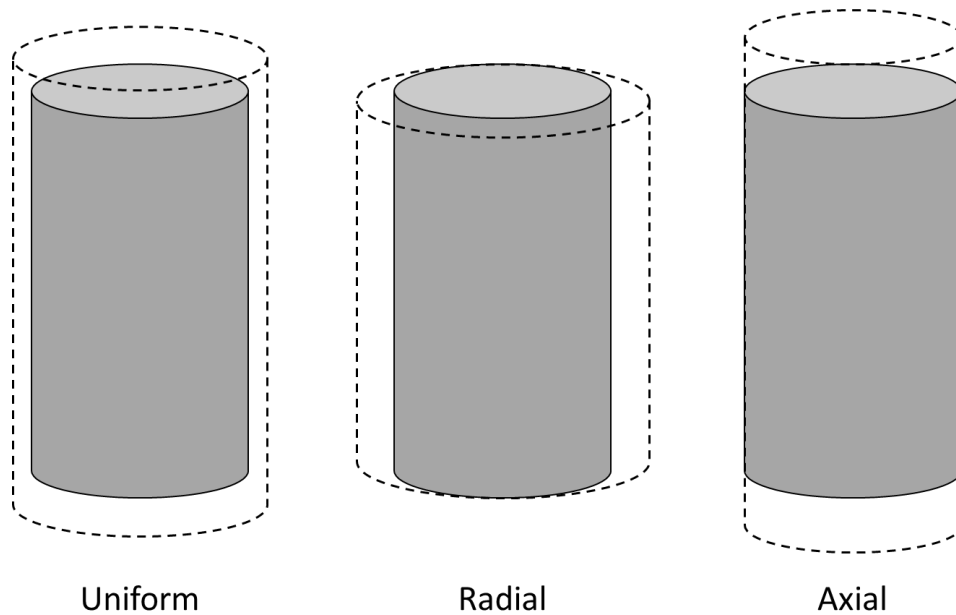


Figure 2.5: Schematic of uniform, radial, and axial cement shrinkage. Uniform volumetric shrinkage assumes the same percent change in volume of both the radial and axial direction. Radial volumetric shrinkage assumes only volumetric shrinkage in the radial direction. Axial volumetric shrinkage assumes only volumetric shrinkage in the axial direction.

Additives

Cement additives are used in cement mixtures to establish or maintain wellbore integrity given specific downhole conditions. Additives can be used in cement slurries for various reasons including but not limited to increasing or decreasing the slurry density, changing mechanical properties (such as compressive strength, tensile strength, fracture resistance, Young’s modulus, Poisson’s ratio, porosity, permeability, temperature dependence, etc.), accelerating or retarding the setting time, increasing bond strength, altering the fluid rheology, or preventing shrinkage by causing expansion (Jones et al. 2014; Beharie et al. 2015; Bhaisora et al. 2015; Mansour et al. 2017; Ritchie et al. 2019; Ziashahabi et al. 2019; Baklushin et al. 2019).

2.2 Well Operations

After a well is constructed, different wellbore operations can alter the loads and conditions within the wellbore. Some common operations are wellbore fracturing (completions), production,

enhanced oil recovery (EOR), and injection of fluids. This section briefly outlines the different effects used in relation to wellbore integrity simulations.

Hydraulic fracturing operations create fractures in reservoir rocks by injecting liquids at high pressures within the casing to perforations at desired locations. In a normal faulting stress regime, such as in the GoM, the pressures required are greater than the minimum horizontal stress within the formation (often referred to as rock fracture gradient). Annular cement sheaths are designed that the density is greater than the pore pressure but less than the fracture gradient. So if the cement is in contact with the injected fluids, it can become fractured. The steel casing protects the cement sheath from direct contact, but injected fluid can cause stress changes in the casing which can be transmitted to the cement sheath. Wellbore temperatures can also cause stress changes due to thermal equalization of the injected fluid at surface temperatures to the reservoir temperature.

Hydrocarbon production occurs after the well is completed in which the subsurface fluids are brought to the surface either through natural pressure driven flow or through artificial lift methods (Jahn et al. 2008). As production declines, the pressure within the wellbore declines resulting in a change of internal casing pressure. The wellbore may not be financially viable that the engineers may decide to “shut in” the well where the wellbore is closed off at the Christmas tree or blowout preventer (BOP) stack. The pressure within the well may increase if a greater pressure is within the reservoir than the pressure of the hydrostatic column. If the shut-in pressure is zero, the pressure of the hydrostatic column balances any formation pressure, and the well may begin the abandoning process.

The requirements for wellbore P&A procedures vary over time and from region to region. The overall goal of P&A is to prevent the influx of fluids into or out of the well. The most common

barrier used to prevent flow from a well is cement (30 CFR 250.420). Cement has physical and chemical limitations in which leakage pathways can occur due to conditions and events that occur for a specific well. When P&A`ing a wellbore, the common assumption is that plugging the casing is sufficient. However, ensuring the cement sheath integrity is intact is critical to prevent leakage. Common wellbore leakage mechanisms are discussed in the following section.

Wellbore leakage

Leakage in a wellbore can occur in the casing, annular/plug cement, and/or in the rock formation. The different leakage pathways can be placed into two categories: primary and secondary (Weideman 2014). The primary leakage pathways are pathways that are created during the cementing job and include:

- 1) An incomplete annular cementing job that does not reach the seal layer (Bois et al. 2011).
- 2) A lack of cement plug or permanent packer (Watson and Bachu 2009).
- 3) Failure of the casing by burst or collapse (Cooke et al. 1983).
- 4) Poor cement bonding caused by drilling fluid cake (Bois et al. 2011).
- 5) Channeling in the cement (Nelson and Guillot 2006).
- 6) Primary permeability in the cement sheath or cement plug (Cooke et al. 1983).

The secondary leakage pathways occur after the cement job is complete and include:

- 7) Debonding due to tensile stress on the casing/cement and cement/rock interfaces (Bois et al. 2012)
- 8) Fractures in the cement and/or rock formation (Bois et al. 2012).
- 9) Chemical dissolution and carbonation of the cement (Nygaard et al. 2011).
- 10) Wear or corrosion of the casing (Watson and Bachu, 2009; Nygaard et al. 2011).

The various leakage pathways that can occur in the near wellbore region are shown in Figure 2.6 and are divided between primary and secondary. The subsequent sections discuss the leakage mechanisms for the rock formation, casing, and cement sheath.

PRIMARY

1. Incomplete annular cementing job that doesn't reach the seal layer.
2. Lack of cement plug or permanent packer.
3. Failure of the casing by burst or collapse.
4. Poor cement bonding caused by mudcake.
5. Channeling in the cement.
6. Primary permeability in the cement sheath or cement plug.

SECONDARY

7. De-bonding due to tensile stress on casing/cement and cement/formation interfaces.
8. Fractures in the cement and/or formation.
9. Chemical dissolution and carbonation of cement.
10. Wear or corrosion of the casing.

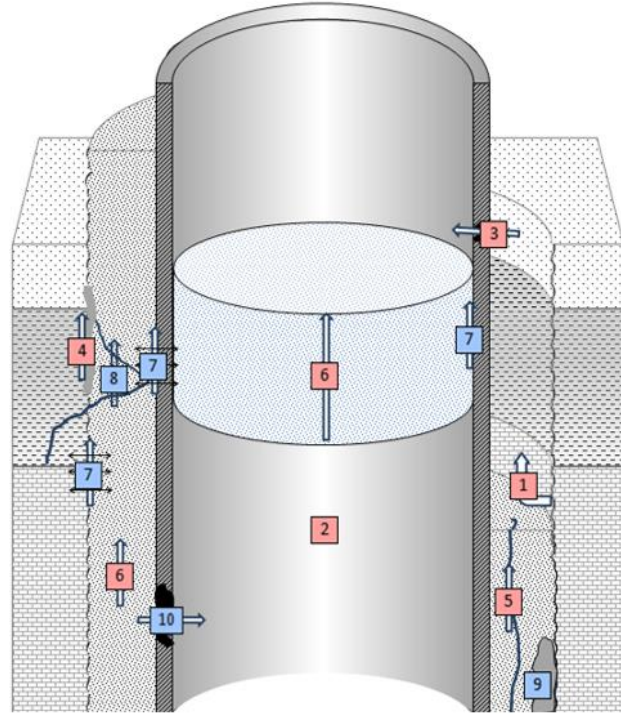


Figure 2.6: Primary and secondary leakage pathways in the near wellbore region. Picture from Weideman (2014).

Steel is a well-studied material. The rock formation has also been studied extensively in the past, however, there are fewer design aspects the engineers can do for long term integrity with respect to the formation. The cement used when completing and eventually plugging the well is less understood with complications from all the different additives. Therefore, this work focuses on determining if leakage occurs through the cement sheath, specifically, secondary leakage mechanisms of debonding and/or fractures.

2.3 Cement Secondary Failure Mechanisms

Secondary failure mechanisms of the cement sheath are shown in Figure 2.7. Debonding occurs at the cement interface when the effective radial stress is less than the tensile bond strength of the interface as shown in Equation 2.21. Radial cracks occur when the effective hoop stress is less than the tensile strength of the cement as shown in Equation 2.22. Shear cracks occur when the effective shear stress is greater than the maximum allowable shear stress of the cement (as

defined by the shear failure criteria) as shown in Equation 2.23. Disking occurs when the effective vertical stress is less than the tensile strength of the cement as shown in Equation 2.24.

$$\sigma'_r \leq \tau^o \quad 2.21$$

$$\sigma'_\theta \leq T_o \quad 2.22$$

$$\tau_f \geq \tau_{criteria} \quad 2.23$$

$$\sigma'_v \leq T_o \quad 2.24$$

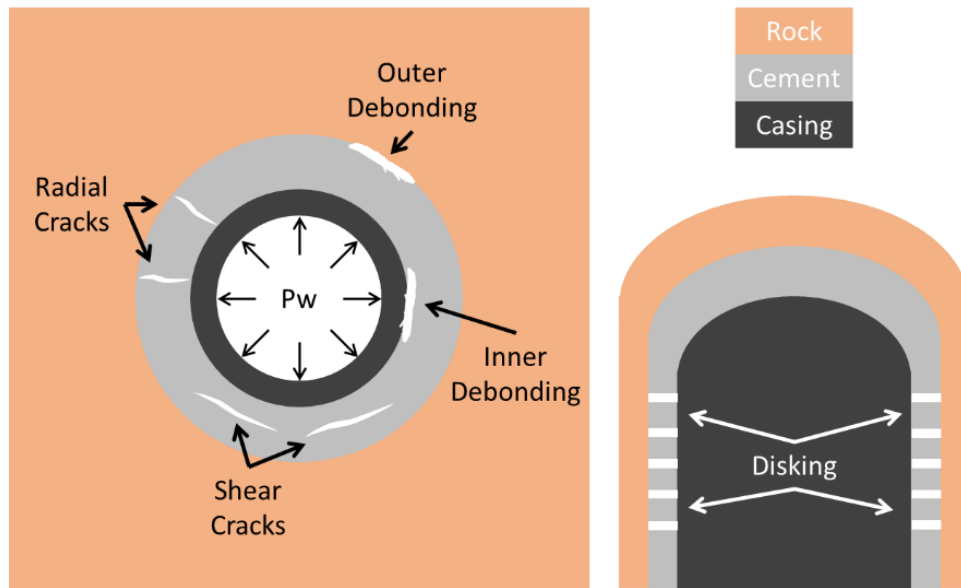


Figure 2.7 A: Failure mechanisms within the cement sheath showing inner and outer debonding, radial cracks, and shear cracks. B: Failure mechanism within the cement sheath showing diskings.

Since physically investigating which secondary leakage mechanism occurs in offshore wells is not expected due to cost and difficult conditions, numerical methods have been used to predict which mechanisms are most likely. FEA models replicating the short and long term behavior of wellbores show that debonding is the predominant failure mechanism (Zhang et al.

2017; Crain et al. 2018; Bois et al. 2019; Patel and Salehi 2019). The theory and physics behind cement sheath debonding are discussed in the following section.

2.3.1 Debonding

Three different types of debonding that can occur in wellbore cement sheaths: tensile, shear, and hydraulic (Opedal et al. 2019). Tensile bond strength is the force required to initiate perpendicular movement between the cement to the casing and/or formation. Shear bond strength is the force required to initiate parallel movement between the cement to the casing and/or formation. Finally, hydraulic bond strength is the fluid force required to propagate fluid flow between the cement and adjacent material. A schematic of each bonding mechanism is shown in Figure 2.8.

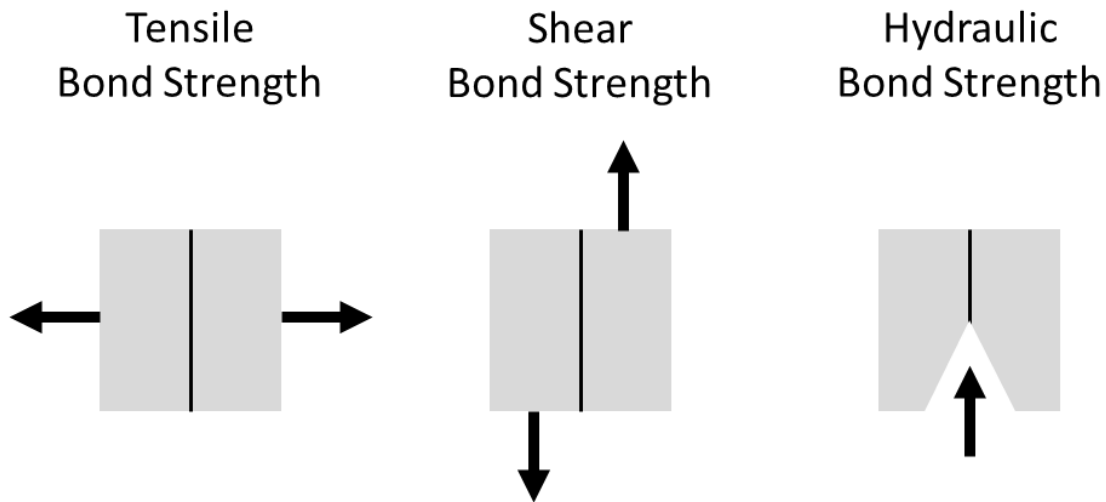


Figure 2.8: Schematic of the three bond strengths: tensile, shear, and hydraulic.

Tensile bond strength has been measured experimentally through different methods. Cerasi and Stroisz (2015) performed direct tensile bond strength experiments with cement/Berea sandstone samples to replicate the cement to formation bonding. These direct tensile bond strength experiments consisted of curing cement directly on top of a sandstone core. A tensile apparatus is connected to one end of the sample while the other end is fixed in place. The force versus

displacement of the test is recorded, and the tensile bond strength can be calculated from the maximum force and the surface area of the bond. Cerasi and Stroisz's (2015) results showed that failure occurs in the sandstone, not the cement/sandstone interface. This result indicates that the cement/sandstone tensile bond strength is stronger than the strength of the sandstone. Cerasi and Stroisz's (2016) experiments were expanded by Stroisz et al. (2019) to investigate the bond strength between the cement/shale interface and concluded that when the cement is bonded with shale, the failure occurs at the interface. This result determined that the strength of shale is stronger than the tensile bond strength of the cement/shale interface. A limitation of the experiments performed by Cerasi and Stroisz (2015) and Stroisz et al. (2019) are that they are performed at atmospheric conditions. Many variables such as access to free water, confinement pressure, and temperature can all play a factor in the bond strength.

The previous experiments by Cerasi and Stroisz (2016) and Stroisz et al. (2019) investigated tensile bond strengths, but the researchers did not consider shear bond strength measurements. One such experiment to determine shear bond strength is the push-out test. Push-out tests are performed such that cement slurry is placed around a steel pipe in order for it to bond circumferentially around the pipe. Once the cement hardens, the pipe is pushed downwards while the force and displacements are measured. The shear bond strength can be determined based on the maximum force and the surface area of the bond. Lavrov et al. (2019) performed push out tests with various dimensions of steel pipe (10 mm to 33.6 mm) and determined that as the size of the steel pipe increases, the shear bond strength decreases. This result contradicts the assumption that bond strength is size independent and can be normalized to surface area (psi or MPa). Lavrov et al. (2019) hypothesized that cement shrinkage may be a contributing factor to their results. The authors created FEA models of cement shrinkage within the pipe and determined that cement

shrinkage does not account for the change in bond strength with respect to pipe diameter. Therefore, Lavrov et al. (2019) concluded that the push out test cannot be used to determine shear bond strength measurement, but it can be used to compare relative change between different cement mixtures or surface conditions (pipe material).

Carter and Evans (1964) performed experiments to measure shear and hydraulic bond strengths of cement to casing. The authors defined the shear bond as the force required to initiate pipe movement from the cement sheath divided by the cement to casing contact surface area. The hydraulic bond strength was defined as the pressure required to cause leakage at the pipe and cement interface using both water and gases (nitrogen and compressed air). The authors showed that the hydraulic water bond strength is significantly higher than both nitrogen gas bond strength and shear bond strength as shown in Table 2.1. An interesting observation is that gas hydraulic bond strength is extremely low, especially during the early cement curing.

Table 2.1: Hydraulic and shear bond strengths from Carter and Evans (1964) with at different curing ages.

Time days	Water Hydraulic psig [MPa]	Nitrogen Gas Hydraulic psig [MPa]	Shear psig [MPa]
1	200 [1.38]	15 [0.10]	59 [0.41]
2	170 [1.17]	10 [0.07]	48 [0.33]
3	210 [1.45]	30 [0.21]	57 [0.40]
4	250 [1.72]	40 [0.28]	59 [0.41]
5	270 [1.86]	55 [0.38]	61 [0.42]

A limitation to the experiments performed by all of the researchers discussed in this section is that they quantified bond strength as a single parameter. As described by Wang and Taleghani (2014), bond strength, fracture energy (related to fracture toughness), and the failure damage process are required to get the complete picture for the mechanism of the debonding process. Debonding can be described numerically by the traction separation law which is discussed in greater detail in the subsequent section.

Traction Separation Law

The traction separation law can be used to simulate cement sheath debonding by relating the fracture surface tractions to material separation (Turon et al. 2006). In fracture mechanics, three modes of separation (debonding) can occur: Mode I, Mode II, and Mode III or a combination of these (SIMULIA 2016; ANSYS 2019). Mode I separation is tensile debonding, Mode II separation is shear debonding, and Mode III separation is a mixture of Mode I and Mode II. To replicate tensile and hydraulic debonding, Mode I separation is assumed. A graphical representation of Mode I separation is shown in Figure 2.9. At point 0 in Figure 2.9, the two surfaces have no separation and are in “bonded” contact. The two surfaces experience linear elastic loading (from points 0 to 2) with a slope being that of the normal contact stiffness (k_c). Once the maximum normal contact stress (τ_{max}) is reached (point 2), debonding starts to occur with plastic separation until the normal contact stress reaches zero (points 2 to 4). After point 4, further separation occurs without any normal contact stress (point 5). The area under the traction-separation curve is the critical fracture energy (G_c), which is the energy released during debonding.

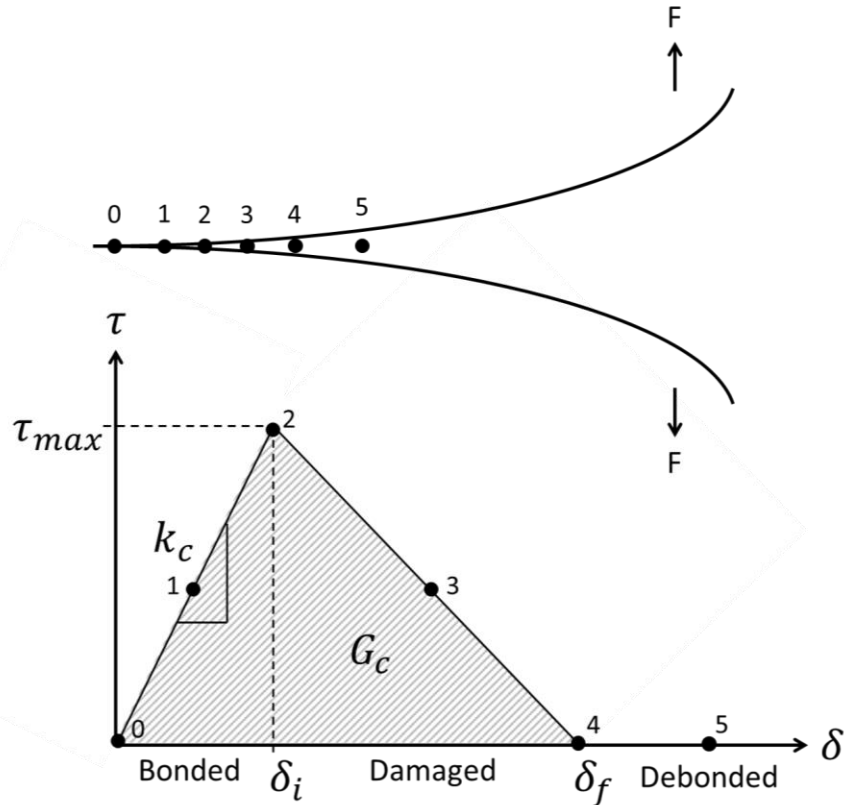


Figure 2.9: Mode I debonding (top) with the corresponding traction separation law (bottom).

To numerically replicate the traction separation law, the following parameters are required: peak tensile stress (τ_{max}), critical [fracture] energy (G_c), complete separation distance (δ_f), and contact stiffness (k_c). However, not all of these parameters are easy to determine in the lab. The most common parameter is the peak tensile stress which is the maximum stress the material can take before complete separation. The peak tensile stress is the value reported by researchers such as Carter and Evans (1964). The critical energy is the total amount of mechanical energy required to cause complete separation. The complete separation distance is the gap width at which the materials are not in contact. The contact stiffness (i.e. shape of the triangle) determines if the debonding mechanism has a linear elastic loading phase (point 0 to 2) or if the bond experiences only plastic separation (point 2 to 4). An example of these two traction separation triangles is shown in Figure 2.10 in which the dashed line represents a mechanism with a linear elastic loading

phase (intrinsic traction separation law). The solid line represents a mechanism that does not have the linear elastic loading phase; the mechanism is only completely bonded or experiencing plastic separation [extrinsic traction separation law] (Alfano et al. 2007). The distinction of the type of traction separation law is important in the numerical models. The default in ANSYS is extrinsic in which the contact stiffness is automatically determined to be an infinitely high number (ANSYS 2019).

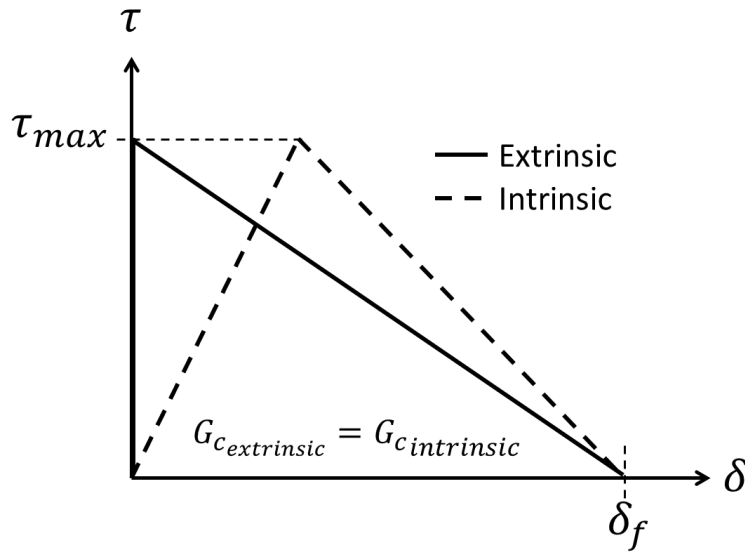


Figure 2.10: Traction separation law (CZM) showing extrinsic (solid line) versus intrinsic (dotted line) behavior.

Three parameters are required to describe an extrinsic traction separation law: τ_{max} , G_c , and δ_f . All three parameters are related to each other by simple triangle geometry shown in Equation 2.25. Therefore, only two parameters are required for input.

$$Area = \frac{base \cdot height}{2} \rightarrow G_c = \frac{\delta_f \cdot \tau_{max}}{2} \quad 2.25$$

It is important to note that when authors describe the traction separation law, some use the term fracture toughness, K_{IC} instead of the fracture energy G_c (Feng et al. 2017; Kumar et al. 2017; Jiang et al. 2020; Xu et al. 2020). Fracture toughness is related to the fracture energy (G_c) in

the traction separation law by Equation 2.26 where E is the Young's modulus and ν is the Poisson's ratio of the material (Kumar et al. 2017).

$$G_c = \frac{K_{IC}^2}{E} (1 - \nu^2) \quad 2.26$$

To determine the correct coefficients for the traction separation law, Wang and Taleghani (2014) performed a numerical analysis of the shear bond test data from Carter and Evans (1964). An example of their analysis is shown in Figure 2.11. The authors converted the load versus time data (Figure 2.11A) into stress versus displacement data (Figure 2.11B). The load is converted to stress by dividing the load by the surface area. The time is converted to displacement by multiplying the time by the strain rate. To get the traction separation law coefficients, the maximum bond strength (Figure 2.9 point 2) is the maximum stress from Figure 2.11. The critical energy of the bond is determined by calculating the area under the stress versus displacement curve by taking the integral of the best fit line or by performing a Riemann sum calculation.

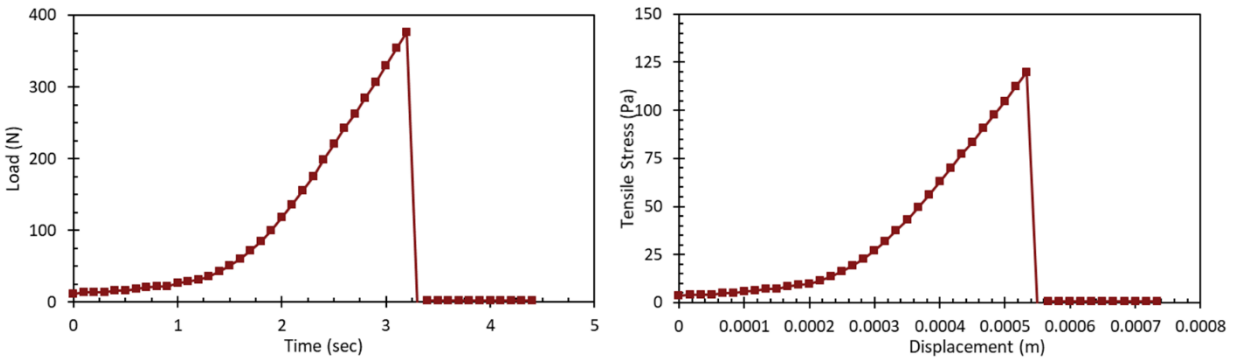


Figure 2.11: A) Example of a load versus time data acquired in bond test experiments. B) Analyzed experimental data in terms of stress versus displacement data.

The Mode I traction separation law parameters determined by Wang and Taleghani (2014) are $\tau_{max} = 0.5$ MPa, $G_c = 100$ J/m², and $\delta_f = 400$ μ m.

Modeling of Leakage

Numerically estimating the fluid flow of hydrocarbons in wellbore cement and along the cement sheath interfaces is a complicated mechanical and chemical process in which some assumptions have to be made. Predicting the dissolution and precipitation of minerals that occur due to chemical reactions of cement with various fluids and gasses within the leakage pathways are not well quantified (Bois et al. 2013). Therefore, experiments and analytical equations have been used to relate flow rates, pressure drops, and leakage pathway sizes to get a generalized idea of leakage patterns in the cement sheath. The following sections discuss the theoretical background of simplifying cased wellbore leakage with classical fluid mechanics analytical equations for geometries related to cased wellbores: circular, annular, and irregular geometries. Circular flow relates to flow within the casing (pipe) presented in de Nevers (2005), Bird et al. (2007), Kleinstreuer (2010), and White (2011). Annular flow represents a uniform microannuli in the cement sheath. Irregular geometries are simplified to parallel plate flow in which the width and height are variable to represent fractures.

2.4 Circular Flow

To model flow for a cased wellbore, the simple case would be to develop the equations of state for a cylinder for incompressible fluids assuming laminar flow in a pipe in which the pressure force exerted on the pipe is equal to the change in pressure (ΔP) times the cross sectional area (πr^2).

$$\text{Pressure Force} = \pi r^2 (\Delta P) \quad 2.27$$

The shear force exerted on the pipe is equal to the force in the opposite direction of the pressure gradient which is in the flow direction. The shear force is equal to the circumference ($2\pi r$) times the length (Δx) times the shear stress (τ).

$$\text{Shear Force} = 2\pi r \cdot \Delta x \cdot \tau \quad 2.28$$

Since pressure and shear are the only forces in the x-direction, the sum of the forces has to be equal to zero. Combining Equations 2.27 and 2.28 and solving for τ result in Equation 2.29.

$$\tau = -\frac{r\Delta P}{2\Delta x} \quad 2.29$$

For a Newtonian fluid in laminar motion, the shear stress is equal to the viscosity and the velocity gradient. Then Equation 2.29 becomes,

$$\mu \frac{dV}{dr} = -\frac{r\Delta P}{2\Delta x} \quad 2.30$$

Integrating Equation 2.30 with respect to the radius of the pipe (r) results in Equation 2.31.

$$V = -\frac{r^2\Delta P}{4\mu\Delta x} + C1 \quad 2.31$$

Assuming no slip condition (slip flow), $V = 0$ when $r = r_o$ results in,

$$0 = -\frac{r_o^2\Delta P}{4\mu\Delta x} + C1 \quad 2.32$$

Equating Equations 2.31 and 2.32 results in Equation 2.33.

$$V = \frac{r_o^2 - r^2}{4\mu} \frac{\Delta P}{\Delta x} \quad 2.33$$

The maximum velocity is when $r = 0$. Then Equation 2.33 reduces to Equation 2.34 and is shown schematically in Figure 2.12.

$$V_{max} = \frac{r_o^2 \Delta P}{4\mu \Delta x} \quad 2.34$$

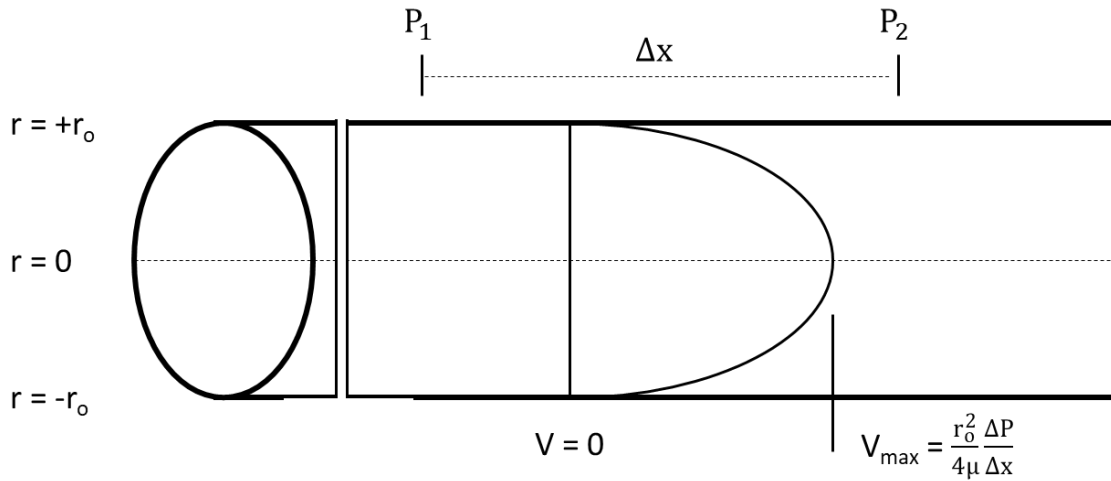


Figure 2.12: Velocity profile in a circular pipe with laminar flow.

Equation 2.33 results in the velocity profile given a specific location (r) within the pipe. For leakage in a cased wellbore, scientists are more interested in the volumetric flow rate (Q) than the local velocity (V). To determine the volumetric flow rate of a uniform velocity flow, the local velocity is multiplied by the cross-sectional area perpendicular to the flow ($2\pi r$). Since the velocity of laminar flow is not uniform (parabolic, as shown in Figure 2.12), an integral is performed across the pipe cross section resulting in the volumetric flow for the pipe.

$$\begin{aligned} Q &= \int_{tube} V da = \int_{r=0}^{r=r_o} \frac{r_o^2 - r^2}{4\mu} \frac{(P_1 - P_2)}{\Delta x} 2\pi r dr = \frac{P_1 - P_2}{\Delta x} \frac{\pi r_o^4}{\mu 8} \\ &= \frac{P_1 - P_2}{\Delta x} \frac{\pi D_o^4}{\mu 128} \end{aligned} \quad 2.35$$

$$Q = \frac{\Delta P \pi r_o^4}{\Delta x \mu 8} \quad 2.36$$

$$Q = \frac{\Delta P \pi D_o^4}{\Delta x \mu 128} \quad 2.37$$

The resulting equations (Equation 2.36 and 2.37) are the Hagen-Poiseuille equation for laminar flow through a circular tube. The only difference is Equation 2.36 is in terms of the pipe radius (r_o) and Equation 2.37 is in terms of the pipe diameter (D_o). It should be noted that small errors in measurements in the pipe diameter (or radius) result in large errors in flow rates since the dimension is to the 4th power.

The assumptions are:

- The flow is laminar (i.e. Reynolds number (N_{Re}) must be less than 2,100).
- Density (ρ) of the fluid is constant (incompressible flow).
- Flow is steady state.
- Fluid is Newtonian (i.e. water, basic oils, gases: molecular weight < 400; [Kleinstreuer 2010]).
- End effects are neglected.
- The fluid behaves as a continuum.
- There is no slip at the wall.
- The system is isothermal. Temperature dependent properties such as viscosity (μ) and density (ρ) are constant.

2.5 Annular Flow

For an annulus with a large gap, the flow rate is defined as:

$$Q = \left(\frac{\Delta P}{\Delta x} \frac{1}{\mu} \right) \frac{\pi}{128} (D_o^2 - D_i^2) \left[D_o^2 + D_i^2 - \frac{D_o^2 - D_i^2}{\ln \left(\frac{D_o}{D_i} \right)} \right] \quad 2.38$$

in which D_o is the diameter of the outside edge of the annulus (inner diameter of the outside pipe) and D_i is the diameter of the inner edge of the annulus (outer diameter of the inside pipe).

When the spacing in the annulus becomes small (i.e. $D_i \rightarrow D_o$), Equation 2.38 reduces to,

$$Q = \left(\frac{\Delta P}{\Delta x} \frac{1}{\mu}\right) \frac{1}{12} \pi D \left(\frac{D_o - D_i}{2}\right)^3 \quad 2.39$$

Rearranging Equation 2.39 in terms of radii for the difference between the annulus results in Equation 2.40.

$$Q = \left(\frac{\Delta P}{\Delta x} \frac{1}{\mu}\right) \frac{1}{12} \pi D \left(\frac{D_o}{2} - \frac{D_i}{2}\right)^3 = \left(\frac{\Delta P}{\Delta x} \frac{1}{\mu}\right) \frac{1}{12} \pi D (R_o - R_i)^3 \quad 2.40$$

Defining the difference between the radii as a gap width (microannuli, w),

$$Q = \frac{\Delta P}{\Delta x} \frac{\pi D w^3}{12\mu} \quad 2.41$$

Equation 2.39 (or 2.40) is useful for determination of any variable in which the annulus (microannuli) is known. For problems in which the microannuli is not known, Equation 2.41 is useful as shown in Aas et al. (2016), Lavrov and Torsaeter (2018), Stormont et al. (2018) and Skadsem et al. (2019).

2.6 Slot Flow

As shown by Equation 2.40, many laminar flow problems can be simplified by converting them to equivalent straight or planar problems. In fluid modeling, leakage can occur within thin slots. The following derivation represents slot flow shown in Figure 2.13.

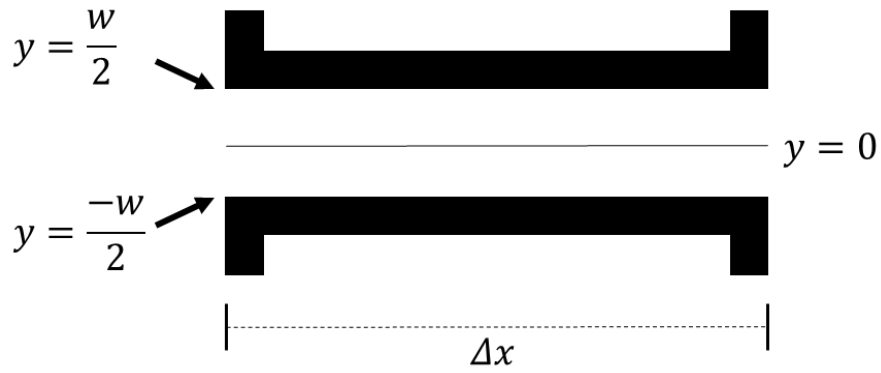


Figure 2.13: Slot flow dimensions used in the derivation of Equation 2.49.

Performing a steady-state force balance on the geometry shown in Figure 2.16 results in Equation 2.42.

$$(P_1 - P_2) \cdot 2 \cdot l \cdot y = 2l\Delta x\tau_y \quad 2.42$$

Where,

$$\tau_y = \left(-\frac{dP}{dx}\right) \cdot y = -\mu \frac{dV}{dy} \quad 2.43$$

$$\int dV = -\left(-\frac{dP}{dx}\right) \frac{1}{\mu} \int y dy \quad 2.44$$

$$V = \frac{dP}{dx} \frac{1}{2\mu} y^2 + C \quad 2.45$$

When, $y = \frac{w}{2}, V = 0$.

$$C = -\frac{dP}{dx} \frac{1}{2\mu} \left(\frac{w}{2}\right)^2 \quad 2.46$$

$$V = -\frac{dP}{dx} \frac{1}{2\mu} \left[\left(\frac{w}{2}\right)^2 - y^2\right] \quad 2.47$$

$$Q = \int V dA = \left(-\frac{dP}{dx}\right) \frac{1}{2\mu} \cdot 2 \cdot l \cdot \int_0^{\frac{w}{2}} \left[\left(\frac{w}{2}\right)^2 - y^2\right] dy \quad 2.48$$

$$Q = \frac{\Delta P}{\Delta x} \frac{1}{\mu} \frac{1}{12} l(w)^3 \quad 2.49$$

Where w is the distance between the plates (i.e. microannuli) and l is the width of the slot. If both sides are divided by l , the left-hand side becomes the volumetric flow rate per unit width. Equation 2.49 is referred to as “slot flow” and is used extensively in the Reynold’s Lubrication Theorem shown in Section 2.10.

Prediction of Fluid Leakage

Prediction of fluid leakage in wellbores has proven to be a complicated process due to the numerous variables, extreme conditions, and unknown physical mechanisms that can occur. The following sections look at lab scale leakage experiments, field leakage prediction/measurements, analytical methods, and numerical methods that combine results/methodologies from the lab, field, and analytical equations.

2.7 Lab Leakage Prediction

Corina et al. (2019) used a lab scale P&A apparatus that tested the sealing ability of a cement plug inside a steel casing with respect to nitrogen gas. The cement plug has a diameter of 5.0 cm and a length of 40 cm and was cured for four days at a determined temperature (66 or 120 °C) and at an elevated pressure (2 MPa). A pressure differential is applied through the cement and the resulting flow rate was measured. The authors tested Portland cement with silica flour at 66 °C (SF66) and 120 °C (SF120) along with a cement mixture with an expanding agent at 120 °C (SF120EA). Figure 2.14 shows the data from Corina et al. (2019) with the corresponding flow rates given the differential pressures for the three test cases.

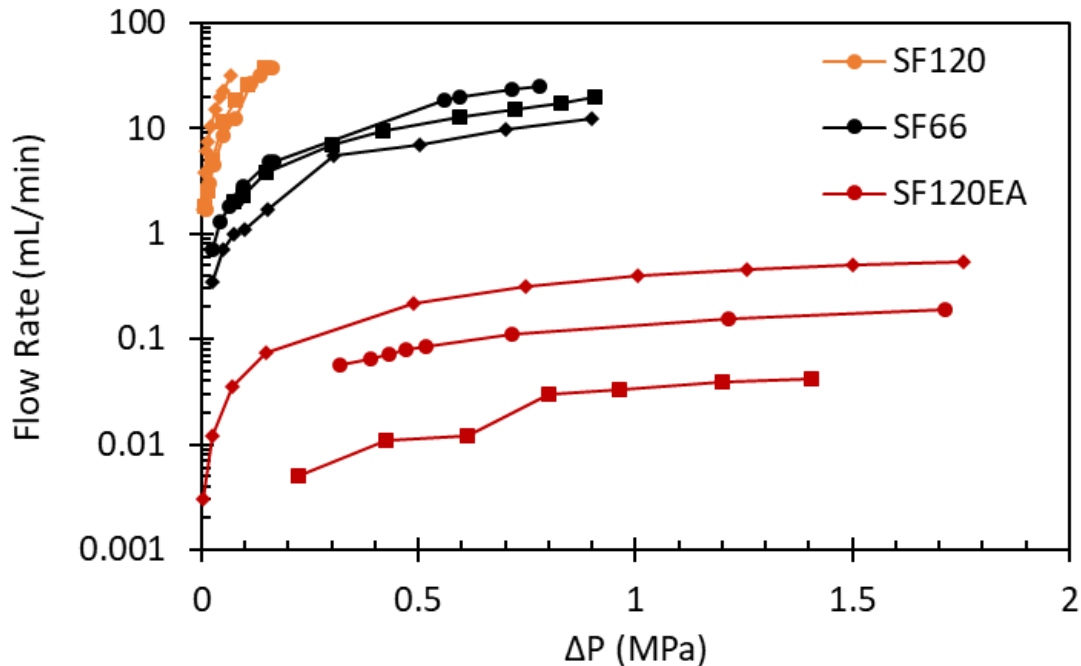


Figure 2.14: Experimental data from Corina et al. (2019) showing the flow rate through the cement plug given the differential pressure (ΔP) with the neat cement at 66 °C (SF66), neat cement at 120 °C (SF120), and neat cement plus expanding agent at 120 °C (SF120EA).

The results from Corina et al. (2019) show that the neat cement at 120 °C (SF120) has the largest flow rate with the smallest pressure drop followed by the neat cement at 66 °C (SF66). The cement with the expanding agent has the smallest flow rates with the largest pressure drops. This data implies two main points: neat cement has much larger potential leakage pathways than the expanding cement, and elevated temperatures cause larger leakage pathways. Cement shrinkage has been known to be a leading concern in terms of cement sealing ability, and the authors determined that cement shrinkage is occurring in their results. To determine the location of the leakage pathways, the authors places a column of water on the top of the cement after the experiment and noted the location of the air bubbles from the water filling the voids. The authors noted that the air bubbles occurred at the cement/steel interface indicating the location of the voids to be at the interface where cement shrinkage would cause microannuli to form due to the difference in stiffness between the cement and steel.

The inner diameter of the casing is 5 cm (1.97 in.) in Corina et al. (2019) apparatus whereas the inner diameter of smaller wellbore casings are at least three times the size. As determined by Lavrov et al. (2019) simulations discussed in Section 2.3.1, cement experiences a size effect in which cement tends to have less integrity as the size increases due to the higher likelihood of fractures/failures within the body. Therefore, smaller dimensions could lead to falsely positive results when compared to realistic wellbore dimensions. This phenomenon states that. Therefore, realistic dimensions of experiments should occur to ensure proper results.

Other considerations not accounted for in Corina et al.'s (2019) series of experiments was that the curing period of the cement was short (4 days) whereas Bensted and Barnes (2002), Saint-Marc et al. (2008), and Bois et al. (2012) have shown that cement properties continuously change throughout cement hydration, which can last up to or past 28 days depending on the environment. Given the physical set up of the experiment, access to free water was not available, but it would be valuable to understand the sealing ability of wellbore cement when free water is accessible since Zhang et al. (2019) has shown that cement properties change depending on free water access.

Aas et al. (2016) performed similar experiments to those done by Corina et al. (2019) except larger scale (36 m and 12 m length versus approximately 0.5 m length) with actual casing (24.4 cm) and tubing (17.8 cm) sizes with conventional and expandable cement in concentric and eccentric cemented casings. Another difference is the authors used water as the injected fluid whereas Corina et al. (2019) used compressed nitrogen gas. These experiments were used to determine the sealing ability of cemented tubing in place by investigating the likelihood and severity of leakage for plugged and abandoned wells. The fluid flow was measured at different pressures, and the authors developed the concept of an "equivalent microannuli". The equivalent

microannuli correlates the pressure drops and flow rates into an idealized uniform geometric gap between the cement and casing. Below is a summary of their experiments.

Two different horizontal assemblies consisted of 9 5/8” (244.48 mm) casing with a 7” (177.8 mm) tubular inside it. The assemblies were cemented using conventional methods replicating the pumping of the cement inside the tubing and into the annular space between the two tubular strings. Two lengths of assemblies were used as summarized in Table 2.2. Figure 2.15 shows a cut-away of one of the assemblies after testing showing the two casing strings with complete cement displacement. Note that in the experiments were not performed with centralizers and therefore the inner 7” tubing has an offset of 11.15 mm resulting in tubing eccentricity.

Table 2.2: Summary of the Aas et al. (2016) experiments used for the FEA model verification.

Assembly	Cement Type	Assembly Length	Flow Length	Curing Time	Temperature
A	Conventional	36 m	18 m	1 week	Ambient
C	Expandable	12 m	6 m	3 weeks	95°C



Figure 2.15: Cut test assembly showing complete cement displacement between the casing and tubing. Figure modified from Aas et al. (2016).

For conventional assemblies A and B, the distance between the pressure inlet and outlet was 18 m and performed under ambient temperature conditions. For the expandable cement, the

distance of the pressure ports was 6 m and performed at an elevated temperature (95°C). The temperature of the experiments was under steady state conditions. Aas et al. (2016) measured the fluid flow at different pressures and developed the concept of an “equivalent microannuli”. The equivalent microannuli correlates the pressure drops and flow rates into an idealized geometric gap between the cement and casing. The equivalent microannuli is equal to the annular Hagen-Poiseuille equation shown in Section 2.5. In other words, the equivalent microannuli correspond to that of a uniform gap given the flow rates and pressure drops. The results from their experiments (assembly A and C) are shown in Table 2.3.

Table 2.3: Experimentally measured pressure drops and equivalent microannuli gaps for both expanding and conventional cement in Aas et al. (2016) experiments.

	Length	Initial Pressure	Flow Rate	Experiment Pressure Drop	Total Microannuli
	(m)	(MPa)	(mL/min)	(MPa)	(μm)
Expanding	6	12.5	98	4.8	22
	6	12.6	94	4.8	22
	6	12.7	92	4.9	22
	6	9.6	49	5.0	18
	6	9.5	48	5.1	17
	6	6.6	23	4.7	14
	6	6.5	23	4.4	14
	6	4.2	13	3.0	13
Conventional	18	5.4	14	0.1	101
	18	9.3	95	0.3	127
	18	5.6	56	0.4	93
	18	9.4	136	0.5	118

Skadsem et al. (2019) expanded the Aas et al. (2016) experiments to include inclined pipe and flow path. These authors determined that microannuli are channels, not uniform gaps. Stormont et al. (2018) performed similar experiments, except they used gas flow instead of fluid flow. They determined that once a gap occurs, it cannot be fixed mechanically. Therefore, the microannuli gaps are permanent. This result shows that the cement sheath debonding is in the

plastic region (or experiences complete debonding) in the traction separation law. To quantify the microannuli gaps and to include the effect of compressibility, Stormont et al. (2018) used a different approach than the equivalent microannuli equation. Since the equivalent microannuli equation is based off Hagen-Poiseuille flow, it is only valid for incompressible fluids (i.e. not gasses). Stormont et al. (2018) used the cubic law (Equation 2.50; Witherspoon et al. 1980) in conjunction with a rewritten version of the Forchheimer's equation (Equation 2.51), where w is the microannuli aperture, k is the effective permeability, A is the wellbore annular area, C is the length of the microannuli aperture (circumference of the outside of the casing), M is the molecular weight of the gas, L is the specimen length, z is the gas compressibility factor, R is the universal gas constant, T is temperature, P_u is the upstream pressure, P_d is the downstream pressure, Q is the volumetric flow rate, μ is the fluid viscosity, ρ is the fluid density, and β is the inertial coefficient (friction factor).

$$w^3 = \frac{12kA}{C} \quad 2.50$$

$$\frac{MA(P_u^2 - P_d^2)}{2zRT\mu L\rho Q} = \frac{1}{k} + \left(\frac{\rho Q}{\mu A}\right)\beta \quad 2.51$$

Two other research groups, Corina et al. (2020) and Al Ramadan et al. (2019), performed a similar analysis as Stormont et al. (2018) in which they investigated fluid flow through cement microannuli. Corina et al. (2020) analyzed their previous data published in Corina et al. (2019) and Opedal et al. (2018) using the cubic law in conjunction with Darcy's law (shown in Equation 2.52). A combination of the cubic law and Darcy's law is shown in Equation 2.53. Results for the microannuli widths with respect to flow rate (Figure 2.16) and pressure differential (Figure 2.17) are shown below.

$$k = \frac{Q\mu L}{A\Delta P} \quad 2.52$$

$$w = \left(\frac{12Q\mu L}{\pi D\Delta P} \right)^{\frac{1}{3}} \quad 2.53$$

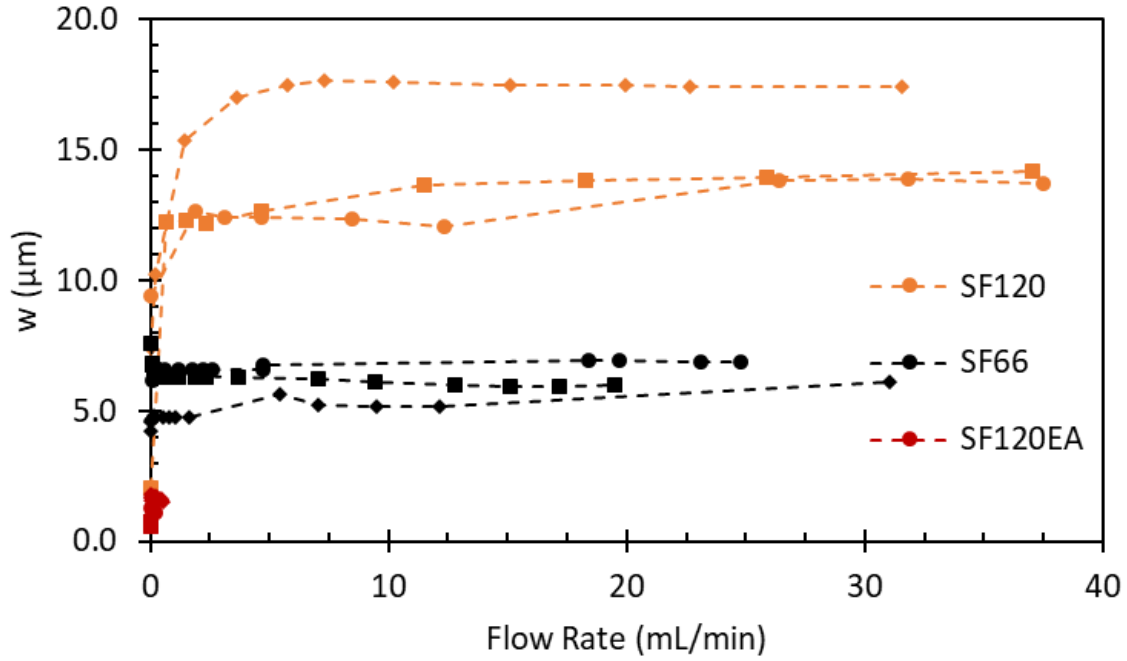


Figure 2.16: Microannuli (w) versus flow rate for the three test cases from Corina et al. (2019) analyzed using the methodology from Corina et al. (2020).

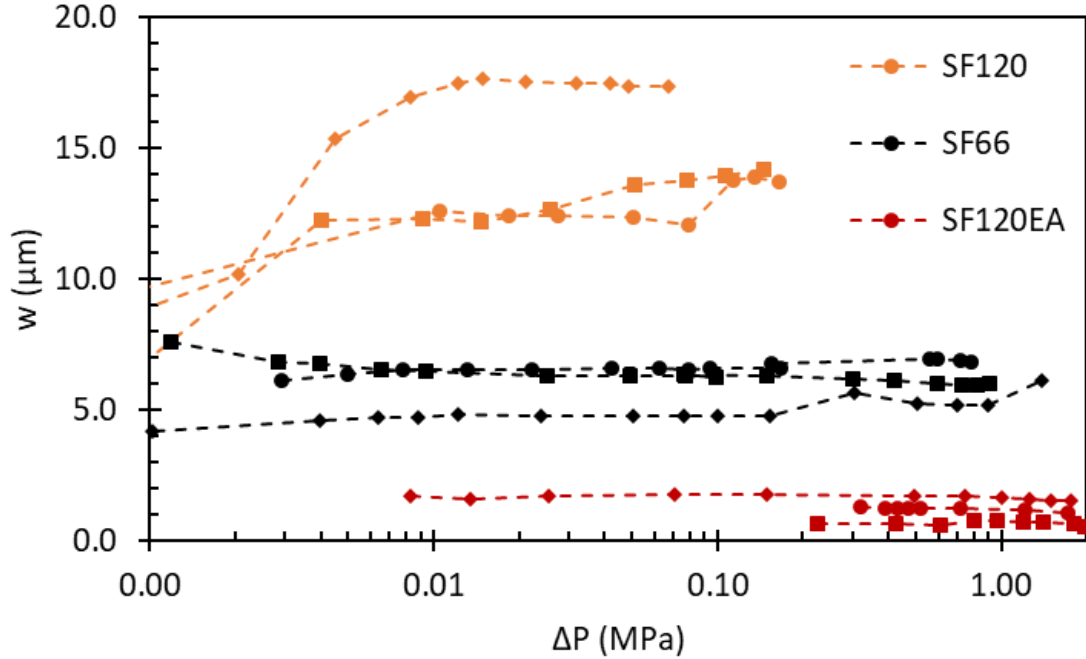


Figure 2.17: Microannuli (w) versus pressure differential (ΔP) for the three test cases from Corina et al. (2019) analyzed using the methodology from Corina et al. (2020).

$$Q = \frac{\Delta P w^3 D \pi}{12 \mu L} \quad 2.54$$

Rearranging Equation 2.53 results in Equation 2.54 which is of the same form as the annular Hagen-Poiseuille equation (Equation 2.41) shown in Section 2.5. This should make Equation 2.54, and the methodology of Corina et al. (2020), not ideal since Hagen-Poiseuille flow is not valid for gases. Some possible explanations exist that show how using annular Hagen-Poiseuille flow (or Darcy flow with the cubic law) is valid for low pressures (the experiments from Opedal et al. (2018) and Corina et al. (2019) use pressures less than 2 MPa). According to Hubbert (1956) and Outmans (1963), the flow behavior of gases in small pore spaces, excluding compressibility (i.e. ideal gases) is similar to that of a liquid. Thus Darcy flow should account for compressibility, especially in gases with low flow rates. Klinkenberg (1941), however, showed that the flow of gases and liquids are not similar. The relationship between the permeability of a

medium for gas is not constant for the permeability of the same medium to a liquid except at “high” pressures (pressures greater than 2 MPa). Klinkenberg states that the permeability with respect to a gas is a function of the mean free path of the gas molecules which depend on pressure, temperature, and the nature of the gas. In other words, compressibility of the gas should be accounted for according to the findings of Klinkenberg (1941).

Since Corina et al. (2020) did not account for compressibility (although compressibility of nitrogen at their test pressures and temperatures is 3.1% different from ideal), Al Ramadan et al. (2019) used a different approach combining the cubic law with a real gas law variation shown in Equation 2.55. The authors used this method, along with total leakage time (Equation 2.56), to determine the total length of cement that should be used given permeability values. The authors claim this method is valid for an ideal gas or a real gas since the real gas law is implemented in Equation 2.55.

$$Q = \frac{M(P_u^2 - P_d^2)wh^3}{24zRTL\rho\mu} \quad 2.55$$

Where Q is the flow rate, M is the gas molecular weight, P_u is the upstream pressure, P_d is the downstream pressure, z is the compressibility factor, R is the universal gas constant, T is the temperature, L is the length, ρ is the density, and μ is the gas viscosity.

$$t = \frac{A_m L}{Q} \quad 2.56$$

Where t is the leakage time and A_m is the flow area.

The issue with this method is twofold. First the cement permeability is unknown in the cubic law (Equation 2.50 from above). The values could stem from experimental data, but lab scale experiments have their own limitations such as downhole conditions and time frames. The second

issue involves the physics behind Equation 2.55. Equation 2.55 allegedly accounts for a real gas, but the derivation or citation for how this equation came to be is missing. The compressibility factor is assuming an average value for the upstream and downstream pressures. Inserting the real gas equation (Equation 2.57) into Equation 2.55 results in Equation 2.58. Simplification (Equation 2.59) shows that the “real gas” equation used in Al Ramadan et al. (2019) assumes an ideal gas since the compressibility factor is in both the numerator and denominator cancels out. Extra pressure terms in the numerator and denominator are the only difference between Equation 2.59 and annular Hagen-Poiseuille flow shown in Equation 2.41 in Chapter 2.5.

$$z = \frac{PM}{RT\rho} \quad 2.57$$

$$Q = \frac{M(P_u^2 - P_d^2)wh^3RT\rho}{24PMRTL\rho\mu} \quad 2.58$$

$$Q = \frac{(P_u^2 - P_d^2)wh^3}{24PL\mu} \quad 2.59$$

From the research done by Aas et al. (2016), Stormont et al. (2018), and Skadsem et al. (2019), the authors investigated cement microannuli formulation due to pressure induced debonding of the cement sheath to the steel casing. The loss of zonal isolation was observed and quantified by measuring pressure-driven flow through the cement sheath. The effective permeability (equivalent microannuli) was calculated using the observed flow rates and derived analytical equations. Due to the nature of the analytical equations, the equivalent microannuli determined in the experiments are assumed to be uniform around the circumference around the casing.

To determine if the microannuli are uniform, Albawi et al. (2014), Vrålstad et al. (2015), De Andrade et al. (2016), Skorpa and Vrålstad (2018), and Vrålstad and Skorpa (2020) developed a lab scale experiment replicating temperature cycles within a wellbore. The experiments consisted of a rock formation with a casing cemented in place. Cement fracture and/or microannuli were created within the cement sheath or along the rock/cement or cement/casing interface due to temperature cycles at different confining pressures. The experiments were then reconstructed in 3D using a CT machine to quantify and visualize the leakage pathways. Skorpa and Vrålstad (2018) extended the experiments by applying pressure-driven flow through the cracks and microannuli. An example of their results is shown in Figure 2.18.

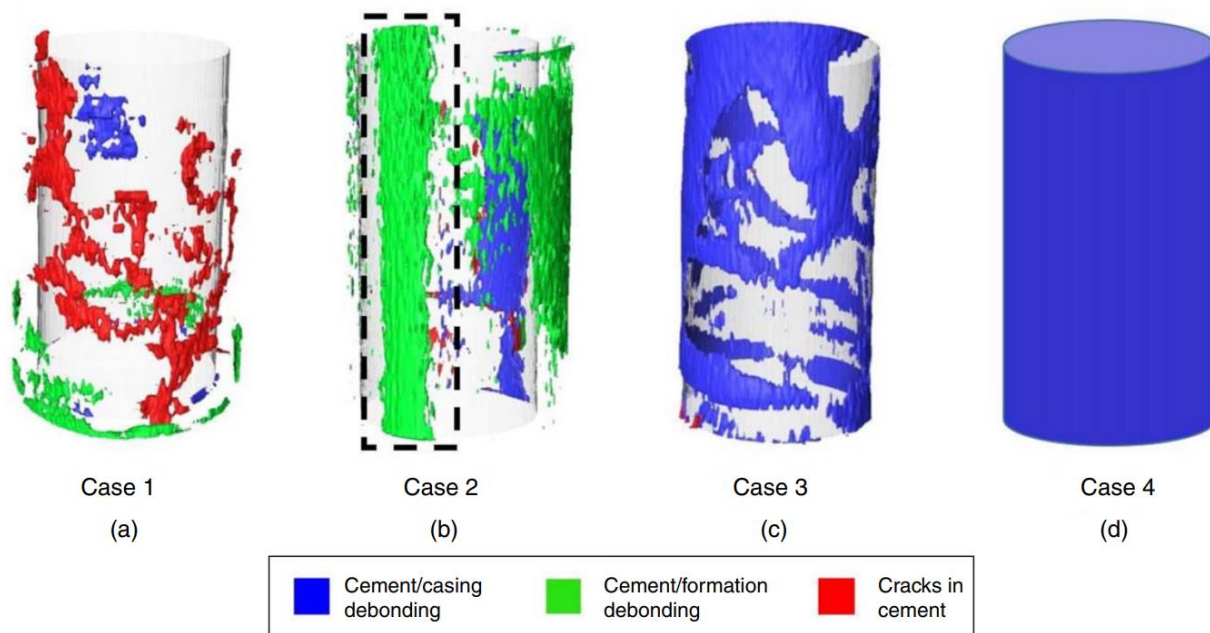


Figure 2.18: Results of experiments from Skorpa and Vrålstad (2018) used in the CFD simulations. A) representation of flow path through connected cracks within the cement sheath. B) debonding channel between the cement and formation (as shown by dashed box). C) partial microannuli between the cement and casing. D) a uniform microannuli at the casing/cement interface as predicted by equivalent microannuli analyses. Figure from Skorpa and Vrålstad (2018).

The flow path geometries from the 3D CT experiments were imported into CFD simulations to quantify fluid flow through the leakage pathways. Four fluid flow geometries were used. Three were from the experiments (Figure 2.18A, B, and C), and one is a uniform microannuli

as predicted by equivalent microannuli analyses (Figure 2.18D). The experimental fluid flow geometries are: a connected fracture network within the cement (Figure 2.18A), a debonded channel between the cement and formation (Figure 2.18B), and a partial microannuli between the casing and cement (Figure 2.18C). Their results show that fluid flow in degraded cement is complex and not easily described. The difference between a crack in the cement (channel) or a microannuli has a significant effect on the mass flow rate. Small changes in the fracture radius have a large effect on flow rate as shown in the analytical equations in Section 2.5. Changes in geometry also affect the flow rate due to the hydraulic radius.

Similar to Corina et al. (2020), the authors used Darcy's law to calculate the effective permeability given the pressure drop and flow rate. Skorpa and Vrålstad (2018) determined that for complex pathways in the cement sheath, Darcy's law is not adequate since the pressure drop and flow rate are nonlinear. For a full microannuli, Darcy's law is validated. The results of the quantification of cement sheath experiments show realistic leakage pathways, but the series of experiments has potential flaws: size scale and cement composition. The experimental modeled after a typical production casing scenario, 31.1 cm borehole and 24.4 cm casing, but scaled down by a factor of 4. The smaller scale could show exaggerated failure mechanisms when compared to full scale. Another possible flaw in the design is that the authors used tap water in mixing of the cement. As Saleh et al. (2018) and Al Ramadan et al. (2019) state, impurities in tap water can affect the properties of hydrated cement.

The methodology using CT imaging to quantify cement sheath leakage pathways is valuable, but current technology does not have the desired resolution. The resolution of the CT machine is 200 μm whereas previous experiments, Aas et al. (2016), Opedal et al. (2018), Stormont

et al. (2018), Corina et al. (2019), Skadsem et al. (2019), Corina et al. (2020), show that microannuli gaps can be much smaller than 200 μm .

2.8 Field Leakage Prediction

Field experiments would be best to understand potential leakage for cased wellbores, but they are not as common due to being expensive, difficult to detect leakage due to many potential leakage zones, hard to control with many realized and unrealized variables, and conditions are not always replicable. Two examples of field experiments include Crow et al. (2010) and Carey et al. (2007) which investigated wellbore sheath integrity with respect to CO₂ conditions. The first well is a 30-year old natural (supercritical) CO₂ production well located in the Dakota Sandstone formation (Crow et al. 2010), while the second well is part of a CO₂ flooding operation located in the Permian Basin (Carey et al. 2007).

A schematic of the wellbore used in Crow et al. (2010) is shown in Figure 2.19. The wellbore was exposed to a 96% CO₂ fluid from the time of completion until the study which is a higher sustained concentration of CO₂ compared to typical enhanced oil recovery wells. Therefore, the cement used to complete this well should show how the long term effect of extreme concentrations of CO₂ affect the cement. The cement provided good zonal isolation due to the lack of sustained casing pressure at the wellhead. Crow et al. (2010) were able to take cement sheath cores along different depths from the reservoir to the caprock to test for integrity. The cores were cut through the casing such that casing, cement, and formation could be compared to determine sealing ability.

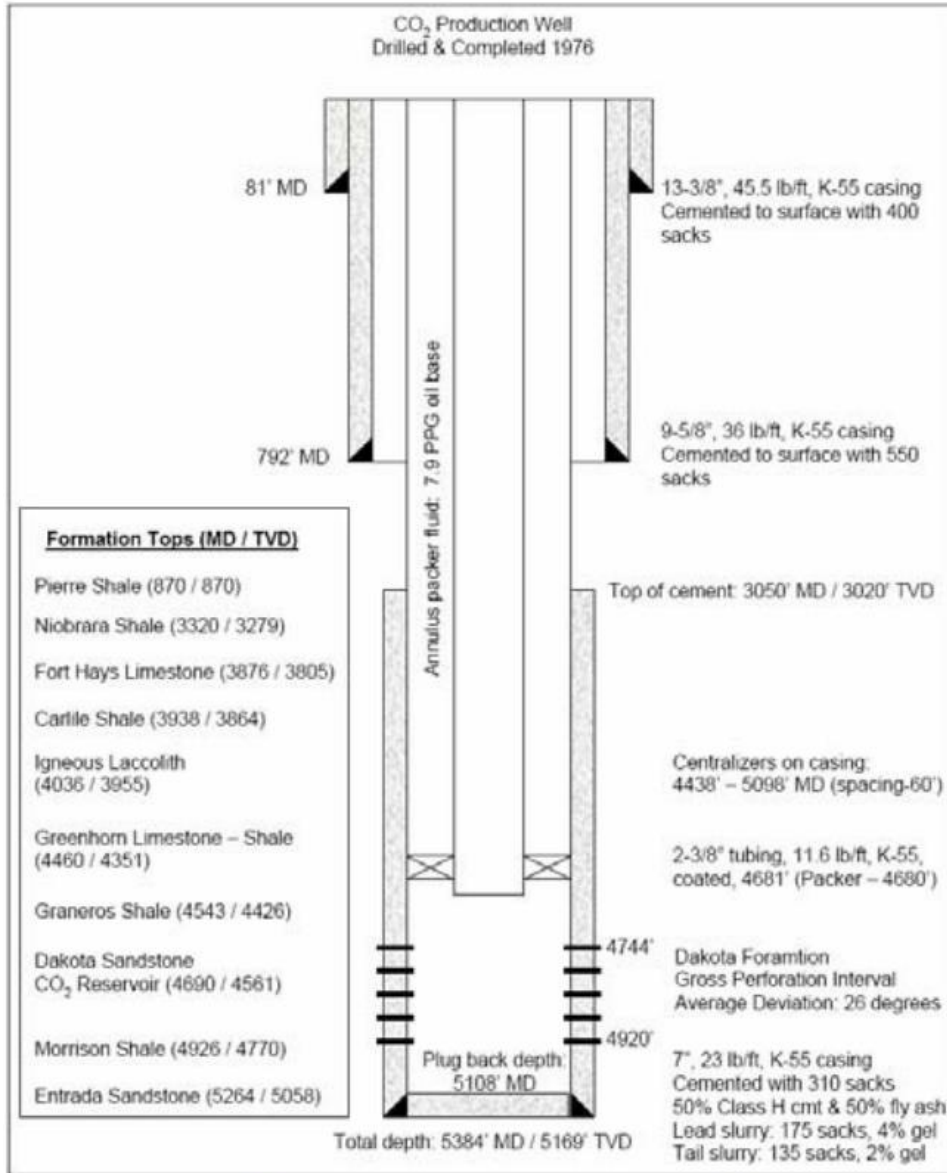


Figure 2.19: Schematic of the CO₂ production well located in the Dakota Sandstone formation used in Crow et al. (2010). The different formation strata depths, cement depths, true vertical depths (TVD), and wellbore dimensions are shown. Figure from Crow et al. (2010).

Samples from the well showed that carbonation occurred in the cement causing the permeability and porosity to increase which is opposite of the laboratory results shown by Tarco and Asghari (2010) and Yalcinkaya et al. (2011). The difference between the actual wellbore and the lab scale experiments are the time frames (30 years versus a maximum of 12 months, respectively). Another interesting result is that the cement interfaces between the casing and formation did not appear to have significant calcium carbonate deposits (<0.1 mm). However,

upon numerical modeling of the effective permeability using the Vertical Interference Test (VIT) analysis, the authors noted that the permeability of the cement interface was approximately 3 to 4 orders of magnitude larger than the cement matrix. The VIT data analysis indicated the effective permeability of the cement sheath to be between 1-10 millidarcies while cement core permeability at the same interval was determined to be 1 microdarcy. The field data from Crow et al. (2010) and the lab data from Tarco and Ashgari (2010) confirm that CO₂ reduces the bond strength of cement indicating that cement interfaces are the primary pathways for potential CO₂ migration.

Even though the interfaces have the largest permeability, the well did not exhibit sustained casing pressure at the surface. One explanation of the lack of sustained casing pressure (evidence of CO₂ leakage through the annular cement sheath) comes from Cerasi et al. (2017). Cerasi et al. (2017) determined that Pierre Shale, which happens to be the caprock in this well as shown in Figure 2.19, experiences formation creep when exposed to supercritical CO₂. So if the CO₂ reduced the bond strength (and increased the effective permeability at the cement interfaces), shale creep could have reduced the microannuli. It is unlikely that the microannuli was reduced completely and uniformly given that the VIT data determined the interface had significant permeability. The shale creep could have created tortuosity at the interface reducing the flow rate of CO₂. Given the tortuosity, length of the cement, and resulting surface roughness, the flow could have been completely reduced, as explained by Vignes and Aadnoy (2008), Lavrov and Torsaeter (2018), and Corinia et al. (2020), resulting in the well not experiencing CO₂ leakage to the surface.

The well investigated by Carey et al. (2007) is part of a CO₂ flooding operation located in the Permian Basin in West Texas. As with Crow et al. (2010), cement cores were reviewed to determine the effect of CO₂ injection has on wellbore cement. A 5 cm diameter core was collected in the well through the casing, cement, and into the caprock (Wolfcamp Shale). Results of this well

are in agreement with Crow et al. (2010) such that the cement matrix was disturbed by the invasion of CO₂; the permeability of the bulk cement was elevated compared to typical cement permeability. Nevertheless, the permeability was still low enough to prevent significant fluid migration through the cement matrix. The authors discovered that CO₂ migration had occurred along both the casing/cement and cement/shale interfaces by visual deposits of various minerals not found in intact cement along both interfaces which agrees with Carey et al. (2007). The cores produced from Carey et al. (2007) did not reach the surface intact therefore mechanical tests were not performed on them. The authors performed a sonic cement bond log (CBL) along the depths of interest, and the CBL did not indicate evidence of cement debonding even though deposits of precipitated minerals were found at the casing/cement and cement/rock interfaces. An explanation of the discrepancy is described by De Andrade et al. (2019). De Andrade et al. (2019) reviewed different acoustic logging tools and determined that a combination of logs cannot detect gas filled microannuli or quantify the size.

Since bond logs are not accurate in detecting gas induced/filled microannuli and field cases are not easily available, researchers have turned to alternative methods to determine leakage in actual wellbores. One such method is the evaluation of sustained casing pressure (SCP)/surface casing vent flow (SCVF) (Watson and Bachu 2007).

Watson and Bachu (2007, 2009) evaluated historical records of SCP data in Alberta, Canada and determined that 3.9% had SCP due to a number of likely factors including geographic area (probably due to outside factors such as CO₂ sequestration sites), wellbore deviation, well type (i.e. cased and abandoned versus cased, completed, and abandoned), abandonment method, economic factors such as oil price and regulatory requirements, and cementing plan. A common denominator in all of the factors majorly affecting SCP is the wellbore cement. Deviated wellbores

are harder to achieve good cement displacement due to eccentricity of the casing strings resulting in channels, poor bonding, or wet microannuli in the cement (Skadsem et al. 2019). If a well is completed before abandonment, perforations and potential fractures in the cement exist whereas cased and abandoned wells do not have perforations. One major factor in resulting in a well having SCP is the length of cement. Watson and Bachu (2007, 2009) noted that the top 200 m of the cement is of bad quality based off CBL measurements. Further implication that the length of the cement is critical is that the majority of SCP originates in locations without a cemented annulus (Watson and Bachu 2007, 2009). As shown by Lavrov and Torsæter (2018) and Al Ramadon et al. (2019), the length of the cemented annulus can reduce if not completely stop flow rates. Given the large section of bad quality cement combined with no cement in formations with CO₂ migration, it should not be a surprise that SCP occurs in 3.9% of Alberta wells (as of 2004).

Just because a well does not exhibit SCP at the surface, does not mean leakage is not occurring. For a wellbore, there are many different formations that fluid leakage can occur in without making it to the surface. Therefore, determining wellbore leakage based on surface measurements is not comprehensive. So researchers have turned to analytical methods to determine potential leakage occurring subsurface.

2.9 Analytical Methods

Given the complexity of controlling all the variables associated with laboratory experiments and measuring and understanding wellbore leakage in the field, scientists have used analytical methods to predict wellbore failure mechanisms and quantify fluid flow rates.

An analytical model of the stress distribution around the near wellbore region is described by thick-walled cylinder equations and the Kirsch solution (Section 2.1). Figure 2.20 depicts a sketch of a cased wellbore with general dimensions used in the analytical model.

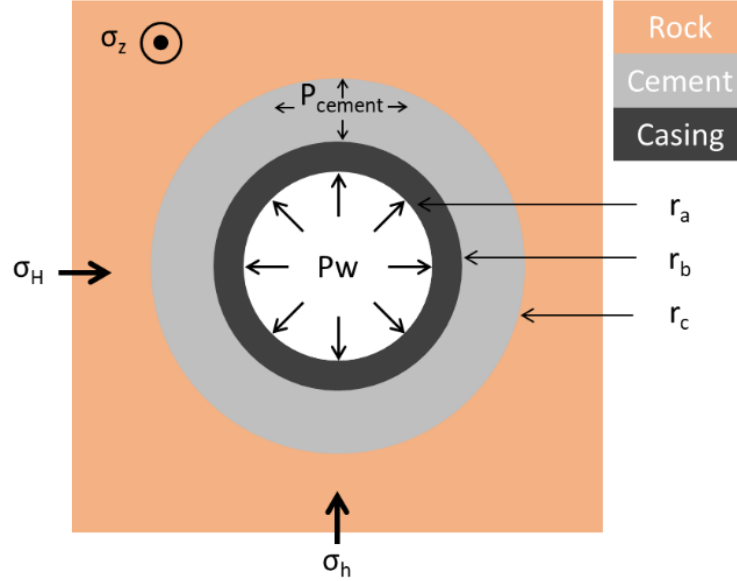


Figure 2.20: Wellbore Sketch showing generalized radii of the three bodies used in the analytical stress distributions equations.

Starting from the center of the wellbore outwards, the stress distributions in the casing and cement are determined from a single thick-walled cylinder. In the casing, a generalized effective stress equation for a thick-walled cylinder is presented in Equations 2.60, 2.61, and 2.62 to represent the radial, hoop, and axial stresses, respectively. Equations 2.63, 2.64, and 2.65 represent the radial, hoop, and axial stresses of the cement sheath (Weideman 2014). It is assumed that the radial stress of the hardened cement (P_{cement}) is known.

$$\sigma'_{r_{casing}} = \frac{r_b^2 P_{cement} + r_a^2 P_w}{r_b^2 - r_a^2} + \frac{r_a^2 r_b^2 (P_w - P_{cement})}{(r_b^2 - r_a^2)r^2} \quad 2.60$$

$$\sigma'_{\theta_{casing}} = \frac{r_b^2 P_{cement} + r_a^2 P_w}{r_b^2 - r_a^2} - \frac{r_a^2 r_b^2 (P_w - P_{cement})}{(r_b^2 - r_a^2)r^2} \quad 2.61$$

$$\sigma'_{z_{casing}} = \sigma_{v_{casing}} \quad 2.62$$

$$\sigma'_{r_{cement}} = \frac{r_c^2 P_{cement} + r_b^2 P_{cement}}{r_c^2 - r_b^2} - P_{cement} \quad 2.63$$

$$\sigma'_{\theta_{cement}} = \frac{r_c^2 P_{cement} + r_b^2 P_{cement}}{r_c^2 - r_b^2} - P_{p_{cement}} \quad 2.64$$

$$\sigma'_{z_{cement}} = \sigma_{v_{cement}} - P_{p_{cement}} \quad 2.65$$

Equations 2.66, 2.67, and 2.68 are modified from the Kirsch analytical solutions to show the radial, hoop, axial, and shear stress relationship in the rock formation between the far-field stresses, initial pore pressure, and stress from the cement.

$$\begin{aligned} \sigma'_{r_{rock}} = & \frac{1}{2}(\sigma_H + \sigma_h - 2P_{p_{rock}}) \left[1 - \left(\frac{r_c}{r}\right)^2 \right] \\ & + \frac{1}{2}(\sigma_H - \sigma_h) \left[1 - 4\left(\frac{r_c}{r}\right)^2 + 3\left(\frac{r_c}{r}\right)^4 \right] \cos 2\theta + (P_{cement} \\ & - P_{p_{cement}}) \left(\frac{r_c}{r}\right)^2 \end{aligned} \quad 2.66$$

$$\begin{aligned} \sigma'_{\theta_{rock}} = & \frac{1}{2}(\sigma_H + \sigma_h - 2P_{p_{rock}}) \left[1 - \left(\frac{r_c}{r}\right)^2 \right] \\ & - \frac{1}{2}(\sigma_H - \sigma_h) \left[1 + 3\left(\frac{r_c}{r}\right)^4 \right] \cos 2\theta - (P_{cement} - P_{p_{cement}}) \left(\frac{r_c}{r}\right)^2 \end{aligned} \quad 2.67$$

$$\sigma'_{z_{rock}} = \sigma_v - 2\nu(\sigma_H - \sigma_h) \left(\frac{r_c}{r}\right)^2 \cos 2\theta - P_{p_{rock}} \quad 2.68$$

Equations 2.60, 2.61, 2.63, 2.64, 2.66 and 2.67 are used to determine the analytical solutions of the radial and hoop stress development along a radius of interest within a wellbore as shown in Weideman (2014). However, these analytical equations do not determine leakage rates for a section of a wellbore or incorporate complex failure analysis.

Other analytical approaches have used methods to determine leakage flow rates within the cement sheath from the entirety of the wellbore instead of one depth. Lavrov and Torsaeter (2018) created synthetic wells and analyzed the summation of annular Hagen-Poiseuille flow to determine

tortuosity leakage rates versus overall lengths while Ford et al. 2017, later expanded by Moeinikia et al. 2018, created a “leakage calculator” to analyze the probability of leakage due to a combination of pathways in wellbore cement.

Lavrov and Torsaeter (2018) stated that the microannuli between the cement sheath and casing would not be smooth and introduced tortuosity that will decrease the flow rate. The objective of their work was to determine the “safe length” of cement required such that the resulting flow rate would be under a pre-determined threshold value of 1.1 $\mu\text{L/s}$. The authors used typical wellbore dimensions (7-5/8” [~ 19.4 cm] casing) and pressure gradients ($\nabla P = 3$ kPa/m). Thin sections of a wellbore are assumed to have a constant microannuli width. To determine the cumulative leakage, the annular Hagen-Poiseulle equation was used with a summation term for the leakage volume as shown in Equation 2.69.

$$Q = \frac{2\pi R_0 \Delta P}{12\mu \Delta z \sum_i w_i^{-3}} \quad 2.69$$

Since the flow rate is a derivation of the Hagen-Poiseulle equation, the fluid is assumed to be incompressible. Therefore, the authors used water as the leakage fluid and classified it as the “leakage capacity of the well” or the “hydraulic conductivity” of the well. The mean microannuli in the Gaussian distribution is 20 μm with a standard deviation of 4 μm (i.e. 20%). 10,000 synthetic wells were produced with cement sheath lengths varying from 10 m to 1,000 m.

Lavrov and Torsaeter (2018) showed that in 95% of the synthetic wells, the cement sheath length of 60 m would prevent 95% of the wells from experiencing leakage greater than 1.1 $\mu\text{L/s}$. The tortuosity of the microannuli causes the resulting leakage to decrease dramatically which is in agreement with Corina et al. (2020), but there are some limitations with the methodology described by Lavrov and Torsaeter (2018). The microannuli width they chose (20 ± 4 μm) is arbitrary.

According to Feng et al. (2017), those authors showed microannuli widths of 200+ μm . Lavrov and Torsaeter (2018) state that even small variations of microannuli changes (2 μm) can cause significant changes in recommended (safe) cement sheath lengths. The example they described showed a difference from 10 m to 250 m. This methodology also is only valid for water. Assuming that water leakage is the “leakage capacity” of a well severely underestimates the leakage potential when considering gas has less viscosity and density. Therefore, gas should have higher flow rates when compared to water. The final issue with this method lies with Equation 2.69. As described in Section 2.4, Hagen-Poiseuille flow was created for horizontal flow in which gravity is neglected. When considering vertical wells (or vertical parts of wells), the weight of the water will have a negative effect on flow rates. Gravity forces would be countering any pressure driven flow upwards and should be accounted for in leakage predictions.

Another method shown by Ford et al. (2017) and later expanded by Moeinikia et al. (2018) combines the cumulative leakage through wellbore cement by performing a Monte Carlo simulation of leakage rates for each leakage pathway resulting in a leakage calculator for a given well. The leakage calculator investigates the combination of different leakage pathways within the wellbore cement and provides confidence intervals for potential leakage rates. The potential leakage pathways are cement permeability, flow through cement cracks, and flow through microannuli at the cement interface. Leakage due to cement permeability is quantified using Darcy flow (Equation 2.52 from Section 2.7), leakage due to cement cracks is quantified by Hagen-Poiseuille slot flow (Equation 2.49 from Section 2.6), and leakage along the microannuli is quantified using the annular Hagen-Poiseuille flow equation (Equation 2.41 from Section 2.5). The authors of both papers showed this method as a proof of concept in which the cement permeability,

microannuli width, fracture aperture, and fracture width are not known. These values are to be determined through physical experiments or other numerical methods such as FEA models.

The issues with these different analytical methods are that the thick wall cylinder with Kirsch analytical equations lack the complexity to accurately represent complex geometries (such as nonconcentric wellbores), complicated boundary conditions, complex failure analysis (such as fracture mechanics), and the solutions are for a discrete depth. The method presented by Lavrov and Torsaeter (2018) assumes a microannuli width (plus variation), has all the assumptions associated with Hagen-Poiseuille flow (i.e. only valid for incompressible fluids), and doesn't incorporate the effect of gravity on the fluid flow. The leakage calculator presented by Ford et al. (2017) and Moeinikia et al. (2018) has too many leakage pathway variables assumed (the user has to input fracture magnitudes and permeability), is only valid for incompressible fluids, and neglect the effect of gravity on the fluid. Given that these analytical methods do not predict the leakage magnitudes (microannuli or fracture width), researchers have used numerical methods to bridge this gap.

2.10 Numerical Methods

The analytical model discussed in the previous section lacks complexity to accurately represent complex geometries (such as non-concentric wellbores), complicated boundary conditions, and complex failure analysis such as fracture mechanics and debonding mechanisms that researchers have used finite element models to address these shortcomings. Finite element models have become an important tool to study the creation and severity of leakage pathways in cement sheaths for over 20 years. The following sections address the various numerical FEA models for leakage estimation. The traditional models did not incorporate fluid propagation

whereas recent models have developed fluid propagation capabilities. The foundation of the FEA methods used in leakage simulations is outlined in Appendix K.

FEA Models without Fluid Propagation

Bosma et al. (1999) used a 2D-FEA to evaluate different forms of cement failure as a thermo-elasto-plastic model with Mohr-Coulomb plasticity to describe shear failure, and smeared cracking to determine debonding. A major conclusion of their work is that the failure of the cement sheath is dependent on the initial stress within the sheath such that if an initial stress in the cement is present, shear failure and debonding were the predominate failure mechanisms. Previous cement integrity analysis used compressive strength as the only indicator for cement integrity, and their research determined that the compressive strength is not sufficient for determining the ability of the cement to provide a seal. Bosma et al. (1999) determined other mechanical properties should be evaluated such as Young's modulus, Poisson's ratio, tensile strength, shear strength, bonding strength, and cement shrinkage and expansion. A limitation of their work is that they did not consider the porous nature of the cement and rock formation.

Fleckenstein et al. (2001) performed linear elastic 2D FEA in which they evaluated von-Mises stresses for cement sheath failure. The authors' determined that the primary failure mechanism of cement sheath failure is radial cracking due to tensile, tangential stresses (tensile hoop stresses). The tangential stresses are reduced with ductile cement compositions that have higher Poisson's ratios and lower values of Young's modulus. Brittle cement compositions tend to develop greater tensile tangential stresses resulting in greater cement failure (cracking). A limitation of Fleckenstein et al. (2001) is that they did not evaluate the cement and rock formation as a poro-elastic material.

Ravi et al. (2002) extended Bosma et al.'s (1999) 2D elasto-plastic model by performing staged simulations to represent the drilling of a wellbore, completion of the well, and production of the well. The same failure modes were analyzed as with Bosma et al.'s (1999) model, except Ravi et al. (2002) also included cement shrinkage and expansion parameters. Ravi et al. (2002) determined that the integrity of the cement sheath is controlled by its mechanical properties, formation properties, and well operating parameters. Pattillo and Kristiansen (2002) implemented a staged 2D elasto-plastic FEA approach to investigate tubular failure based off Drucker-Prager criteria in horizontal wellbores with imperfect cementing placement. Their simulation stages included the history of the formation from discovery in-situ stresses, global pore pressure depletion for the field, addition of the wellbore to the formation, and local production. The goal of their study was to investigate how the changes in vertical stresses affect horizontal wellbore failure. A limitation of Pattillo and Kristiansen's (2002) 2D approach is that anisotropic stresses were not included. Only the vertical and one horizontal stress were analyzed due to the 2D nature of horizontal wellbores.

Gray et al. (2009) established a framework for a 3D elasto-plastic life-of-well FEA to evaluate cement debonding (based off contact bond strength) and failure (based off Mohr-Coulomb criterion) at all stages of a wellbore after construction. Their model included far-field stresses, cement hardening and shrinkage, and debonding at the casing/cement and cement/formation interfaces. Nygaard et al. (2014) and Weideman and Nygaard (2014) expanded Gray et al.'s (2009) model to include temperature changes and poroelasticity while evaluating wellbore near term and long-term integrity, cement and casing deformation (Li and Nygaard 2017), and quantify micro-annuli widths (Bois et al. 2012; Zhang et al. 2017; Crain et al. 2018). The results of the expanded Gray et al. (2009) models determined that changes in wellbore pressure

and temperature are predominant factors that cause cement sheath debonding, but the authors are not in agreement on which cement sheath interface is experiencing debonding. Zhang et al. (2017) concluded that debonding occurs at the cement/rock formation interface while Nygaard et al. (2014) and Weideman and Nygaard (2014) determined debonding to occur at the casing/cement interface. Gray et al. (2009) experienced debonding at the casing/cement interface, but the authors only modeled debonding criterion at the casing/cement interface.

The studies presented in the previous paragraph have either attempted to quantify which parameters are important in cement sheath failure (but ignored important cement sheath characteristics such as cement pore pressure) or focused on specific scenarios without considering variations in wellbore parameters. The summary of the staged FEA models that do not evaluate fluid interaction show that cement sheath debonding is the primary failure mechanisms and the main causes are as follows:

- Changes in Internal Casing Pressure
 - Nygaard et al. 2014; Weideman and Nygaard 2014; Patel and Salehi 2019.
- Changes in Internal Casing Temperature
 - Nygaard et al. 2014; Lavrov et al. 2015; Zhang et al. 2017.
- Depths/Wellbore Dimensions
 - Crain et al. 2018.

The primary limitations of the staged well life cycle models are that they consist of thin sections that do not investigate if a leakage path to the top of cement is continuous and they do not implement the effect of fluid propagation.

FEA Models with Fluid Propagation

To compensate for the limitations of FEA models that do not include fluid interactions, a new approach was developed by Zielonka et al. (2014) that replicates the hydraulic fracturing process of an injected fluid at an interface, such as cement sheath interfaces. The new methodology

involves Reynold's Lubrication Theorem (Equation 2.70) which states that the change in gap width with respect to time $\left(\frac{\delta w}{\delta t}\right)$ plus the fracturing fluid flux per unit width $(\nabla \cdot \mathbf{q})$ plus the normal flow velocities through the top (v_t) and bottom (v_b) surfaces of the fracture (leak-off velocities) is equal to the injection rate (Q_o) multiplied by the Dirac delta function $[\delta(x - x_o)]$. A schematic of the fracturing fluid velocities within a fracture is shown in Figure 2.21.

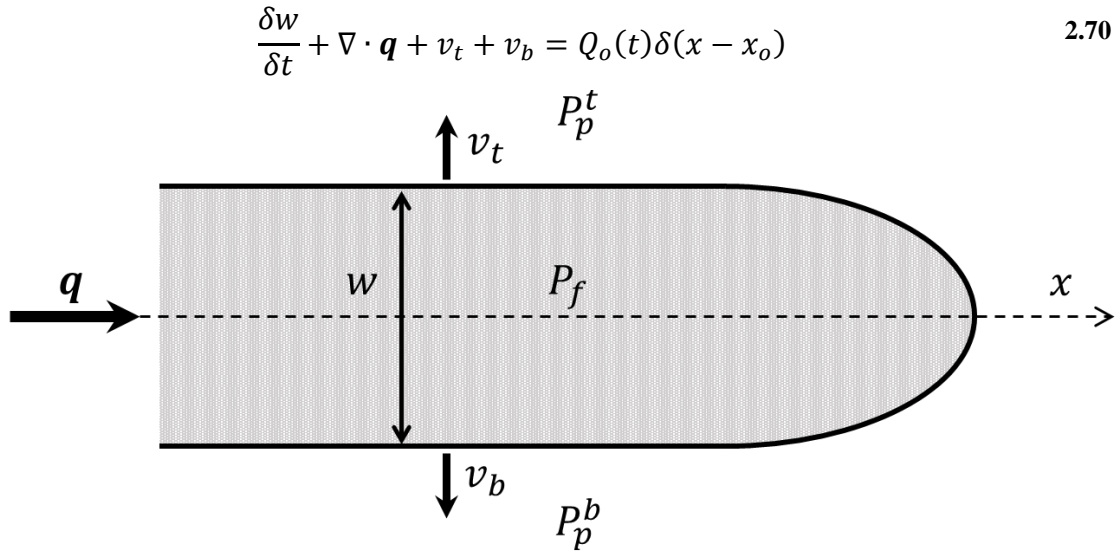


Figure 2.21: Schematic showing the fracturing fluid flow (q), fracture width (w), pressures surrounding the fracture (P_p^t, P_p^b), and the leak-off velocities (v_t, v_b).

The fracturing fluid velocity (q) in Equation 2.70 is quantified by the Hagen-Poiseuille equation for 2D slot flow shown in Equation 2.71 where ΔP_f is the pressure drop through the fracture, Δx is the length, and μ_f is the fracturing fluid viscosity. Since Equation 2.71 is from the Hagen-Poiseuille equation, the assumptions listed in Section 2.4 apply to the fracturing fluid velocity.

$$q = -\frac{w^3}{12\mu_f} \nabla P_f = -\frac{w^3}{12\mu_f} \frac{\Delta P_f}{\Delta x} \quad 2.71$$

The leak-off velocities are described by Equations 2.72 (v_t) and 2.73 (v_b) in which c_t and c_b are the leak-off coefficients for the top and bottom respectively, and P_p^t and P_p^b are the pore pressure for the top and bottom, respectively.

$$v_t = c_t(P_f - P_p^t) \quad 2.72$$

$$v_b = c_b(P_f - P_p^b) \quad 2.73$$

The Reynold's Lubrication Theorem only describes the fluid velocities. The fracture gap (w) within Equation 2.70 is determined by failure criteria within the FEA model which is the traction separation cohesive law (SIMULIA 2016; ANSYS 2019).

One limitation of this methodology is that for the fluid pressure to be applied in the fracture, the separation distance between the interfaces has to be completely debonded. From Section 2.3.1, the cohesive zone is considered completely debonded when the separation gap is larger or equal to the complete separation distance (δ_f). This nuance has two implications: first for the hydraulic fracture to initiate, a defect has to be imposed in the FEA model. Secondly, δ_f is dependent on the traction separation law parameters used. As described in Section 2.3.1, the parameters determined by Wang and Taleghani (2014) resulted in a complete separation distance of 400 μm ($\delta_f = 400 \mu\text{m}$). Feng et al. (2017) implemented an initial crack defect (w_i) of 2 mm. As reported by Gray et al. (2009) and Crain et al. (2018), microannuli magnitudes are in the order of microns (μm), not millimeters (mm). Both Gray et al. (2009) and Crain et al. (2018) report magnitudes of less than 100 μm . For the R.L.T. FEA model methodology to work, significant defects have to be implemented in the models.

Another nuance of the R.L.T. FEA methodology is shown in Equation 2.70. The right hand side consists of the injection rate term (Q_o). This implies that an injection rate has to be occurring for the model to have hydraulic fluid propagation. If zero injection is applied, then the fracturing fluid flux ($\nabla \cdot \mathbf{q}$) is dependent on the leak-off velocities (v_t and v_b). Without an injection fluid, the pore pressure of the top and bottom (P_p^t and P_p^b) will be larger than the hydraulic fluid pressure (P_f). The pore pressures would not be high enough to cause hydraulic fracture propagation (if they were high enough, then the wellbore would have been fractured during completions). So the R.L.T. FEA model can replicate the hydraulic fracturing process (such as during completions), but cannot predict fluid leakage during the life of the well.

An additional limitation of models that implement R.L.T. is that the simulations are not staged like the traditional well life cycle models described in the previous section. Neglecting to stage the construction of the well results in inaccurate stresses at material interfaces as described by Weideman (2014). The methodology presented by Zielonka et al. (2014), Feng et al. (2017), Gosavi et al. (2017), Kumar et al. (2017), Searles et al. (2018), Jiang et al. (2020), and Xu et al. (2020) use a two-step model in which the cement boundary conditions are applied in the first step (far-field stresses, pore pressure, casing pressure), and the fluid injection occurs in the second step. This methodology ignores the microannuli that occur during the well's lifecycle. From the previous section, the microannuli occurs due to a difference in stresses between the cement sheath and casing. One scenario where microannuli occurs is during cement hydration (Bois et al. 2017; Vu et al. 2018; Bois et al. 2019; Gheibi et al. 2021).

Bois et al. (2017) developed a 2D thermo-chemo-poro-elasto-plastic FEA model which investigates gas migration within the cement sheath. The unique aspect with this method is that the model determines the cement mechanical and chemical properties based off the degree of

cement hydration (according to Arrhenius thermo-activated law) whereas previous models (such as Nygaard et al. (2014), Lavrov et al. (2015), Zhang et al. (2017), and Crain et al. (2018) to name a few) assume mechanical properties for the cement. According to Bois et al. (2017), two conditions are required for gas migration: a leakage pathway and underbalanced conditions which are when the formation pore pressure is larger than the cement pore pressure. This methodology was later expanded by Vu et al. (2018) which the model determines cement sheath failure from a hydration point of view. Debonding of the cement sheath to the steel casing can occur due to changes within the cement itself such as cement shrinkage. The last expansion of the cement hydration methodology is performed by Bois et al. (2019) in which the authors included hydraulic propagation of the microannuli caused by cement hydration. The authors state that debonding is the most likely failure mechanism, and the mechanical properties of cement are not important. One issue with the methodology introduced by Bois et al. (2019) is that the hydraulic propagating fluid is incompressible. The authors do not consider the fluid propagation of a gas. Bois et al.'s (2019) methodology also simulates the wellbore as decoupled entities. The decoupled simulations are referred to as system response curves (SRC) in which the components of the wellbore are modeled individually to get the stress versus displacement curves. Then the authors match the stresses for the components since the stresses at the boundaries of the individual components have to match (due to Newton's third law). If the displacements are different between the components, then the difference is the resulting gap. Using this method, complex bonding properties (such as the traction separation law) are not included. Bonding is boiled down to a zero-traction tensile failure.

Another method that investigates the cement sheath during hydration is presented by Gheibi et al. (2021). The authors developed a modified discrete element model based approach that analyzes the integrity of the cement sheath by considering the cement as an aging material in

which its poro-elastic properties (pore pressure, setting stress, and compaction) are estimated using micro-mechanical methods. The model incorporates both of the cement's continuum and discontinuum features. When the cement is in the elastic region, the elements are acting as a continuum which is normal finite element methods. Once failure occurs, the discontinuum code is activated and the fractures form utilizing special elements with "springs" that break to form fractures when the stress exceeds Mohr-Coulomb failure criterion. The results from Gheibi et al. (2021) show that an increase in the wellbore pressure can cause radial fractures and shear failure in the cement, but the cement failure was limited to the cement sheath and did not propagate into the rock formation or the steel casing. The magnitude of the fractures from Gheibi et al.'s (2021) model ranged from 1 to 50 μm .

One critical limitation of the fluid penetration models is that they do not accommodate for gas hydraulic propagation. Since the R.L.T. is based upon Hagen-Poiseuille flow, the fluid is assumed to be incompressible. The R.L.T. models have to have large fractures for the interfaces to be considered "open" with a fluid penetrating pressure and have to have an injection pressure. The methodologies presented by Bois et al. (2017) [and expansions Vu et al. (2018) and Bois et al. (2019)] assume 2D models that investigate cement hydration induced failure. However, these models do not consider the entire wellbore or life cycle events that occur after hydration. Gheibi et al. (2021) also considers 2D models and investigates failure during cement hydration. The failure mechanics used (Mohr-Coulomb) incorporate bulk cement failure, but does not look at interface failure.

Summary of Previous Work

From all the potential leakage pathways in a wellbore, the general consensus from experimental and numerical methods is that the cement used when completing and abandoning

wellbores is the most at risk for integrity issues. The steel casing has been well studied and is designed with safety factors and design considerations for extreme conditions in the GoM. The surrounding rock formation has also been studied extensively in the past however, there are less design aspects engineers can do for long term integrity with respect to the formation. The cement used when completing and eventually plugging the well is less understood with many design aspects that can change the properties. Even with all the research focusing on the cement sheath, many aspects have not been addressed. Numerical models that predict cement sheath integrity assume the leaking fluid is incompressible, but do not investigate gases (Gray et al. 2009; Zielonka et al. 2014; Feng et al. 2017; Gosavi et al. 2017; Kumar et al. 2017; Crain et al. 2018; Searles et al. 2018; Bois et al. 2019; Jiang et al. 2020; Xu et al. 2020; Gheibi et al. 2021). The methods that do investigate gases, have assumptions that are voided for wellbore conditions (Al Ramadan et al. 2019; Corina et al. 2020) or assume microannuli/effective permeability values (Ford et al. 2017; Lavrov and Torsaeter 2018; Moeinika et al. 2018; Al Ramadan et al. 2019;).

The various models have shown the likely leakage mechanisms and locations, but have failed to provide comprehensive quantification of the microannuli widths. Many models just assume a microannuli (or permeability) value (Ford et al. 2017; Lavrov and Torsaeter 2018; Moeinkia et al. 2018). Other models have treated wellbore leakage as a hydraulic fracturing process but due to their assumptions, water is assumed to be the fracturing fluid (Zielonka et al. 2014; Feng et al. 2017; Jiang et al. 2020). The water assumption makes the numerical approximation simple, but could potentially underestimate wellbore leakage if gas is the fracturing fluid. Therefore, this dissertation will investigate if leakage occurs in GoM wells by developing a realistic FEA model with fluid propagation mechanics to determine if a continuous leakage pathway is occurring and to provide accurate fluid leakage rates.

Chapter 3: Field Description

This section gives an overview of the current status of the wells in the Gulf of Mexico (GoM) and describes the fields used in the numerical analysis.

Gulf of Mexico

Drilling in the GoM started in the early 1900's with very primitive rigs connected to land by piers in shallow water (~6 m [~20 ft.]). The oil industry boomed in the GoM after the Second World War leading to two major changes: more wells were drilled, and technological advancements allowed wells to be in deeper waters (BSEE.gov). The deepest wells are now drilled in 3,048 m (10,000 ft.) of water, but the majority of wells drilled are still in shallow water (<73 m [240 ft.]).

The GoM is categorized into two major areas: state owned seabed and federal owned seabed. The individual coastal states own the seabed within three miles of the individual state's coast while the Federal government owns the seabed from the three-mile mark to a line approximately 200-300 miles offshore. Only the federal area known as the Outer Continental Shelf (OCS)² is considered in this dissertation.

The OCS is divided up into three regions: the Western Gulf of Mexico Planning Area, the Central Gulf of Mexico Planning Area, and the Eastern Gulf of Mexico Planning Area as illustrated in Figure 3.1. Only the Western Planning Area and the Central Planning Area have active leases at the time of this publication. The Eastern Planning Area is under a congressional moratorium

² All of the wells in the GoM located in the OCS are under the jurisdiction of the Bureau of Ocean Energy Management (BOEM) and their sister agency, the Bureau of Safety and Environmental Enforcement (BSEE). The BOEM manages the development of energy and mineral resources while the BSEE promotes and enforces safety in offshore energy exploration and production within the OCS.

and cannot be drilled. The planning areas are then subdivided into Official Projection Diagrams (OPD's) which are then divided into grids similar to onshore townships and ranges.

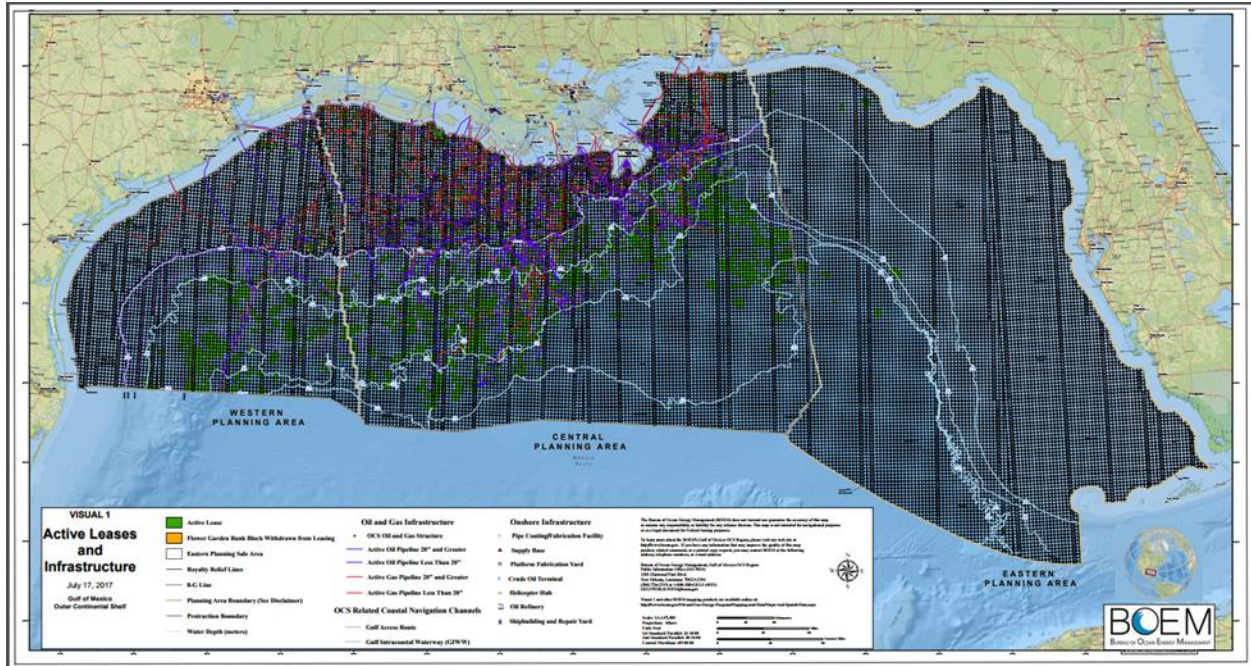
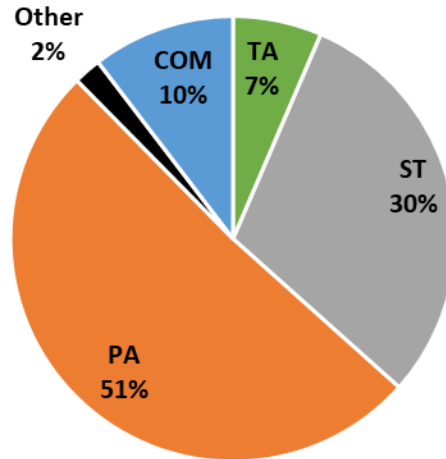


Figure 3.1: The Outer Continental Shelf (OCS) of the Gulf of Mexico showing the three planning areas: the Western Planning Area, the Central Planning Area, and the Eastern Planning Area. Figure from www.boem.gov.

As of 9/13/18, there are 54,291 wells in the OCS of the GoM. There are 31,192 abandoned wells in which 27,691 wells are permanently abandoned (PA), and 3,501 wells are temporarily abandoned (TA). The distribution of wellbore statuses in the OCS are shown in Figure 3.2.



54,291 Total Wells

As of 9/13/18

Figure 3.2: The distribution of wells in the Outer Continental Shelf (OCS) in the Gulf of Mexico. Note: TA = temporarily abandoned, PA = permanently abandoned, COM = borehole completed, ST = sidetracked wellbore, and Other = various wellbore statuses for wellbores in the planning stage.

Of the 54,291 wells in the OCS, the Eugene Island OPD, located in the Central GoM planning area, was selected for the parametric study to represent wells with a range of ages, statuses, and depths with a similar distribution shown in Figure 3.2. For the case study well, the High Island OPD, located in the Western GoM planning area, was selected, and a representative well was selected.

Eugene Island OPD

In the Eugene Island OPD, there are 6,167 unique API Well Numbers according to the BSEE. Available data from BSEE include specific well names, API well identifiers, lease numbers, sea floor area, bottom block number, water depth, lease owner, spud dates, total TVD, total depth (TD), well status, dates for well status changes, and much more information. All of the wells in the Eugene Island OPD have a status of: “Cancelled (CNL)”, “Completed (COM)”, “Permanently Abandoned (PA)”, “Temporarily Abandoned (TA)”, “Sidetracked (SI)”, or “Approved Sidetrack (AST)”.

Sidetracked wells are considered a separate well and have a unique API number. However, sidetracked wells share the parent well’s surface and intermediate casings. To avoid duplications,

wells that had a status code of “ST” or “AST” were omitted from the data set. Wells that were canceled (“CNL” status) were also omitted because only wells that were completed or abandoned are of interest in this study. Omitting those wells lowered the number of unique wells from 6,167 to 4,030. The distribution of wells before and after omission are shown in Figure 3.3. As indicated in Figure 3.3, the average well in the Eugene Island OPD has a status of permanently abandoned.

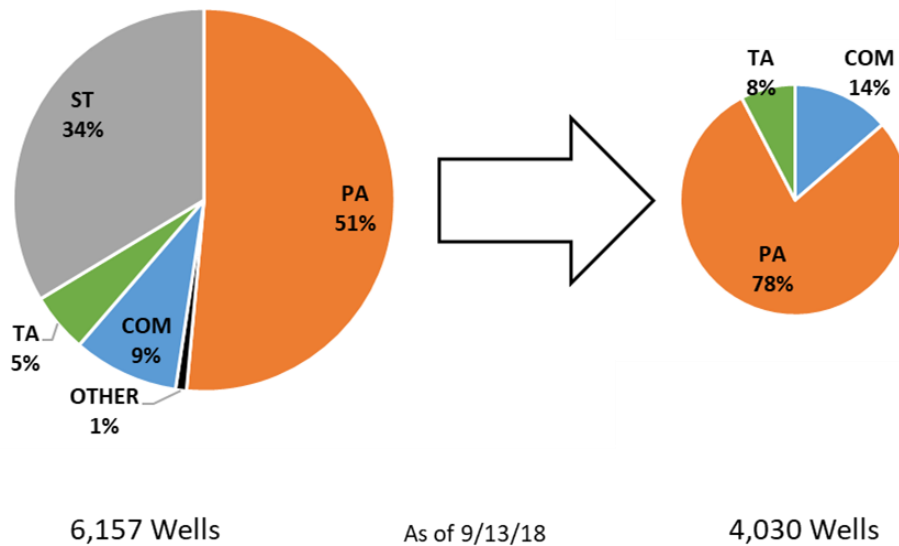


Figure 3.3: The distribution of wells from the Eugene Island OPD before and after removing 2,127 wells that had a status of CNL, ST, and AST.

The distribution of the total depth (TD) of the wells in the Eugene Island OPD are shown in Figure 3.4. The wells range from a non-zero depth³ of 75 m (245 ft.) to 10,413 m (34,162 ft.). The average TD is 2,989 m (9,808 ft.) with a standard deviation of 1,098 m (3,604 ft.). Figure 3.4 indicates that of the Eugene Island OPD wells, the medium TD range is between 1,219 – 3,658 m (4,000 – 12,000 ft.).

³ Some wells had a depth of 0 m (0 ft.). This is due to a lack of complete records in which the TD was not known.

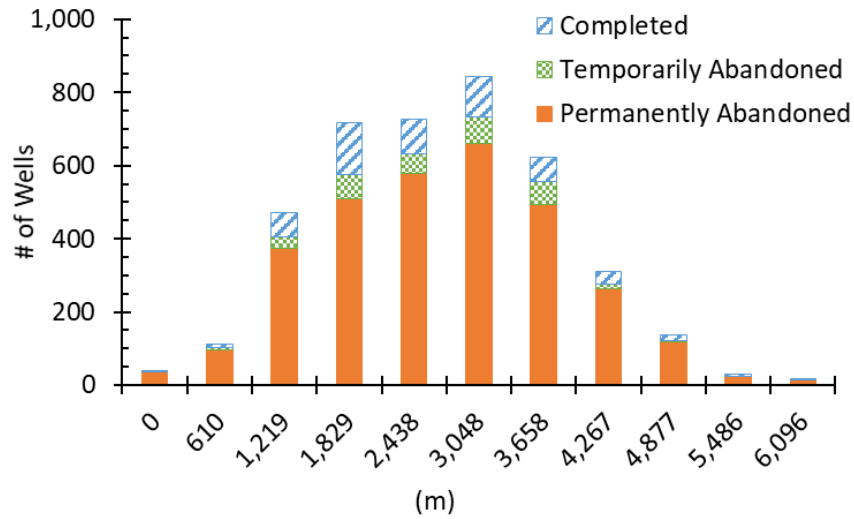


Figure 3.4: Total depth distribution of the wells in the Eugene Island OPD including the distribution of their respective status codes of Completed (COM), Temporarily Abandoned (TA), or Permanently Abandoned (PA).

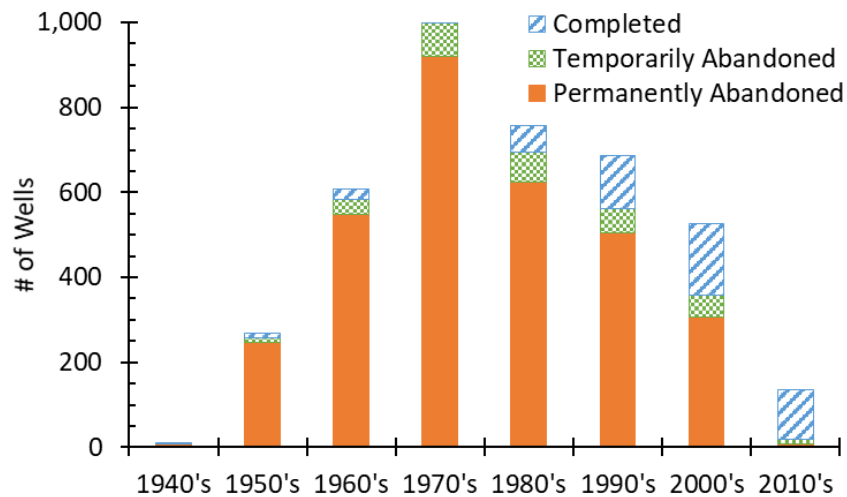


Figure 3.5: Spud date distribution of the wells in the Eugene Island OPD including the distribution of their respective status codes of COM, TA, or PA.

The distribution of borehole spud dates with their respective status codes is shown in Figure 3.5. The first borehole spud in the Eugene Island OPD was May 1947, and the most recent borehole was spud in June 2018. It is important to note that active drilling is still occurring in this OPD, and the data used in this project was acquired in September 2018. The average borehole spud date is 07/06/1982 with a standard deviation of 15.3 years. Figure 3.5 shows that the majority of the wells

that are still producing are recently drilled (within the last three decades). 13% of the 135 wells drilled after 2010 are abandoned (9 TA & 9 PA).

The distribution of well water depths with their respective status codes is shown in Figure 3.6. The range of non-zero water depths are from 2 m (8 ft.) to 168 m (550 ft.). The average water depth is 46 m (151 ft.) with a standard deviation of 32 m (105 ft.) (data for water depths was missing for nine wells and had a water depth of zero. These values were omitted from the figure).

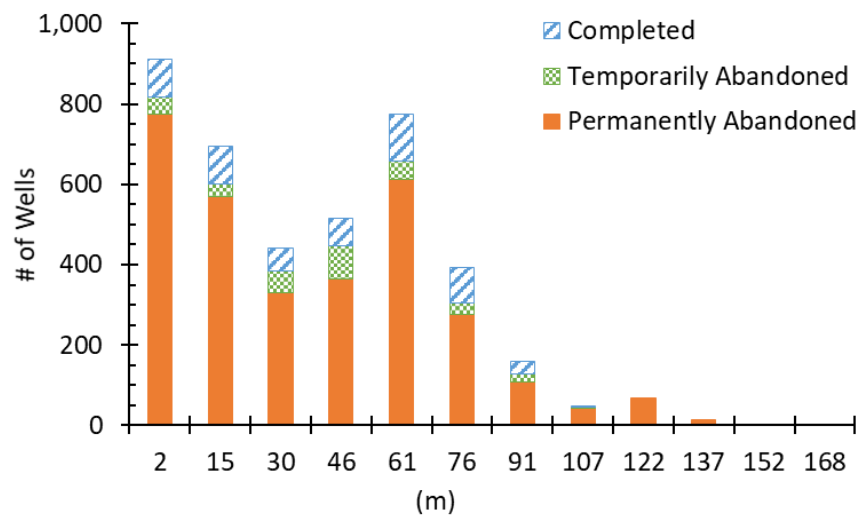


Figure 3.6: Water depth distribution of the wells in the Eugene Island OPD including the distribution of their respective status codes of COM, TA, or PA.

After an analysis of all the distribution for wells in the Eugene Island OPD, the well characteristics in this region are:

- Status Code: PA
- TD: $2,989 \pm 1,098$ m ($9,808 \pm 3,604$ ft.)
- Spud Date: $7/6/1982 \pm 15.3$ years
- Water Depth: 46 ± 32 m (151 ± 105 ft.)

3.1 Three Representative Wells

A case study for the Eugene Island OPD will be performed with the characteristics of a medium depth well. The well that was selected as the medium deep well was Well API Number 177100002670. The characteristics of this well are as follows:

Medium Well

- API Well Number: 177100002670
- Status Code: PA
- TD: 3,014 m (9,889 ft.)
- MD: 3,067 m (10,063 ft.)
- Spud Date: 04/30/1981
- Water Depth: 55 m (180 ft.)
- Production Data: Yes
- Bottom Hole Pressure (BHP) Gradient: 9.50 kPa/m (0.420 psi/ft.)

This well is considered the base well, but we are also interested in the wells on the low and high ends of the TD, excluding outliers, to create three representative well scenarios for the OPD. The criteria for the deep and shallow depth wells were TD, production data, and a BHP that is similar to the medium depth well. The wells on the deep and shallow end of the TD are as follows:

Deep Well

- API Well Number: 177094046200
- Status Code: COM
- TD: 6,028 m (19,776 ft.)
- MD: 6,127 m (20,103 ft.)
- Spud Date: 08/07/1981
- Water Depth: 7 m (22 ft.)
- Production Data: Yes
- BHP Gradient: 8.84 kPa/m (0.391 psi/ft.)

Shallow Well

- API Well Number: 177104115600
- Status Code: PA
- TD: 797 m (2,614 ft.)
- MD: 1,204 m (3,950 ft.)
- Spud Date: 09/18/1985
- Water Depth: 66 m (215 ft.)
- Production Data: Yes
- BHP Gradient: 11.1 kPa/m (0.490 psi/ft.)

Figure 3.7 depicts a schematic of the three wells: the shallow, the medium, and the deep wells including casing dimensions and depths, casing (or liner) strings, and the approximate locations of the perforations. The simulation depth will be set at the bottom of the previous casing strings above the perforations to analyze if the barrier above the production horizon is intact (i.e. ensure that the cement in the annulus is not damaged). The medium and deep wells have minor deviation [53 m (174 ft.) and 100 m (327 ft.), respectively] while the shallow well appears to be a horizontal well [407 m (1,336 ft.) given the difference between the measured depth (MD) and the total depth (TD)]. Therefore, the three wells studied are assumed to be vertical wells.

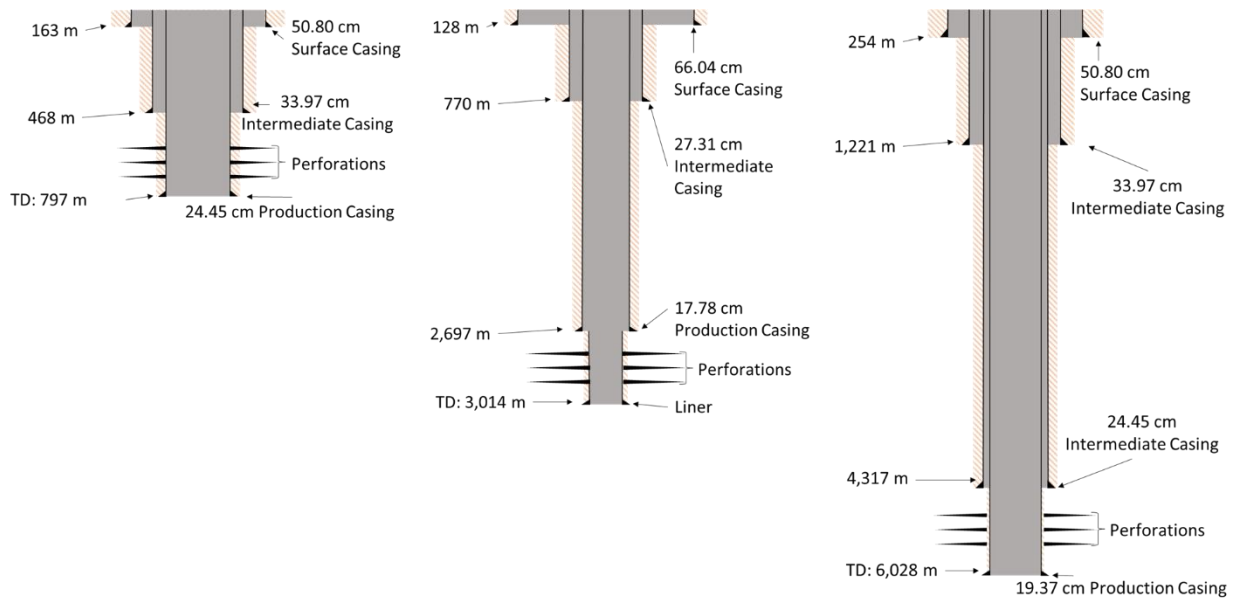


Figure 3.7: Schematic of the shallow well (left), medium well (centered), and deep well (right). Included are the depths of the casing strings, dimensions of the casings, number of casing strings, and the approximate location of the perforations.

3.2 Formation Properties

Finkbeiner et al. (1996) performed a study in the Eugene Island OPD in which they determined the overburden stress (σ_v) and minimum horizontal stress (σ_h) for certain depths from available leak-off test (LOT) and fracture completion data. The authors determined that the area is in a normal stress regime which constrains minimum horizontal stress (σ_H) to a minimum value of

$0.7 \cdot \sigma_v$ to a maximum value equal to σ_v . The range of minimum horizontal stress is shown in Equation 3.1. The normal stress regime is showed in Equation 3.2. From Equations 3.1 and 3.2, all three principal stresses can be constrained if the overburden stress is known.

$$0.7\sigma_v \leq \sigma_h \leq \sigma_v \quad 3.1$$

$$\sigma_h \leq \sigma_H \leq \sigma_v \quad 3.2$$

Finkbeiner et al. (1996) recorded the overburden stress at different depths for the Eugene Island OPD and is shown in Figure 3.8. A linear trendline was determined such that the overburden stress can be calculated for a given depth (Equation 3.3). The minimum horizontal stress can be calculated based off Equation 3.1. The maximum horizontal stress is assumed to be the average of the minimum horizontal stress and the overburden stress.

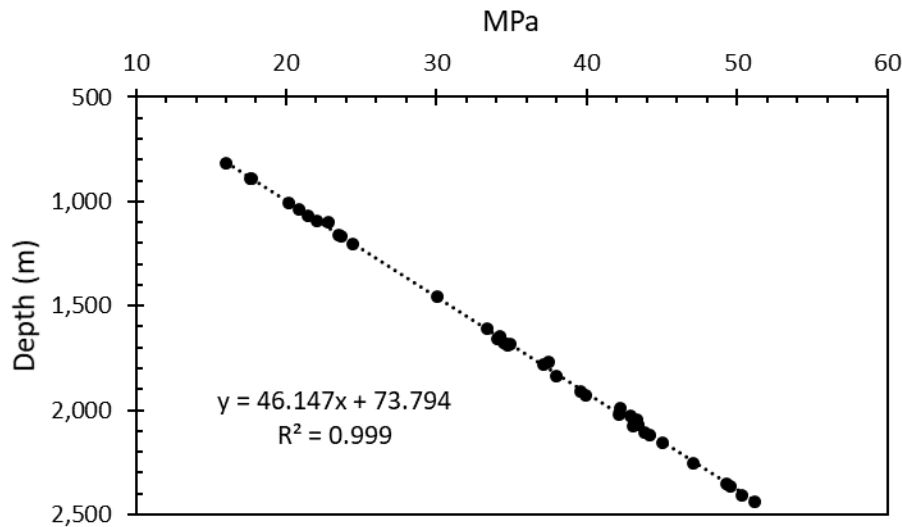


Figure 3.8: Finkbeiner et al. (1996) data overburden stress (σ_v) with respect to depth. A linear approximation was determined such that the overburden stress can be determined for any depth in the Eugene Island OPD.

$$\sigma_v = \frac{\text{Depth} - 73.794}{46.147} \quad 3.3$$

The rock formation is assumed to be shale. The mechanical values for shale come from Zhang et al (2016) for the Young's modulus (E) and from Weideman (2014) for the Poisson's ratio (ν) since direct measurements for this region are not known. The rock mechanical values are assumed to be the same for all three representative wells.

High Island OPD

The case study well was selected from the High Island OPD in the Western GoM planning area. In the High Island OPD, there are 3,828 unique API Well Numbers issued by BSEE. Similar to the Eugene Island OPD, all of the wells in the High Island OPD have a status of: "Cancelled (CNL)", "Completed (COM)", "Permanently Abandoned (PA)", "Temporarily Abandoned (TA)", "Sidetracked (SI)", or "Approved Sidetrack (AST)". To avoid duplications, wells with a status code of "ST" or "AST" were omitted from the data set. Wells that were canceled ("CNL" status) were also omitted because only wells that were completed or abandoned are of interest in this study. Omitting those wells lowered the number of unique wells from 3,828 to 2,773. The distribution of wells before and after omission are shown in Figure 3.9. As indicated in Figure 3.9, the average well in the High Island OPD has a status of permanently abandoned.

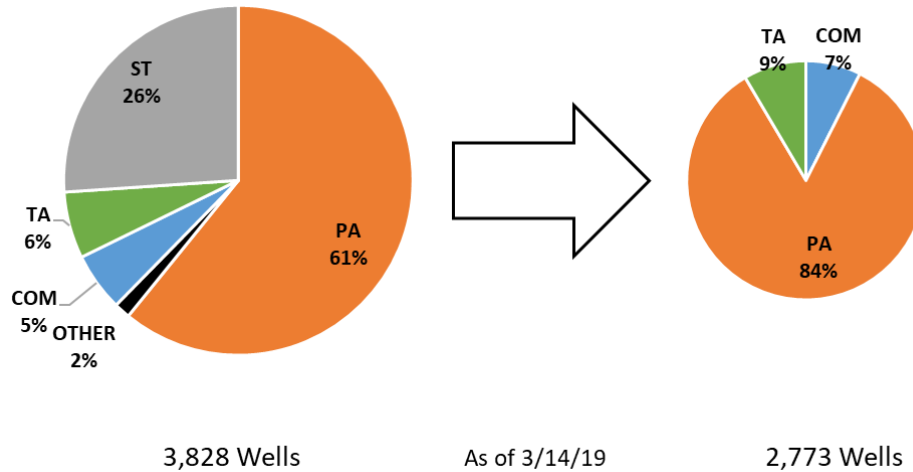


Figure 3.9: The distribution of wells from the High Island OPD before and after removing 1,055 wells that did not have a status of TA, COM, or PA.

The distribution of the TD of the wells in the High Island OPD are shown in Figure 3.10. The wells range from a non-zero depth of 93 m (305 ft.) to 8,651 m (28,382 ft.) The average TD is 2,541 m (8,336 ft.) with a standard deviation of 928 m (3,044 ft.). A well (API 427094116400) with TD close to the mean depth of the OPD was chosen to be a representative well.

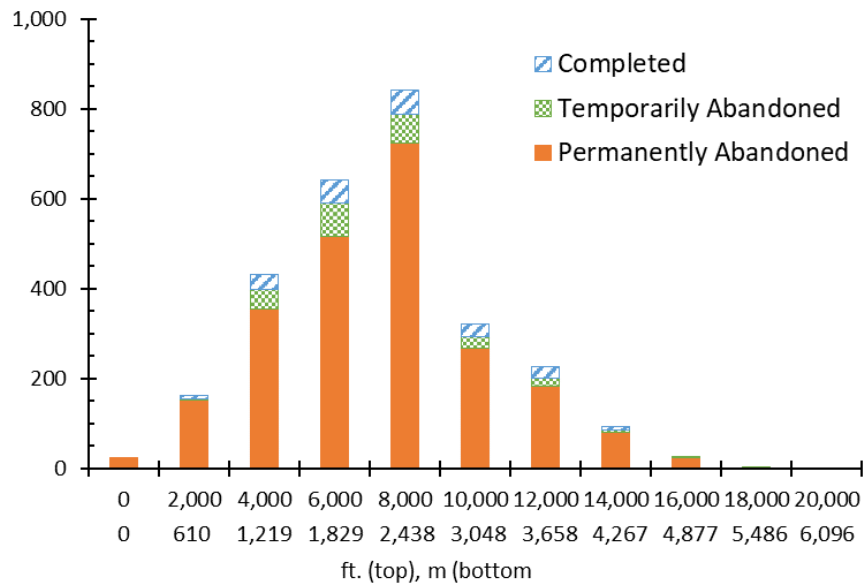


Figure 3.10: Total Depth (TD) distribution of the number of wells in the High Island OPD with the distribution of their respective status codes of completed (COM), temporarily abandoned (TA), or permanently abandoned (PA) with an average being 2,541 m (8,336 ft.). Raw data from BSEE (2019).

3.3 Case Study Well

The plans, reports, and corresponding log data for the representative well (API 427094116400), were purchased through BOEM or BSEE and 36 files were available including the bottomhole pressure (BHP) survey report, end of operations report (EOR), application for permit to drill a new well (APD), well activity report (WAR), application for a permit to modify, drilling fluid logs, raw logs, and directional surveys. For the FEA models, the APD and BHP report contain all the information needed to simulate the well. The information used from the reports include the wellbore dimensions, depths of the casing strings, pore pressure gradients, drilling fluid weight gradients, formation fracture pressure gradients, BHP gradient, and the cement slurry design. Copies of the APD and BHP report are provided in Appendix D.

The vertical well is located in a gas field as stated in the BHP report along with the information that the production fluid has a specific gravity of 0.57 (methane has a specific gravity of 0.55). Figure 3.11 and Figure 3.12 show a schematic of the well with the casing sizes and depths, pore pressures, and drilling fluid weight gradients for both standard and metric units.

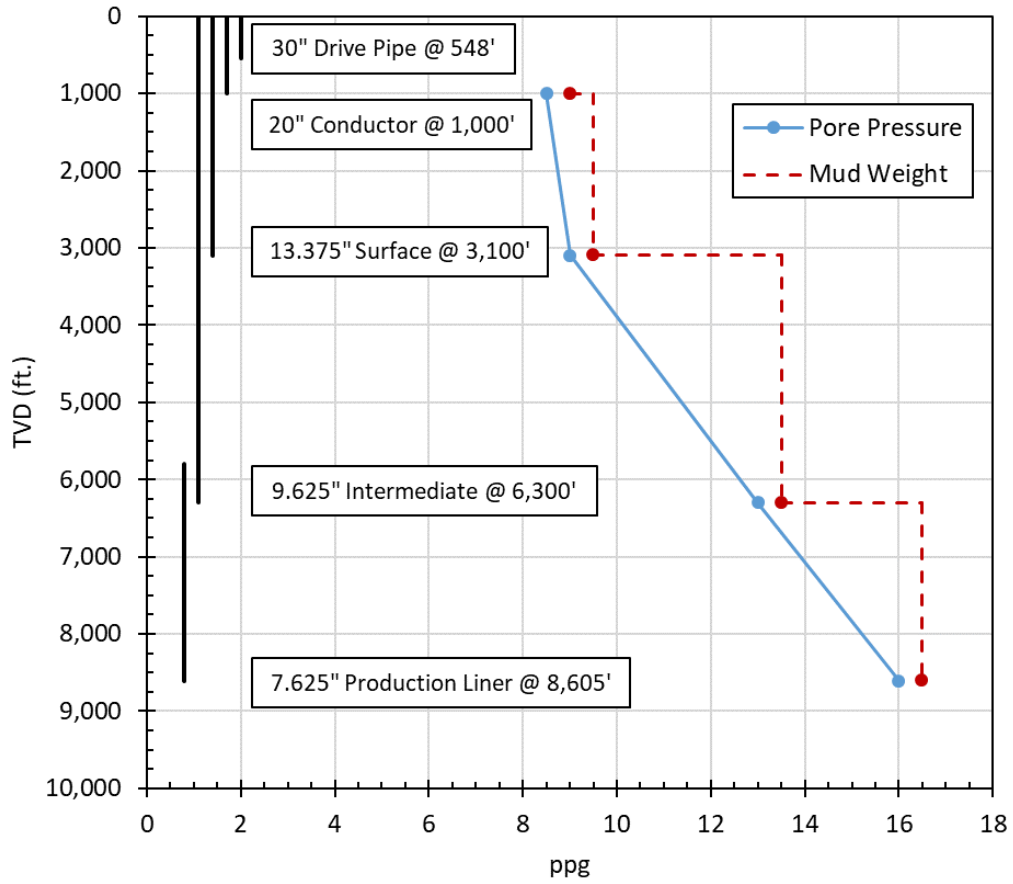


Figure 3.11: High Island well API 427094116400 casing size and depths along with pore pressure and drilling fluid weight gradients in standard units.

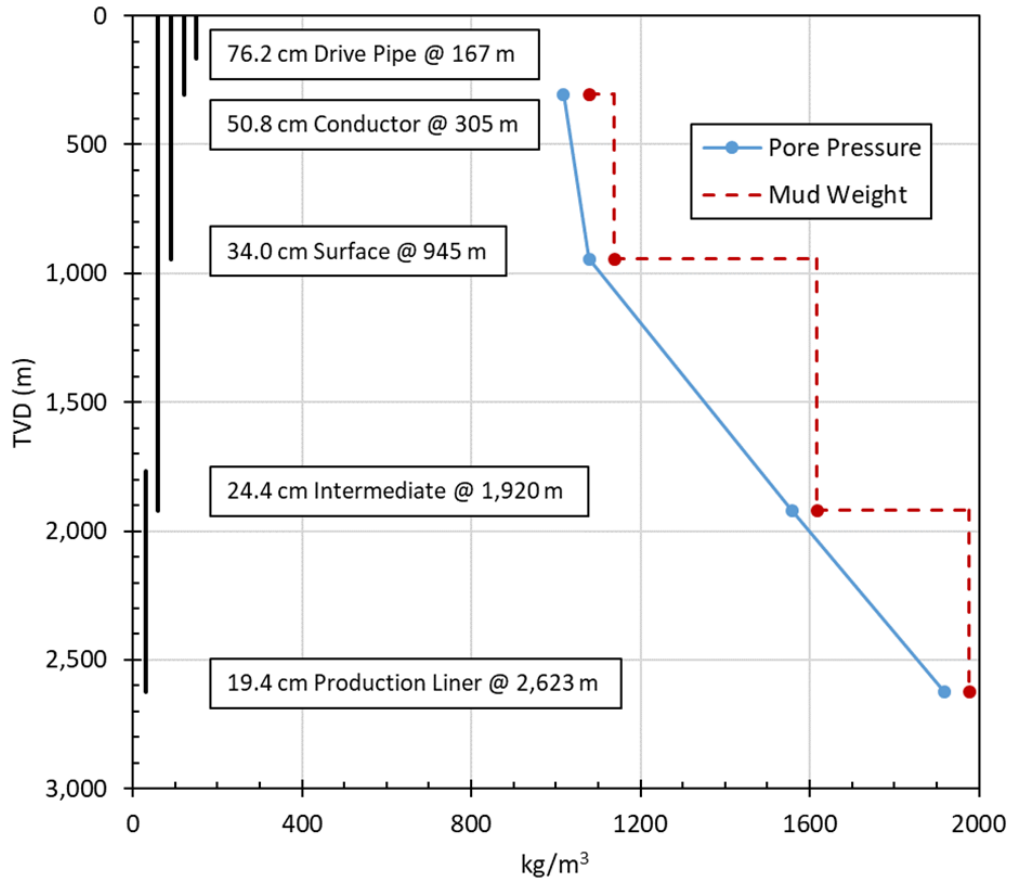


Figure 3.12: High Island well API 427094116400 casing size and depths along with pore pressure and drilling fluid weight gradients in metric units.

3.4 Formation Properties

The in-situ stress gradients for the High Island OPD, reported to be a normal faulting regime, is based on correlations from Breckels and van Eekelen (1982), Wojtanowicz et al. (2000), Meng et al. (2018) as well as the drilling report for the well (OMB Control Number 1010-0141, shown in Appendix D). The overburden stress gradient (σ_v) is based on data from Meng et al. (2018) for the Gulf of Mexico and is shown in Equation 3.4 where the units of σ_v are MPa, true vertical depth (*TVD*) is m, and P_p is MPa. The minimum horizontal stress is taken to be the average from the correlation from Breckels and van Eekelen (1982) [Equation 3.5], measured leak off test (LOT) data from Wojtanowicz et al. (2000) [Equation 3.6], and the fracture pressure gradient listed

in the well APD (Appendix D). The maximum horizontal stress (σ_H) is taken to be the average of the overburden (σ_v) and minimum horizontal stress (σ_h).

$$\sigma_v = \frac{0.944 \cdot \left(\frac{TVD}{0.3048}\right)}{145.038} \quad 3.4$$

$$\sigma_h = \left(0.197 \cdot \left(\frac{TVD}{0.3048}\right)^{1.145} + 0.46 \left((P_p \cdot 145.038) - \left(0.465 \cdot \frac{TVD}{0.3048}\right) \right) \right) \div 145.038$$

When $TVD \leq 3,505$ m

3.5

$$\sigma_h = \left(1.167 \cdot \frac{TVD}{0.3048} - 4.596 + 0.46 \left((P_p \cdot 145.038) - \left(0.465 \cdot \frac{TVD}{0.3048}\right) \right) \right) \div 145.038$$

When $TVD > 3,505$ m

$$\sigma_h = \frac{\left(\frac{TVD}{0.3048}\right) - 836.45}{144.21} \quad 3.6$$

At the end of cement hydration, the pore pressure (P_p) of the cement is assumed to be equal to the pore pressure of the surrounding rock formation (Li and Nygaard 2017; Zhang et al. 2017; Gray et al. 2009). The setting stress of the cement (σ_{cement}) is assumed to be equal to the hydrostatic column of the cement slurry (Bosma et al. 1999; Gray et al. 2009; Bois et al. 2012; Nygaard et al. 2014). The mechanical and thermal properties of the cement were determined from a cement database created for this model with Class H and G cement data, which are common cements for wellbore completions. The summary of the cement database is listed in Table 3.1. The median values were considered the base case while the upper and lower bounds for the parametric study were the 75% and 25% quartiles, respectively. The quartiles were chosen to represent

realistic upper and lower bounds of the mechanical and thermal properties to exclude the outliers that may occur within the dataset.

Table 3.1: Cement database for Class H and Class G cements.

	E	ν	α	κ	c
Max	26.22	0.32	1.25E-05	1.00	1.30
75% Quartile	9.51	0.24	9.40E-06	0.81	1.12
Median	6.38	0.18	8.64E-06	0.41	1.05
25% Quartile	4.22	0.15	7.49E-06	0.36	0.99
Min	0.00	0.02	5.36E-06	0.33	0.15
Data Points	69	26	26	5	34
Reference	1	2	3	4	5

¹McDaniel et al. (2014); Weideman (2014); Ichim & Teodoriu (2017); Wehling (2008); Le Roy-Delage et al. (2000); Deshpande et al. (2019); James & Boukgelifa (2015); Morris et al. (2003); Won et al. (2016)

²McDaniel et al. (2014); Ichim & Teodoriu (2017); Wehling (2008); Deshpande et al. (2019); James & Boukgelifa (2015); Morris et al. (2003)

³Philippacopoulos & Berndt (2002); Loiseau (2014); Weideman (2014)

⁴Weideman (2014)

⁵Philippacopoulos & Berndt (2002); Weideman (2014)

Log analysis of High Island OPD wells has been performed to determine representative rock mechanical values for this region since direct measurements are not known. Well logs from the High Island OPD were collected from BSEE and American Association of Petroleum Geologist (AAPG) databases. The logs were analyzed and two wells with available sonic and gamma ray log data were selected for analysis and digitized to obtain values for Young's modulus (E) and Poisson's ratio (ν). Two well logs contained sonic travel times, gamma ray, and bulk density data. The two wells included a shallow well (API: 427094038700) with a caprock between 2,005 m (6,578 ft.) to 2,010 m (6,595 ft.) and a deep well (API: 427084008900) with a caprock between 3,659 m (12,003 ft.) to 3,688 m (12,100 ft.).

The gamma ray index for the wells was found using Equation 3.7:

$$I_{GR} = \frac{GR_{log} - GR_{sand}}{GR_{shale} - GR_{sand}} \quad 3.7$$

Where GR_{log} is the gamma ray reading taken from the well log, GR_{min} is the minimum gamma ray reading, and GR_{max} is the maximum gamma ray reading. Using the gamma ray index, shale volume for the logged interval is determined in Equation 3.8.

$$V_{shale} = \frac{I_{GR}}{3 - 2I_{GR}} \quad 3.8$$

Using the sonic log data and known sonic travel time values for seawater and shale, Wyllie porosity (ϕ_{Wyllie}) is calculated using Equation 3.9.

$$\phi_{Wyllie} = \frac{\Delta t_{log} - \Delta t_{shale}}{\Delta t_{seawater} - \Delta t_{shale}} \quad 3.9$$

Bulk density (ρ_b) is calculated in Equation 3.10 using known shale and seawater densities.

$$\rho_b = \phi_{Wyllie} \cdot \rho_{seawater} + (1 - \phi_{Wyllie}) \cdot V_{shale} \cdot \rho_{shale} + (1 - V_{shale}) \cdot \rho_{sand} \quad 3.10$$

Compressional (V_p) and shear (V_s) velocities were determined using Equations 3.11 and 3.12, respectively (Greenberg and Castagna, 1992).

$$V_p = \frac{10^6}{\Delta t_{log}} \quad 3.11$$

$$V_s = 0.8042 \cdot V_p - 855.9 \quad 3.12$$

The compressional and shear velocities are used to calculate the Poisson's ratio (Archer and Rasouli 2012).

$$v = \frac{V_p^2 - 2V_s^2}{2V_p^2 - V_s^2} \quad 3.13$$

Using the compressional velocity, shear velocity, and bulk density, the dynamic Young's modulus (E_{dyn}) is determined using Equation 3.14 (Archer and Rasouli 2012).

$$E_{dyn} = \frac{\rho_b \cdot V_s^2 \cdot 3V_p^2 - 4V_s^2}{V_p^2 - V_s^2} \quad 3.14$$

The dynamic Young's modulus is used to determine the static Young's modulus (E_{static}) using Equation 3.15 (Wang 2017).

$$E_{static} = 0.414E_{dyn} - 1.0593 \quad 3.15$$

Chapter 4: Methodology

This section outlines the research methodology and the tasks performed to achieve the objective. First, the derivation of an annular gas flow model is presented in *Derivation of Real Gas Fluid Flow* along with a comparison of the developed flow equations in Section 4.1. Two FEA models were developed for this work; one investigates the stresses at the cement interfaces as a continuum (*Staged Poro-Elastic FEA Stress Continuum Model*) and the other includes failure criteria at the cement interfaces (*Staged Poro-Elastic FEA Fracture Model*). The *Continuous Leakage Pathway Model* explicitly couples the FEA fracture model with real gas flow to replicate hydraulic fracture propagation. The numerical experiments performed in this work are subdivided into verification of the gas flow and FEA models in Section 4.2, a GoM parametric study in Section 4.3, a GoM continuous leakage pathway investigation in Section 4.4, and a case study of a well in the High Island OPD in Section 4.5.

Derivation of Real Gas Fluid Flow

In this section, the derivation of a gas flow equation is presented. As discussed in Section 2.9, the Hagen-Poiseuille model is used to quantify potential cement sheath leakage. The Hagen-Poiseuille model assumes laminar and incompressible flow in the horizontal direction which limits leakage analysis to water or oil as the leaking fluid. The following section derives the gas flow equation from Hagen-Poiseuille flow to account for gas leakage.

For a wellbore where the leakage fluid is an ideal gas in a circular cross-section, Equation 2.36 and Figure 4.1 describes the Hagen-Poiseuille flow where Q is the volumetric flow rate, $\frac{dP}{dx}$ is the pressure drop per unit distance, P_1 is the inlet pressure, P_2 is the outlet pressure, L is the length, R is the radius, and μ is the viscosity.

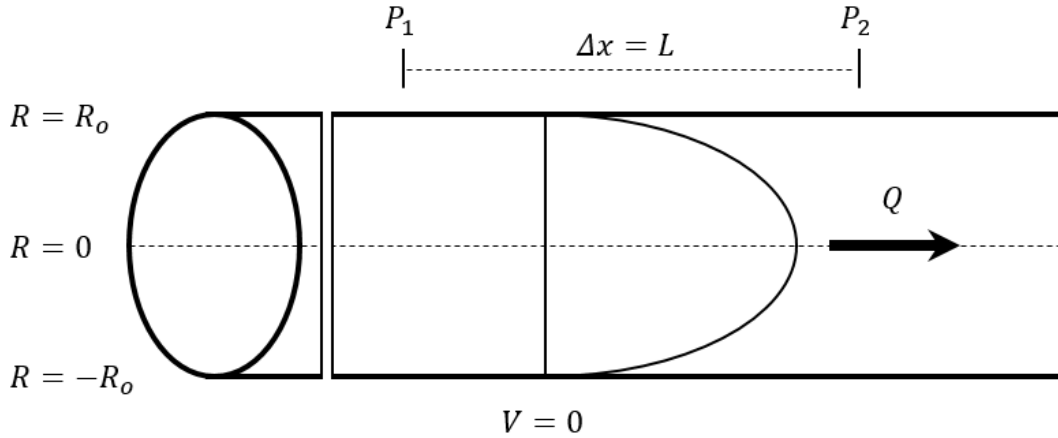


Figure 4.1: Velocity profile in a circular pipe with Hagen-Poiseuille flow. Where, R is the radius of the pipe, P_1 and P_2 are the inlet and outlet pressures, respectively, V is the velocity, Q is the volumetric flow rate, and L are the length.

Re-arranging Equation 2.36 in terms of pressure drop gives,

$$-\frac{dP}{dx} = \frac{8\mu Q}{\pi R^4} \quad 4.1$$

The ideal gas law is,

$$PV = nRT \quad 4.2$$

where V is the volume of the gas, n is the number of moles of the gas, R is the ideal gas constant, and T is the absolute temperature of the gas. Equation 4.2 is converted in terms of flowrate by dividing both sides by time, t .

$$\frac{PV}{t} = \frac{nRT}{t} \quad 4.3$$

$$P \left(\frac{V}{t} \right) = PQ = \left(\frac{n}{t} \right) RT \quad 4.4$$

Where Q is the volumetric flow rate and $\left(\frac{n}{t} \right)$ is the molar flowrate.

Boyle's Law states that for an ideal gas with constant temperature, the product of pressure and volume is constant for a given mass (Equation 4.5).

$$P_1V_1 = P_2V_2 \quad 4.5$$

By using Boyle's Law with the form of the ideal gas law in Equation 4.4, the volume is proportional to the volumetric flow rate, Q . Therefore Equation 4.5 can be converted into terms of Q in Equation 4.6. The flow rate and pressure at point 1 represent the inlet flow rate (Q_1) and the inlet pressure (P_1). The flow rate and pressure at point 2 represent the outlet flow rate (Q_2) and the outlet pressure (P_2). This relationship is shown in Equation 4.6.

$$QP = Q_1P_1 = Q_2P_2 \quad 4.6$$

$$Q = \frac{Q_2P_2}{P} \quad 4.7$$

By substituting Equation 4.7 into Equation 4.1, Equation 4.8 is formed.

$$-\frac{dP}{dx} = \frac{8\mu Q_2P_2}{\pi R^4P} \quad 4.8$$

Assuming a small distance (dx), the compressibility effect on the local pressure gradient can be ignored. The change in gas viscosity (μ) with pressure is negligible, therefore we can integrate over the length of the pressure drop (L) on the right and integrate over the inlet and outlet pressures (P_1 and P_2 , respectively) on the left.

$$-PdP = \frac{8\mu Q_2P_2}{\pi R^4} dx \quad 4.9$$

$$-\int_{P_1}^{P_2} P dP = \int_0^L \frac{8\mu Q_2 P_2}{\pi R^4} dx \quad 4.10$$

$$\frac{P_1^2 - P_2^2}{2} = \frac{8\mu Q_2 P_2 L}{\pi R^4} \quad 4.11$$

$$Q_2 = \frac{P_1^2 - P_2^2}{2} \cdot \frac{\pi R^4}{8\mu L P_2} \quad 4.12$$

The separation of terms for Equation 4.12 looks similar to the Hagen-Poiseulle equation for circular flow (Equation 2.36) but with an additional term. The additional term, $\left(\frac{P_1+P_2}{2P_2}\right)$, represents a pressure correction in addition to circular Hagen-Poiseulle flow (Landau and Lifschitz 1987). Equation 4.13 is referred to as *circular ideal gas flow*.

$$Q_2 = \frac{\Delta P R^4 \pi}{8\mu L} \cdot \frac{P_1 + P_2}{2P_2} \quad 4.13$$

Annular Ideal Gas Flow

The circular ideal gas flow equation (Equation 4.13) can be useful for estimating gas leakage in cement if the leakage path is a circular channel but according to recent literature, the leakage path in cement is assumed to be a uniform annular microannuli (Aas et al. 2016; Stormont et al. 2018; Lavrov and Torsaeter 2018; Skadsem et al. 2019). Therefore, an annular ideal gas flow equation is required. The Hagen-Poiseulle equation for an annulus is given in Equation 2.41.

Re-arranging in terms of pressure drop per length and assuming Boyle's law (Equation 4.6) gives,

$$-\frac{dP}{dx} = \frac{12\mu Q_2 P_2}{\pi D w^3 P} \quad 4.14$$

Applying the same assumption in regards to pressure compressibility as above results in the *annular ideal gas flow* equation shown in Equation 4.15.

$$Q_2 = \frac{\Delta P w^3 D \pi}{12 \mu L} \cdot \frac{P_1 + P_2}{2 P_2} \quad 4.15$$

Annular Real Gas Flow

Equation 4.15 represents an ideal gas; for a real gas assuming the real gas law,

$$\frac{PV}{z} = nRT \quad 4.16$$

The real gas law in terms of flow rate, becomes

$$\frac{PV}{zt} = \frac{nRT}{t} \quad 4.17$$

$$\frac{P}{z} \left(\frac{V}{t} \right) = \frac{PQ}{z} = \frac{nRT}{t} \quad 4.18$$

Boyle's law gives,

$$\frac{P_1 V_1}{z_1} = \frac{P_2 V_2}{z_2} \quad 4.19$$

$$\frac{QP}{z} = \frac{Q_1 P_1}{z_1} = \frac{Q_2 P_2}{z_2} \quad 4.20$$

$$Q = \frac{Q_2 P_2 z}{P z_2} \quad 4.21$$

Then the Q for a real gas can be represented as,

$$Q = \frac{dP}{dx} \frac{\pi D w^3}{12 \mu} \Rightarrow \frac{dP}{dx} = \frac{12 \mu Q}{\pi D w^3} = \frac{12 \mu Q_2 P_2 z}{\pi D w^3 P z_2} \quad 4.22$$

$$-\frac{dP}{dx} = \frac{12\mu Q_2 P_2 z}{\pi D w^3 P z_2} \quad 4.23$$

$$-\frac{P}{z} dP = \frac{12\mu Q_2 P_2}{\pi D w^3 z_2} dx \quad 4.24$$

$$\int_{P_1}^{P_2} -\frac{P}{z} dP = \int_0^L \frac{12\mu Q_2 P_2}{\pi D w^3 z_2} dx \quad 4.25$$

Assuming an average z-factor given the inlet and outlet pressure, the compressibility can be pulled out of the integral.

$$\bar{z} = \frac{z_1 + z_2}{2} \quad 4.26$$

$$\int_{P_1}^{P_2} -\frac{P}{\bar{z}} dP = \int_0^L \frac{12\mu Q_2 P_2}{\pi D w^3 z_2} dx \quad 4.27$$

$$-\frac{2}{z_1 + z_2} \int_{P_1}^{P_2} P dP = \int_0^L \frac{12\mu Q_2 P_2}{\pi D w^3 z_2} dx \quad 4.28$$

$$-\frac{2}{z_1 + z_2} \left(\frac{P_2^2}{2} - \frac{P_1^2}{2} \right) = \frac{12\mu Q_2 P_2 L}{\pi D w^3 z_2} \quad 4.29$$

$$\frac{P_1^2 - P_2^2}{z_1 + z_2} = \frac{12\mu Q_2 P_2 L}{\pi D w^3 z_2} \quad 4.30$$

$$Q_2 = \frac{\pi D w^3 z_2}{12\mu P_2 L} \left(\frac{P_1^2 - P_2^2}{z_1 + z_2} \right) \quad 4.31$$

The end result is the annular flow equation for a real gas in which the z-factor for the gas at the inlet (P_1) and outlet (P_2) is included. It should be noted that Equation 4.31 reduces to Equation 4.15 when the gas is ideal ($z_1 = z_2 = 1$).

Annular Ideal Gas Flow Including Gravity

Equation 4.15 was developed for horizontal flow in which gravity can be neglected. For a vertical wellbore, a gravity term (ρg) should be included. From Suter and Skalac (1993), the Hagen-Poiseuille equation for vertical flow including the gravity term results in Equation 4.32.

$$Q = \frac{\pi R^4}{8\mu} \left(\frac{dP}{dz} + \rho g \right) \quad 4.32$$

Which can be shown as,

$$Q = \frac{\pi R^4}{8\mu} \left(\frac{\Delta P}{L} + \rho g \right) \quad 4.33$$

For an annulus,

$$Q = \frac{w^3 D \pi}{12\mu} \left(\frac{\Delta P}{L} + \rho g \right) \quad 4.34$$

Since Equation 4.34 has the form: flow rate = constant (pressure gradient + gravity), Equation 4.15 can be converted to the form shown in Equation 4.34. Equation 4.35 has the assumption that the fluid density is constant with respect to pressure. This assumption assumes that with a small enough distance (dL), the local pressure gradient is not large enough to effect the density and can therefore be constant.

$$Q_2 = \frac{w^3 D \pi}{12\mu} \left(\frac{\Delta P}{L} \frac{P_1 + P_2}{2P_2} + \rho g \right) \quad 4.35$$

Equation 4.35 is for a vertical well. To account for a deviated wellbore, the gravity term can be broken into components which adds the term, $\sin \theta$, for the vertical component. The angle of inclination of the wellbore to the horizontal is represented by the θ term. For a vertical well, $\theta = 90^\circ$. The complete version of the *annular ideal gas flow equation with gravity* is defined in Equation 4.36.

$$Q_2 = \frac{w^3 D \pi}{12 \mu} \left(\frac{\Delta P}{L} \frac{P_1 + P_2}{2 P_2} + (\sin \theta) \rho g \right) \quad 4.36$$

Annular Real Gas Flow Including Gravity

Adding gravity to real gas flow (Equation 4.31) gives,

$$Q_2 = \frac{w^3 D \pi}{12 \mu} \left[\left(\frac{z_2}{P_2 L} \right) \left(\frac{P_1^2 - P_2^2}{z_1 + z_2} \right) + (\sin \theta) \rho g \right] \quad 4.37$$

The assumptions associated with the developed gas flow equations are that:

- The flow is laminar (Reynolds number is less than 2,100).
- Flow is steady state.
- The fluid is Newtonian.
- End effects are neglected.
- The fluid behaves as a continuum.
- There is no slippage at the wall.
- The system is isothermal.
- The local pressure gradient is not large enough to affect the fluid density.

4.1 Comparison of Fluid Flow Models

A comparison of the six analytical equations (Hagen-Poiseuille flow, Hagen-Poiseuille flow with gravity, ideal gas, ideal gas with gravity, real gas, and real gas with gravity) for an annular isothermal geometry is performed for a synthetic vertical wellbore with a uniform (arbitrary) microannuli of 100 μm . The parameters for the synthetic wellbore are shown in Table 4.1.

Hagen-Poiseulle Flow $Q = \frac{\Delta P \pi D w^3}{12 \mu L}$ **2.41**

Hagen-Poiseulle Flow + Gravity $Q = \frac{\pi D w^3}{12 \mu} \cdot \left(\frac{\Delta P}{L} + (\sin \theta) \rho g \right)$ **4.34**

Ideal Gas $Q_2 = \frac{\Delta P w^3 D \pi}{12 \mu L} \cdot \frac{P_1 + P_2}{2 P_2}$ **4.15**

Ideal Gas + Gravity $Q_2 = \left(\frac{\pi D w^3}{12 \mu} \right) \cdot \left(\frac{\Delta P}{L} \frac{P_1 + P_2}{2 P_2} + (\sin \theta) \rho g \right)$ **4.36**

Real Gas $Q_2 = \frac{\pi D w^3 z_2}{12 \mu P_2 L} \cdot \left(\frac{P_1^2 - P_2^2}{z_1 + z_2} \right)$ **4.31**

Real Gas + Gravity $Q_2 = \left(\frac{\pi D w^3}{12 \mu} \right) \cdot \left[\left(\frac{z_2}{P_2 L} \right) \left(\frac{P_1^2 - P_2^2}{z_1 + z_2} \right) + (\sin \theta) \rho g \right]$ **4.37**

Table 4.1: Values for the synthetic wellbore to compare the analytical equations derived in this work with the Hagen-Poiseuille flow equation.

Parameter	Value
D (m)	0.2445
w (μm)	100.0
w (m)	1.00E-04
μ_{water} (Pa·s)	4.81E-04
μ_{gas} (Pa·s)	2.20E-05
P_1 (Pa)	2.94E07
P_2 (Pa)	1.84E07
L (m)	1,127
ρ_{water} (kg/m^3)	995.71
ρ_{gas} (kg/m^3)	174.25
z_1	0.94
z_2	0.87
θ ($^\circ$)	90
T ($^\circ\text{C}$)	59.0

Staged Poro-Elastic FEA Stress Continuum Model

The first model that replicates the lifecycle of the well is the staged poro-elastic FEA stress continuum model. The FEA stress continuum model was created and simulated using ANSYS™ 19.1 and is a 3D poro-elastic model that incorporates Mohr-Coulomb failure criteria in the cement sheath and utilizes a three-dimensional mesh composed of 18,384 CPT216 quadratic brick elements. Figure 4.2 depicts a 3D and 2D (A and B, respectively) schematic of the model including the dimensions used in the medium well case study, the far-field stresses, and the internal casing pressure.

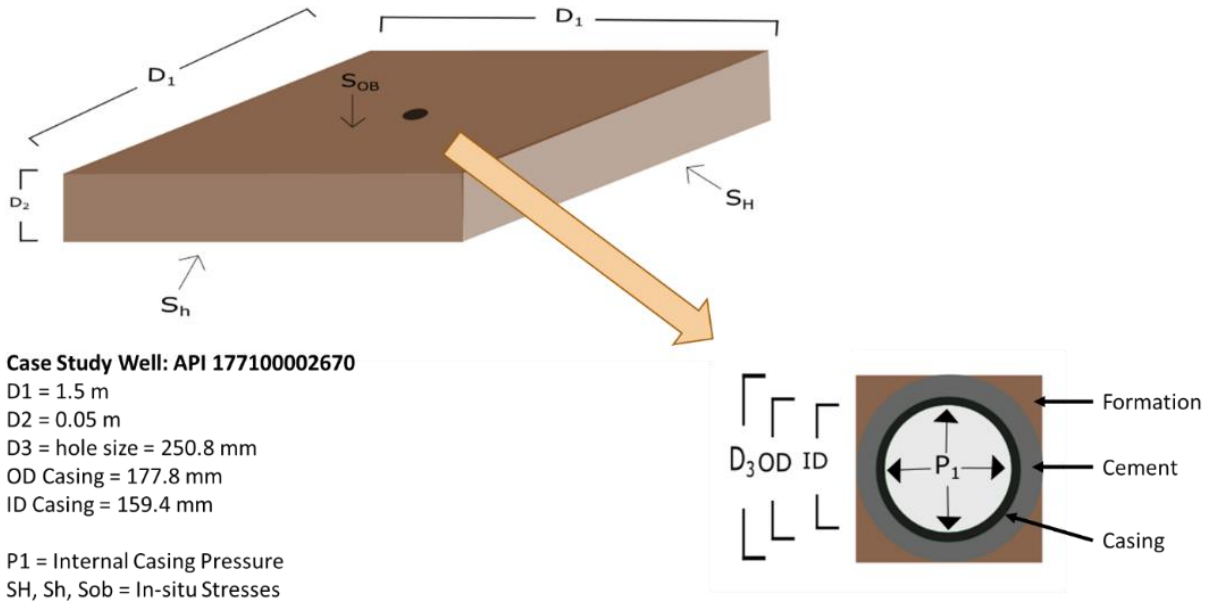


Figure 4.2 A) FEA 3D model schematic with dimensions and far-field stresses for the medium well case study. B) 2D schematic of the medium well wellbore with dimensions and internal casing pressure.

The element dimensions are designed to be smaller towards the center of the model (center of the wellbore) while increasing in size towards the model boundaries. This configuration calculates the stress patterns more accurately in the casing, cement, and near rock formation while saving computational time by having larger elements towards the boundaries. Verification of the stresses in the FEA stress continuum model are shown in Section 5.2.2. Figure 4.3 shows a 2D and 3D cutaway of the model. Figure 4.3A shows the three different materials included within the model (casing, cement, and rock formation) with their respective finite element grid pattern. Figure 4.3B shows a 3D view of the finite element gridded model.

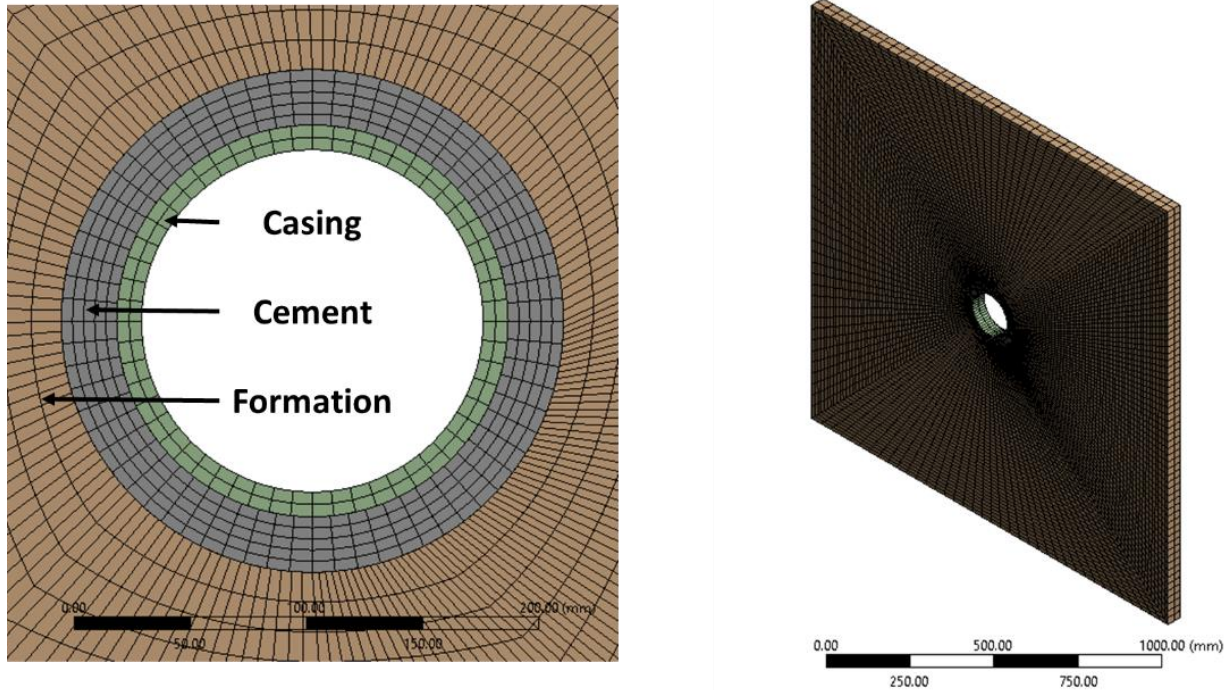


Figure 4.3 A) Cutaway of the well model showing the three different materials included in the near wellbore region with casing (green), cement (gray), and rock formation (brown) and the finite element grid pattern for the materials. B) 3D view of the finite element gridded model consisting of a total of 18,384 elements.

The outer dimensions of the model are 1.5 meters in length and width (x, y) and 0.05 meters in height (z). The outer dimensions are such that boundary conditions will not affect the stress in the near borehole region. The dimensions of the near wellbore region are based off actual wells defined in Chapter 3. The near wellbore region dimensions change for the individual wells while the large scale dimensions stay constant. The model is constrained using frictionless supports on all six sides to represent infinite supports and to reduce undesired boundary effects. The thickness (height) of the model is 0.05 m thick to represent a 3D cross section of the wellbore.

The staged approach uses the property of superposition to build the model's initial conditions before the next load step is implemented. The advantage of performing a staged approach is that the stress and deformation changes can be monitored in each load step. The load steps used within this model were modified from Weideman (2014). The load steps are:

- Step 1. The model is loaded with horizontal (σ_H & σ_h) and vertical (σ_v) in-situ stresses.
- Step 2. The borehole is drilled, and a fluid weight is applied to the rock formation.
- Step 3. The casing is added to the borehole with the fluid weight being applied to the inner and outer surfaces of the casing and the borehole.
- Step 4. This step represents the completion of the wellbore and has two parts:
 - a. The cement slurry is pumped into the well. A hydrostatic pressure caused by the cement slurry is applied to the outer surface of the casing and the borehole while the inner casing surface has the fluid weight pressure.
 - b. Cement hydrates and hardens. The cement elements are added to the model with framework stress, pore pressure, and zero shrinkage assuming the cement is fully bonded to the rock formation and outer casing surface. The hardened cement is inserted with zero deformation but with framework stress in all three principal directions equivalent to the hydrostatic pressure. The fluid weight pressure is still applied to the inner surface of the casing.
- Step 5. The wellbore is producing. The fluid weight pressure is removed from the inner surface of the casing and replaced with the production pressure referenced as the “Internal Casing Production Pressure”.

The interface between the casing and cement and between the cement and rock formation are assumed to have fully bonded interfaces in this model. The stresses in the casing are calculated assuming it is a linear elastic material since steel does not have a pore pressure. The stresses in the cement and rock formation are calculated assuming poro-elastic materials. The cement and rock formation calculate the total stress in the materials within the model, and the effective stress is determined in the post-analysis.

Staged Poro-Elastic FEA Fracture Model

The approach used to simulate the staged poro-elastic FEA fracture models is similar to the stress continuum method used in the previous section except the fracture model quantifies cement sheath debonding. The FEA fracture model was created and simulated using ANSYS™ 19.1. The model is a static structural 3D thermo-poro-elastic model that uses the traction separation law to model debonding of the casing/cement and cement/rock formation interfaces and includes Mohr-Coulomb shear failure and a tensile failure analysis on the cement stresses during simulations. The 3D model uses 25,552 CPT216 quadratic brick elements in which the element

size in the interface zones is based on the Turon et al. (2006) approach which uses the element length determined by Hillerborg et al. (1976) and further divides the element length by three to ensure the element size is fine enough to capture the delamination in the cohesive zones. Further refinement of the mesh was conducted using a mesh sensitivity analysis. The maximum microannuli gap width versus mesh density was analyzed to determine the optimal mesh density and is shown in Appendix H.

The outer and near borehole dimensions of the model are the same as the FEA stress continuum model. The differences between this model and the previous are that the fracture model uses the traction separation law to quantify the gaps and includes the effect of temperature whereas the first model analyses the stress continuum across the interfaces. Since the fracture model incorporates debonding, the model explicitly implements pore pressure in the elements whereas the stress continuum model implemented them in the post-analysis. Implementing pore pressure in a homogeneous model is standard procedure in ANSYSTM with and without fracture capabilities. However, implementing pore pressure in a fracture analysis when one material is poro-elastic and the other is linear elastic (i.e. cement and casing) is not standard. Therefore, custom code was developed to define the pore pressure in the poro-elastic elements (and interfaces) while maintaining the correct stress structure for the linear elastic elements. Model screenshots and developed APDL code snippets used within the model are included in Appendix E. The load steps used in this model follow a similar trend to the FEA stress model previously. The differences between the stress model and the explicit poro-elastic model are underlined in the load steps below.

- Step 1. The model is loaded with horizontal (σ_H & σ_h) and vertical (σ_v) in-situ effective stresses. The rock formation pore pressure and Biot coefficient (γ) are added to the elements.
- Step 2. The borehole is drilled, and a fluid weight is applied to the rock formation.
- Step 3. The casing is added to the borehole with the fluid weight being applied to the inner and outer surfaces of the casing and the borehole.

- Step 4. This step represents the completion of the wellbore and has two parts:
- a. The cement slurry is pumped into the well. A hydrostatic pressure caused by the cement slurry is applied to the outer surface of the casing and the borehole while the inner casing surface has the fluid weight pressure.
 - b. Cement hydrates and hardens. The cement elements are added to the model with framework effective stress, pore pressure within the elements, cement Biot coefficient, pore pressure at the interfaces, and zero shrinkage assuming the cement is fully bonded to the rock formation and outer casing surface. The hardened cement is inserted with zero deformation but with framework effective stress in all three principal directions equivalent to the hydrostatic pressure minus the pore pressure. The fluid weight pressure is still applied to the inner surface of the casing.
- Step 5. The wellbore is producing. The fluid weight pressure is removed from the inner surface of the casing and replaced with the production pressure referenced as the “Internal Casing Pressure” (ICP).

Continuous Leakage Pathway Models

The model in the previous section quantifies the microannuli gap at the cement sheath interfaces, but it does not show if the fracture is can propagate up the depth of the wellbore. To determine if the fracture propagates up to the top of cement depth, the wellbore is modeled as multiple thin slices explicitly coupled with fracture fluid propagation (Figure 4.4). The models replicate an iterative process such that the first model (located at TD) is performed first. Then the next segment is performed and so on. The purpose of using discrete model segments is that the in-situ stress can be assumed to be constant for the thin section for any given model. Therefore, the in-situ stresses can be used for the initial conditions. so that for any given model, constant in-situ stresses can be used for initial conditions.

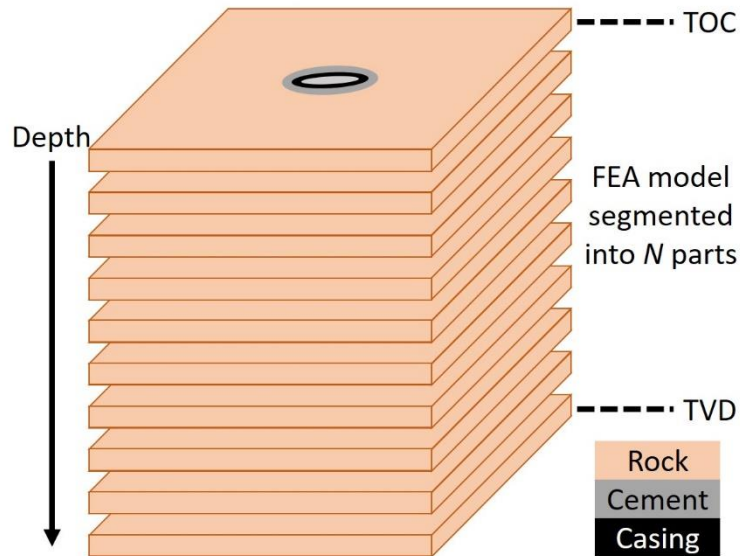


Figure 4.4: Illustration of the segmented discrete method used to model the wellbore from the simulation depth to the top of cement depth (TOC).

The load steps for this model are the same as previously except for one addition; an additional step is added to apply the gas migration pressure in the microannuli (step 6).

- Step 1. The model is loaded with horizontal (σ_H & σ_h) and vertical (σ_v) in-situ effective stresses. The rock formation pore pressure and Biot coefficient (γ) are added to the elements.
- Step 2. The borehole is drilled, and a fluid weight is applied to the rock formation.
- Step 3. The casing is added to the borehole with the fluid weight being applied to the inner and outer surfaces of the casing and the borehole.
- Step 4. This step represents the completion of the wellbore and has two parts:
 - a. The cement slurry is pumped into the well. A hydrostatic pressure caused by the cement slurry is applied to the outer surface of the casing and the borehole while the inner casing surface has the fluid weight pressure.
 - b. Cement hydrates and hardens. The cement elements are added to the model with framework effective stress, pore pressure within the elements, cement Biot coefficient, pore pressure at the interfaces, and zero shrinkage assuming the cement is fully bonded to the rock formation and outer casing surface. The hardened cement is inserted with zero deformation but with framework effective stress in all three principal directions equivalent to the hydrostatic pressure minus the pore pressure. The fluid weight pressure is still applied to the inner surface of the casing.
- Step 5. The wellbore is producing. The fluid weight pressure is removed from the inner surface of the casing and replaced with the production pressure referenced as the “Internal Casing Pressure” (*ICP*).
- Step 6. This step represents gas migration up the cement sheath to the top of cement (TOC). This step is an iteration that applies the gas migration pressure on the walls of the microannuli until the width stabilizes.

Step 7. Steps 1-6 repeat for the next segmented part until the TOC depth is reached.

Steps 1-6 are used to determine if a microannuli at the simulation depth can propagate up the depth of the wellbore providing a continuous leakage pathway. The *ICP* at the simulation depth is known, but how does the *ICP* vary with depth? Assuming that the *ICP* is from a gas producing well (from the well production data), the pressure of the gas with respect to depth is determined by using the static single phase real gas equation shown in Equation 4.38 where P_1 is the pressure at the top of the segment (*KPa*), P_2 is the pressure at the bottom of the segment (*KPa*), γ_{gas} is the specific gravity of the gas (assuming methane for a pure gas), L is the length between the top and bottom segments (*m*), \bar{z} is the average compressibility of the gas for the segment, \bar{T} is the average temperature of the segment (*K*), and θ is the angle from horizontal ($^\circ$) [which is 90° for a vertical well].

$$P_1^2 = P_2^2 \cdot \exp\left(0.06835 \frac{\gamma_{gas} L}{\bar{z} \bar{T}} \sin \theta\right) \quad 4.38$$

Equation 4.38 is broken up into the wellbore segments such that the *ICP* is calculated every 1 m from the simulation depth to the TOC. Equation 4.38 is used to calculate the pressure 1 m above the simulation depth and so on. Since compressibility of the gas (z) should be taken into account, the compressibility of methane is calculated given the depths and assuming a constant temperature from the simulation depth to TOC. The compressibility is calculated using Equation 4.39 which uses the relationship between the pressure and temperature of the system with respect to the critical pressure (P_c) and temperature (T_c) of the gas⁴ (Kumar 2004).

$$z = A + B P_{Pr} + (1 - A) \exp(-C) - D \left(\frac{P_{Pr}}{10}\right)^4 \quad 4.39$$

⁴For methane, the critical pressure and temperature are $P_c = 4.6$ MPa and $T_c = 190.6$ K (NIST).

$$A = -0.101 - 0.36T_{P_r} + 1.3868\sqrt{T_{P_r} - 0.919} \quad 4.40$$

$$B = 0.021 + \frac{0.04275}{T_{P_r} - 0.65} \quad 4.41$$

$$C = P_{P_r}(E + FP_{P_r} + GP_{P_r}^4) \quad 4.42$$

$$D = 0.122 \exp(-11.3(T_{P_r} - 1)) \quad 4.43$$

$$E = 0.6222 - 0.224T_{P_r} \quad 4.44$$

$$F = \frac{0.0657}{T_{P_r} - 0.85} - 0.037 \quad 4.45$$

$$G = 0.32 \exp(-19.53(T_{P_r} - 1)) \quad 4.46$$

$$T_{P_r} = \frac{T}{T_c} \quad 4.47$$

$$P_{P_r} = \frac{P}{P_c} \quad 4.48$$

Equation 4.39 was shown to be within 1.4% compared to the Peng-Robinson equation of state with pressures and temperatures used within the case study well. The Peng-Robinson equation of state could not be used explicitly in the FEA fracture model since solving for

compressibility requires solving for third order roots which could lead to complex numbers. The verification of Equation 4.39 is shown in Appendix F.

For the migration of the gas pressure from the simulation depth up the well, the same method of calculating a real gas pressure with respect to depth is used as was for the *ICP*. The model does not take leak-off of the gas migration pressure into the cement sheath into consideration due to the low permeability of wellbore cement.

Numerical Experiments Performed

4.2 Verification of Models

To verify the numerical approaches, the following verification scheme was conducted. First the verification of the developed gas flow equations were compared to nitrogen gas flow cement sealing experimental data performed by Corina et al. (2019). The staged poro-elastic FEA model is verified using thick-walled cylinder equations and the Kirsch solution described in Section 2.1.9. The methodology of using the traction separation law with an explicitly coupled fluid flow FEA model replicating cased wellbore P&A is verified with the experimental data from Aas et al. (2016).

4.2.1 Fluid Flow Models versus Cemented Wellbore Experiments

Verification of the gas flow equations is performed by analyzing experimental values of pressure differential (ΔP) and corresponding flow rates (Q) of nitrogen gas through cement microannuli from Corina et al. (2019) (Figure 2.14) The authors' analysis of their experimental data (Corina et al. 2020) is shown in Figure 2.16 and Figure 2.17. The developed gas flow equations (ideal: Equation 4.17, and real: Equation 4.33) are re-arranged to solve for microannuli (w) and compared to Corina et al.'s (2020) predicted values.

4.2.2 FEA Near Wellbore Stress Distribution versus Kirsch Analytical Solution

The near wellbore stress distribution of the staged FEA stress continuum model is compared to the analytical solution consisting of the thick-walled cylinder equation and the Kirsch solution described in Section 2.9. The parameters of the model are from the medium well in the Eugene Island OPD.

4.2.3 FEA Fluid Rheology Model versus Cemented Wellbore Experiments

A one-way explicit coupled FEA fracture model replicating cased wellbore plug and abandonment was developed and verified with experimental data regarding flowpath size in cement sheaths. The purpose of this simulation is to determine if FEA models can accurately predict cement sheath microannuli in cemented wellbores. Two length of cemented annuli were modeled, each with conventional and expanding cement to replicate the Aas et al. (2016) experiments.

The FEA model was created and simulated using ANSYSTM 19.1. The model is a 2D linear elastic model that utilizes a two-dimensional mesh composed of 4,774 PLANE183 quadratic rectangular elements. Since the cement between the tubing and casing does not have access to free water, the pore pressure within the cement is equal to the cavitation pressure which is rounded down to be zero⁵. The interface between the cement sheath and casing uses a softening traction-separation law to replicate debonding while the geometry is supported using cylindrical supports. Surface pressures are applied to the geometry of the inner diameter of the casing and outer diameter of the cement sheath to replicate the fluid pressure. The pressure is applied at this location since the injected fluid will exert a pressure between the cement and casing wall due to the location of

⁵ Water at ambient temperature and 95 °C has a cavitation pressure of 0.002 and 0.085 MPa, respectively. Therefore, the pore pressure was simplified to being zero.

the injection ports. Figure 4.5 shows the finite element gridded mesh for the concentric and eccentric test cases with the location of the surface pressure.

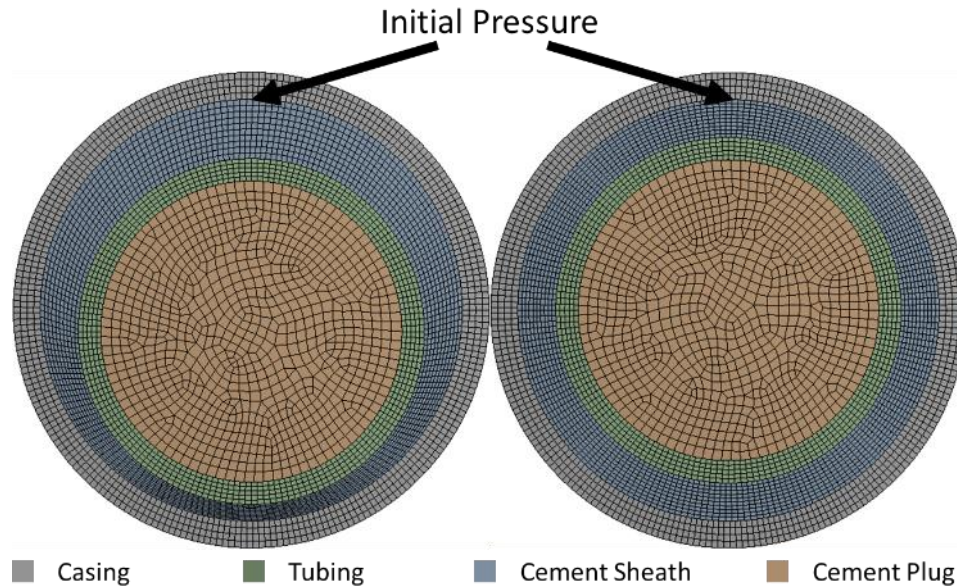


Figure 4.5: Finite element gridded eccentric tubing configuration (left) and concentric tubing configuration (right) showing the casing (gray), cement sheath with initial pressure location (blue), tubing (green), and cement plug (brown).

The dimensions and mechanical properties used in the FEA model are shown in Table 4.2. The softening traction-separation law values are from Wang and Taleghani (2014). The mechanical properties of class G cement with respect to curing time were taken from Teodoriu et al. (2012). The temperature of the experiments was in steady state, therefore, the FEA models did not include temperature. The temperature dependent properties of the injection fluid were included as shown in Table 4.2.

Table 4.2: Dimensions and mechanical properties used in the FEA model.

Parameter	
Casing OD (mm)	244.48
Casing ID (mm)	216.80
Tubing OD (mm)	177.80
Tubing ID (mm)	154.80
Cement Shrinkage	1%
ν Steel	0.30
E Steel (GPa)	200.0
ν Conventional Cement	0.18
E Conventional Cement (GPa)	9.81
ν Expanding Cement	0.18
E Expanding Cement (GPa)	17.60
τ^o (MPa)	0.50
G_C (J/m ²)	100.0
ρ at 95°C (kg/m ³)	961.9
ρ at 25°C (kg/m ³)	997.0
ν at 95 °C (Pa·s)	2.96E-4
ν at 25 °C (Pa·s)	8.89E-4

To compensate for cement shrinkage in the models, a uniform 1% volumetric shrinkage is assumed for the two test lengths. To determine a uniform 1% volumetric shrinkage, Equation 4.49 is used in which $V_{shrinkage}$ is the volume of the cement after shrinkage, and $V_{original}$ is the volume of the cement before shrinkage.

$$\%_{shrinkage} = \left(1 - \frac{V_{shrinkage}}{V_{original}} \right) \times 100\% \quad 4.49$$

The volume of the cement depends on the geometry of the cement (i.e. plug or sheath). The shrinkage of a cement sheath is shown in Equation 4.50 where L is the axial length of the cement, OD is the outer diameter of the cement sheath, and ID is the inner diameter of the cement sheath. $V_{original}$ is calculated using $OD = 0.2168$ m, $ID = 0.1778$ m, and $L = 6.0$ m.

$$\%_{shrinkage} = \left(1 - \left(\frac{\frac{\pi L}{4} (OD^2 - ID^2)}{V_{original}} \right) \right) \times 100\% \quad 4.50$$

The microannuli width (w) between the casing and cement sheath is determined by taking the difference between the original outer diameter of the cement sheath (OD_{pre}) and the outer diameter of the shrinkage induced cement sheath (OD_{post}) as shown in Equation 4.51.

$$w = \frac{(OD_{pre} - OD_{post})}{2} \quad 4.51$$

Since determining the outer diameter of the shrinkage induced cement is not easily accessible, an iteration was performed in which the percent change from V_{post} to V_{pre} was kept the same while varying the cement dimensions (OD , ID , and L). This calculation resulted in a microannuli gap width of 101.2 μm and is applied as an initial microannuli gap width between the cement sheath and the casing.

To calculate the fluid pressure drop from the estimated microannuli gap, frictional pressure loss (dp_f) per unit length (ds) is calculated with Equation 4.52 since the microannuli gap created in the FEA models replicates annular flow with a Newtonian fluid.

$$\frac{dp_f}{ds} = \frac{2f\rho v^2}{d_w - d_p} \quad 4.52$$

f , ρ , v , d_w , and d_p represent the Fanning friction factor, density, viscosity, casing inner diameter, and cement sheath outer diameter, respectively. The difference between the casing inner diameter and the cement sheath outer diameter is the microannuli gap determined from the FEA models (Equation 4.51). Characteristically, flow in the cemented annulus has a relatively low Reynold's number (given in Equation 4.53) and is laminar. The Fanning friction factor, given in Equation 4.54, describes laminar frictional losses. A more detailed description of the Fanning friction factor is discussed in Appendix L.

$$N_{Re} = \frac{D\rho v}{\mu} \quad 4.53$$

$$f = \frac{16}{N_{Re}} \quad 4.54$$

To calculate the total pressure loss, the tubing was discretized into segments. For each segment, Equation 4.52 was iterated until the microannuli gap and pressure drop converged. A sensitivity analysis was performed to determine the optimal number of segments to achieve accurate pressure drops. Figure 4.6 shows that breaking the total length into 1,000 segments results in accurate representation of the pressure drops.

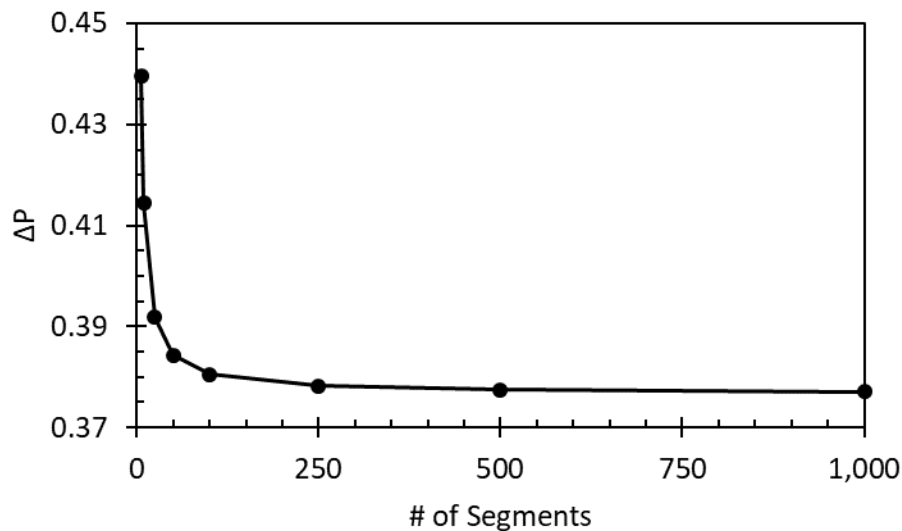


Figure 4.6: Sensitivity analysis showing the pressure drop (ΔP) versus number of segments relationship used for the explicitly coupled FEA model with the frictional pressure equation (4.54). 1,000 segments was determined to be sufficient for both casing lengths.

The relationship between the microannuli gap versus pressure was performed for both conventional and expanding cements with concentric and eccentric configurations. The corresponding pressure versus microannuli curves are shown in Figures 4.7-4.10.

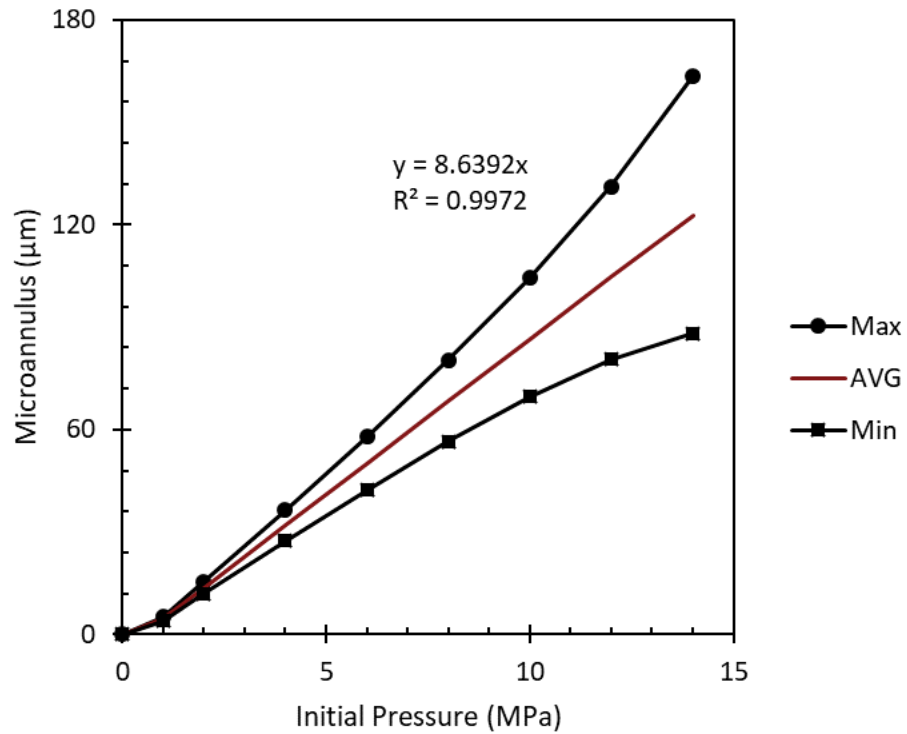


Figure 4.7: Maximum and minimum initial pressure versus microannuli gap with corresponding average linear correlation for conventional cement with eccentric configuration. Note that for no pressure applied to system, there is not a microannuli gap.

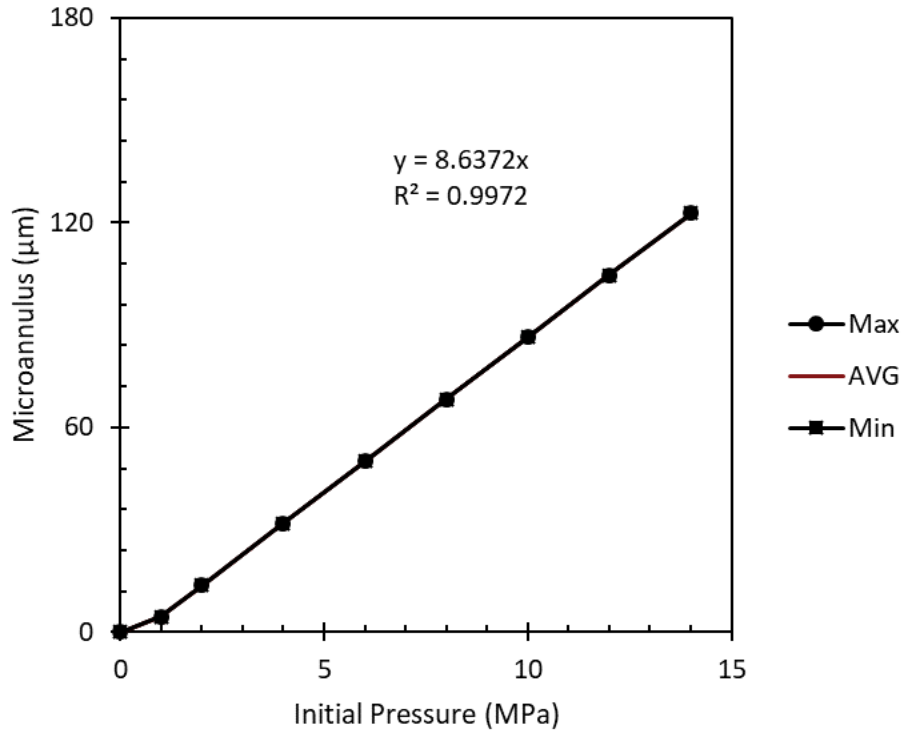


Figure 4.8: Maximum and minimum initial pressure versus microannuli gap with corresponding average linear correlation for conventional cement with concentric configuration.

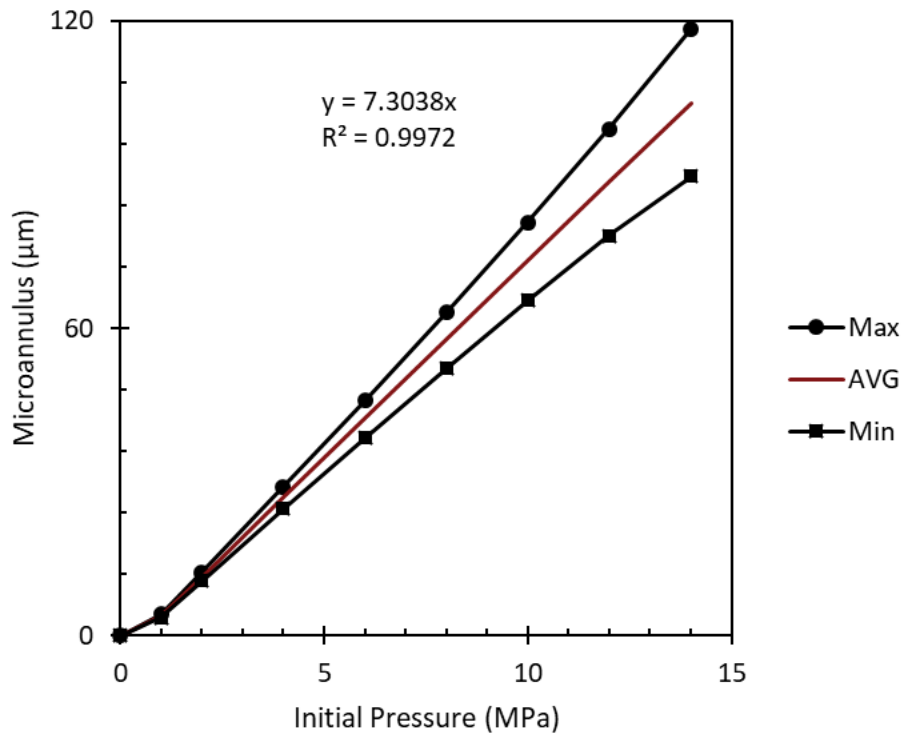


Figure 4.9: Maximum and minimum initial pressure versus microannuli gap with corresponding average linear correlation for expanding cement with eccentric configuration.

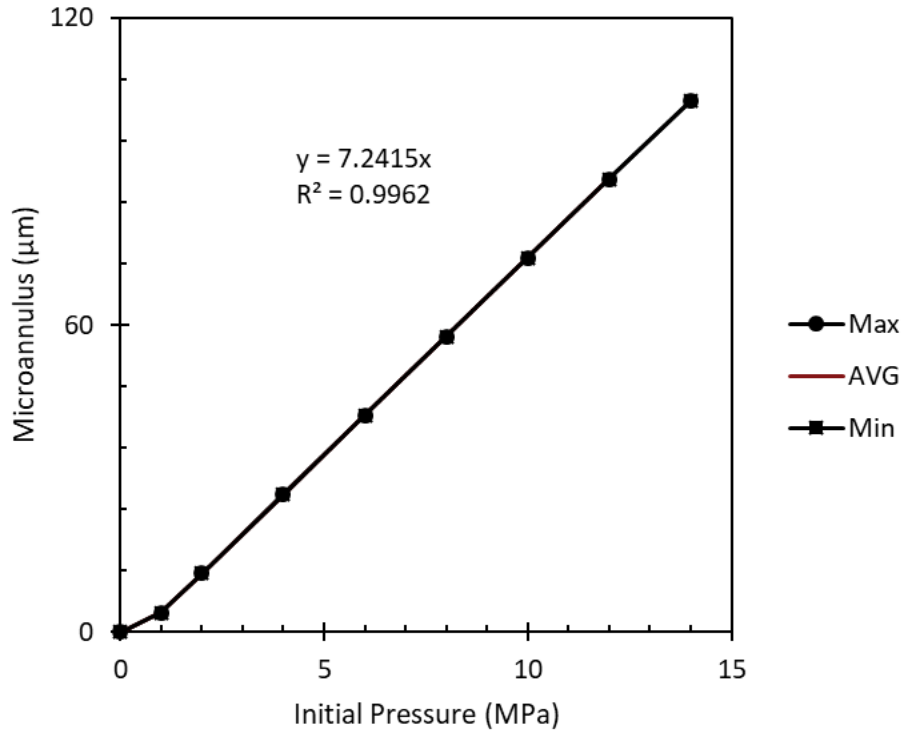


Figure 4.10: Maximum and minimum initial pressure versus microannuli gap with corresponding average linear correlation for expanding cement with concentric configuration.

The correlations for pressure versus microannuli for the expanding cement with concentric geometry, expanding cement with eccentric geometry, conventional cement with concentric geometry, and conventional cement with eccentric geometry are shown in Table 4.3. As mentioned previously, cement shrinkage is added on to the calculations for the microannuli gap. Since expanding cement does not have an initial microannuli gap, the intercept of the linear correlation is 0. Shrinkage is not included in the FEA models for the conventional cement, so the 1% volumetric shrinkage calculated previously (101.2 μm) is added to the y-intercept for the conventional cement.

Table 4.3: Linear correlations for the initial pressure versus the microannuli gap for the test cement types with respect to their eccentricity. Note the intercept is the shrinkage induced gap.

	Cement Type	Slope	Intercept
Concentric	Expanding	7.2415	0
Eccentric	Expanding	7.3038	0
Concentric	Conventional	8.6372	101.2
Eccentric	Conventional	8.6392	101.2

From Table 4.3, the difference between the slope of the concentric and eccentric geometries is less than 1% for both the expanding and conventional cement indicating that cement geometry has little effect on the pressure induced microannuli. As a result, the eccentric geometry is used for the pressure drop analysis.

4.3 GoM Parametric Study

The GoM parametric study serves two purposes: the first is to identify and rank the contributing factors of stress development for three GoM wells, in the Eugene Island OPD, at different depths. The second purpose is to compare the two staged FEA models to show the effect of including fracture criteria. The two models are the staged poro-elastic FEA stress continuum model and the staged poro-elastic FEA fracture model. The main difference between the models, other than including fracture criteria, is how pore pressure in the rock formation and cement sheath is applied. The fracture model applies pore pressure explicitly within the elements (resulting in effective stress initial conditions) whereas the pore pressure is applied in the post analysis in the stress continuum model. The input parameters used for the three GoM wells are listed in Table 4.4 including the source of the values.

Table 4.4: Base case input parameters for the three wells in the Eugene Island OPD and the source of their values.

	Parameter	Shallow	Medium	Deep	
	<i>TVD</i> (m)	797	3,014	6,028	1
	<i>Simulation Depth</i> (m)	468	2,697	4,317	
Dimensions	<i>Hole Size</i> (cm)	44.45	25.07	31.12	1
	<i>Casing OD</i> (cm)	33.96	17.78	24.46	1
	<i>Casing ID</i> (cm)	32.03	15.95	22.00	1
In-Situ Stresses	σ_H (MPa)	7.74	49.49	84.89	4
	σ_h (MPa)	6.38	40.76	69.91	4
	σ_v (MPa)	9.11	58.23	99.88	4
Casing	ν	0.30	0.30	0.30	2
	E (GPa)	200	200	200	3
Cement	Pp (g/cc)	0.99	1.35	1.18	1
	γ_{cement}	1.0	1.0	1.0	
	ρ_{slurry} (g/cc)	1.22	1.53	1.55	1
	σ_{cement} (MPa)	5.62	40.43	65.61	
	ν	0.25	0.25	0.25	2
	E (GPa)	10.0	10.0	10.0	2
	UCS (MPa)	40.0	40.0	40.0	3
	τ^o (MPa)	3.00	3.00	3.00	3
	τ_o (MPa)	15.0	15.0	15.0	3
	ϕ (°)	30.0	30.0	30.0	3
Rock	Pp (g/cc)	0.99	1.35	1.18	1
	γ_{rock}	1.0	1.0	1.0	
	ν	0.27	0.27	0.27	3
	E (GPa)	25.0	25.0	25.0	2
Casing/Cement Bond	τ^o (MPa)	0.50	0.50	0.50	5
	G_C (J/m ²)	100.0	100.0	100.0	5
Cement/Rock Bond	τ^o (MPa)	0.42	0.42	0.42	5
	G_C (J/m ²)	100.0	100.0	100.0	5
Loads	MW (g/cc)	1.13	1.41	1.29	1
	ICP (MPa)	5.18	25.60	38.23	1

¹Log, ²Zhang et al. (2016), ³Weideman (2014), ⁴Finkbeiner et al. (1996), ⁵Wang and Taleghani (2014)

The simulation depth was chosen to be the depth of the deepest casing string before the production zones in the well. The cement sheath can be assumed to be intact and not damaged from perforations at this location. The TD of the well would not be relevant for modeling cement sheath integrity since it is below the perforation and production zones and not acting as a barrier in preventing hydrocarbon migration or fresh water contamination. The cement sheath located at and/or above the perforations is either damaged or has a potential to be damaged from the perforation procedure. The extent of the damage is not known and was not investigated in this

study. The cement sheath at shallower depths of the wells was not investigated either. The sheaths at shallow depths can include multiple casings and (potentially) multiple cement sheaths. The additional parameters would complicate the model and the contributing stress development factors could be altered. Therefore, the single cement sheath and single casing was investigated to determine which parameters cause the stress development for a single casing, cement sheath, and rock formation that is the primary barrier in preventing leakage or water contamination above the production zone (perforations). The in-situ stress gradients for the Eugene Island OPD was based on Finkbeiner et al. (1996). Values of shale mechanical properties were used for the rock formation based off Weideman (2014) and Zhang et al. (2016).

4.4 GoM Continuous Leakage Path Model

The GoM continuous leakage path models investigate the potential leakage pathway for the three GoM wells investigated in the previous section (Section 4.3). These models assume long term, steady state conditions excluding factors such as formation compaction or subsidence. The in-situ stresses and pore pressure do not change with time. Existing fractures within the formation or cement sheath are not considered. The wellbores are assumed to be perfectly concentric with 100% cement slurry to mud weight displacement with perfect initial bonding to the casing and rock formation. Cement shrinkage is not considered in the FEA models. The *ICP* at the simulation depth is assumed to be the pressure reduction of 40%. The dimensions of the individual wellbores do not change with depth. The mechanical properties of the casing, cement, and rock formation ($\nu, E, UCS, \tau_o, \phi, \tau^o, \text{ and } G_c$) are assumed to not change with depth. The variables in these models are the in-situ stresses ($\sigma_H, \sigma_h, \sigma_v, P_p$), cement stress (σ_{cement}), and loads (*MW* and *ICP*). Figure 4.11 shows the *ICP*, pore pressure, and microannuli gas pressure for the shallow, medium, and deep well.

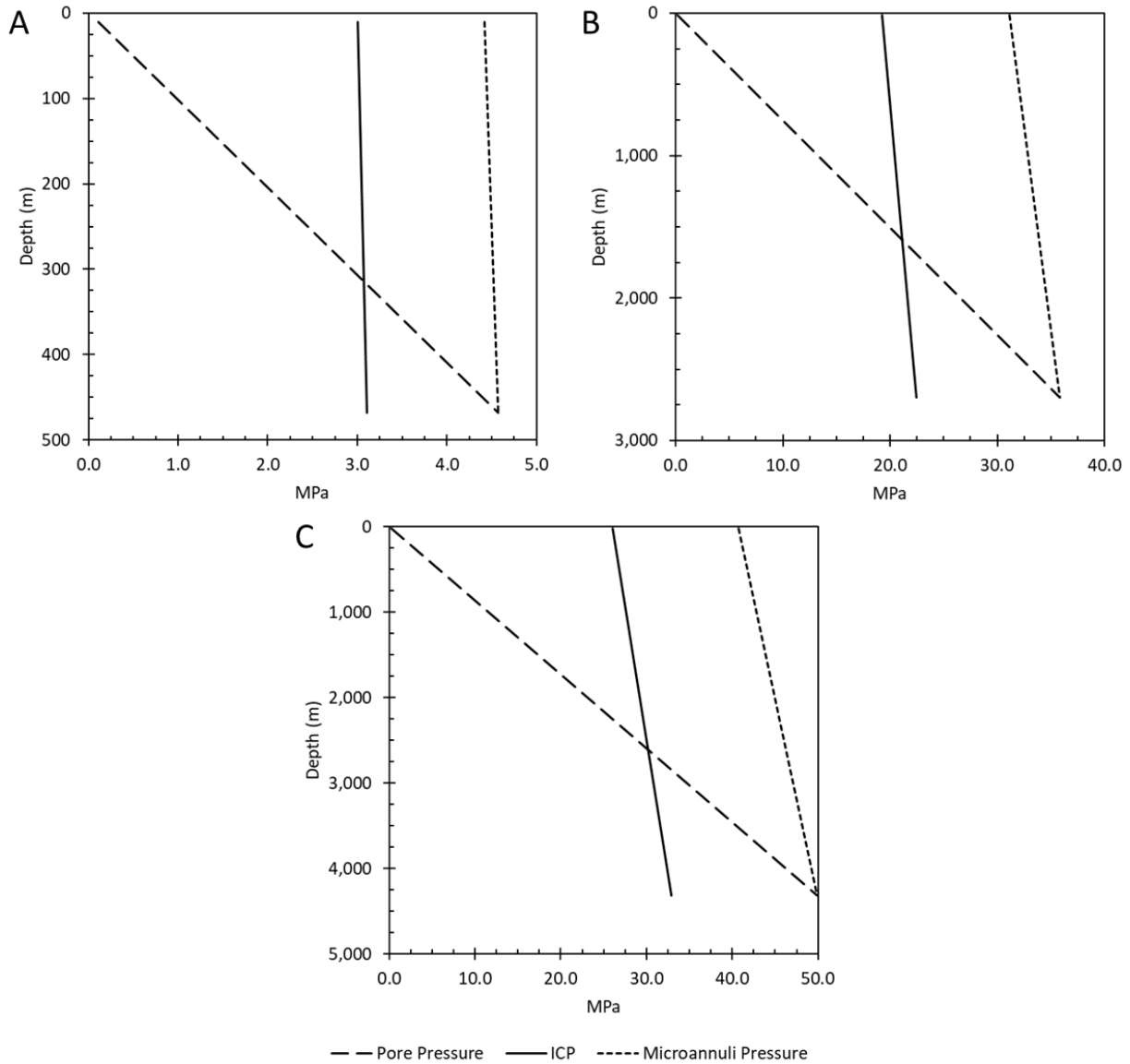


Figure 4.11: Pore pressure (long dash), ICP (solid line), and microannuli pressure (short dash) with respect to depth for the shallow GoM well (A), medium GoM well (B), and deep GoM well (C). The pore pressure and microannuli pressure start at the same magnitude but decrease with depth at different rates due to the density difference between a water/brine (pore pressure) and a gas (microannuli pressure).

As shown in the figure, the pore pressure and fracture pressure are the same at the simulation depth. However, as the wells becomes shallower, the pore pressure decreases with the hydrostatic head while the microannuli pressure does not lose pressure as significantly. This is due to the fact that the microannuli pressure is a gas while the pore pressure is a brine/water at shallower depths of the well. In simulation step 6, the microannuli pressure is applied to the

surfaces of the microannuli since it is larger than the in-situ pore pressure. Therefore, this method uses a one-way gas pressure coupling (using the single phase static real gas law) in conjunction with the FEA well life cycle model. The model inputs for the in-situ stresses (mud weight, cement stress, minimum and maximum horizontal stress, and overburden stress) with respect to depth are shown in Figure 4.12 for the shallow, medium, and deep well.

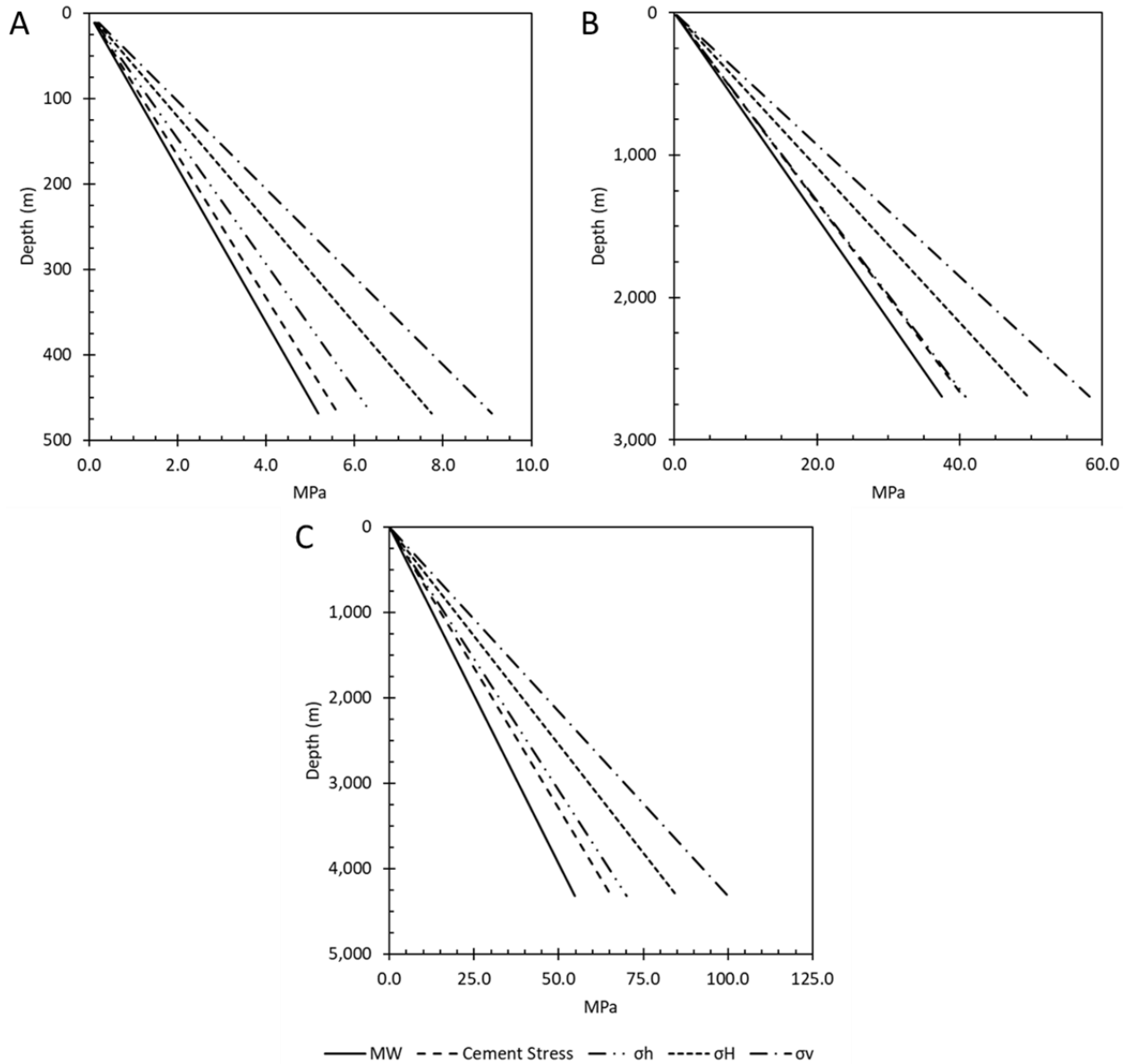


Figure 4.12: Model input parameters for mud weight (MW), cement stress, minimum (σ_h) and maximum (σ_H) horizontal stress, and overburden stress (σ_v) with respect to depth for the shallow well (A), medium well (B), and deep well (C).

4.5 Case Study Well

The case study well was chosen to investigate one wellbore in more detail than the previous models. This will be a comprehensive analysis showing how this methodology can be used to determine if a wellbore is at risk for cement sheath debonding, quantify the microannuli and the resulting pathway, and provide a realistic leakage rate estimate.

4.5.1 FEA Model

The FEA model for the case study well is the same model as the *Continuous Leakage Pathway Model* except this model includes the effect of temperature. The case study well is a static structural 3D thermo-poro-elastic model that uses the traction separation law to model debonding of the casing/cement and cement/rock formation interfaces and includes Mohr-Coulomb failure criteria in the cement sheath. The 3D model uses 25,552 CPT216 quadratic brick elements. The 3D model dimensions are 1.5 m in the x and y (i.e. horizontal) directions and 0.05 m in the z (i.e. vertical) direction. A model with a vertical thickness of 0.05 m has 140,440 nodes with a computational run time of approximately 10 minutes. Thicker geometries of 0.5 m and 1.0 m would have 1,110,504 and 2,189,216 nodes, respectively with at least 12 hour run times for a single simulation. The resulting microannuli is the same magnitude between 0.05 m and 0.5 m thick models. Therefore, 0.05 m thickness was chosen. 3D geometry is chosen such that plain-strain assumptions do not have to be made for the model.

The load steps for this model follow the same trend as the previous models except for one addition. In step 5, a thermal load is applied.

- Step 1. The model is loaded with horizontal (σ_H & σ_h) and vertical (σ_v) in-situ effective stresses. The rock formation pore pressure and Biot coefficient (γ) are added to the elements.
- Step 2. The borehole is drilled, and a fluid weight is applied to the rock formation.
- Step 3. The casing is added to the borehole with the fluid weight being applied to the inner and outer surfaces of the casing and the borehole.
- Step 4. This step represents the completion of the wellbore and has two parts:
 - c. The cement slurry is pumped into the well. A hydrostatic pressure caused by the cement slurry is applied to the outer surface of the casing and the borehole while the inner casing surface has the fluid weight pressure.
 - d. Cement hydrates and hardens. The cement elements are added to the model with framework effective stress, pore pressure within the elements, cement Biot coefficient, pore pressure at the interfaces, and zero shrinkage assuming the cement is fully bonded to the rock formation and outer casing surface. The hardened cement is inserted with zero deformation but with framework effective stress in all three principal directions equivalent to the hydrostatic

pressure minus the pore pressure. The fluid weight pressure is still applied to the inner surface of the casing.

Step 5. The wellbore is producing. There are two loads applied to the wellbore either individually or simultaneously.

a. The fluid weight pressure is removed from the inner surface of the casing and replaced with the production pressure referenced as the “Internal Casing Pressure” (*ICP*).

b. Thermal loading is occurring within the wellbore. The thermal load is applied using a transient model with two days’ worth of temperature change such that the temperature load propagates completely throughout the cement sheath.

Step 6. This step represents gas migration up the cement sheath to the top of cement (TOC). This step is an iteration that applies the gas migration pressure on the walls of the microannuli until the width stabilizes.

Step 7. Steps 1-6 repeat for the next segmented part until the TOC depth is reached.

Steps 1- 5B are used to determine at which point changes in pressure or temperature cause

microannuli gaps to initiate, which interface the cement sheath experiences debonding, and to better understand how certain wellbore parameters can affect the initiation and gap magnitude.

Steps 1-7, excluding 5B, are used to determine if a microannuli at the simulation depth can propagate up the depth of the wellbore providing a continuous leakage pathway.

4.5.2 Mechanical Properties

The rock mechanical values from the log data depth intervals are listed in Table 4.5. The maximum, minimum, average, and standard deviation are representative of all the calculated values for the respective depth range based of the correlations described above. The average E_{static} and average ν for the well depth interval 2,005 m – 2,010 m was chosen to represent the base case mechanical properties for the model since the depth most closely represents the simulation depth. For the parametric analysis, the maximum and minimum mechanical properties include the maximum and minimum values from both depth values to represent the upper and lower rock formation mechanical properties.

Table 4.5: Summary of the two High Island Well logs for the rock mechanical properties.

Well Depth Interval (m)		E_{dyn} (GPa)	E_{static} (GPa)	ν
2,005 - 2010	Average	9.43	3.90	0.34
	Max	11.18	4.63	0.35
	Min	8.21	3.40	0.33
	Std. Dev.	0.78	0.32	0.01
3,659 – 3,688	Average	12.37	5.12	0.27
	Max	17.33	7.17	0.30
	Min	8.83	3.66	0.25
	Std. Dev.	1.52	0.63	0.01

The initial mechanical and thermal loads within the wellbore (MW and T_i , respectively) were determined from the drilling report.

The mechanical properties for the case study well (API# 427094116400) are listed in Table 4.6 including the source(s) of the values. The simulation depth was chosen to be the depth of the deepest casing string prior to the production zones in the well. At this location, the cement sheath is assumed to be intact and not damaged from perforations. The TD of the well would not be relevant for modeling cement sheath integrity due to the fact that it is below perforations and production zone and not acting as a primary barrier in preventing hydrocarbon migration or fresh water contamination. Methane gas and water were chosen as the leakage fluids.

Table 4.6: Parameters for the case well (API# 427094116400) in the High Island OPD and the source of their value(s).

	Parameter	Value	
	<i>TVD</i> (m)	2,623	1
	<i>Simulation Depth</i> (m)	1,920	
Dimensions	<i>Hole Size</i> (cm)	31.12	1
	<i>Casing OD</i> (cm)	24.45	1
	<i>Casing ID</i> (cm)	21.68	1
In-Situ Stresses	σ_H (MPa)	38.99	
	σ_h (MPa)	36.98	1,2,3
	σ_v (MPa)	41.00	4
Casing	ν	0.30	5
	E (GPa)	200.00	5
	ρ (kg/m ³)	7,938.00	1
	α (K ⁻¹)	1.14E-05	5
	κ (W/m·K)	43.00	5
	c (J/kg·K)	490.00	5
Cement	Pp (g/cc)	1.56	
	ρ_{slurry} (g/cc)	1.68	1
	σ_{cement} (MPa)	31.73	
	ν	0.18	6
	E (GPa)	6.38	6
	ρ_{dry} (kg/m ³)	1,965.00	1
	α (K ⁻¹)	8.64E-06	6
	κ (W/m·K)	0.41	6
	c (J/kg·K)	490	6
Rock	Pp (g/cc)	1.56	1
	ν	0.34	7
	E (GPa)	3.9	7
	ρ (kg/m ³)	2,600.00	7
	α (K ⁻¹)	1.00E-05	5
	κ (W/m·K)	2.40	5
	c (J/kg·K)	900.00	5
Casing/Cement	τ^o (MPa)	0.50	8
	G_C (J/m ²)	100.00	8
Cement/Rock	τ^o (MPa)	0.42	8
	G_C (J/m ²)	100.00	8
Loads	MW (g/cc)	30.49	1
	T_i (°C)	58.93	1
Fluid Properties	$\mu_{methane}$ (Pa·s)	2.20E-05	NIST
	$\rho_{methane}$ (kg/m ³)	174.25	NIST

¹Log, ²Breckels and van Eekelen (1982), ³Wojtanowicz et al. (2000), ⁴Meng et al. (2018), ⁵Weideman (2014), ⁶Cement Database, ⁷High Island Log Analysis, ⁸Wang and Taleghani (2014)

A parametric analysis of parameters with uncertainties (in-situ stresses, cement mechanical and thermal properties, rock mechanical and thermal properties, and softening traction separation law properties) as well as parameters that are easily changeable from an engineering perspective (wellbore dimensions) will be simulated. The upper and lower bounds of the sensitivity analysis are shown in Table 4.7.

Table 4.7: High and low values for the parametric study. These values apply for all three well depth parameters.

Parameter	Low	High
Dimensions	-40%	+40%
Isotropic Horizontal Stress Variation	$\sigma_v = \sigma_{v,base}$ $\sigma_H = \sigma_{h,base}$ $\sigma_h = \sigma_{h,base}$	$\sigma_v = \sigma_{v,base}$ $\sigma_H = \sigma_{v,base}$ $\sigma_h = \sigma_{v,base}$
Anisotropic Stress Variation	$\sigma_v = \sigma_{v,base}$ $\sigma_H = \sigma_{h,base}$ $\sigma_h = \sigma_{h,base}$	$\sigma_v = \sigma_{v,base}$ $\sigma_H = \sigma_{v,base}$ $\sigma_h = \sigma_{h,base}$
Vertical Stress Variation	$\sigma_v = -5\% \cdot \sigma_{v,base}$ $\sigma_H = \frac{\sigma_v + \sigma_h}{2}$ $\sigma_h = \sigma_{h,base}$	$\sigma_v = +5\% \cdot \sigma_{v,base}$ $\sigma_H = \frac{\sigma_v + \sigma_h}{2}$ $\sigma_h = \sigma_{h,base}$
Cement Stress (MPa)	<i>MW</i>	<i>P_{fracture}</i>
Cement Mechanical and Thermal Properties	<i>25% Quartile</i>	<i>75% Quartile</i>
Rock Mechanical Properties	Min from Log Data	Max from Log Data
Rock Thermal Properties	-40%	+40%
Traction Law Properties	-40%	+40%

The results are reported in terms of changes in pressure (ΔP) and temperature (ΔT) and are normalized with respect to initial conditions in Equations 4.55 and 4.56 respectively. As defined, a positive Δ indicates a reduction in pressure or temperature, and a negative Δ indicates an increase in pressure or temperature. It is important to note that the pressure load is referred to as “internal casing pressure” (*ICP*) in other sections.

$$\Delta P = 1 - \frac{\text{Pressure Load}}{MW} \cdot 100\% \quad 4.55$$

$$\Delta T = 1 - \frac{\text{Temperature Load}}{T_i} \cdot 100\% \quad 4.56$$

The leakage rate estimate is calculated using a modified approach used by Lavrov and Torsaeter (2018) which summates the leakage volume for a non-constant microannuli using the annular ideal gas (Equation 4.57) and real gas (Equation 4.58) flow equations. A description for performing a Riemann sum integral to determine the summation of the fracture volume ($\sum_i \Delta L_i w_i^{-3}$) is discussed in greater detail and validated in Appendix G.

$$Q_2 = \frac{\pi D \Delta P}{12 \mu \sum_i \Delta L_i w_i^{-3}} \cdot \frac{P_1 + P_2}{2 P_2} \quad 4.57$$

$$Q_2 = \frac{\pi D z_2}{12 \mu P_2 \sum_i \Delta L_i w_i^{-3}} \cdot \left(\frac{P_1^2 - P_2^2}{z_1 + z_2} \right) \quad 4.58$$

Chapter 5: Results

The results for this project are presented in five sections. Section 5.1 compares the fluid flow models developed in Section 4.1 with the Hagen-Poiseuille flow equation. The verification of the ideal gas flow equation with experimental data, the verification of the near wellbore stress distributions of the FEA models with the analytical solution, and the verification of an FEA fluid rheology model with experimental data are shown in Section 5.2. Section 5.3 presents the Gulf of Mexico (GoM) parametric study for the three well depths with both the stress continuum and fracture models. The continuous leakage pathway potential for the three GoM wells is discussed in Section 5.4 while Section 5.5 investigates the leakage potential of a case study well in the High Island OPD in the GoM.

5.1 Fluid Flow Model Comparison

A comparison of the developed gas flow equations with the Hagen-Poiseuille annular equation is performed in this section. The developed gas flow equations include the ideal gas equation (Equation 4.15), ideal gas with gravity equation (Equation 4.36), real gas equation (Equation 4.31), and real gas with gravity equation (Equation 4.37). The Hagen-Poiseuille flow is analyzed with and without the effect of gravity (Equation 2.41 and 4.36, respectively). The comparison for the six methods is shown in Table 5.1.

Table 5.1: Comparison of the six analytical equations for the synthetic well. Note that Hagen-Poiseulle flow was determined for both water and gas. Equation 4.15 resulted in the highest flow rate while Equation 4.34 did not have a flow rate.

Fluid	Models	Eq.	m^3/s	m^3/day	L/day
Water	Hagen-Poiseulle Flow	2.41	1.30E-06	0.11	112
	Hagen-Poiseulle Flow + Gravity	4.34	0.0	0.0	0.0
Gas	Hagen-Poiseulle Flow	2.41	2.84E-05	2.46	2,458
	Hagen-Poiseulle Flow + Gravity	4.34	2.35E-05	2.03	2,028
	Ideal Gas	4.15	3.70E-05	3.20	3,195
	Ideal Gas + Gravity	4.36	3.20E-05	2.76	2,765
	Real Gas	4.31	3.57E-05	3.08	3,082
	Real Gas + Gravity	4.37	3.07E-05	2.65	2,652

Comparing the results for the different flow equations in Table 5.1, the following observations were made. First is that including the effect of gravity decreases the flow rates; especially for water which results in no flow due to the pressure differential being the hydrostatic pore pressure. The effect of gravity on the gas flow equations (4.34, 4.36, and 4.37) is not as dramatic. Gravity causes a 100% flow rate decrease for Hagen-Poiseulle flow with water as the fluid (Equation 4.34 versus Equation 2.41), a 17.5% decrease for Hagen-Poiseulle flow with gas as the fluid (Equation 4.34 versus Equation 2.41), a 13.5% decrease for ideal gas flow (Equation 4.36 versus Equation 4.15), and a 14.0% decrease for real gas flow (Equation 4.37 versus Equation 4.31). A second observation is that using Hagen-Poiseulle flow with gas viscosity (Equation 2.41) has a 23.1% difference compared to the ideal gas flow (Equation 4.15) and a 20.3% difference compared to real gas flow (Equation 4.31).

To verify that the developed flow equations are in a laminar flow regime, the Reynold's number (N_{Re}) is calculated. As shown in Table 5.2, the Reynold's number for each flow equation is well below the cutoff of 2,100 ($N_{Re} \leq 2,100$). Therefore, the developed flow equations (ideal gas, ideal gas + gravity, real gas, and real gas + gravity) are valid for the synthetic wellbore scenario.

Table 5.2: Corresponding Reynold’s numbers (N_{Re}) for the fluid flow models for the synthetic wellbore. All eight fluid flow models are in the laminar flow regime ($N_{Re} \leq 2,100$).

Fluid	Models	Eq.	N_{Re}
Water	Hagen-Poiseulle Flow	2.41	293.5
	Hagen-Poiseulle Flow + Gravity	4.34	242.2
Gas	Hagen-Poiseulle Flow	2.41	3.5
	Hagen-Poiseulle Flow + Gravity	4.34	0.0
	Ideal Gas	4.15	381.6
	Ideal Gas + Gravity	4.36	330.2
	Real Gas	4.31	368.1
	Real Gas + Gravity	4.37	316.7

5.2 Verification of Models

The verification of the models are presented in three sections. The first section (Section 5.2.1) validates the analytical gas flow equations (Equation 4.15 and 4.31) with experimental data from Corina et al. (2019). Section 5.2.2 compares the near wellbore stress distribution of the FEA stress continuum model with the thick wall cylinder and Kirsch solution to show that the modeling approach used is accurate. Finally, Section 5.2.3 compares the FEA fracture model’s pressure drops and resulting microannuli with experimental data from Aas et al. (2016).

5.2.1 Fluid Flow Models versus Cemented Wellbore Experiments

The experimental verification of the developed gas flow equations (ideal and real) is presented in this section. The ideal gas flow equation (Equation 4.15) and real gas flow equation (Equation 4.31) used the pressure differential (ΔP) and flow rate data from Corina et al. (2019) to predict the corresponding microannuli. A comparison of the predicted microannuli from the ideal gas (solid line) and real gas (dashed line) equations are shown in Figure 5.1 for microannuli (w) versus flow rate and in Figure 5.2 for microannuli (w) versus pressure differential (ΔP). As shown in the figures, the real and ideal gas variations have little deviation from each other.

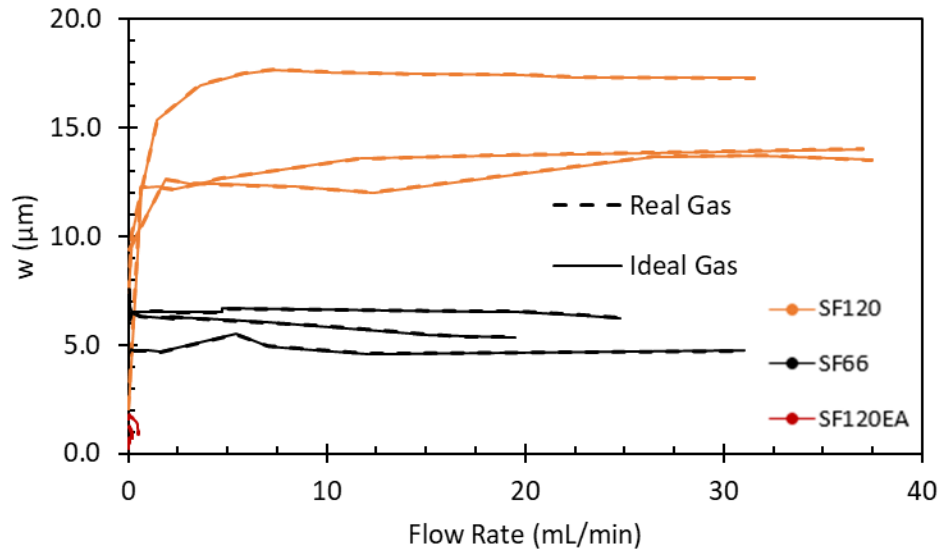


Figure 5.1: Microannuli (w) versus flow rate for the developed real and ideal gas flow equations (Equation 4.15 and Equation 4.31, respectively) using experimental data from Corina et al. (2019). The difference between the real and ideal gas flow equations is a maximum of 0.04%, 0.25%, and 0.50% for SF120, SF66, and SF120EA, respectively.

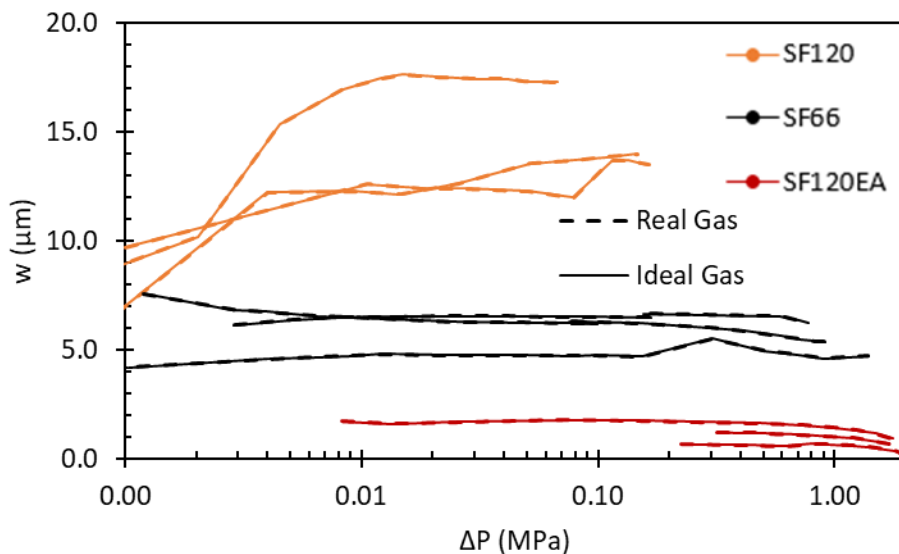


Figure 5.2: Microannuli (w) versus pressure differential (ΔP) for the developed real and ideal gas flow equations (Equation 4.15 and Equation 4.31, respectively) using experimental data from Corina et al. (2019). The difference between the real and ideal gas flow equations is a maximum of 0.04%, 0.25%, and 0.50% for SF120, SF66, and SF120EA, respectively.

To quantify the maximum deviation, Table 5.3 lists the maximum percent difference of the microannuli from the real gas equation (Equation 4.31) and the ideal gas equation (Equation 4.15) shown in Figures 5.1 and 5.2. The maximum difference of all three cement mixtures is 0.5% for SF120EA. The compressibility of methane at 2.0 MPa at 66 °C and 120 °C is 0.979 and 0.997,

respectively. Since the compressibility of methane at these conditions is negligible, the ideal gas flow equation will be used in this section to compare with Corina et al.'s (2020) microannuli results.

Table 5.3: Maximum percent difference (% Diff.) of the variation between the real and ideal gas flow.

Mixture	Max % Diff.
SF120	0.04%
SF66	0.25%
SF120EA	0.50%

Figures 5.3 and 5.4 compare the microannuli from the ideal gas flow equation and Equation 2.53 (Corina et al. 2020) for both flow rate (Figure 5.3) and pressure differential (Figure 5.4). As shown in Figures 5.3 and 5.4, the two flow equations match within 1.5% for the SF120 and samples. However, there is a noticeable difference for the SF66 and SF120EA samples. The SF66 samples have a maximum percent difference of 25.3%. The SF120EA samples have a larger percent difference of 55.7% due to the microannuli being significantly smaller than the SF66 microannuli. This analysis shows that even though the pressures of this system are low, the ideal gas predicted microannuli varies from the Darcy flow predicted microannuli. This contradicts Hubbert (1956) and Outmans (1963) which claim that for low pressures, the flow of gases in small pore spaces is equivalent to liquid Darcy flow.

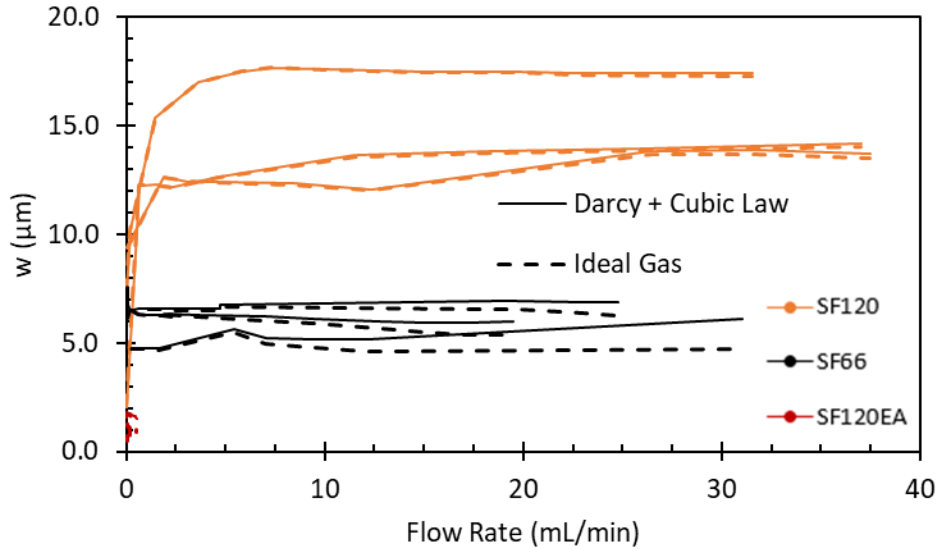


Figure 5.3: Microannuli (w) versus flow rate for the developed ideal gas flow equation (Equation 4.15) and the Darcy flow equation used in conjunction with the cubic law (Equation 2.54). The maximum percent difference between Equation 4.15 and Equation 2.54 is 1.5% for SF120, 25.3% for SF66, and 55.7% for SF120EA.

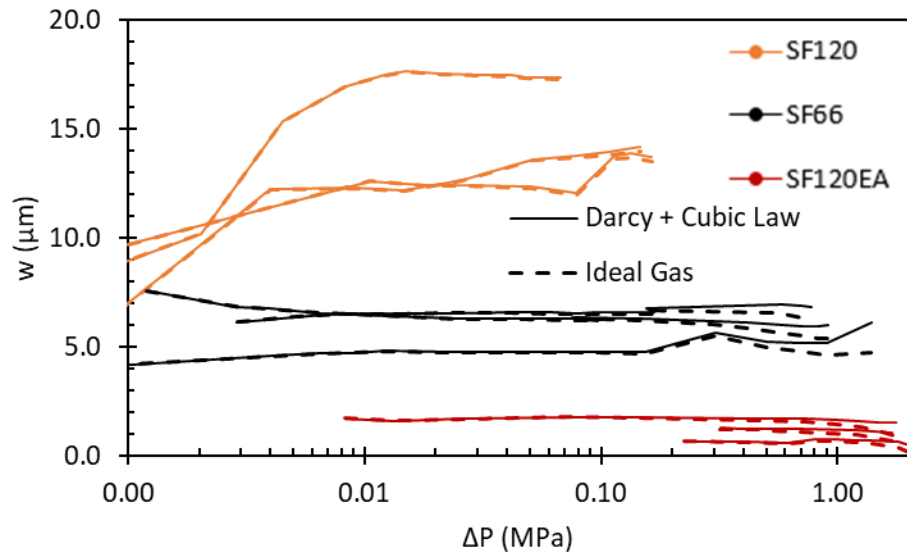


Figure 5.4: Microannuli (w) versus pressure differential (ΔP) for the developed ideal gas flow equation (Equation 4.15) and the Darcy flow equation used in conjunction with the cubic law (Equation 2.54). The maximum percent difference between Equation 4.15 and Equation 2.54 is 1.5% for SF120, 25.3% for SF66, and 55.7% for SF120EA.

To verify that the experiments are in a laminar flow regime, the Reynold's number (N_{Re}) of the gas flow is evaluated. As shown in Table 5.4, the Reynold's number for each cement mixture is well below the cutoff of 2,100 ($N_{Re} \leq 2,100$). Therefore, the nitrogen gas flow is laminar, and the derived equations are valid for this analysis.

Table 5.4: Corresponding maximum Reynold’s numbers (N_{Re}) for the cement mixtures SF120, SF66, and SF120EA. The Reynold’s numbers are all in the laminar flow regime.

Mixture	N_{Re}
SF120	2.9
SF66	2.1
SF120EA	0.03

The results of using the ideal gas flow equation (Equation 4.15) and the Hagen-Poiseulle flow equation (Equation 2.53) with a gas viscosity showed little variation for the SF120 samples. This is due to the pressure differential and cement length used in the experiments. As shown in Table 5.1, wellbore hydrostatic pore pressures with a length of 1,127 m result in a 23.1% difference between the ideal gas flow equation and using a gas viscosity with the Hagen-Poiseulle flow equation. Therefore, for realistic wellbore leakage models, correct flow equations for the specific type of leaking fluid should be used.

5.2.2 FEA Near Wellbore Stress Distribution versus Kirsch Analytical Solution

The staged poro-elastic FEA stress continuum and fracture model was verified using the analytical equations (Kirsch and thick wall cylinder) discussed in Section 2.9. The results for the two models are shown in Figure 5.5 along with the results for the analytical solution. Initial observations of Figure 5.5 show that the two FEA models appear to overlap the analytical solution completely except the hoop stress in the rock formation. Table 5.5 shows the maximum percent stress variation of the two models with the analytical solution.

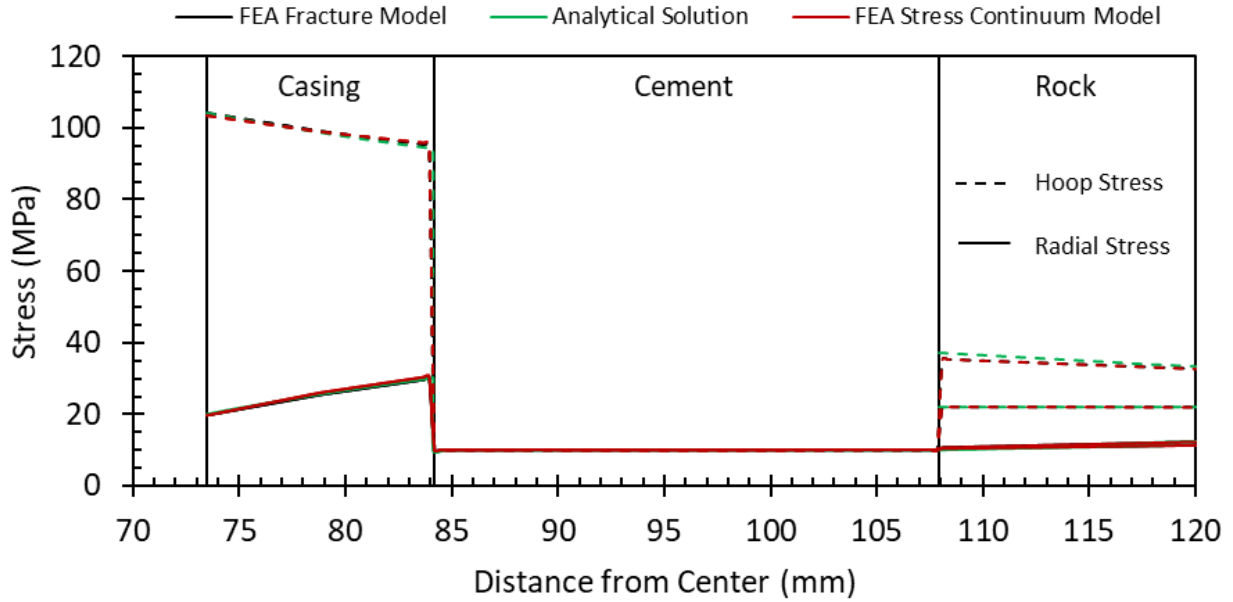


Figure 5.5: FEA stress continuum and fracture model compared to the analytical solution showing less than 2.6% variation of the casing hoop and radial stress, less than 1.4% variation of the cement hoop and radial stress, and less than 7.2% variation of the rock formation hoop and radial stress for the medium well in the Eugene Island OPD.

Table 5.5: Effective stress percent difference of the FEA stress continuum and fracture model from the analytical solution for the casing, cement, and rock formation.

	Stress Continuum Model		Fracture Model	
	Radial % Diff.	Hoop % Diff	Radial % Diff.	Hoop % Diff
Casing	±1.0%	±0.5%	±2.6%	±1.2%
Cement	±0.4%	±0.2%	±1.4%	±0.5%
Rock Formation	±7.2%	±5.4%	±6.7%	±5.3%

From Table 5.5, the FEA stress continuum model matches with the analytical solution better than the FEA fracture model for all three materials. But the stress model is not able to replicate fractures at the cement sheath interfaces. Both FEA models are within 3% for the casing and cement, but neither are as accurate for the rock formation. The discrepancy with the stress in the rock formation is due to element gridding. A finer grid should result in a more accurate stress representation. However, a finer grid results in longer simulation times. Since the objective is to determine if leakage is occurring through the cement sheath, the finite element grid is determined

to be accurate for the both models since the cement sheath stress is within 1.4% of the analytical solution.

5.2.3 FEA Fluid Rheology Model versus Cemented Wellbore Experiments

The simulated pressure drops and corresponding microannuli of the two-way coupled cased wellbore FEA fracture model is compared to the experimental data from Aas et al. (2016) to determine if the model can accurately predict cement sheath microannuli in cemented wellbores. Table 5.6 shows the results of the pressure drop calculations for conventional and expanding cement compared to the experimental data. For expanding cement, the simulated pressure drops were lower than those that were experimentally recorded except for the pressure of 4.2 MPa and flow rate of 13 mL/min. The simulated microannuli were larger than the total microannuli of the experiments except for the pressure of 4.2 MPa in which the model did not predict a complete leakage path for the length of the casing. For the conventional cement with shrinkage, the simulated pressure drops were within 0.1 MPa of the experiments. However, the simulated microannuli were at least 40 μm higher than the total microannuli of the experiments. Not adding shrinkage to the conventional cement caused the simulations to not converge.

Table 5.6: Calculated pressure drops and simulated microannuli gaps for both expanding and conventional cement in comparison to the experimentally measured pressure drops and equivalent microannuli gaps.

Length (m)	Initial Pressure (MPa)	Flow Rate (mL/min)	Experiment Pressure Drop (MPa)	Total Microannuli (μm)	Simulated		Simulated Microannuli			
					Pressure Drop (MPa)	Pressure Drop (MPa)	Inlet (max) (μm)	Outlet (min) (μm)	Inlet (max) (μm)	Outlet (min) (μm)
6	12.5	98	4.8	22	0.4	0.4	91	89		
6	12.6	94	4.8	22	0.4	0.4	92	90		
6	12.7	92	4.9	22	0.3	0.3	93	90		
6	9.6	49	5.0	18	0.4	0.4	70	67		
6	9.5	48	5.1	17	0.4	0.4	69	66		
6	6.6	23	4.7	14	0.7	0.7	48	43		
6	6.5	23	4.4	14	0.7	0.7	48	42		
6	4.2	13	3.0	13	4.2	4.2	31	0		
					0%	1%	0%	1%		
18	5.4	14	0.1	101	5.4	0.1	47	0.0	148	147
18	9.3	95	0.3	127	9.3	0.4	80	0.0	182	178
18	5.6	56	0.4	93	5.6	0.4	48	0.0	150	149
18	9.4	136	0.5	118	9.4	0.6	81	0.0	182	177

* Values in grey indicate model shrinkage.

Figure 5.6 shows the sensitivity analysis of the cement mechanical properties (E and PR) with respect to the percent change of the resulting microannuli gap between the cement and casing. The base microannuli gap is $13.6\ \mu\text{m}$. For the cement Young's modulus (E), the lower the value, the higher the resulting microannuli. As the cement Young's modulus increased, the microannuli decreased. The same trend is seen for the cement Poisson's ratio (PR) however, the degree of magnitude is not as large. For a 25% value of E (2.45 GPa), the resulting microannuli increased 78.3% to a magnitude of $24.3\ \mu\text{m}$ whereas a 125% value of E (17.2 GPa) caused a decrease of 14.9% to a magnitude of $11.6\ \mu\text{m}$. For a 25% value of PR (0.05), the resulting microannuli increased 3.8% to a magnitude of $14.2\ \mu\text{m}$ whereas a 125% value of PR (0.32) caused a decrease of 4.6% to a magnitude of $13.0\ \mu\text{m}$.

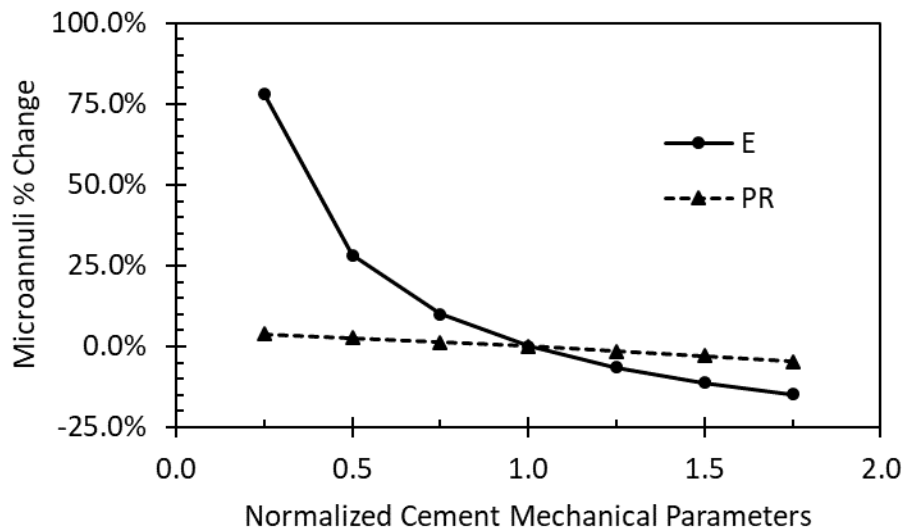


Figure 5.6: Sensitivity analysis of the cement mechanical parameters with respect to the percent change in resulting microannuli. The base microannuli is $13.6\ \mu\text{m}$. Cement Young's modulus (E) has a nonlinear effect on microannuli percent change whereas cement Poisson's ratio (PR) appears to have a linear effect.

The pressure drop calculations for the cased wellbore FEA fracture model show inconsistent results for the expanding cement. For the lowest initial pressure of 4.2 MPa, the calculations resulted in complete pressure drop causing the microannuli to close before the length of the model. The rest of the initial pressures for the expanding cement resulted in lower simulated

pressure drops than were measured experimentally. This indicates that the model overestimated the flow pathway as shown by the larger simulated microannuli. The overestimation could be due to the fact that the volume created by the simulated microannuli gaps is significantly larger than what occurs in experiments. Figure 5.7 depicts a 0.5x magnified directional deformation of the eccentric expandable cement model. As shown in Figure 5.7, the microannuli gap is continuous and almost uniform (2.30 μm versus 2.34 μm) around the circumference of the cement sheath.

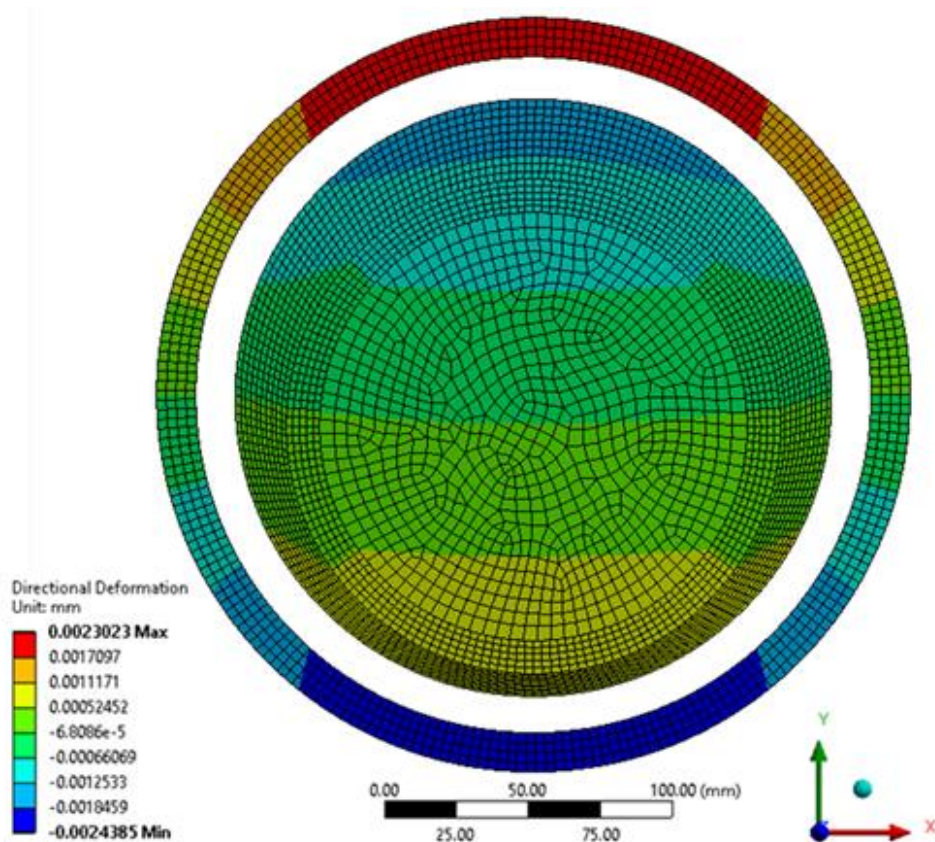


Figure 5.7: 0.5x magnified directional deformation of the eccentric expanding cement model. Note the pressure induced microannuli gap is continuous throughout the circumference of the cement sheath.

The conventional cement simulations shown in Table 5.6 gave comparable pressure drops and higher microannuli gap widths than the experiments when 1% volumetric shrinkage was included in the model. The Fanning friction factor (f) used in this analysis assumes laminar flow for a smooth constant flow path width. As discussed in detail in Appendix L, the Fanning friction factor is dependent on the Reynold's number, the roughness of the surface, and the tortuosity of

the flow path unless the fluid is laminar. When the fluid is laminar, the Fanning friction factor is only dependent on the Reynold’s number as shown in Equation 4.54. In the numerical analysis, there are two potential variations that could cause the conventional cement results to match the experimental pressure drops: shrinkage and friction factor. Table 5.7 shows that altering either the shrinkage or the friction factor independently can force the simulation to have the same pressure drop as the experimental data. Since the friction factor should not be a variable for laminar flow, the frictional pressure drop fluid model is not the optimal method to model cased wellbore potential leakage.

Table 5.7: Representation that the simulated pressure drops can mimic the experimental data by altering either the shrinkage or the fluid friction factor in the simulations.

Initial Pressure (MPa)	Flow Rate (mL/min)	Pressure Drop (MPa)	Shrinkage (%)	Friction Factor $\frac{\alpha}{N_{Re}}$
5.4	14.0	0.1	1.4%	0.2
9.3	95.0	0.3	1.3%	0.8
5.6	56.0	0.4	1.1%	0.4
9.4	136.0	0.5	1.2%	1.1

5.3 GoM Parametric Study

The results of the GoM parametric study of the three wells in the Eugene Island OPD compare the effect of wellbore parameters in terms of stress development and compare the effect of modeling the staged wellbore as a stress continuum or with fracture criteria at the cement interface. The results of the staged poro-elastic FEA stress continuum model were completed previously in Wise et al. (2019). The full results for the stress continuum model are listed in Appendix I. The results of the comparison are presented in two sections. The first section (Section 5.3.1) compares the effective stress of the base case wellbores for the stress continuum and fracture model. Section 5.1.5 compares the parameter sensitivity analysis for the stress contributing factors.

5.3.1 Base Case Wells

The three base case wells compare the effective stress at the cement/rock (C/R) and casing/cement (C/C) interfaces for the stress continuum and fracture model in Table 5.8. The gray shadowed coloring indicates tensile stresses in the stress continuum model and the orange shading indicates tensile stresses in the fracture model. The base results for the continuum model show that the medium and deep wells are experiencing tensile stresses in the radial directions which indicates debonding. The medium well is experiencing debonding at both the casing/cement and cement/rock formation interfaces while the deep well is only debonding at the casing/cement interface in the continuum model. However, only the medium well is experiencing debonding at the casing/cement interface in the fracture model. The shallow well is not experiencing any tensile stresses for both models. Disking of the cement sheath is not a concern for the three wells since the effective vertical stresses are all compressive.

Table 5.8: Base case wellbores comparison between the stress continuum model (stress model) and the fracture model for the shallow, medium, and deep depth wellbores. The gray shaded cells represent tensile failure in the stress continuum model whereas the orange shaded cell represents tensile failure in the fracture model resulting in a microannuli gap width of 13.6 μm .

Effective Interface Stresses	Shallow Well			Medium Well			Deep Well		
	Stress Model MPa	Fracture Model MPa	Avg. Diff. %	Stress Model MPa	Fracture Model MPa	Avg. Diff. %	Stress Model MPa	Fracture Model MPa	Avg. Diff. %
Hoop Stress C/C	0.90	0.95	5.4%	5.70	5.00	13.1%	15.22	15.16	0.4%
Hoop Stress C/R	0.83	0.89	7.0%	3.70	3.73	0.8%	12.67	12.50	1.4%
Radial Stress C/C	0.58	0.66	12.9%	-2.75	-0.40	149%	-1.13	0.37	395%
Radial Stress C/R	0.62	0.72	14.9%	-0.84	0.88	8,600%	2.44	3.05	22.2%
Vertical Stress C/C	0.89	0.93	3.9%	3.03	3.44	12.8%	11.39	11.75	3.1%
Vertical Stress C/R	0.89	0.93	4.9%	3.01	3.44	13.5%	11.65	11.76	1.0%

To analyze the potential of shear failure, Mohr-Coulomb criterion was used to evaluate whether the shear stresses were in failure for the fracture model. Figure 5.8 shows that all three wells are far from being in shear failure. The deepest well proves closest to shear failure, but the gap between its Mohr circle and the failure envelope is significant. An interesting observation is that the shear stresses in the shallow well are not significant. The stresses are barely visible when compared to the medium and deep wells let alone the failure envelope. Another observation is that Figure 5.8 shows that the medium well has tensile stresses, however, they are not to the tensile failure of the cement. Comparing Figure 5.8 with Table 5.8 shows that debonding of the cement sheath is occurring at the casing/cement interface for the fracture model yet tensile cracks are not occurring.

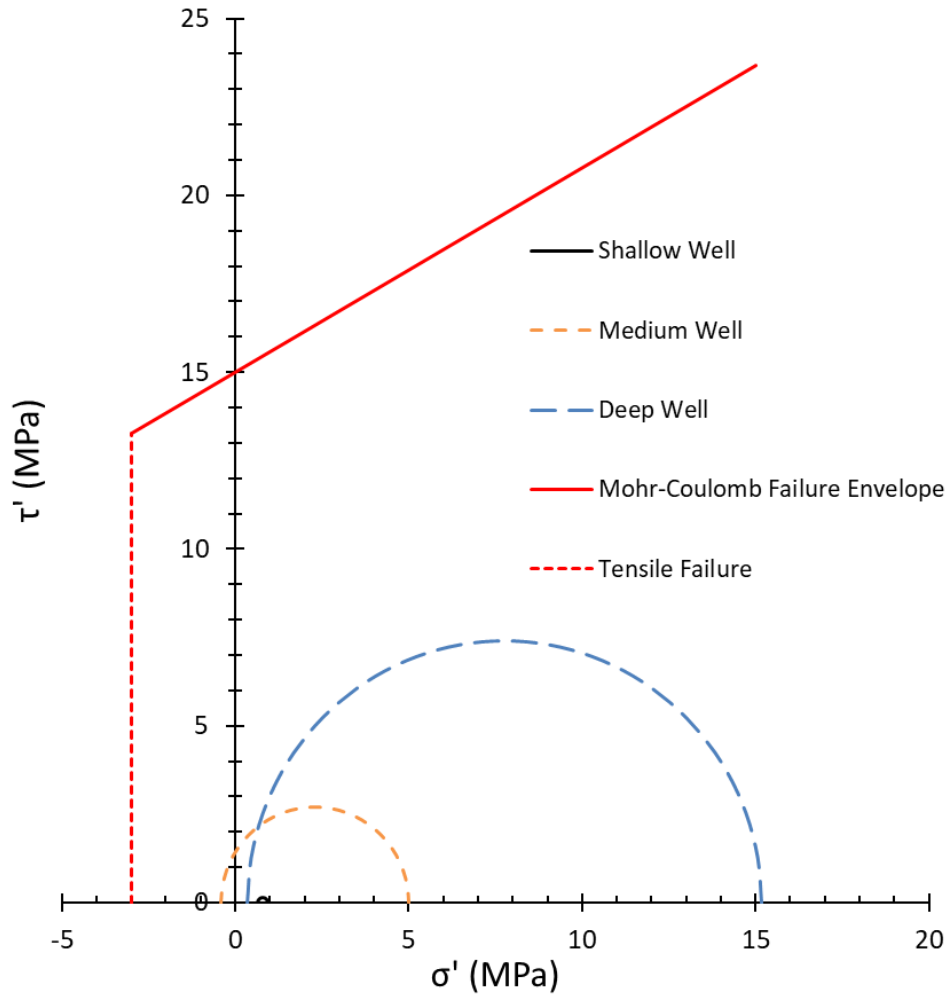


Figure 5.8: Mohr-Coulomb shear failure envelope of the cement sheath for the shallow (black), medium (orange), and deep (blue) wells. All three wells are not close to shear failure or cement tensile failure.

Figure 5.9 depicts the graphical results of the base case cement sheaths for the three wells. The effective shear stresses $\left(\frac{\sigma'_1 - \sigma'_3}{2}\right)$ are depicted on the left, and the effective minimum principal stresses (σ'_3) are shown on the right. The inner radius of the sheath is the casing/cement interface while the outer radius is the cement/rock formation interface.

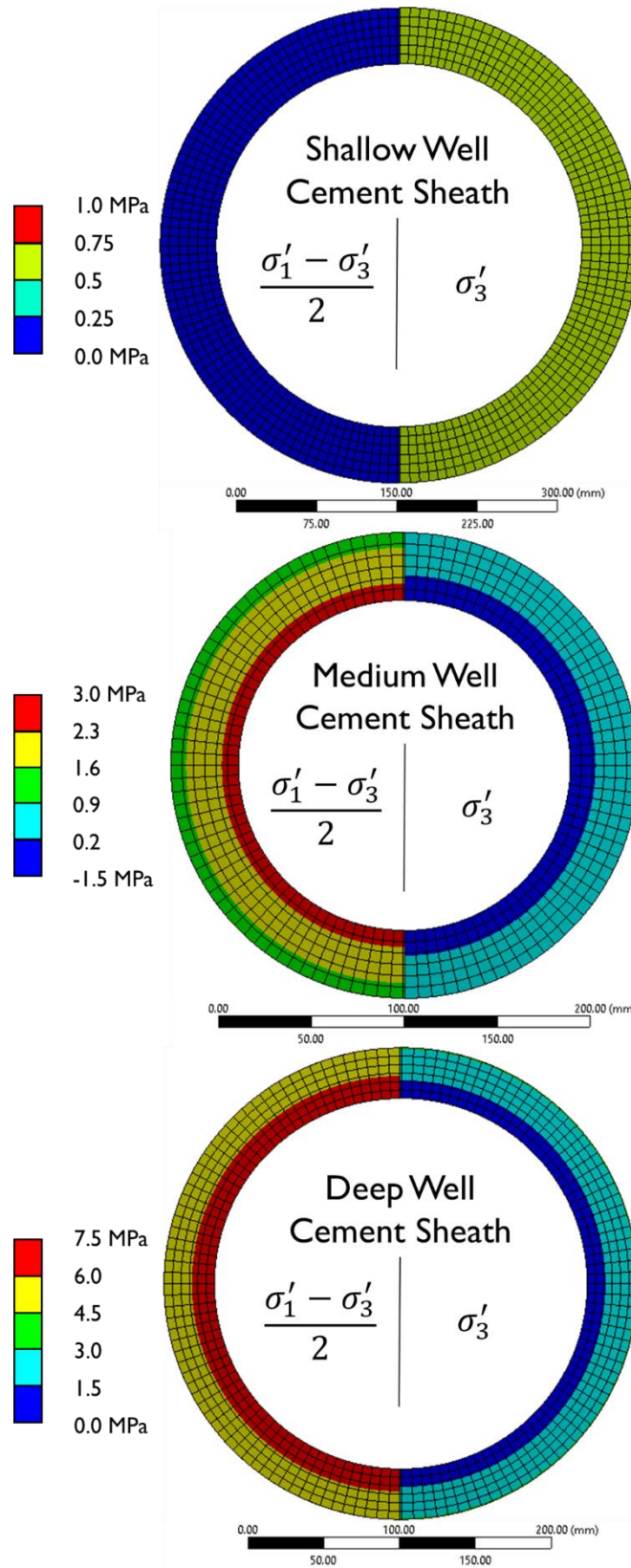


Figure 5.9: Graphical results of the base case stress values shown in Table 5.8 for the shallow, medium, and deep wells for the fracture model. The shear stresses are depicted on the left and the minimum principal stresses are depicted on the right.

For the shallow well, the scale resolution shows that the radial stress is constant throughout the thickness of the cement sheath. Table 5.8 shows that the interface stresses are not tensile and Figure 5.9 shows that the bulk cement is not in tensile. The medium well is experiencing tensile stress at the casing/cement interface, but Figure 5.9 shows that the tensile stress is focused towards the interface and does not extend throughout the cement sheath. The deep well follows a similar trend as the medium well except the effective minimum principal stress is not tensile. The results of Figure 5.9 shows that the cement sheath will experience tensile debonding before radial cracks occur. For the shear stress of the wells, the stress concentrations are located at the casing/cement interface of the medium and deep well (and most likely the shallow well, but the scale resolution is not fine enough). This result is interesting since the failure mechanism of debonding is occurring at the casing/cement interface of the medium well. The shear stress is concentrated at this interface due to the shear failure criteria, $\left(\frac{\sigma'_1 - \sigma'_3}{2}\right)$. The maximum and minimum effective stresses (hoop and radial) are at the casing/cement interface, as shown in Table 5.8, which results in the shear stress concentration being at that location.

5.3.2 Parametric Analysis

The second analysis for the three GoM wells is the parametric study of the base case wells to rank the stress contributing factors in comparison of the two models. The results for the stress continuum model are shown in Figures 5.10, 5.12, and 5.14 for the shallow, medium, and deep well, respectively. The results for the fracture model are shown in Figures 5.11, 5.13, and 5.15 for the shallow, medium, and deep well, respectively. The maximum and minimum normalized effective stress values for the three wells are shown. Due to the large variation of the parameters, log scales were used for the x-axis. The solid bars represent a positive percent change while the checkered bars represent a negative percent change.

Continuum Stress Model: Shallow Well Stress Variation

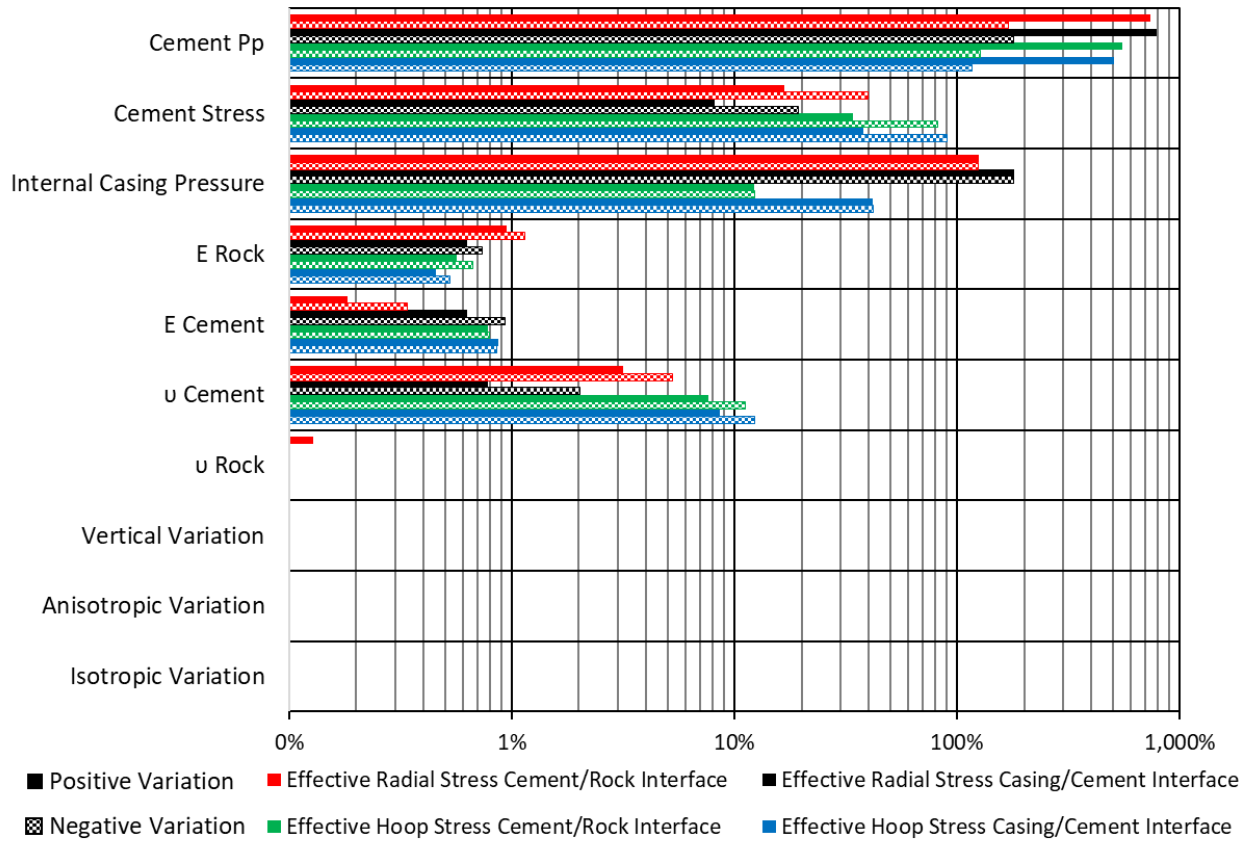


Figure 5.10: Results of the parametric study with the continuum stress model ranking the parameters with the largest impact on stress development for the shallow well. The cement pore pressure (P_p), cement stress, and internal casing pressure have the most effect on the effective cement stress for the shallow well stress continuum model.

Fracture Model: Shallow Well Stress Variation

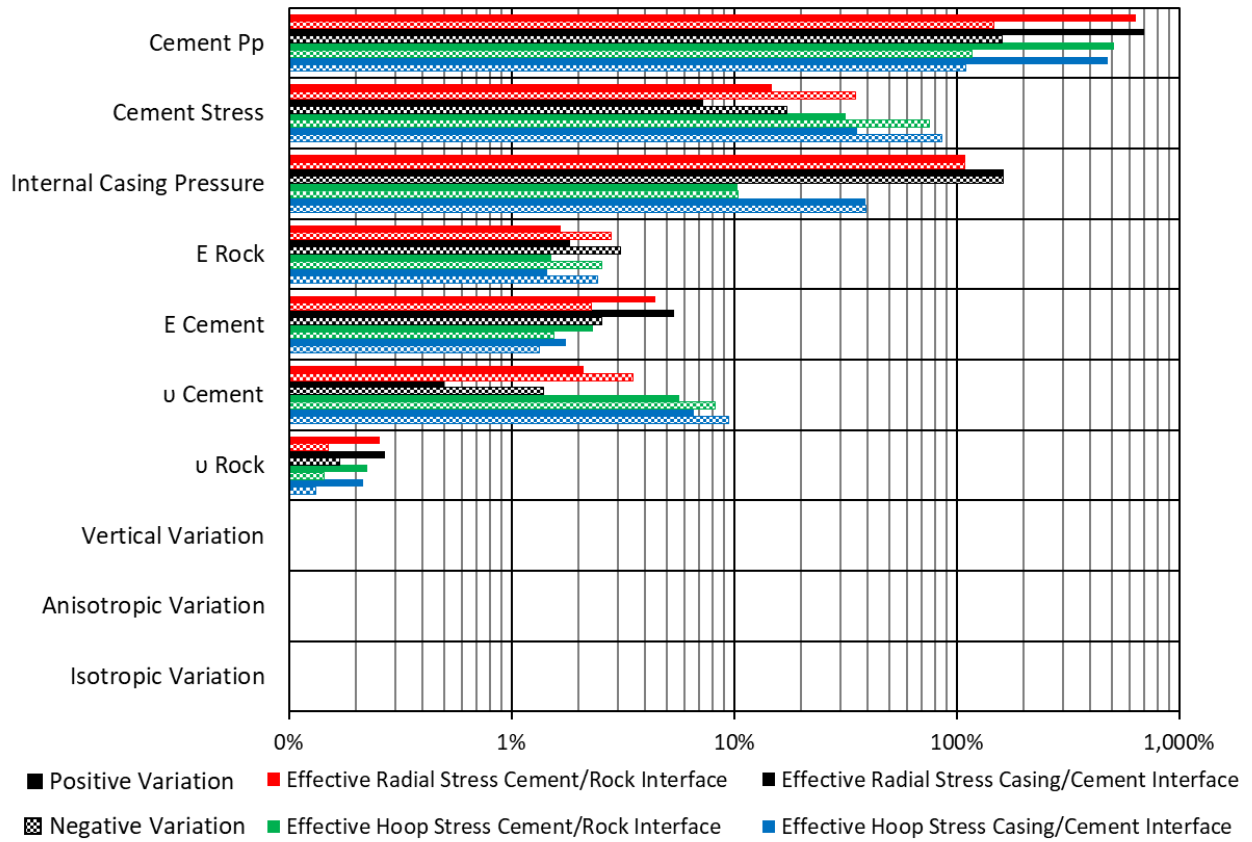


Figure 5.11: Results of the parametric study with the fracture model ranking the parameters with the largest impact on stress development for the shallow well. The cement pore pressure (P_p), cement stress, and internal casing pressure have the most effect on the effective cement stress for the shallow well fracture model.

Continuum Stress Model: Medium Well Stress Variation

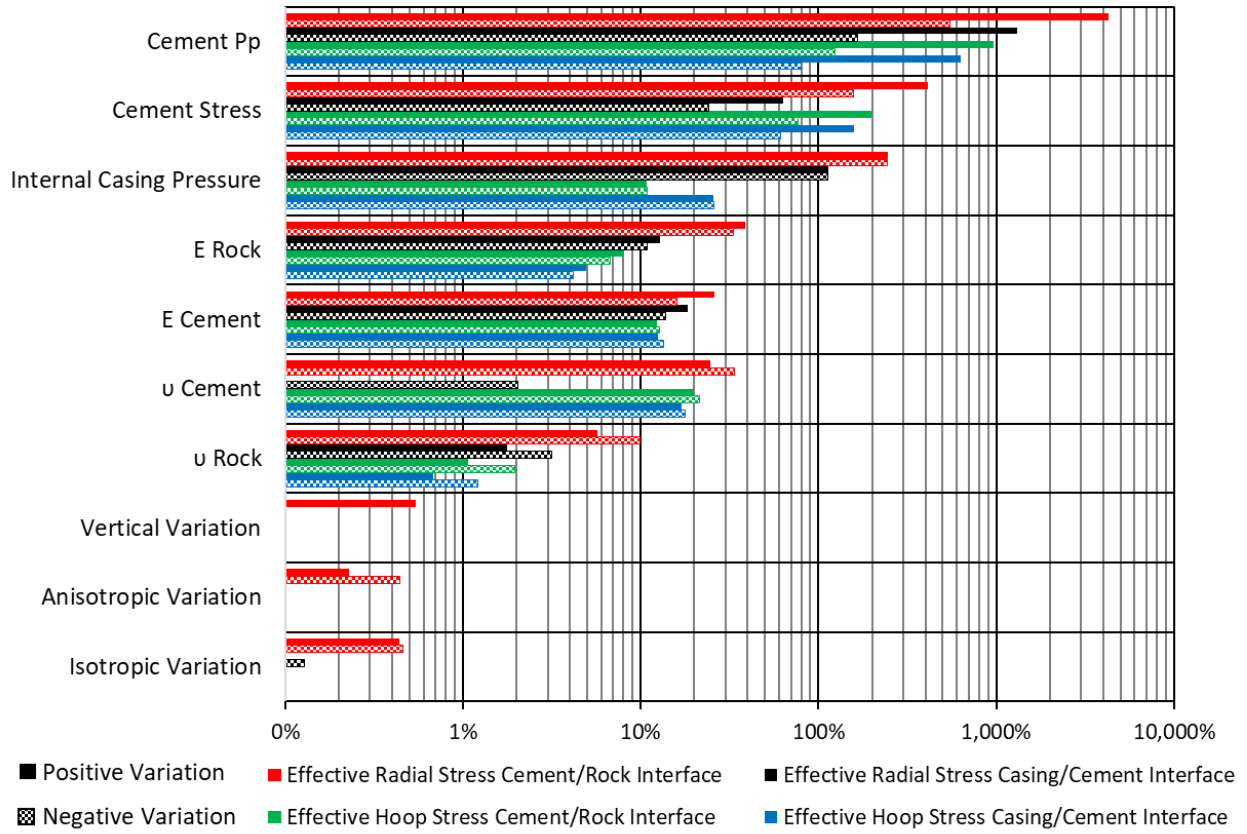


Figure 5.12: Results of the parametric study with the continuum stress model ranking the parameters with the largest impact on stress development for the medium well. The cement pore pressure (P_p), cement stress, and internal casing pressure have the most effect on the effective cement stress for the medium well stress continuum model.

Fracture Model: Medium Well Stress Variation

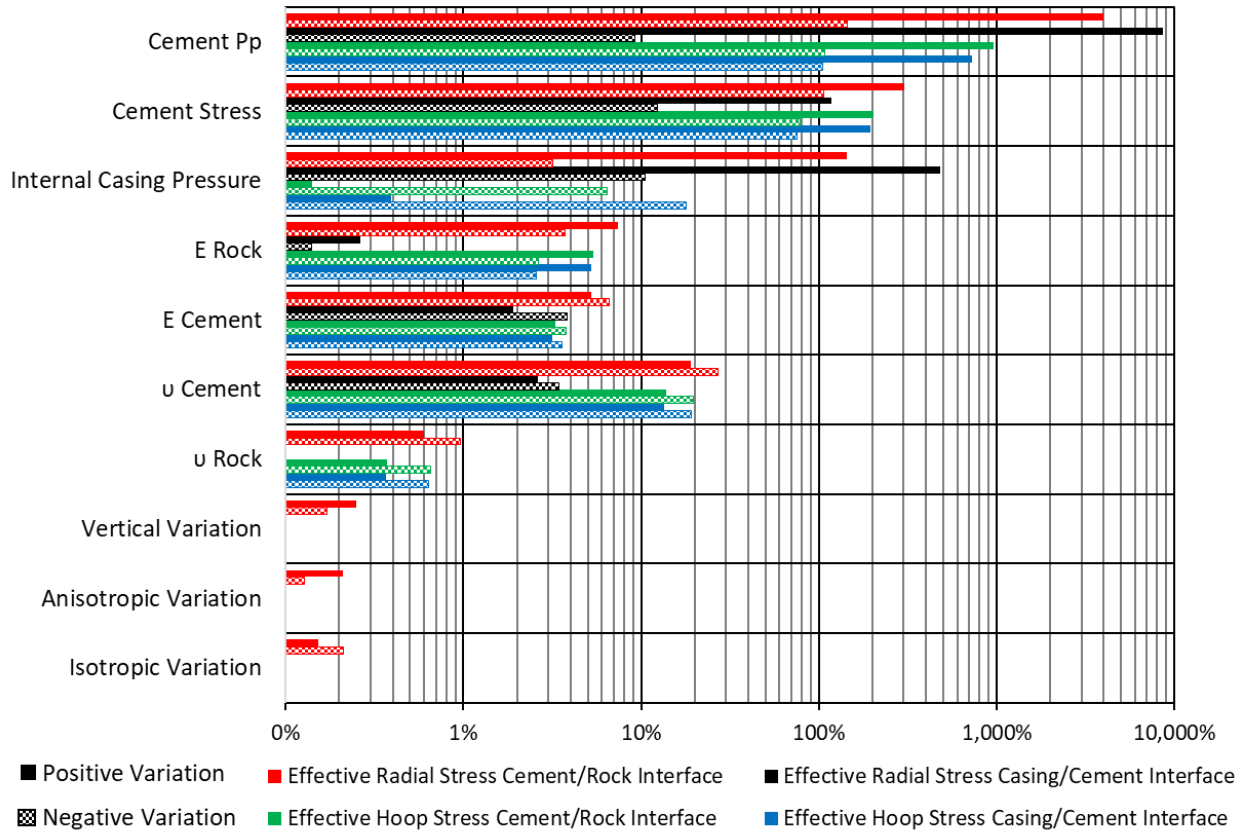


Figure 5.13: Results of the parametric study with the fracture model ranking the parameters with the largest impact on stress development for the medium well. The cement pore pressure (P_p), cement stress, and internal casing pressure have the most effect on the effective cement stress for the medium well fracture model.

Continuum Stress Model: Deep Well Stress Variation

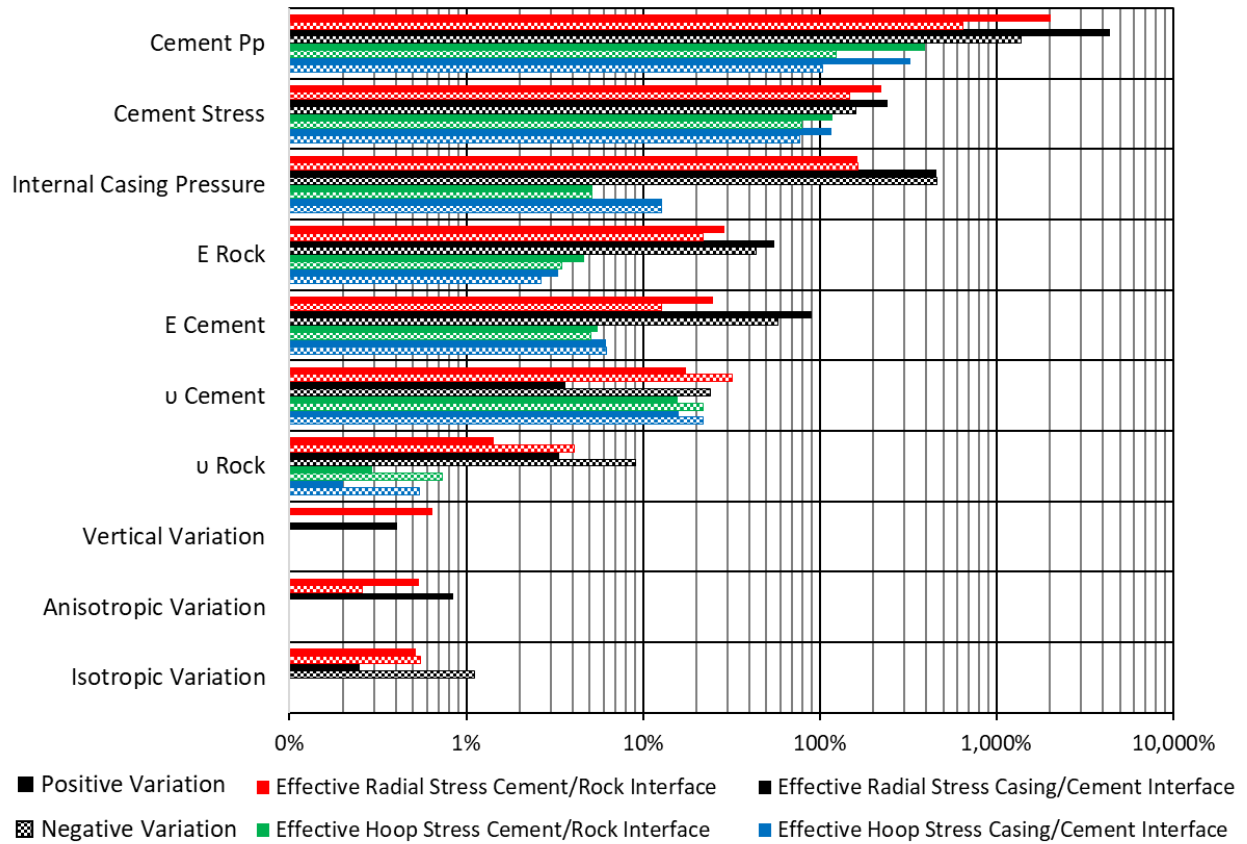


Figure 5.14: Results of the parametric study with the continuum stress model ranking the parameters with the largest impact on stress development for the deep well. The cement pore pressure (P_p), cement stress, and internal casing pressure have the most effect on the effective cement stress for the deep well stress continuum model.

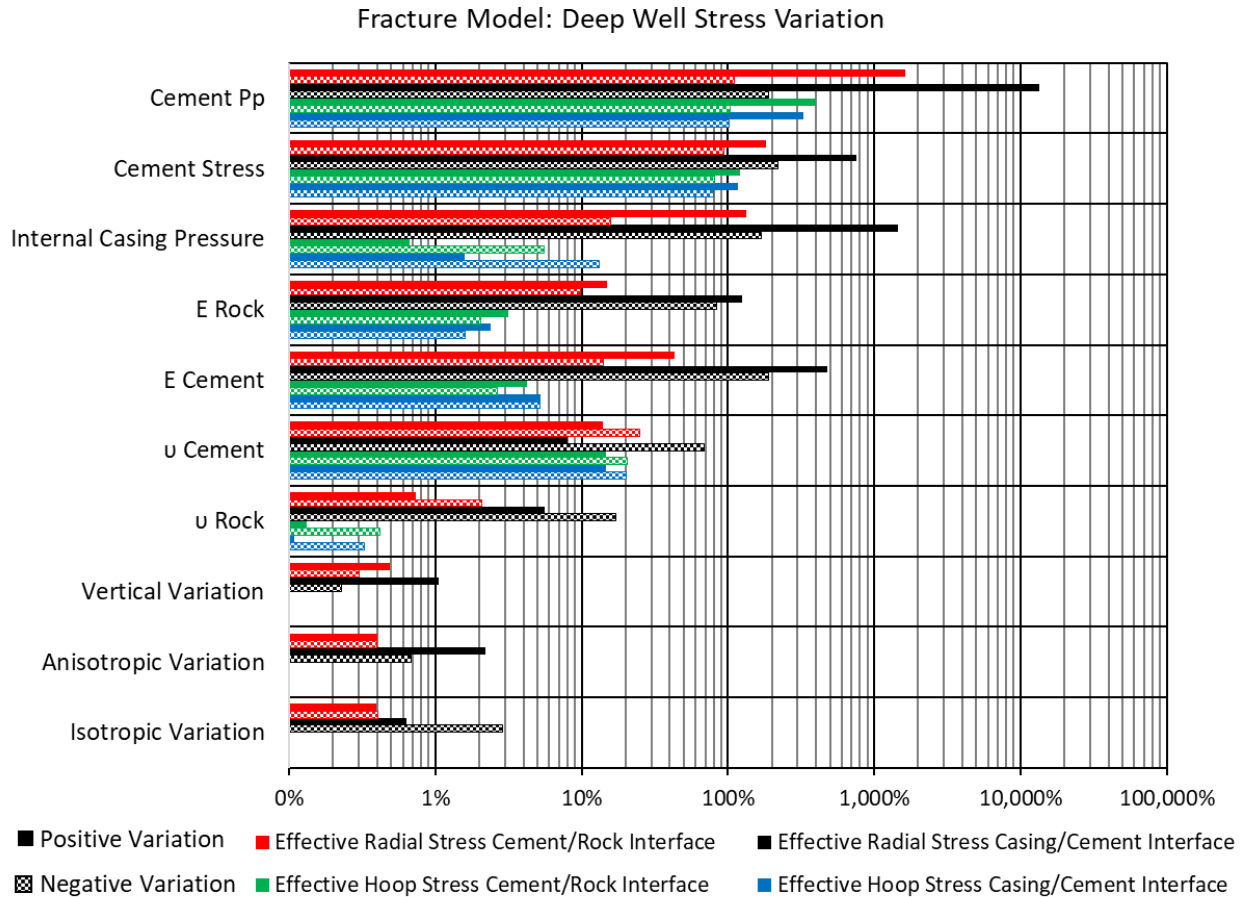


Figure 5.15: Results of the parametric study with the fracture model ranking the parameters with the largest impact on stress development for the deep well. The cement pore pressure (P_p), cement stress, and internal casing pressure have the most effect on the effective cement stress for the deepwell fracture model.

Figures 5.10-5.15 show that the ranking of the parameters are not the same for all three wells for the stress model. For both the stress continuum and fracture models, cement pore pressure, cement setting stress, and *ICP* cause the most stress variation. The rest of the wellbore parameters (cement mechanical properties, rock formation mechanical properties, and in-situ stress configurations) have less than 100% change in effective stress values. Therefore, these parameters do not cause the stress to change from compressive to tensile or vice versa.

For the fracture model, all three wells follow the same trend as with the stress continuum model. The cement pore pressure, cement setting stress, and *ICP* cause the most change in the effective stresses. For the shallow well, only the cement pore pressure and *ICP* have larger than

100% change in effective stress values. The cement pore pressure, cement stress, and *ICP* have larger than 100% change in effective stress values for the medium well. However, for the deep well the wellbore parameters follow a different trend. The Young's modulus of the rock formation, the Young's modulus of the cement, the cement pore pressure, cement stress, and *ICP* have more than 100% change in effective stress values.

From the parametric analysis, the cement hydration parameters and the *ICP* are two of the most critical parameters in the stress development of the cement sheath. The results of this study are in agreement with Bois et al. (2011) which states that the cement hydration parameters (pore pressure and setting stress) one of the most critical aspects of cement sheath integrity. Simulating the setting stress from the maximum possible value (minimum horizontal stress) to the lowest possible scenario (zero effective stress) significantly affects the cement sheath stress by 100% in both the radial and hoop stresses. The change in effective stresses is significant enough to take the cement sheath from compressive to tensile and vice versa. The cement pore pressure acts the same way. A maximum pore pressure (equal to the setting stress resulting in an effective stress of zero) and a minimum pore pressure (zero pore pressure) affects the cement stress from 100% to greater than 1,000% in some instances. From Figures 5.12-5.17, the radial stresses in the cement are more sensitive to than the hoop stresses with variations in the hydration parameters which indicate that tensile debonding is more probable than radial cracks. This is in agreement with Bois et al. (2017) and Vu et al. (2018) in which the authors' numerical model showed that hydration can cause debonding of the cement sheath.

5.4 GoM Continuous Leakage Path

The leakage path from the simulation depth to the surface of the three GoM wells is investigated when the pressure reduction is 40%. The results for the continuous leakage path for the three wells are shown in Figure 5.16. The shallow well is shown with black data, the medium well is shown with blue data, and the deep well is shown with orange data. The leakage paths due to water filled microannuli are shown in the solid lines whereas the leakage path due to gas filled microannuli are shown in the dashed lines.

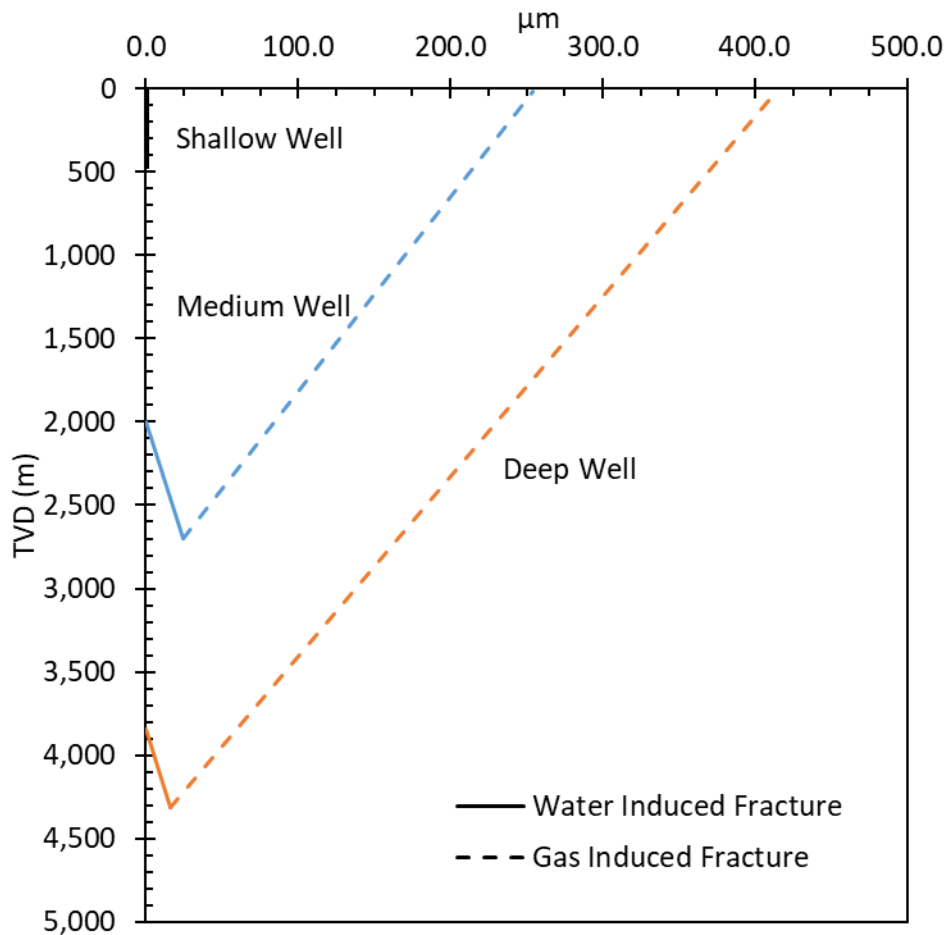


Figure 5.16: Continuous leakage pathways for the shallow well (black), medium well (blue), and deep well (orange) in the Eugene Island OPD. The solid line is the water induced microannuli while the dashed line is the gas induced microannuli. The water induced microannuli do not propagate up the wellbore whereas the gas induced microannuli propagate up the wellbore for the medium and deep wells.

From Figure 5.16, the shallow well did not have a microannuli at 40% ΔP at the simulation depth of 468 m (1,536 ft.) or at the surface. The medium well has a 24.2 μm microannuli at 40% ΔP at the simulation depth of 2,697 m (8,850 ft.). With the water induced fracture, the microannuli decreases as the well becomes shallow until a microannuli does not form at a depth of 1,999 m (6,558 ft.). With the gas induced fracture, the microannuli increases as the depth decreases. The microannuli at the surface is 254.5 μm . Therefore, a continuous leakage pathway occurs for the medium well. The deep well has a 15.9 μm microannuli at 40% ΔP at the simulation depth of 4,317 m (14,165 ft.). With the water induced fracture, the microannuli decreases as the well becomes shallow until a microannuli does not form at a depth of 3,842 m (12,606 ft.). With the gas induced fracture, the microannuli increases as the depth decreases. The microannuli at the surface is 414.1 μm . Therefore, a continuous leakage pathway occurs in the deep well.

5.5 Case Study Well

The methodology developed to analyze the Eugene Island OPD wells is used for a comprehensive analysis for a case study well in the High Island OPD. The analysis consists of investigating debonding of the cement sheath when pressure or temperature inside the casing is reduced (Section 5.5.1). Section 5.5.2 presents the results for the wellbore parameter sensitivity analysis with respect to casing/cement microannuli magnitude. Heat maps at four different depths are analyzed for concurrent pressure and temperature variations in Section 5.5.3. The continuous leakage pathway from the simulation depth to the top of cement (TOC) is discussed in Section 5.5.4 with a leakage rate assessment in Section 5.5.5.

5.5.1 Microannuli versus Pressure and Temperature Reductions

The microannuli at the casing/cement and rock formation/cement interface with respect to temperature and pressure reductions are presented below. Figure 5.17 shows the reduction (Δ)

versus microannuli width for the casing/cement interfaces and Figure 5.18 shows the cement/rock interfaces results. The microannuli primarily occur at the interface between the casing and cement sheath (Figure 5.17). The cement/rock interface has microannuli, yet they are on the nanometer scale whereas the microannuli associated with the casing/cement interface are on the micron scale. Therefore, the microannuli (or lack thereof) at the cement/rock interface are deemed negligible.

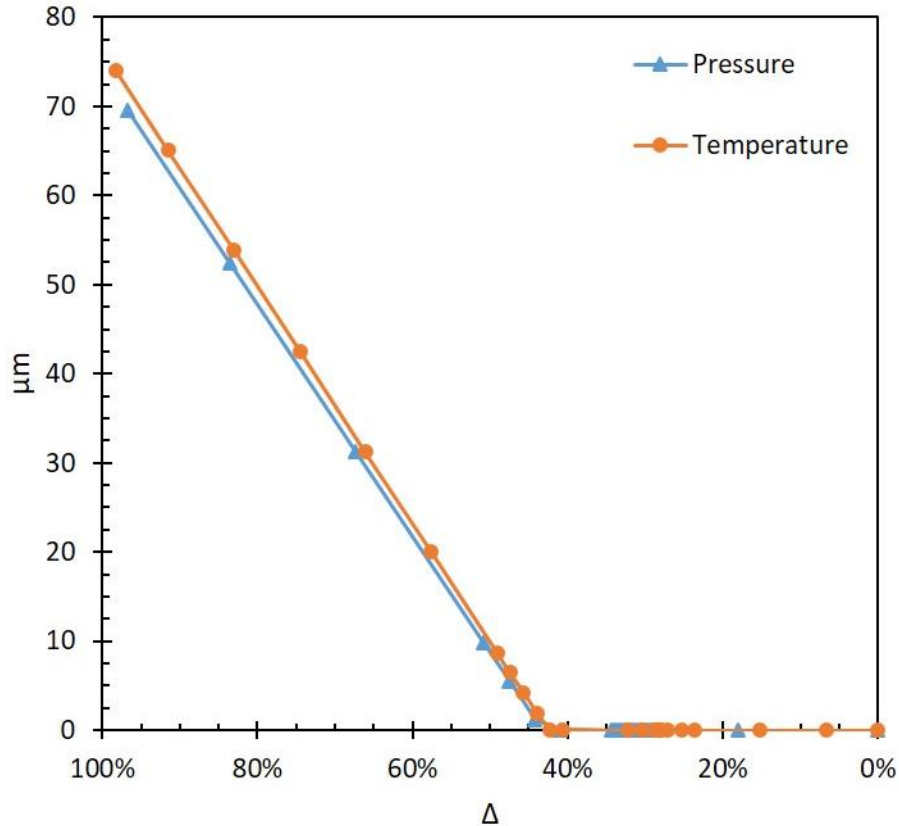


Figure 5.17: Microannuli magnitude versus reduction in pressure (ΔP) and temperature (ΔT) at the casing/cement interface. Micron (μm) sized microannuli initiate at $\Delta P = 43.3\%$ and $\Delta T = 42.5\%$.

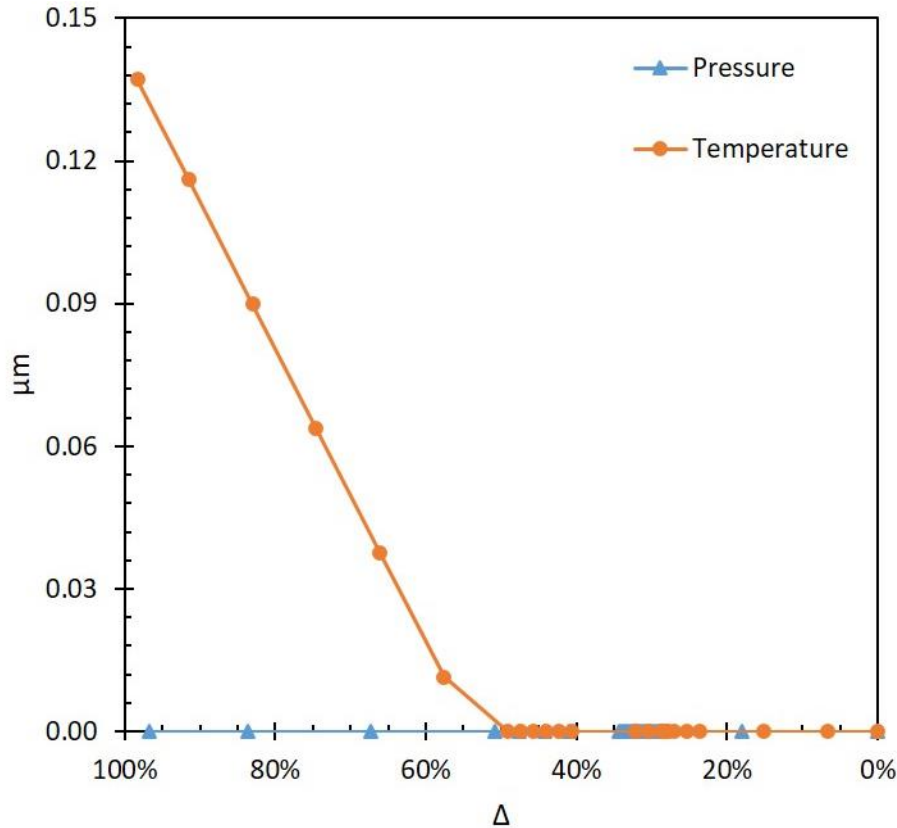


Figure 5.18: ΔP and ΔT and their respective microannuli sizes at the cement/rock interface. Note that the max size of the microannuli are two orders of magnitude smaller than the microannuli at the casing/cement interface.

The microannuli shown in Figure 5.17 first occur (>1 nm) when pressure and temperature have a reduction of 29.5% and 28.4% respectively for this wellbore. Performing a linear fit to the significant microannuli portion of the data can be used to determine the ΔP and ΔT that causes significant microannuli (>1 μm). This method determines that micron sized microannuli initiate at 43.3% and 42.5% for ΔP and ΔT , respectively. The change from nanometer to micron microannuli sizes is a decrease in load of approximately 14% for both pressure and temperature. The non-linearity of microannuli size versus load reduction is due to the traction separation law. The microannuli are initiated at $\Delta = 29\%$ but do not reach linearity until $\Delta = 43\%$. For the remainder of this work, the microannuli initiation threshold of micron sized microannuli will be used, but it is important to note that nanometer sized microannuli are occurring prior to this point. The

maximum microannuli for both $\Delta P = 0$ and $\Delta T = 0$ are 73.8 and 76.3 μm , respectively, as shown in Table 5.9. The slope of the temperature induced microannuli is steeper than the pressure induced microannuli curve indicating that ΔT has a slightly greater impact on microannuli magnitude versus ΔP . The results of the microannuli initiation are in agreement with Nygaard et al. (2014) and Gray et al. (2009) in which debonding occurs at the casing/cement interface whereas Zhang et al. (2017) and Crain et al. (2018) observed debonding at the cement/rock interface.

Table 5.9: Microannuli gap initiation reduction changes for ΔP and ΔT including nanometer (nm) gap and micrometer (μm) gap initiation Δ 's.

	Max Gap		
	nm gaps	μm gaps	(μm)
ΔP	29.5%	43.3%	73.8
ΔT	28.4%	42.5%	76.3

The results from Figure 5.18 indicate that debonding occurs at the cement/rock interface on the nanometer scale whereas Zhang et al. (2017) observed micron sized microannuli. Debonding of the cement to the casing is most likely due to the vast difference between the material stiffness (Young's modulus, E). The stiffness of casing is an order of magnitude larger than the stiffness of the cement whereas the stiffness of the rock formation is the same order of magnitude as the cement. Therefore, it is to be expected that debonding occurs at the casing/cement interface. The results from this paper are in agreement with experimental results from Vrålstad et al. (2015) and later expanded by De Andrade et al. (2016). The experiments consisted of thermal cycle tests on casing/cement/formation samples which were then scanned by CT. Their results show that cement sheath debonding occurs between the cement/casing interface when shale is the rock formation. Debonding between the cement/rock formation occurs when sandstone is the rock formation.

The magnitude of the microannuli at the casing/cement interface is in agreement with the reported value from Gray et al. (2009). Gray et al. (2009) reported a microannuli of 13.7 μm with a $\Delta P = 61\%$. From Figure 5.17, $\Delta P = 61\%$ results in a microannuli of 23.1 μm . The slight discrepancy between the results can be attributed to the difference in wellbore dimensions (311.15 mm [12.25"] hole size with 244.48 mm [9.625"] casing thickness versus 241.30 mm [9.5"] hole size with 193.68 mm [7.625"] casing thickness), simulated depths (1,920 m [6,300 ft.] versus 4,572 m [15,000 ft.]), and specific wellbore parameters.

5.5.2 Wellbore Parameter Sensitivity Analysis

The change in pressure and temperature (ΔP and ΔT) have been shown to cause microannuli gaps, but there are numerous parameters within a wellbore that can affect the magnitude and initiation of such gaps. The wellbore parameters are tested with different ΔP 's and ΔT 's to determine which parameters are contributing factors to microannuli initiation and magnitude. The Δ 's are a reduction in both pressure and temperature of 29%, 44%, 50%, and 67% based off of the curves shown in Figure 5.17. For a reduction of 29%, nanometer gaps were created from the base case curves and micron gaps were initiated at a 44% reduction. A reduction of 50% resulted in microannuli of approximately 10 μm . A reduction of 67% resulted in microannuli of approximately 30 μm . The results for all four percent reductions are shown in Figure 5.19 for ΔP and Figure 5.20 for ΔT for the maximum and minimum microannuli gap sizes. An individual analysis of each percent reduction for both ΔP and ΔT is discussed in the subsequent sections.

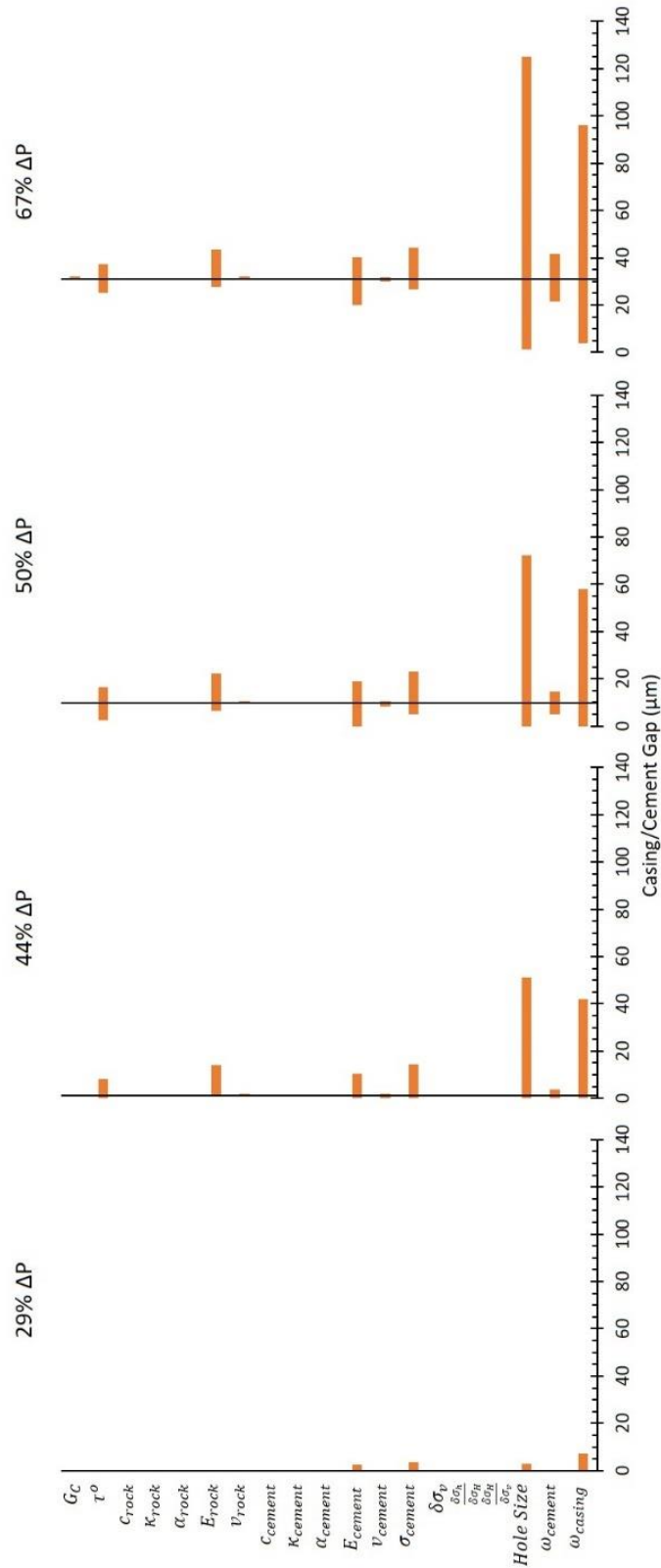


Figure 5.19: Parametric analysis of the maximum and minimum variables tested for change in wellbore pressures (ΔP) of 29%, 44%, 50%, and 67%. Variances in the hole size and casing thickness have the largest change in resulting gap magnitudes.

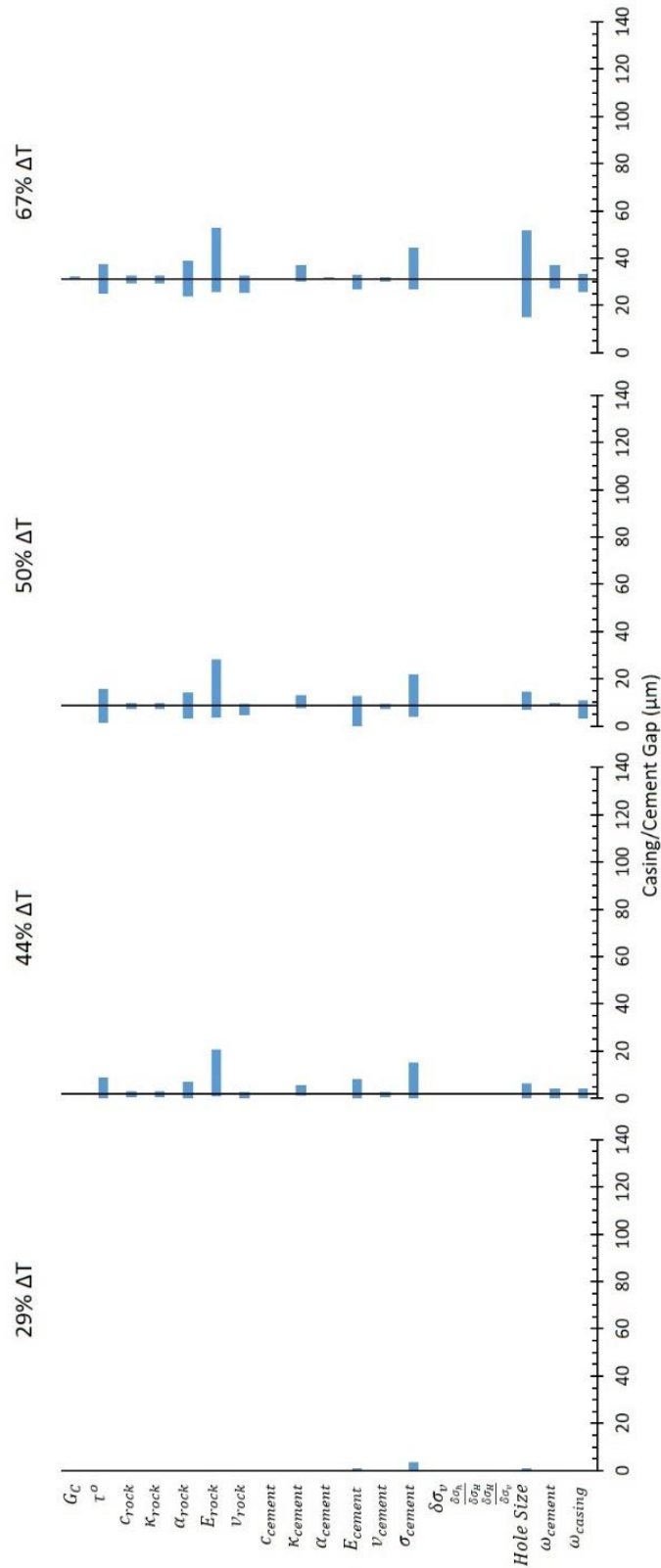


Figure 5.20: Parametric analysis of the maximum and minimum variables tested for change in wellbore temperatures (ΔT) of 29%, 44%, 50%, and 67%. None of the wellbore parameters change gap magnitude as significantly as hole size and casing thickness do for change in pressures (ΔP).

29% Reduction

For a reduction of 29%, nanometer sized gaps occur in the base well, but variations of E_{cement} , σ_{cement} , *Hole Size*, and ω_{casing} cause micron sized gaps to occur. It should be noted that only E_{cement} and σ_{cement} cause gaps to occur with ΔT while all four cause gaps to occur with ΔP . The microannuli range from a size of 0 μm (no gap/nanometer size gap) to a maximum gap of 7.2 μm implying that these four parameters can cause the gap initiation to decrease from 43% to 29% (i.e. lower ΔP and ΔT). The variations of the four parameters are shown in Table 5.10 along with their respective gap sizes. An interesting observation is that the change in hole size effects the gaps created by pressure and temperature inversely. A larger hole size results in gaps with a 29% ΔP while a smaller hole size results in gaps with a 29% ΔT .

Table 5.10: Gap magnitudes created by change in wellbore parameters for a 29% ΔP and ΔT . These parameters cause gaps to occur when the base case wellbore did not have gaps at 29% ΔP and ΔT .

Parameter	ΔP		ΔT	
	Parameter Change	Gap (μm)	Parameter Change	Gap (μm)
ω_{casing}	0.60	7.21		
σ_{cement}	1.21	3.71	1.21	3.50
<i>Hole Size</i>	1.40	2.73	0.60	0.90
E_{cement}	1.49	2.52	1.49	1.10

44% Reduction

The microannuli gaps for a 44% reduction in ΔP and ΔT range in size from 0 μm to 51.2 μm . For the base wellbore, ΔP resulted in a gap of 1.25 μm and variations of τ^o , E_{rock} , E_{cement} , v_{cement} , σ_{cement} , *Hole Size*, ω_{cement} , and ω_{casing} caused changes in the base gap width. For the base wellbore, ΔT resulted in a gap of 1.95 μm and variations in τ^o , c_{rock} , κ_{rock} , α_{rock} , E_{rock} , v_{rock} , E_{cement} , v_{cement} , σ_{cement} , *Hole Size*, ω_{cement} , and ω_{casing} all resulted in changes from the base gap. The reduction in temperature had variations in gap size due to more parameters than

ΔP , but ΔP resulted in larger magnitude of gaps; primary due to ω_{casing} and *Hole Size*. Both of these parameters had gaps larger than 25 μm . One observation with the 44% reduction is that many of the wellbore parameters could be altered such that the base gaps for ΔP and ΔT (1.25 μm and 1.95 μm respectively) can be reduced down to no gap (0 μm). These parameters are listed in Table 5.11. Another observation is that the same trend occurs with the 44% reduction as with the 29% reduction. The hole size variations have inverse effects on gap widths depending on ΔP or ΔT . A similar trend occurs for the casing thickness, except that thicker casings have smaller gaps for ΔP while thinner casings have smaller gaps for ΔT .

Table 5.11: Parameters that caused the microannuli gap magnitudes to be eliminated (0 μm) with a 44% ΔP and ΔT .

Parameter	ΔP Parameter Change	ΔT Parameter Change
<i>Hole Size</i>	0.60	1.20
ω_{casing}	1.40	0.60
σ_{cement}	0.93	0.93
E_{cement}	0.66	0.66
τ^o	1.40	1.40
ω_{cement}	1.20	0.80
ν_{cement}	1.33	
α_{rock}		0.60
ν_{rock}		0.74

50% Reduction

The microannuli gaps for a 50% reduction in ΔP and ΔT range from a size of 0 μm to 72.2 μm . For the base case with a reduction of 50%, ΔP resulted in a gap of 9.79 μm and ΔT resulted in a gap of 8.72 μm . Every parameter that caused variations in the base gaps with ΔP and ΔT at 44% reduction caused variations in gap widths with 50% reduction. As with the 44% reduction, ω_{casing} and *Hole Size* created large variations in the gap widths for ΔP . The variations due to ΔT are not as significant. With a reduction of 50% in ΔP and/or ΔT , three of the parameters can be

altered such that the base case gap can be reduced down to no gap (0 μm). The parameters that can be altered such that there is not a gap are ω_{casing} , *Hole Size*, and E_{cement} . All three parameters can eliminate the gap for ΔP , but only E_{cement} significantly reduced the gap for ΔT (0.1 μm).

67% Reduction

The microannuli gaps for a 67% reduction in ΔP and ΔT range in size from 1.3 μm to 125.2 μm . For the base case with a reduction of 67%, ΔP resulted in a gap of 31.13 μm and ΔT resulted in a gap of 31.25 μm . Similar to the 50% and 44% reduction, ω_{casing} and *Hole Size* have the largest variation in gap width for ΔP . The largest gap variation for ΔT is the change in hole size with a range of 36.9 μm whereas the largest gap variation for ΔP is change in hole size with a range of 123.9 μm . The change in *Hole Size* did not have a major effect with respect to microannuli gap sizes with respect to ΔT with the 29%, 44%, and 50% reductions, but the *Hole Size* has a major effect with a 67% reduction most likely due to the softening traction-separation law. The 67% reduction in ΔT exceeded the threshold required to initiate significant microannuli gap growth with *Hole Size* variations whereas lesser temperature reductions did not. Based on the results from the 67% ΔP and ΔT reduction, changes in pressure with respect to wellbore parameters are more critical than changes in temperature.

The results of the parametric analysis are sorted based off their percent change of the maximum gap width (%MGW) from the base microannuli gap as shown in Table 5.12 in terms of 1st, 2nd, and 3rd Order Parameters. 3rd Order Parameters are defined as parameters with their %MGW less than 10%. 3rd Order Parameters have little to no effect on the development of the gap magnitude and therefore are not critical inputs into the well life cycle model. 2nd Order Parameters are defined as parameters with their %MGW larger than 10% but less than 100%. These parameters have some effect on the gap with magnitude, but are not critical. Finally, 1st Order Parameters are

defined as parameters that have their %MGW larger than 100%. These input parameters (*Hole Size* and ω_{casing}) have the largest impact on the gap width development. It is important to note that only reductions in pressure (ΔP) have 1st Order Parameters. Reductions in temperature (ΔT) have 2nd and 3rd Order Parameters and therefore do not have a large impact on gap width development when compared to ΔP .

Table 5.12: Wellbore parameters sorted based off their percent change of the maximum gap width (%MGW) from the base gap magnitude. 1st Order Parameters are critical in the development of the gap width magnitude at the casing/cement interface. 2nd Order Parameters have minor effect, and 3rd Order Parameters have little to no effect on the development of the gap widths.

	ΔP	%MGW	ΔT	%MGW
1 st Order Parameters	<i>Hole Size</i>	302%		
	ω_{casing}	208%		
2 nd Order Parameters	σ_{cement}	42%	E_{rock}	69%
	E_{rock}	40%	<i>Hole Size</i>	66%
	ω_{cement}	34%	σ_{cement}	42%
	E_{cement}	29%	α_{rock}	24%
	τ^o	20%	τ^o	20%
			ω_{cement}	19%
3 rd Order Parameters			κ_{cement}	18%
	G_C	3%	ω_{casing}	7%
	ν_{rock}	3%	E_{cement}	6%
	ν_{cement}	2%	C_{rock}	5%
	α_{rock}	0%	κ_{rock}	5%
	$\delta\sigma_V$	0%	ν_{rock}	4%
	α_{cement}	0%	G_C	3%
	κ_{cement}	0%	ν_{cement}	2%
	C_{cement}	0%	α_{cement}	2%
	κ_{rock}	0%	C_{cement}	0%
	C_{rock}	0%	$\delta\sigma_V$	0%
	$\delta\sigma_H$	0%	$\delta\sigma_H$	0%
	$\overline{\delta\sigma_V}$		$\overline{\delta\sigma_V}$	
	$\overline{\delta\sigma_h}$	0%	$\overline{\delta\sigma_h}$	0%
	$\overline{\delta\sigma_H}$		$\overline{\delta\sigma_H}$	

5.5.3 Microannuli Prediction

Using the analyses from the previous section, the microannuli gaps at the casing/cement interface are primarily a function of ΔP , ΔT , ω_{casing} , and *Hole Size*. For the purpose of determining if wells are intact and able to provide zonal isolation, the history of pressure and temperatures should be investigated. If the casing/cement interface experiences debonding at one point in the life cycle of a well, the bond is not going to “heal” and provide zonal isolation (Stormont et al. 2018). Figures 5.21-5.24 depict the casing/cement interface gap when changing the pressure and temperature for the case study at four depths (1,920 m [6,300 ft.], 1,595 m [5,233 ft.], 1,270 m [4,167 ft.], and 945 m [3,100 ft.]) along the primary cement barrier (i.e. intermediate casing string). The results of Figures 5.21-5.24 show that when both pressure and temperature are reduced in the wellbore, the gap magnitude increases.

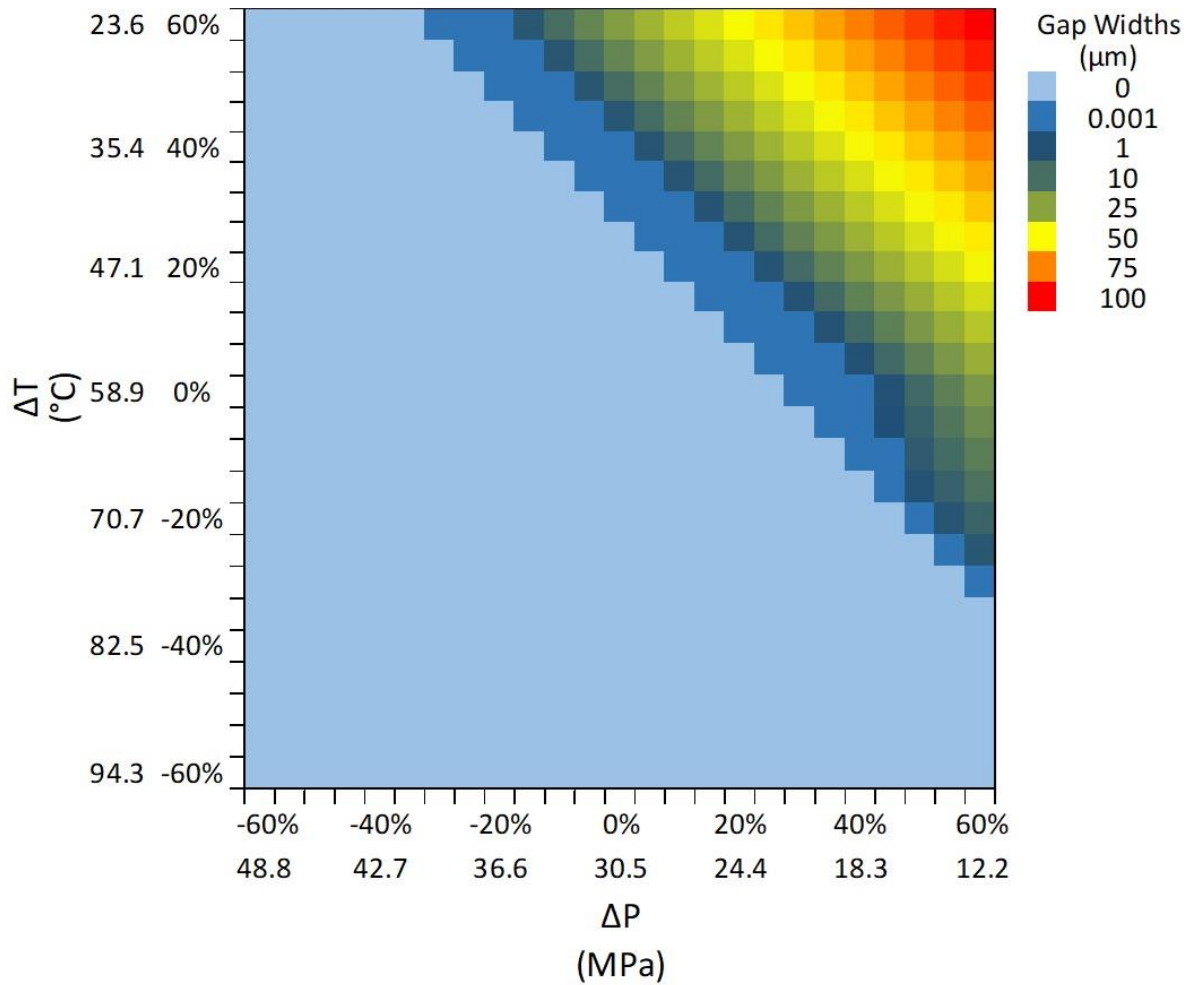


Figure 5.21: Heat map showing the gap magnitudes resulting from a combination of ΔP and ΔT . A positive Δ indicates a reduction while a negative Δ is an increase. Note in the legend that nanometer (nm) sized gaps are indicated (0.001 μm) along with micron (μm) sized gaps. The results of this heat map are indicative of a 31.12 cm (12.25”) hole size with 24.45 cm (9.625”) P-110EC casing at a depth of 1,920 m (6,300 ft.).

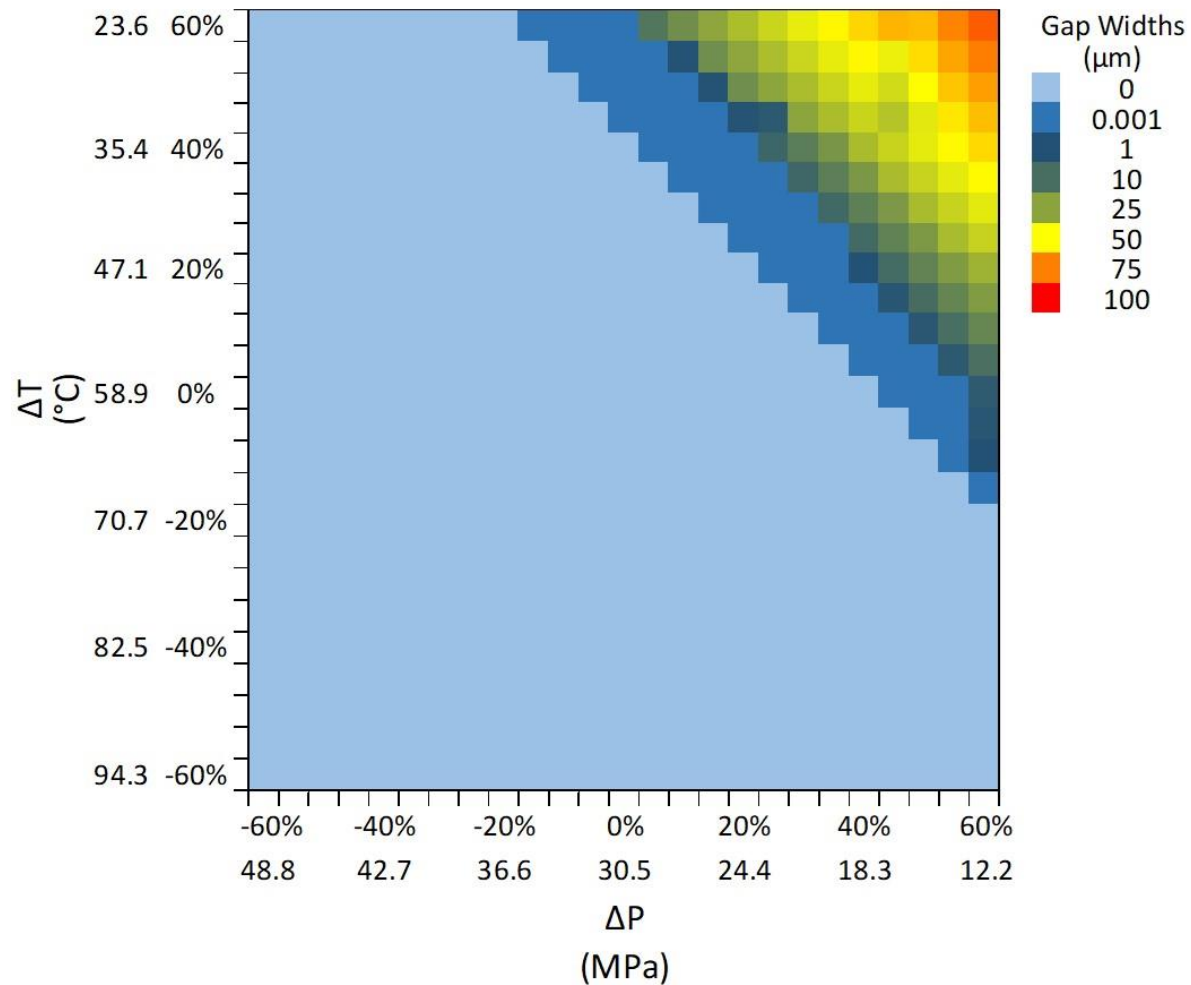


Figure 5.22: Heat map showing the gap magnitudes resulting from a combination of ΔP and ΔT . A positive Δ indicates a reduction while a negative Δ is an increase. Note in the legend that nanometer (nm) sized gaps are indicated (0.001 μm) along with micron (μm) sized gaps. The results of this heat map are indicative of a 31.12 cm (12.25") hole size with 24.45 cm (9.625") P-110EC casing at a depth of 1,595 m (5,233 ft.).

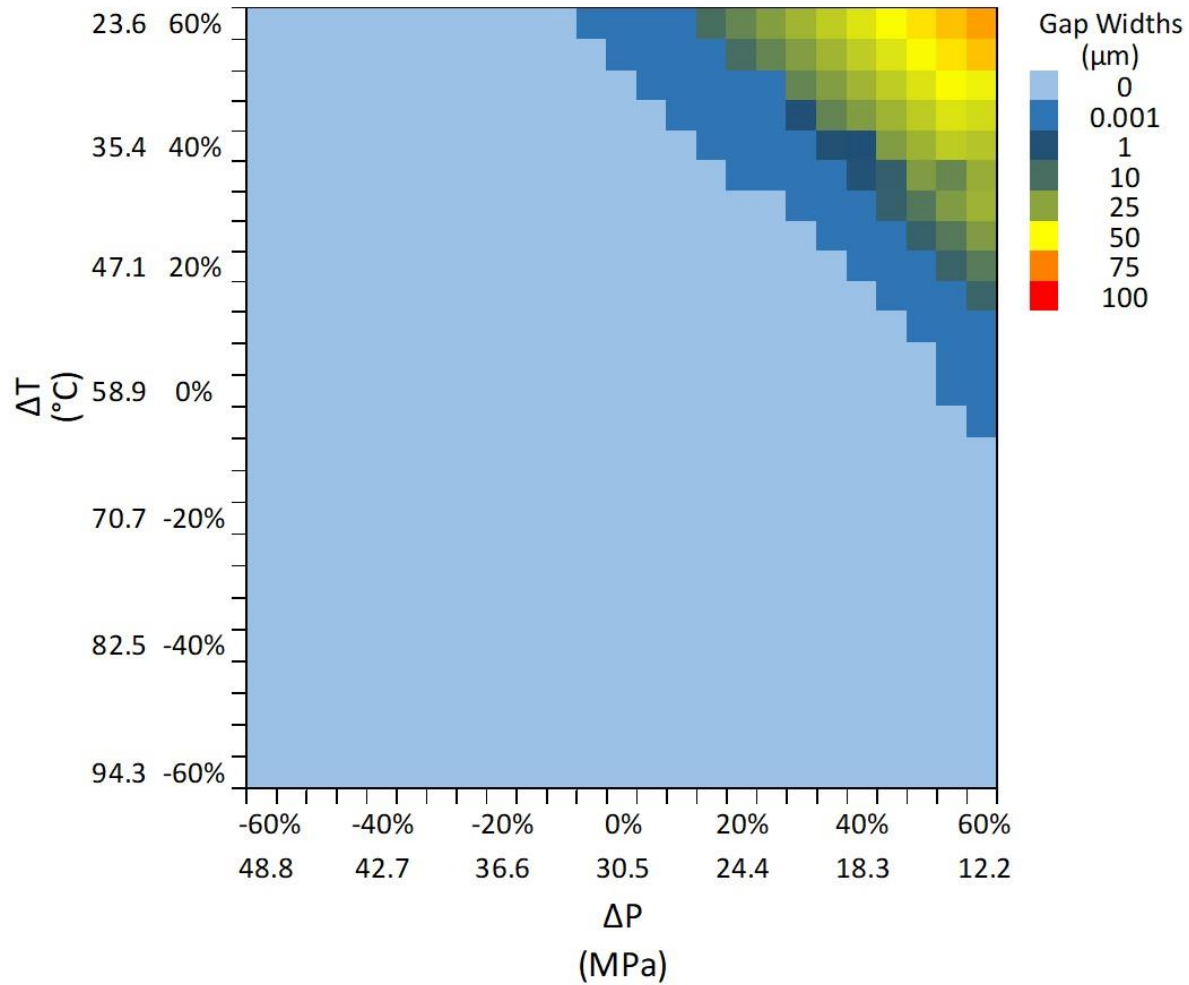


Figure 5.23: Heat map showing the gap magnitudes resulting from a combination of ΔP and ΔT . A positive Δ indicates a reduction while a negative Δ is an increase. Note in the legend that nanometer (nm) sized gaps are indicated (0.001 μm) along with micron (μm) sized gaps. The results of this heat map are indicative of a 31.12 cm (12.25") hole size with 24.45 cm (9.625") P-110EC casing at a depth of 1,270 m (4,167 ft.).

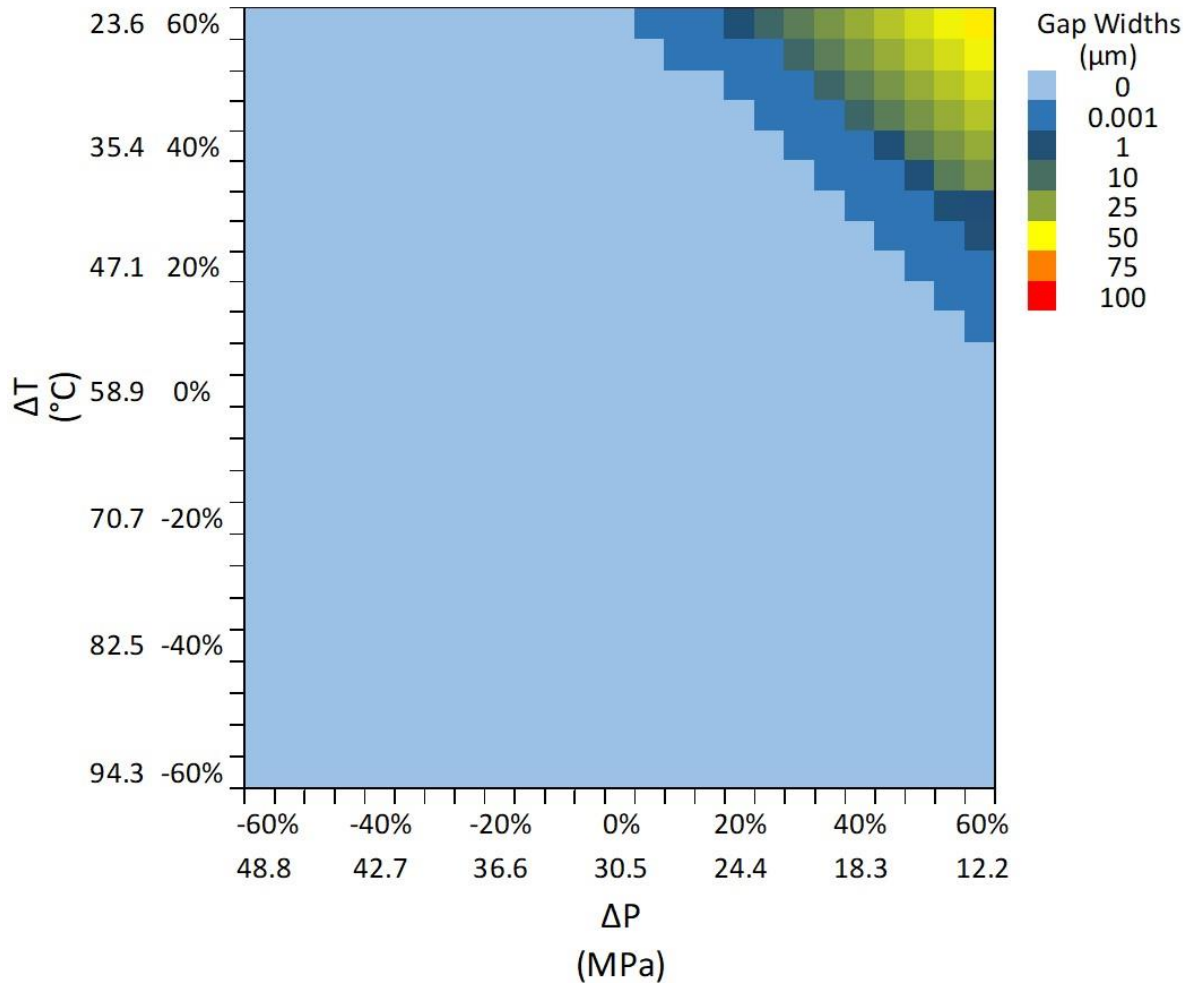


Figure 5.24: Heat map showing the gap magnitudes resulting from a combination of ΔP and ΔT . A positive Δ indicates a reduction while a negative Δ is an increase. Note in the legend that nanometer (nm) sized gaps are indicated (0.001 μm) along with micron (μm) sized gaps. The results of this heat map are indicative of a 31.12 cm (12.25”) hole size with 24.45 cm (9.625”) P-110EC casing at a depth of 945 m (3,100 ft.).

The maximum gap magnitude caused by only a reduction of pressure or only a reduction of temperature is 73.8 μm and 76.3 μm , respectively as shown previously. However, Figure 5.21 shows that a reduction of pressure can be offset by an increase in temperature and vice versa. A pressure reduction of 60% ($\Delta P = 60\%$) and an increase in temperature of 60% ($\Delta T = -60\%$) results in zero gap width whereas a reduction of only pressure or temperature of 60% results in gaps as shown in Figure 5.17. It should be noted that the pressure and temperature curves are not symmetric in Figure 5.21 as shown by the micron sized gaps occurring due to pressure reduction of 60% ($\Delta P = 60\%$) and a temperature increase of 25% ($\Delta T = -25\%$) while a temperature reduction

of 60% ($\Delta T = 60\%$) and a pressure increase of 15% ($\Delta P = 15\%$) develops micron sized gaps. This phenomenon is explained by the individual pressure and temperature curves in Figure 5.17. The individual curves do not overlap exactly and therefore this asymmetry is shown in Figure 5.21. It is important to note that the apparent symmetry shown for other combinations of ΔP and ΔT is due to the legend scale resolution.

5.5.4 Leakage Pathway to Top of Cement Depth

The microannuli gaps at various depths with concurrent changes in pressure and temperature were discussed in Section 5.5.3, but how does the microannuli propagate if it occurs at the simulation depth? Figure 5.25 shows the results of the microannuli propagating up the wellbore to the top of cement (TOC) depth with the blue line representing water induces microannuli propagation and the orange line representing gas fracture propagation at the cement/casing interface.

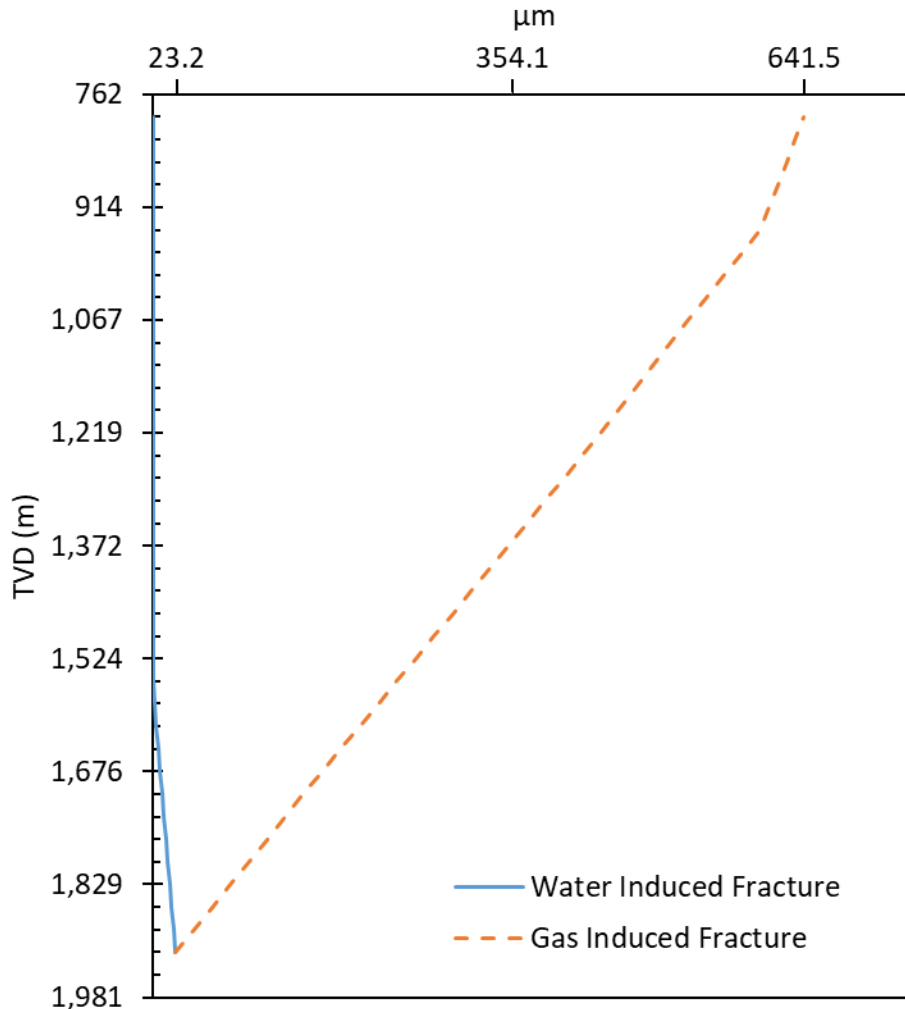


Figure 5.25: Cement/casing interface microannuli size from the simulation depth to the top of cement (TOC) depth for pore pressure induced (water) microannuli (fracture) and gas induced microannuli (fracture). The water induced microannuli propagates up the wellbore for 365 m before it does not form. The gas induced microannuli propagates up the entire cement sheath to the TOC depth.

The water induced microannuli propagate up the wellbore from the simulation depth of 1,920 m (6,300 ft.) with a microannuli size of 23.2 µm to no microannuli forming at a depth of 1,555 m (5,100 ft.) Assuming only water in the microannuli does not provide a complete leakage pathway to the TOC. The gas migration induced microannuli propagate up the wellbore from the simulation depth with an initial magnitude of 23.2 µm to the TOC depth with a magnitude of 641.5 µm. Gas does not lose hydrostatic pressure as quick as water due to the difference in density. Therefore, if the wellbore provides an initial path for gas to travel (as happens with a ΔP of 40%),

the gas has a larger magnitude than the pore pressure at the corresponding depths. The increased pressure is able to propagate the microannuli and increases as the depth gets shallower.

The resulting microannuli from the FEA model shows significant difference than the methods shown in the literature. Ford et al. (2017), Moeinikia et al. (2018), and Al Ramadan et al. (2019) all assume a constant microannuli while Lavrov and Torsaeter (2018) assume an average microannuli with tortuosity. To visually compare the three methods (FEA, constant, and tortuosity), the microannuli predicted from the FEA model at the simulation depth is used for the constant microannuli model and the tortuosity model, which is 23.2 μm . The constant microannuli will stay constant from the simulation depth to the TOC depth. For the tortuosity method, the FEA predicted microannuli at the simulation depth will be used with a 20% standard deviation, which is 4.64 μm . The results for the microannuli magnitude of the three methods is shown in Figure 5.26. To show the effect of the fracture volume between the methods, the next section incorporates the developed flow equations with the three methods and compares the corresponding leakage flow rates.

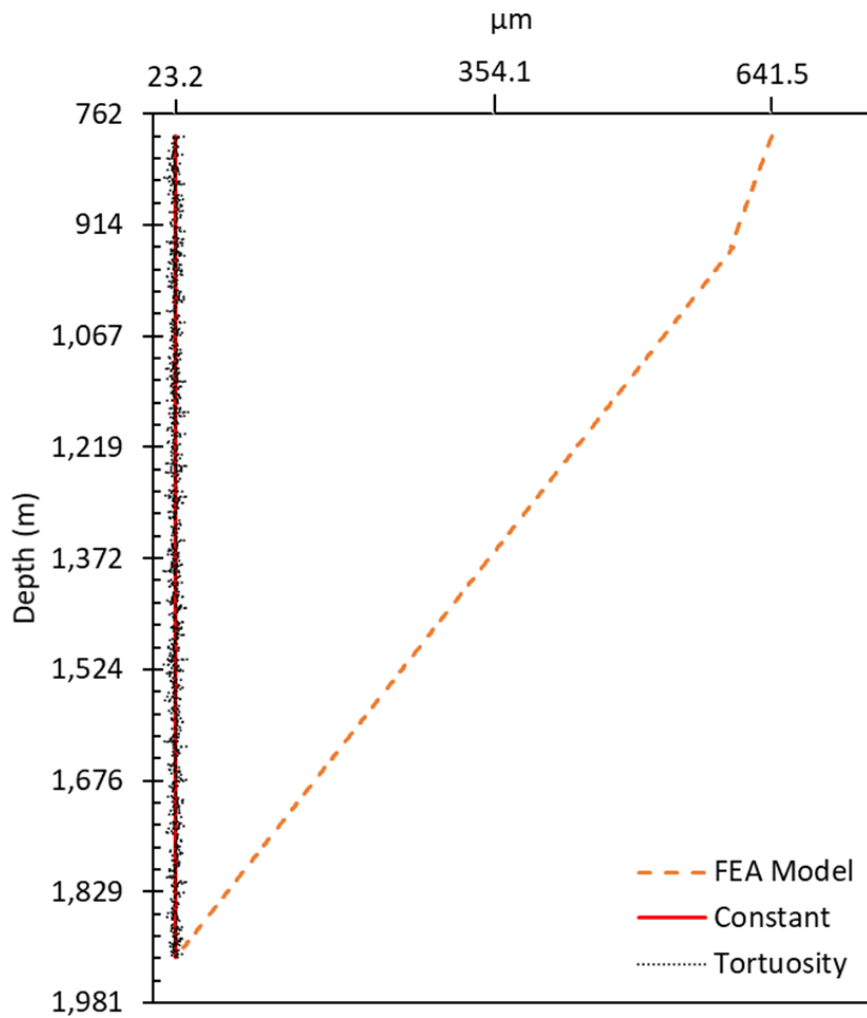


Figure 5.26: Microannuli width (w) with respect to depth for the FEA model (orange long dash), a constant microannuli (red solid line), and a microannuli with tortuosity (gray short dash). The FEA model microannuli starts off at 23.2 μm and ends at 641.5 μm . The constant microannuli method stays at 23.2 μm from the simulation depth to TOC. The tortuosity method has an average microannuli of 23.2 μm with a Gaussian distribution of 4.64 μm standard deviation.

5.5.5 Leakage Rate Assessment

The leakage rate for the three leakage path methods (FEA model, constant gap, and tortuosity gap) are analyzed for an ideal gas (methane without compressibility) and a real gas (methane including compressibility).

Table 5.13: Comparison of the three flow paths for the volume of the leakage path for an ideal and real gas with and without the effect of gravity. The constant gap method produces the largest flow rate while the FEA gap method produces the smallest flow rate.

Fluid	Leakage Pathway Method	Q (m ³ /s)	Q (m ³ /day)
Ideal MH ₃ Gas	Constant Gap	6.67E-08	5.77E-03
	Constant Gap + Gravity	8.16E-09	7.05E-04
	Tortuosity Gap	5.28E-08	4.56E-03
	Tortuosity Gap + Gravity	6.46E-09	5.58E-04
	FEA Gap	4.09E-06	3.53E-01
	FEA Gap + Gravity	5.00E-07	4.32E-02
Real MH ₃ Gas	Constant Gap	6.61E-08	5.71E-03
	Constant Gap + Gravity	7.49E-09	6.47E-04
	Tortuosity Gap	5.23E-08	4.52E-03
	Tortuosity Gap + Gravity	5.93E-09	5.12E-04
	FEA Gap	4.04E-06	3.49E-01
	FEA Gap + Gravity	4.58E-07	3.96E-02

Investigating the three fracture methodologies (FEA, constant, and tortuosity) show that assuming a constant microannuli results in the smallest flow rate whereas the FEA predicted microannuli results in the largest flow rate for both an ideal and real gas. The FEA predicted fracture volume is larger than assuming the microannuli remains constant from the simulation depth to TOC. Including tortuosity in the fracture path decreases the flow rate from assuming a constant microannuli. This result is in agreement with Corina et al. (2020) in which the authors state that tortuosity decreases flow rate. However as shown by Lavrov and Torsaeter (2018), the degree of tortuosity (standard deviation in this case) can affect the flow rate dramatically. The result from the methodologies shows that just assuming a constant microannuli value can underestimate gas leakage rates, even if the assumed value is an average from a justified source (lab experiments or numerical simulations).

From Table 5.13, the percent difference between an ideal gas and a real gas is 1.0% for the constant gap, tortuosity gap, and FEA predicted gap. This result shows that when not accounting for gravity, the difference between a real gas and ideal gas is minor. Yet when the effect of gravity

is included in the leakage rate, all three methods have a percent difference of 8.6%. The difference of 8.6% for this well is not minor which indicates that not including compressibility of the gas and excluding the effect of gravity can overestimate gas leakage rates.

Analyzing the potential leakage rates of the case study well using the methodologies presented in the literature (water leakage, gas leakage, constant microannuli gap, and tortuosity gap) is shown in Table 5.14.

Table 5.14: Comparison of the literature methods for calculating cumulative leakage for the case study well in comparison with the method presented in this work. The effect of using the FEA predicted microannuli along with analyzing a real gas with the effect of gravity reduces the total flow rate from the case study well.

Fluid	Leakage Pathway Method	Q (m ³ /day)	Reference
Water	Constant Gap	2.54E-04	Ford et al. (2017) Moeinikia et al. (2018)
Water	Tortuosity Gap	2.01E-04	Lavrov and Torsaeter (2018)
Ideal Gas	Constant Gap	5.77E-03	Al Ramadan et al. (2019)
Real Gas + Gravity	FEA Gap	3.96E-02	

For the conditions and assumptions of the case study well, the methodology of Ford et al. (2017) and Moeinikia et al. (2018) would have predicted a leakage rate of 2.54E-04 m³/day for water with a constant microannuli gap. Lavrov and Torsaeter’s (2018) water tortuosity method would predict a lower leakage rate of 2.01E-04 m³/day. Al Ramadan et al.’s (2019) ideal gas leakage with a constant gap would predict a higher leakage rate of 5.77E-03 m³/day. The method presented in this work shows that using a realistic microannuli geometry with respect to depth, accounting for gas as the leaking fluid, and including the effect of gravity results in a leakage rate of 3.96E-02 m³/day. From the results in Table 5.14, the methods presented in the literature of using water or an ideal gas as a leaking fluid, neglecting the effect of gravity, and not including realistic microannuli geometry underestimate the potential cement sheath leakage of the case study well.

Chapter 6: Discussions

The four main results presented in Chapter 5 are discussed in this chapter. First, is the effect of modeling the leaking fluid as a water versus a gas. Second, is the effect cement shrinkage has on cement sheath integrity. Third, is the effect of including in-situ confining stresses when modeling cement sheaths. Finally, the effect of including the shear failure and traction separation law in the FEA models is addressed.

Effect of Modeling Gas versus Water

Modeling leakage by assuming water as the leaking fluid has become standard in the industry, but is this method accurate? Researchers have performed experiments that replicated water leakage through cemented annuli (Aas et al. 2016). Performing numerical analysis of the experiments is valid since the experiments used water. But assuming water for all leakage simulations is not accurate due to the following evidence. The driving force for wellbore leakage is the difference in pressure from the reservoir and the hydrostatic gradient. For a liquid (water, oil, etc.), the difference can quickly dissipate due to the effect of gravity. Table 5.1 shows that Hagen-Poiseuille flow of water with gravity results in zero flow. Zero flow indicates that the pressure differential and the hydrostatic head of the water column cancel out. This analysis also presents another conclusion: previous work (Ford et al. 2017; Lavrov and Torsaeter 2018; Al Ramadan et al. 2019) focus on flow rates when it should consider pressure differential. Pressure differentials drive the fluid (water, oil, methane, nitrogen, etc.) causing leakage. Flow rates are a result of pressure differentials.

With a gas as the leaking fluid, the density is much lower causing the pressure loss to become much lower. Because the hydrostatic gradient stays the same, the driving pressure of the gas will easily displace the pore pressure fluid as shown in Figure 4.11. Even the assumption of

neglecting the effect on gravity results in gas having a much higher leakage rate than water as shown in Table 5.1.

For a wellbore that has a microannuli path from the simulation depth to the top of cement, the geometry of the microannuli affects the leakage rate. Assuming an average microannuli produces a smaller leakage rate than the FEA predicted microannuli (Table 5.13). Combining the FEA predicted microannuli with gas as the leaking fluid results in a larger leakage rate than assuming a constant microannuli with water neglecting gravity. The leakage rates of the case study well predicted by the methods of Ford et al. (2017), Lavrov and Torsaeter (2018), Moeinikia et al. (2018), and Al Ramadan et al. (2019) all underestimated the leakage rate by orders of magnitudes. Therefore, leakage models that yield an accurate prediction of the microannuli should include the effect of gravity, and represent a real gas.

Effect of Shrinkage

The effect of cement shrinkage on wellbore cement sheath integrity is currently not included as a primary leakage pathway. Cement shrinkage was shown numerically to occur when analyzing fluid flow through cement sheath experiments from Aas et al. (2016). The shrinkage was determined to be between 1.0-1.4% for the conventional cement. From the experiments performed by Corina et al. (2019), the authors determined that shrinkage was occurring in their cement mixture that did not have the expanding agent (samples SF120 and SF66), without quantifying the shrinkage percent. Assuming the microannuli of the expanding agent samples (SF120EA) is purely hydraulically induced, the average microannuli can be subtracted from the average microannuli of the SF120 samples to determine the shrinkage induced microannuli. The difference in the average microannuli of SF120 and SF120EA is 13.5 μm . Using the equations for uniform shrinkage (Equations 4.49, 4.50, and 4.51), the sample SF120 experienced 0.13%

shrinkage. The shrinkage experienced in the samples, 0.13%, appears to be negligible, but provided a continuous leakage pathway at the cement interface even though the system was cured at an elevated pressure and temperature.

The shrinkage values from the Corina et al. (2019) and Aas et al. (2016) experiments do not appear to be very significant given that they are 0.13% and 1.4% respectively. Extrapolating these shrinkage values for the wellbore cement sheath dimensions for the case study well (casing OD = 0.2445 m and casing ID = 0.2168 m), the resulting microannuli is 9.5 μm for 0.13% shrinkage and 102.4 μm for 1.4% shrinkage. Consequently, even minuscule cement shrinkage values can result in microannuli that can provide a leakage pathway. Therefore, cement shrinkage should be included as a primary failure mechanism of wellbores and included in wellbore integrity risk analysis. Cement shrinkage preventative additives are critical in maintaining wellbore integrity.

Effect of Confinement

Using FEA to model wellbore cement to predict potential failure behavior has many benefits in that it is quick and cheap to produce accurate stress responses. However, accurately modeling cement needs to include all the parameters to replicate downhole conditions. Downhole pressures and temperatures play a factor in cement stress, but the results from Chapter 5 show that confining stress plays a factor too. The effect of confining stress on cement elements in the FEA models is shown by examining the models presented in Section 5.2.3 and Section 5.3. Cement mechanical properties were varied in three FEA models shown in this work: the FEA fluid rheology model (Section 5.2.3; P&A model), the fracture model in Section 5.3 (medium well), and the fracture model in Section 5.5 (case study well). The P&A model varied the cement mechanical properties by $\pm 75\%$. The medium well model varied the properties by $\pm 40\%$. The case study well

model varied the mechanical properties based on the developed cement database ($34\% \leq E \leq 149\%$; $17\% \leq PR \leq 133\%$). The resulting percent change (% Change) in reference to the microannuli gap is shown in Figure 6.1 for the cement Young's modulus (E) and in Figure 6.2 for the cement Poisson's ratio (PR).

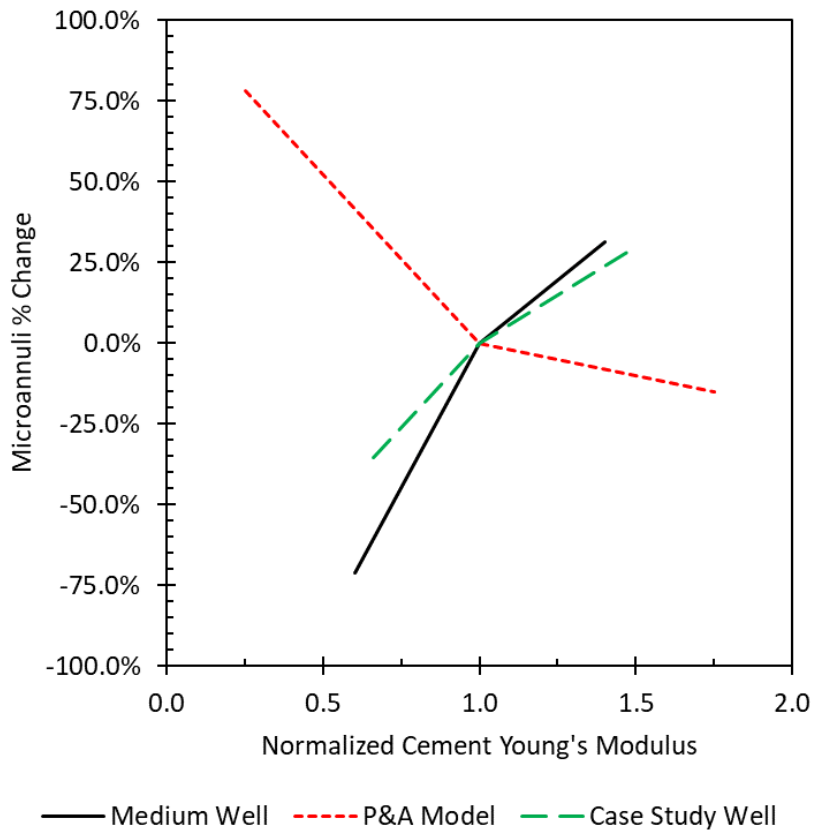


Figure 6.1: Sensitivity plot for normalized cement Young's modulus (E) versus the percent change in microannuli gap width. Medium well (Section 4.3) and case study well (Section 4.5) have confining stresses while P&A model (Section 4.2.3) has no confinement. The model confinement reverse the effect Young's modulus has on gap width.

As shown in Figure 6.1, E has various effects on the microannuli gap width depending on the model. For the P&A model, a decrease in E causes an increase in microannuli width while an increase in E causes a decrease in microannuli width. This effect is opposite for the medium well and the case study well. The difference between the P&A model and the two wellbores is confinement on the model. The P&A model does not have in-situ stresses whereas the two wellbores

models have rock in-situ stresses. This result shows that the cement mechanical properties has inverse effects depending on boundary conditions of the cement being modeled. However, even varying E by $\pm 75\%$ (in the P&A model), the change in microannuli gap width does not change from open to close.

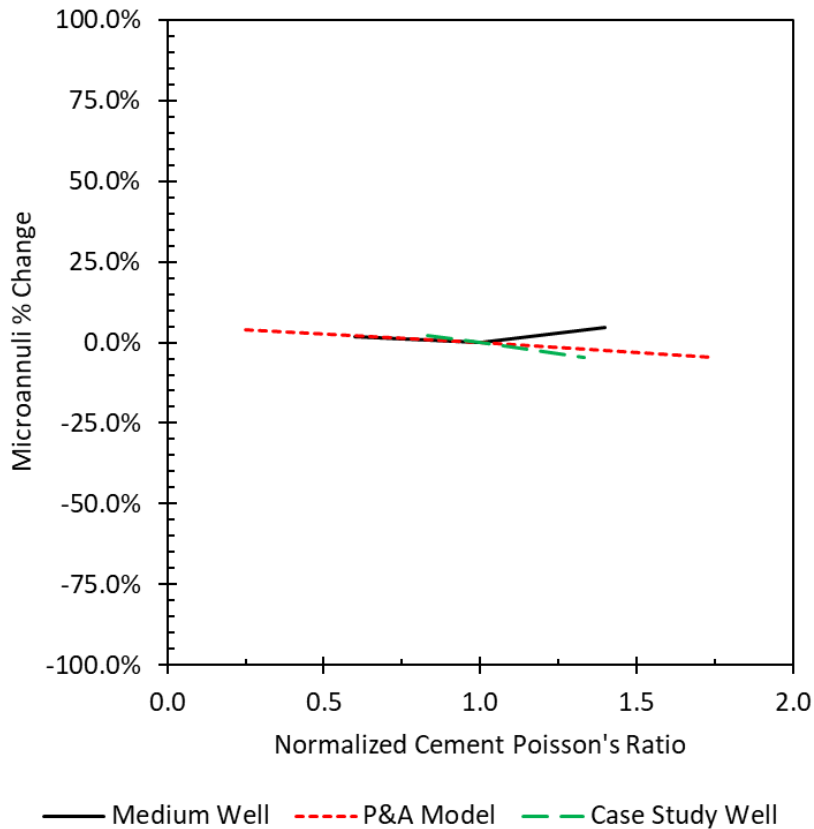


Figure 6.2: Sensitivity plot for normalized cement Poisson's ratio (PR) versus the percent change in microannuli gap width. The medium well (Section 4.3) and case study well (Section 4.5) have confining stresses while the P&A model (Section 4.2.3) has no confinement. The cement Poisson's ratio has less than 5% effect on the microannuli gap with and without confinement.

From Figure 6.2, the PR does not have as much of an effect as variation in E . E has a maximum and minimum effect of 75% whereas PR has a maximum and minimum effect of 5%. A conclusion from the sensitivity analysis for the cement mechanical properties shows that changing the values of E and PR does not change the integrity of the cement sheath(i.e. if a microannuli gap is present, changing the mechanical properties does not prevent it from forming). As shown in Table 5.12, altering the bond strength between the cement and steel casing cause a

20% change on the resulting microannuli. The effect of confining stress on wellbore cements show that cement additives used to enhance the compressive strength, tensile bond strength, and elasticity of wellbore cements tend to have miniscule effect on maintaining cement sheath integrity.

Effect of Traction Separation Law

Debonding of the cement sheath failure was shown to be the primary failure mechanism in wellbores from performing simulations with the staged poro-elastic FEA stress continuum model. Shear failure, diskings, and radial cracks were shown to not be a concern for confined cement sheaths. From Figures 5.8 and 5.9, the Mohr circles for the cement sheath interfaces show that tensile bond failure will occur before Mohr-Coulomb shear failure and radial cracking in the cement. To understand tensile bond failure (debonding) more accurately, the traction separation law was incorporated into the staged FEA models (staged poro-elastic FEA fracture model) to replicate cement sheath debonding. The two main differences between the stress continuum and fracture model are: the fracture model includes the traction separation law whereas the stress continuum model does not allow the different materials (casing, cement, and formation) to separate. The second difference is that the fracture model explicitly incorporates pore pressure in the cement and rock formation elements whereas the stress continuum model incorporates pore pressure in the post analysis. The difference in the models is shown in in Table 5.8. For the medium well, the stress continuum model predicts cement debonding at the casing/cement and cement/rock formation interface whereas the fracture model predicts debonding at the casing/cement interface. A similar trend is shown in the deep well. The stress continuum model predicts debonding at the casing/cement interface, but the fracture model does not. Not including failure criteria explicitly within the model, such as Bois et al. (2017), Vu et al. (2018), and Bois et al. (2019), can result is

exaggerated failure prediction in the model. Bois et al. (2019) (and all the previous models from their work) simulate their FEA well lifecycle models as decoupled system response curves that have a zero traction separation failure criteria. That means, that if the effective radial stress at the cement interface is tensile, a microannuli is forming. Table 5.8 shows that just because the cement sheath interface has tensile stress, a microannuli is not necessarily forming due to the mechanics of the traction separation law. Therefore, to accurately replicate wellbore cement sheath integrity, explicit poro-elastic FEA models with the traction separation law should be performed. The fracture model represents a more realistic wellbore scenario since it incorporates the non-linearity of fracture mechanics explicitly within the model.

An observation from Table 5.8 is that the effective stress of the medium well at the casing/cement interface in the fracture model is -0.40 MPa resulting in a microannuli gap width of 13.6 μm . As recalled from Table 4.3, the tensile bond strength of the casing/cement bond is 0.50 MPa. Remembering the traction separation law from Section 2.3.1, microannuli start to form when the tensile bond strength is reached. So for a microannuli gap to occur in the medium well, the tensile bond strength was reached. Since a microannuli is present, following the traction triangle (Figure 2.9; Figure 2.10), the stress at the bond is decreasing until the complete separation distance (δ_f) is reached. This separation distance is 400 μm ($\delta_f = 400 \mu\text{m}$) given the parameters used for the traction separation law described in Section 4.3. Therefore, we know that the casing/cement bond is in the plastic region meaning that permanent damage is occurring, but the bond is not completely separated. Since the bond is not completely separated, methods that replicate fluid penetration, such as the Reynold's Lubrication Theorem in Section 2.10, are not able to model fluid leakage.

Implications of Wellbore Leakage in the Gulf of Mexico

The results of this dissertation show that a flow chart can be developed to determine if a wellbore is at risk for leakage. The flowchart is shown in Figure 6.3.

Wellbore Leakage Flow Chart

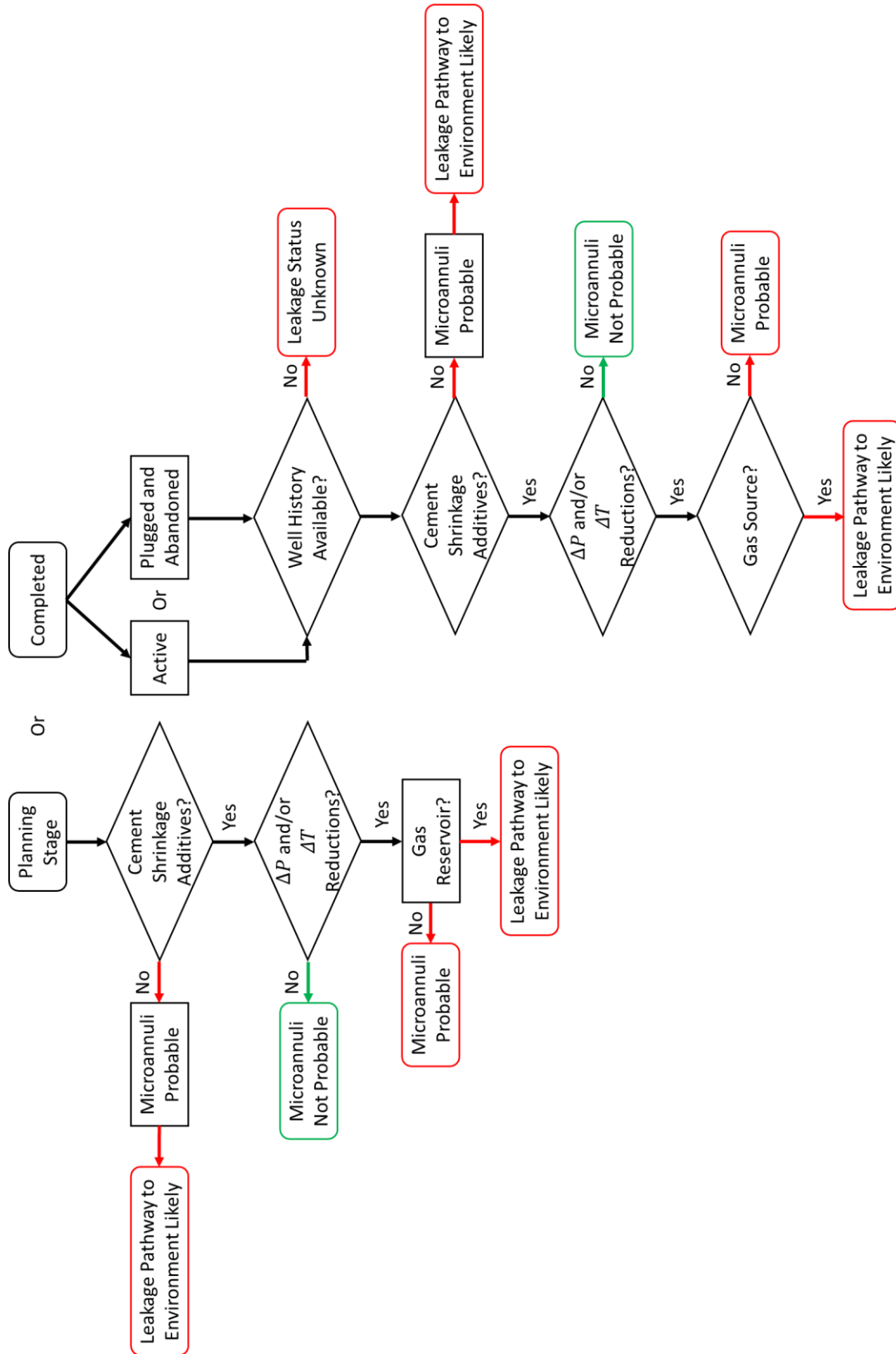


Figure 6.3: Flow chart for identifying if a well is at risk for microannuli and for leakage pathways to the environment based on cement shrinkage, reductions of pressure and/or temperature, and a gas source. The flow chart can either be used for wellbores in the planning stage or previously completed.

To predict if a wellbore will be experiencing leakage, two scenarios of the wellbore leakage flow chart exist: wellbores are either in the planning stage or they were previously completed. For wellbores in the planning stage, cement shrinkage additives are critical in preventing microannuli from forming. If shrinkage preventative additives are not included, microannuli are likely to form causing a pathway for leakage. If additives are included, the next condition required for microannuli to form are pressure and/or temperature reductions. If pressure is maintained throughout the life of the well and the temperature does not decrease, microannuli are not probable. However, production is likely to cause the pressure to decrease resulting in the formation of microannuli. If a microannuli forms, the fracture needs a gas source for the propagation of the microannuli to the TOC. Without a gas source, water/oil is not likely to cause the fracture to propagate to the TOC.

If the wellbore has been completed, the wellbore can be classified as either active or P&A'ed. If a wellbore is active, it probably has recent enough records to show if the cement used to complete the well had shrinkage preventative additives. If additives are not included, cement shrinkage will result in microannuli leading to leakage into the environment. If shrinkage preventative additives are included, the history of the well needs to be investigated. Did the well experience significant pressure reductions or did an event cause the temperature to decrease? If the answer to either of those questions is yes, then microannuli most likely occurred. If neither condition existed, microannuli are not probable. With a microannuli forming due to pressure and/or temperature reductions, a gas source is required for the fracture to propagate up the wellbore leading to leakage. If a gas source is not available, microannuli are most likely in the well, but the fluid does not have a complete leakage path to migrate. If the wellbore was already P&A'ed and

has been abandoned for decades in which the history or cement composition of the well is unknown, the leakage status of the well is not known and further investigation is required.

Chapter 7: Conclusions, Recommendations, and Future Work

Conclusions and Recommendations

The objective of this work was to determine if leakage is occurring through the cement sheath in Gulf of Mexico wells. The literature review shows that current methods for predicting wellbore leakage are lacking in two major areas: current methods either assume a microannuli width and/or do not predict gas fluid leakage. The outcome of this dissertation resulted in the development of FEA models for wells of different depths in the Eugene Island OPD and an in-depth case study of a well in the High Island OPD that was able to quantify microannuli magnitudes along the cement sheath. This work also resulted in the development of gas flow equations that were coupled with the FEA models to quantify realistic leakage rates through the microannuli by performing simulations in segments to replicate fracture propagation to the top of cement depth. The total leakage volume (fracture volume) can be determined through the use of a Riemann sum integral.

The main conclusions of this study show that:

- The most likely failure mechanism of wellbores in the study area is debonding between the cement sheath and casing. Tensile or shear fractures within the cement, and debonding of the cement-rock interface is not shown to be common.
- A comparison of FEA models with failure criteria and stress continuum models was performed. Including failure criteria on the cement sheath interfaces in the FEA models predicts less cement failure compared to stress continuum models.
- Changes in internal casing pressure and/or temperature cause microannuli to form at the cement/casing interface. The magnitude of the microannuli can be estimated using the staged 3D FEA model developed within this work.

- Sensitivity analysis of the wellbore input parameters on fracture width show that the parameters are more sensitive to reductions in pressure than temperature. The results were summarized into 1st, 2nd, and 3rd order parameters based on the change in maximum gap width from the base case scenario. The 1st order parameters had the largest effect while the 3rd order parameters had little to no effect. The 1st order parameters are reductions in pressure with larger borehole size and thinner casing thickness. Reductions in temperature did not have any 1st order parameters.
- Combinations of reduction in pressure and temperature increase the magnitude of the microannuli in the wellbore. Alternatively, reductions in pressure and increases in temperature can reduce the magnitude of the microannuli and vice versa. Heat maps for four separate depths with ΔP and ΔT of $\pm 60\%$ were developed. These results can determine if existing wellbores likely have cement sheath integrity issues or can be used to plan the design and construction of a wellbore with integrity.
- Wellbore cement additives (excluding shrinkage preventative additives) used for achieving mechanical wellbore cement sheath integrity by changing the Young's modulus or Poisson's ratio have a minimal effect on maintaining cement integrity in terms of cement sheath debonding.
- Analysis of cemented tubing in casing wellbore leakage experiments show that volumetric shrinkage of conventional cement is approximately 1% and is the dominant factor of fracture width in leakage simulations. Shrinkage preventative additives should be included in the cement slurry design to ensure wellbore cement sheath integrity.
- The fracture volume of the GoM well estimated by the FEA model can be used in conjunction with the developed real gas flow equation to predict potential leakage rates.

The leakage rates calculated using the gas flow model predict an order of magnitude higher leakage rates than using Hagen-Poiseuille flow.

- Brine (water) leakage is not likely in GoM wells. Analyzing fracture volumes with real gas flow models that include the effect of gravity results in an order of magnitude difference in leakage rates from brine leakage extrapolated from experimental results.
- If a GoM well experiences a fracture at a gas source, gas leakage is likely since gas can propagate fractures to shallow depths whereas brine leakage is less likely since brine pressure loses momentum due to the heavier density.
- Accurate flow rate models used to predict wellbore leakage are dependent on pressure differentials, not flowrates.
- The results of this thesis were consolidated into a flow chart which can be used as a first order evaluation to determine if a wellbore is experiencing leakage in the cement sheath in the form of microannuli.

Future Work

The results of this dissertation quantified leakage pathways in the annular cement sheath due to gas migration. The leakage pathways were initiated as “uniform” microannuli at the cement/casing interface. The hydraulic propagation was a process explicitly coupled with the real gas law implemented as interface pressures which could be improved by implementing the real gas flow developed in this work into the Reynold’s Lubrication Theory elements already in the finite element software. Other future work includes performing experiments to create more accurate representation of the traction separation law for gas hydraulic debonding versus mechanical tensile debonding that is currently used. Finally, actual field experiments need to be undertaken to create realistic leakage rates.

Nomenclature

ϕ_{Wyllie}	Wyllie porosity
D_i	Outer diameter of inside pipe in an annulus
D_o	Inner diameter of outside pipe (in an annulus)
E_{cement}	Young's modulus of cement
E_{dyn}	Dynamic Young's modulus
E_{rock}	Young's modulus of rock
E_{static}	Static Young's modulus
F_N	Normal Force
F_S	Shear Force
G_C	Critical Energy
GR_{log}	Well log gamma ray
GR_{shale}	Maximum gamma ray
GR_{sand}	Minimum gamma ray
I_{GR}	Gamma Ray Index
N_{Re}	Reynold's number
P_p	Pore Pressure
$P_{fracture}$	Fracture Gradient
T_i	Initial Temperature
V_{avg}	Average velocity
V_{max}	Maximum velocity
V_p	Compressional velocity
V_s	Shear velocity
V_{shale}	Shale volume
b_{max}	upconing of brine in relation to CO2
c_{cement}	Specific Heat of cement
c_{rock}	Specific Heat of rock
$\frac{dW_{n.f.}}{dm}$	Work term in Bernoulli Equation
$f_{D.W.}$	Darcy-Weisbach friction factor
$f_{Fanning}$	Fanning friction factor
r_i	Outer radius of inside pipe in an annulus
r_o	Inner radius of outside pipe (in an annulus)
ν_{cement}	Poisson's ratio of cement
ν_{rock}	Poisson's ratio of rock
$\frac{\Delta P}{\Delta X}$	Pressure loss per unit length
α_{cement}	Linear Coefficient of Thermal Expansion of cement
α_{rock}	Linear Coefficient of Thermal Expansion of rock
$\frac{\delta \sigma_h}{\delta \sigma_H}$	Isotropic Stress Variation
$\frac{\delta \sigma_H}{\delta \sigma_V}$	Anisotropic Stress Variation
κ_{cement}	Thermal Conductivity of cement
κ_{rock}	Thermal Conductivity of rock

ρ_b	Bulk density
ρ_{dry}	Hardened Cement Density
ρ_{shale}	Shale density
ρ_{sand}	Sand density
$\rho_{seawater}$	Seawater density
ρ_{slurry}	Cement Slurry Density
σ'	Effective Stress
σ_1	Principal Stress 1
σ_2	Principal Stress 2
σ_3	Principal Stress 3
σ_h	Minimum Horizontal Stress
σ_H	Maximum Horizontal Stress
σ_r	Radial Stress
σ_v	Vertical or Overburden Stress
σ_x	Normal Stress in x
σ_y	Normal Stress in y
σ_z	Normal Stress in z
σ_θ	Hoop Stress
τ^o	Tensile Bond Strength
τ_{xy}	Shear Stress in xy
τ_{xz}	Shear Stress in xz
τ_{yx}	Shear Stress in yx
τ_{yz}	Shear Stress in yz
τ_{zx}	Shear Stress in zx
τ_{zy}	Shear Stress in zy
ω_{casing}	Casing Thickness
ω_{cement}	Cement Thickness
ϵ_x	Strain in x
Δt_{log}	Sonic travel time from log
Δt_{shale}	Sonic travel time of shale
$\Delta t_{seawater}$	Sonic travel time of seawater
ΔP	Change in wellbore pressure
ΔT	Change in wellbore temperature
A	Area
D	Diameter of the pipe
E	Young's modulus
F	Force
HR	Hydraulic Radius
ICP	Internal Casing Pressure
L	Length
MW	Mud Weight
$P1$	Pressure at point 1
$P2$	Pressure at point 2
Pp	Pore Pressure
Q	Volumetric flow rate/injection rate

T	Load Temperature
V	Velocity
$V(t)$	cumulative volume of injected fluid at t
a	Area
c	Specific Heat
dz	Depth Increment
f	Friction factor
g	Acceleration Due to Gravity
k	permeability
l	width of slit in slot flow
r	radial distance
r	Radius
t	time
ν	Poisson's ratio
ξ	Friction loss term
ΔP	Change in pressure
Δgz	Gravitational potential energy
Δx	Change in length
α	Linear Coefficient of Thermal Expansion
γ	Biot's Coefficient
$\delta\sigma_v$	Vertical Stress Variation
δR	Gap width
κ	Thermal Conductivity
μ	Viscosity
ρ	Density
$\rho(z)$	Bulk Density at Depth z
σ	Stress
τ	Shear stress
ν	Poisson's Ratio
ϵ	Strain
ϵ	Surface roughness
ϕ	porosity

References

- 76 FR 64462, Oct. 18, 2011, as amended at 77 FR 50892, Aug. 22, 2012; 81 FR 26018, Apr. 29, 2016.
- Aas, B., Sørbo, J., Stokka, S. et al. 2016. Cement placement with tubing left in hole during plug and abandonment operations. In IADC/SPE Drilling Conference and Exhibition, 1-3 March, Fort Worth, Texas, USA. SPE-178840-MS. <https://doi.org/10.2118/178840-MS>.
- Al Ramadan, M., Salehi, S., and Teodoriu, C. 2019. Robust Leakage Modeling for Plug and Abandonment Applications. In *International Conference on Offshore Mechanics and Arctic Engineering* (Vol. 58875, p. V008T11A054). American Society of Mechanical Engineers.
- Albawi, A., De Andrade, J., Torsaeter, M. et al. 2014. Experimental Set-Up for Testing Cement Sheath Integrity in Arctic Wells. In OTC Arctic Technology Conference, 10-12 February, Houston, Texas, USA. OTC-24587-MS. <https://doi.org/10.4043/24587-MS>.
- Alfano, M., Furguele, F., Leonardi, L. et al. 2007. Fracture analysis of adhesive joints using intrinsic cohesive zone models. *Key Eng Mater*, 348, 13-16.
- ANSYS. 2019. Academic Research Mechanical, Release 19.1, Help System, Theory Reference, Thin Fluid Film Flow, ANSYS, Inc.
- API 2010. Isolating Potential Flow Zones During Well Construction API Standard 65—Part 2, Second Edition, December 2010.
- API 2015, API TR 5C3/ISO 10400:2007 – Technical Report on Equations and Calculations for Casing, Tubing, and Line Pipe used as Casing or Tubing; and Performance Properties Tables for Casing and Tubing (includes Addendum 1 dated October 2015).
- Archer, S., & Rasouli, V. 2012. A log based analysis to estimate mechanical properties and in-situ stresses in a shale gas well in North Perth Basin. *WIT Transactions on Engineering Sciences*, 81, 163-174.
- Bachu, S., & Watson, T. L. (2006). Possible indicators for CO₂ leakage along wells. In *8th International conference on greenhouse gas control technologies* (pp. 19-22).
- Baklushin, M., Velikaya, N., Zyryanov, V. et al. 2019. Applying a Resin-Cement System to Help Prevent Fluid Migration in the Annulus: A Case Study, Western Siberia. Presented at the SPE Russian Petroleum Technology Conference, Moscow, Russia, 22-24 October. SPE-196799-MS. <https://doi.org/10.2118/196799-RU>.
- Beharie, C., Francis, S. and Øvestad, K.H. 2015. Resin: An Alternative Barrier Solution Material. Presented at the SPE Bergen One Day Seminar, Bergen, Norway, 22 April. SPE-173852-MS. <https://doi.org/10.2118/173852-MS>.
- Bensted, J. and Barnes, P. 2002. *Structure and Performance of Cements*: CRC Press. 565.
- Bhaisora, D., Aly, A., Morsy, A. et al. 2015. Innovative Application of Ultra-Lightweight Epoxy Resin-Cement Slurry Mixture Achieved Zonal Isolation Objectives and Secured Well Integrity: Case History From Offshore Gulf of Suez. Presented at the International Petroleum Technology Conference, Doha, Qatar, 6-9 December. IPTC-18504-MS. <https://doi.org/10.2523/IPTC-18504-MS>.
- Bird, R.B., Stewart, W.E., and Lightfoot, E.N. 2007. *Transport Phenomena*, revised second edition. New York: Wiley.

- Bois, A. P., Garnier, A., Galdiolo, G. et al. 2012. Use of A Mechanistic Model to Forecast Cement-Sheath Integrity. *SPE Drilling & Completion*, 27(02), 303-314. <https://doi.org/10.2118/139668-PA>.
- Bois, A. P., Vu, M. H., Ghabezloo, S. et al. 2013. Cement sheath integrity for CO2 storage—An integrated perspective. *Energy Procedia*, 37, 5628-5641. <https://doi.org/10.1016/j.egypro.2013.06.485>.
- Bois, A.P., Garnier, A., Rodot, F. et al. 2011. How to Prevent Loss of Zonal Isolation Through a Comprehensive Analysis of Microannulus Formation. *SPE Drilling & Completion* 26 (01): 13-31. SPE-124719-PA. <https://doi.org/10.2118/124719-PA>.
- Bois, A.P., Vu, M.H., Galdiolo, G. et al. 2017. Use of Advanced Gas Migration Model to Optimize Zonal Isolation. Paper presented at the 2017 AADE National Technical Conference and Exhibition, Houston, Texas.
- Bois, A.P., Vu, M.H., Noël, K. et al. 2019. Evaluating Cement-Plug Mechanical and Hydraulic Integrity. *SPE Drilling & Completion*. SPE-191335-PA. <https://doi.org/10.2118/191335-PA>.
- Bosma, M., Ravi, K., Van Driel, W. et al. 1999. Design Approach to Sealant Selection for the Life of the Well. In SPE Annual Technical Conference and Exhibition, 3-6 October, Houston, TX, USA. SPE-56536-MS. <https://doi.org/10.2118/56536-MS>.
- Bourgoyne, A.T., Millheim, K.K., Chenevert, M.E. et al. 1986. Applied Drilling Engineering, Vol. 2. In: SPE textbook series. Society of Petroleum Engineers.
- Bradley, W. B. 1979. Failure of inclined boreholes. *Journal of Energy Resources Technology*, 101(4), 232-239.
- Breckels, I.M. & van Eekelen, H.A.M. 1982. Relationship Between Horizontal Stress and Depth in Sedimentary Basins. *Journal of Petroleum Technology* 34(09): 2-191. SPE-10336-PA. <https://doi.org/10.2118/10336-PA>.
- Carey, J. W., Wigand, M., Chipera, S. J. et al. 2007. Analysis and performance of oil well cement with 30 years of CO2 exposure from the SACROC Unit, West Texas, USA. *International Journal of Greenhouse Gas Control*, 1(1), 75-85. [https://doi.org/10.1016/S1750-5836\(06\)00004-1](https://doi.org/10.1016/S1750-5836(06)00004-1).
- Carter, L. G., & Evans, G. W. 1964. A study of cement-pipe bonding. *Journal of Petroleum Technology*, 16(02), 157-160.
- Cerasi, P. and Stroisz, A. 2015. Experimental investigation of cement to rock bonding. In 49th US Rock Mechanics/Geomechanics Symposium. American Rock Mechanics Association, 28 June-1 July, San Francisco, California, USA. ARMA-2015-237.
- Cerasi, P., Lund, E., Kleiven, M. L. et al. 2017. Shale creep as leakage healing mechanism in CO2 sequestration. *Energy Procedia*, 114, 3096-3112. <https://doi.org/10.1016/j.egypro.2017.03.1439>.
- Colebrook, C. 1939. Turbulent Flow in Pipes, With Particular Reference to The Transition Region Between the Smooth and Rough Pipe Laws. *Journal of the Institution of Civil Engineers*, 11(4), 133-156.
- Cooke, C. E., Jr., Kluck, M. P., and Medrano, R. 1983. Field Measurements of Annular Pressure and Temperature During Primary Cementing. *Journal of Petroleum Technology* 35 (08): 1429-1438. <https://doi.org/10.2118/11206-PA>.
- Corina, A.N., Opedal, N., Vrålstad, T. et al. 2019. Cement plug sealing studies of silica cement systems. In ASME 2019 38th International Conference on Ocean, Offshore and Arctic Engineering, Glasgow, Scotland, UK, 09-14 June. OMAE2019-95928.

- Corina, A.N., Opedal, N., Vrålstad, T. et al. 2020. The Effect of Casing-Pipe Roughness on Cement-Plug Integrity. *SPE Drilling & Completion*. PREPRINT. SPE-194158-PA. <https://doi.org/10.2118/194158-PA>
- Crain, D., Zhang, W., and Eckert, A. 2018. Numerical Simulation of Micro-Annuli Attributes Imposed by Stress Regime and Elastic Contrast. In 52nd US Rock Mechanics/Geomechanics Symposium, 17-20 June, Seattle, Washington, USA. ARMA-2018-1026.
- Crow, W., Carey, J. W., Gasda, S. et al. 2010. Wellbore integrity analysis of a natural CO₂ producer. *International Journal of Greenhouse Gas Control*, 4(2), 186-197. <https://doi.org/10.1016/j.ijggc.2009.10.010>.
- Data.bsee.gov. (2018). Borehole Online Query. [online] Available at: <https://www.data.bsee.gov/Well/Borehole/Default.aspx> [Accessed 22 Aug. 2018].
- De Andrade, J., Fagerås, S., and Sangesland, S. 2019. A Novel Mechanical Tool for Annular Cement Verification. In SPE/IADC International Drilling Conference and Exhibition. Society of Petroleum Engineers, 5-7 March, The Hague, The Netherlands. SPE-194135-MS. <https://doi.org/10.2118/194135-MS>.
- De Andrade, J., Sangesland, S., Skorpa, R. et al. 2016. Experimental laboratory setup for visualization and quantification of cement-sheath integrity. *SPE Drilling & Completion*, 31(04), 317-326. SPE-173871-PA. <https://doi.org/10.2118/173871-PA>.
- de Nevers, N. 2005. *Fluid Mechanics for Chemical Engineers*, third edition. New York, NY: McGraw-Hill.
- Deshpande, A., Jones, P., Jadhav, R. et al. 2019. Comparative Study of the Mechanical Properties of Reduced Density Cements. In SPE Middle East Oil and Gas Show and Conference, 18-21 March, Manama, Bahrain. SPE-194918-MS. <https://doi.org/10.2118/194918-MS>.
- Feng, Y., Li, X., and Gray, KE. 2017. Development of a 3D numerical model for quantifying fluid-driven interface debonding on an injector well. *International Journal of Greenhouse Gas Control* 62: 76-90. <https://doi.org/10.1016/j.ijggc.2017.04.008>.
- Finkbeiner, T., Stump, B. B., Zoback, M. D. et al. 1996. Pressure (Pp), overburden (Sv), and minimum horizontal stress (SHMIN) in Eugene Island Block 330, offshore Gulf of Mexico. Topical report, April 1-July 1, 1996(No. PB-97-124549/XAB). Pennsylvania State Univ., University Park, PA (United States). Dept. of Geosciences.
- Fjaer, E., Holt, R.M., Horsrud, P., Raaen, A.M., & Risnes, R. 2008. Petroleum related rock mechanics, Vol. 53: Elsevier.
- Fleckenstein, W.W., Eustes, A.W. III, and Miller, M.G. 2001. Burst-Induced Stresses in Cemented Wellbores. *SPE Drill & Compl* 16 (2): 74–82. SPE-72059-PA. doi: 10.2118/72059-PA.
- Ford, E. P., Moeinikia, F., Lohne, H. P. et al. 2017. Leakage calculator for plugged and abandoned wells. In SPE Bergen One Day Seminar, 5 April, Bergen, Norway. SPE-185890-MS. <https://doi.org/10.2118/185890-MS>.
- Fourmaintraux, D. M., Bois, A. P., and Fraboulet, B. 2005. Efficient wellbore cement sheath design using the SRC (System Response Curve) method. In SPE Europe/EAGE Annual Conference. 13-16 June, Madrid, Spain. SPE-94176-MS. <https://doi.org/10.2118/94176-MS>.
- Ghabezloo, S., Sulem, J., Guédon, S. et al. 2008. Poromechanical behaviour of hardened cement paste under isotropic loading. *Cement and Concrete research*, 38(12), 1424-1437.

- Gheibi, S., Agofack, N., and Sangesland, S. 2021. Modified discrete element method (MDEM) as a numerical tool for cement sheath integrity in wells. *Journal of Petroleum Science and Engineering*, 196, 107720.
- Gosavi, S. V., Kumar, S., Kirane, K. et al. 2017. Advanced Fracture Modeling: Lab Experiments to Field Applications. In *Abu Dhabi International Petroleum Exhibition & Conference*. Society of Petroleum Engineers.
- Gray, K.E., Podnos, E., and Becker, E. 2009. Finite-element studies of near-wellbore region during cementing operations: Part I. *SPE drilling & completion* 24: 127-136. SPE-106998-PA. <https://doi.org/10.2118/106998-PA>.
- Greenberg, M. L. and Castagna, J. P. 1992. Shear-wave velocity estimation in porous rocks: Theoretical formulation, preliminary verification and applications: *Geophys. Prosp.*, 40, 195-210.
- Hillerborg, A., Mod er, M., and Petersson, P.E. 1976. Analysis of crack formation and crack growth in concrete by means of fracture mechanics and finite elements. *Cement and Concrete Research* 6(6): 773-781. [https://doi.org/10.1016/0008-8846\(76\)90007-7](https://doi.org/10.1016/0008-8846(76)90007-7).
- Hiramatsu, Y., & Oka, Y. 1968. Determination of the stress in rock unaffected by boreholes or drifts, from measured strains or deformations. *International Journal of Rock Mechanics and Mining Sciences & Geomechanics Abstracts* (Vol. 5, No. 4, pp. 337-353).
- Hubbert, M. K. 1956. Darcy's law and the field equations of the flow of underground fluids. *Transactions of the AIME*, 207(01), 222-239.
- Ichim, A. and Teodoriu, C. 2017. Development of a Cement Repository to Improve the Understanding of Well Integrity Behavior with Time. In *SPE Oklahoma City Oil and Gas Symposium*, 27-31 March, Oklahoma City, OK, USA. SPE-185089-MS. <https://doi.org/10.2118/185089-MS>.
- Ingraffea, A. R., Wells, M. T., Santoro, R. L. et al. 2014. Assessment and risk analysis of casing and cement impairment in oil and gas wells in Pennsylvania, 2000–2012. *Proceedings of the National Academy of Sciences*, 111(30), 10955-10960.
- Jaeger, J. C., Cook, N.G.W. & Zimmerman, R.W. 2007. *Fundamentals of rock mechanics*, 4th edition. Malden, MA: Blackwell Pub.
- Jahn, F., Cook, M., & Graham, M. 2008. *Hydrocarbon exploration and production*. Elsevier.
- James, S.G. and Boukhelifa, L. 2006. Zonal Isolation Modelling and Measurements-Past Myths and Today's Realities. In *Abu Dhabi International Petroleum Exhibition and Conference*, 5-8 November, Abu Dhabi, U.A.E. SPE-101310-MS. <https://doi.org/10.2118/101310-MS>.
- Jiang, J., Li, J., Liu, G. et al. 2020. Numerical simulation investigation on fracture debonding failure of cement plug/casing interface in abandoned wells. *Journal of Petroleum Science and Engineering*, 192, 107226.
- Jones, P.J., Karcher, J.D., Ruch, A. et al. 2014. Rigless Operation to Restore Wellbore Integrity using Synthetic-based Resin Sealants. Presented at the *SPE/EAGE European Unconventional Conference and Exhibition*, Vienna, Austria, 25-27 February. SPE-167759-MS. <https://doi.org/10.2118/167759-MS>.
- Kang, M., Kanno, C. M., Reid, M. C. et al. 2014. Direct measurements of methane emissions from abandoned oil and gas wells in Pennsylvania. *Proceedings of the National Academy of Sciences*, 111(51), 18173-18177.
- Kell, S. 2011. *State Oil and Gas Agency Groundwater Investigations: And Their Role in Advancing Regulatory Reform; a Two-state Review, Ohio and Texas*. GWPC.

- Khodami, E., Ramezanzadeh, A., and Noroozi, M. 2021. Numerical modeling of oil well integrity with a particular view to cement (case study: Maroon Oilfield in southwest of Iran). *Journal of Petroleum Science and Engineering*, 196, 107991.
- Kirsch. 1898. Die Theorie der Elastizitat und die Bedurfnisse der Festigkeitslehre. *Zeitschrift des Vereines deutscher Ingenieure* 42, 797-807.
- Kleinstreuer, C. 2010. *Modern Fluid Dynamics: Basic Theory and Selected Applications in Macro- and Micro-Fluidics*. New York, NY: Springer.
- Klinkenberg, L. J. 1941. The permeability of porous media to liquids and gases. In *Drilling and production practice*. American Petroleum Institute.
- Kumar, N. A. 2004. Compressibility factors for natural and sour reservoir gases by correlations and cubic equations of state (Doctoral dissertation, Texas Tech University).
- Kumar, S., Zhou, F., Searles, K. H. et al. 2017. Modeling of fluid-driven fractures using XFEM. In *51st US Rock Mechanics/Geomechanics Symposium*. American Rock Mechanics Association.
- Kumar, S., Zielonka, M., Searles, K. et al. 2017. Modeling of hydraulic fracturing in ultra-low permeability formations: the role of pore fluid cavitation. *Engineering Fracture Mechanics*, 184, 227-240.
- Landau, L. D. and Lifshitz, E. M. 1987. *Fluid Mechanics: Volume 2* (Vol. 2). Butterworth-Heinemann.
- Lavrov, A. and Torsæter, M. 2018. All microannuli are not created equal: Role of uncertainty and stochastic properties in well leakage prediction. *International Journal of Greenhouse Gas Control*, 79, 323-328. <https://doi.org/10.1016/j.ijggc.2018.09.001>.
- Lavrov, A., Bhuiyan, M., and Stroisz, A. 2019. Push-out test: Why bother?. *Journal of Petroleum Science and Engineering*, 172, 297-302. <https://doi.org/10.1016/j.petrol.2018.09.067>.
- Le Roy-Delage, S., Baumgarte, C., Thiercelin, M. et al. 2000. New Cement Systems for Durable Zonal Isolation. In IADC/SPE Drilling Conference, 23-25 February, New Orleans, LA, USA. SPE-59132-MS. <https://doi.org/10.2118/59132-MS>.
- Lee, H. H. 2017. *Finite element simulations with ANSYS Workbench 17*. SDC publications.
- Loiseau, A. 2014. Thermal Expansion of Cement and Well Integrity of Heavy Oil Wells. In SPE Heavy and Extra Heavy Oil Conference: Latin America, 24-26 September, Medellin, Colombia. SPE-171066-MS. <https://doi.org/10.2118/171066-MS>.
- Mansour, A.K., Taleghani, A.D., and Li, G. 2017. Smart Lost Circulation Materials for Wellbore Strengthening. Presented at the 51st US Rock Mechanics/Geomechanics Symposium, San Francisco, CA, 25-28 June. ARMA-17-0492.
- McDaniel, J., Watters, L., and Combs, N.K. 2014. Zonal Isolation Assurance: Relating Cement Mechanical Properties to Mechanical Durability. In SPE/AAPG/SEG Unconventional Resources Technology Conference, 25-27 August, Denver, CO, USA. URTEC-1913405-MS. <https://doi.org/10.15530/URTEC-2014-1913405>.
- Meng, J., Pashin, J. C., Nygaard, R. et al. 2018. Analysis of the stress field in the DeSoto canyon Salt Basin for ensuring safe offshore carbon storage. *International Journal of Greenhouse Gas Control* 79: 279-288. <https://doi.org/10.1016/j.ijggc.2018.11.006>.
- Moeinikia, F., Ford, E. P., Lohne, H. P. et al. 2018. Leakage Calculator for Plugged-and-Abandoned Wells. *SPE Production & Operations*, 33(04), 790-801. SPE-185890-PA. <https://doi.org/10.2118/185890-PA>.
- Morris, W., Criado, M.A., Robles, J. et al. 2003. Design of High Toughness Cement for Effective Long Lasting Well Isolations. In SPE Latin American and Caribbean Petroleum

- Engineering Conference, 27-30 April, Port-of-Spain, Trinidad and Tobago. SPE-81001-MS. <https://doi.org/10.2118/81001-MS>.
- Nelson, E. B. 1990. *Well cementing. Development of petroleum Science* (Vol. 28. Elsevier Science, 600.
- Nelson, E. B., & Guillot, D. 2006. *Well Cementing 2nd edition*: Schlumberger 773.
- Nygaard, R., Salehi, S., and Lavoie, R.G. 2011. Effect of Dynamic Loading on Wellbore Leakage for the Wabamun Area CO₂ Sequestration Project. In Canadian Unconventional Resources Conference, Calgary, Alberta, Canada. November 15-17. SPE-146640-MS. <https://doi.org/10.2118/146640-MS>.
- Nygaard, R., Salehi, S., Weideman, B. et al. 2014. Effect of Dynamic Loading on Wellbore Leakage for the Wabamun Area CO₂-Sequestration Project. *Journal of Canadian Petroleum Technology*, 53(01), 69-82. SPE-146640-PA. <https://doi.org/10.2118/146640-PA>.
- Opedal, N., Cerasi, P., and Vrålstad, T. 2019. Cement Bond Strength Measurements. In *International Conference on Offshore Mechanics and Arctic Engineering* (Vol. 58875, p. V008T11A039). American Society of Mechanical Engineers.
- Opedal, N., Corina, A. N., and Vrålstad, T. 2018. Laboratory test on cement plug integrity. In *International Conference on Offshore Mechanics and Arctic Engineering* (Vol. 51296, p. V008T11A071). American Society of Mechanical Engineers.
- Outmans, H. D. 1963. Mechanics of static and dynamic filtration in the borehole. *Society of Petroleum Engineers Journal*, 3(03), 236-244.
- Patel, H. and Salehi, S. 2019. Development of an Advanced Finite Element Model and Parametric Study to Evaluate Cement Sheath Barrier. *Journal of Energy Resources Technology*, 141(9), 092902. <https://doi.org/10.1115/1.4043137>.
- Pattillo, P.D. and Kristiansen, T.G. 2002. Analysis of Horizontal Casing Integrity in the Valhall Field. Paper SPE 78204 presented at the SPE/ISRM Rock Mechanics Conference, Irving, Texas, USA, 20–23 October. doi: 10.2118/78204-MS.
- Philippacopoulos, A.J. and Berndt, M.L. 2002. Mechanical Response and Characterization of Well Cements. In SPE Annual Technical Conference and Exhibition, 29 September-2 October, San Antonio, TX, USA. SPE-77755-MS. <https://doi.org/10.2118/77755-MS>.
- Piau, J.M., Le Parc, G., Fourmaintraux, D.: “Etude de l’étanchéité des gaines cimentées”, Elf Aquitaine Production, Internal report (1995).
- Ravi, K., Bosma, M., and Gastbled, O. 2002. Improve the Economics of Oil and Gas Wells by Reducing the Risk of Cement Failure. In IADC/SPE Drilling Conference, Dallas, 26–28 February. SPE-74497-MS. <https://doi.org/10.2118/74497-MS>.
- Reddy, B. R., Xu, Y., Ravi, K. et al. 2007. Cement Shrinkage measurement in oilwell cementing- A comparative study of laboratory methods and procedures. In *Rocky Mountain Oil & Gas Technology Symposium*. Society of Petroleum Engineers.
- Ritchie, M., Hareland, G., Kjeldal, V. N. et al. 2019. An Unconventional Study on the Bond Strength of the Casing/Cement Interface and the Benefits of Nanoparticle Additives. In *SPE Symposium: Decommissioning and Abandonment*. Society of Petroleum Engineers.
- Saint-Marc, J., Garnier, A., and Bois, A.P. 2008. Initial State Of Stress: The Key to Achieving Long-Term Cement-Sheath Integrity. In SPE Annual Technical Conference and Exhibition, 21–24 September, Denver, CO, USA. SPE-116651-MS. <https://doi.org/10.2118/116651-MS>.

- Saleh, F. K., Rivera, R., Salehi, S. et al. 2018. How does mixing water quality affect cement properties. In SPE International Conference and Exhibition on Formation Damage Control, 7-9 February, Lafayette, Louisiana, USA. SPE-189505-MS. <https://doi.org/10.2118/189505-MS>.
- Searles, K. H., Zielonka, M. G., and Garzon, J. L. 2018. Fully Coupled 3-D Hydraulic Fracture Models—Development and Validation. In *Hydraulic Fracture Modeling* (pp. 155-193). Gulf Professional Publishing.
- SIMULIA. 2016. Abaqus Version 2016 Analysis User's Guide. Providence. Dassault Systèmes, RI, USA.
- Skadsem, H. J., Kragset, S., and Sørbo, J. 2019. Cementing an Irregular Annulus Geometry: Full-Scale Experiments and 3D Simulations. In SPE/IADC International Drilling Conference and Exhibition, 5-7 March, The Hague, The Netherlands. SPE-194091-MS. <https://doi.org/10.2118/194091-MS>.
- Skorpa, R. and Vrålstad, T. 2018. Visualization of fluid flow through cracks and microannuli in cement sheaths. *SPE Journal*, 23(04), 1-067. SPE-180019-PA. <https://doi.org/10.2118/180019-PA>.
- Smith, D. K. 1987. *Cementing*: H.L. Doherty Memorial Fund of AIME, Society of Petroleum Engineers. 254.
- Smith, R. C. 1984. Successful Primary Cementing Can Be a Reality. *Journal of Petroleum Technology* 36 (11): 1851-1858. <https://doi.org/10.2118/13498-PA>.
- Stormont, J. C., Fernandez, S. G., Taha, M. R. et al. 2018. Gas flow through cement-casing microannuli under varying stress conditions. *Geomechanics for Energy and the Environment*, 13, 1-13. <https://doi.org/10.1016/j.gete.2017.12.001>.
- Sutera, S. P. and Skalak, R. 1993. The history of Poiseuille's law. *Annual review of fluid mechanics*, 25(1), 1-20.
- Tarco, J. C., and Asghari, K. 2010. Experimental study of stability and integrity of cement in wellbores used for CO₂ storage. *Journal of Canadian Petroleum Technology*, 49(10), 37-44. SPE-142004-PA. <https://doi.org/10.2118/142004-PA>.
- Teodoriu, C., Yuan, Z., Schubert, J. et al. 2012. Experimental Measurements of Mechanical Parameters of Class G Cement. In SPE/EAGE European Unconventional Resources Conference & Exhibition-From Potential to Production, 20-22 March, Vienna, Austria. <https://doi.org/10.3997/2214-4609-pdb.285.spe153007>.
- Turon, A., Dávila, C.G., Camanho, P.P. et al. 2006. An engineering solution for mesh size effects in the simulation of delamination using cohesive zone models. *Engineering Fracture Mechanics* 74(2007): 1665-1682. <https://doi.org/10.1016/j.engfracmech.2006.08.025>.
- Vignes, B. and Aadnoy, B. 2008. Well Integrity Issues Offshore Norway. In IADC/SPE Drilling Conference, 4-6 March, Orlando, Florida, USA. SPE-112535-MS. <https://doi.org/10.2118/112535-MS>.
- Vrålstad, T. and Skorpa, R. 2020. Digital Cement Integrity: A Methodology for 3D Visualization of Cracks and Microannuli in Well Cement. *Sustainability*, 12(10), 4128.
- Vrålstad, T., Saasen, A., Fjær, E. et al. 2018. Plug & abandonment of offshore wells: Ensuring long-term well integrity and cost-efficiency. *Journal of Petroleum Science and Engineering*, 173, 478-491. <https://doi.org/10.1016/j.petrol.2018.10.049>.
- Vrålstad, T., Skorpa, R., Opedal, N. et al. 2015. Effect of thermal cycling on cement sheath integrity: Realistic experimental tests and simulation of resulting leakages. In SPE Thermal

- Well Integrity and Design Symposium, 23-25 November, Banff, Alberta, Canada. SPE-178467-MS. <https://doi.org/10.2118/178467-MS>.
- Vu, M. H., Bois, A. P., and Badalamenti, A. 2018. Gas Migration Modeling to Prevent Sustained Casing Pressure and Casing Vent Flow. In SPE/IADC Middle East Drilling Technology Conference and Exhibition, 29-31 January, Abu Dhabi, UAE. SPE-189384-MS. <https://doi.org/10.2118/189384-MS>.
- Wang, H. F. 2017. *Theory of linear poroelasticity with applications to geomechanics and hydrogeology*. Princeton University Press.
- Wang, W. and Taleghani, A. D. 2014. Three-dimensional analysis of cement sheath integrity around Wellbores. *Journal of Petroleum Science and Engineering*, 121, 38-51. <https://doi.org/10.1016/j.petrol.2014.05.024>.
- Watson, T. L. and Bachu, S. 2008. Identification of wells with high CO₂-leakage potential in mature oil fields developed for CO₂-enhanced oil recovery. In SPE Symposium on Improved Oil Recovery, 20-23 April, Tulsa, Oklahoma, USA. SPE-112924-MS. <https://doi.org/10.2118/112924-MS>.
- Watson, T. L., and Bachu, S. 2007. Evaluation of the potential for gas and CO₂ leakage along wellbores. In E&P Environmental and Safety Conference, 5-7 March, Galveston, Texas, USA. SPE-106817-MS. <https://doi.org/10.2118/106817-MS>.
- Watson, T. L., and Bachu, S. 2009. Evaluation of the potential for gas and CO₂ leakage along wellbores. *SPE Drilling & Completion*, 24(01), 115-126. SPE-106817-PA. <https://doi.org/10.2118/106817-PA>.
- Weideman, B. and Nygaard, R. 2014. How cement operations affect your cement sheath short and long term integrity. In 2014 American Association of Drilling Engineers Fluids Technical Conference and Exhibition, April 15-16, Houston, TX, USA. AADE-14-FTCE-20.
- Weideman, B.L. 2014. Investigation of Cased Wellbore Integrity in the Wabamun Area Sequestration Project. *MS Thesis*, Missouri University of Science and Technology, Rolla, MO.
- White, F.M. 2011. *Fluid Mechanics*, seventh edition. New York, NY: McGraw-Hill.
- Wise, J., Nygaard, R., and Hareland, G. 2019. Numerical Analysis of Wellbore Integrity and Cement Sheath Debonding for Wells in the Eugene Island OPD, Gulf of Mexico. In 53rd US Rock Mechanics/Geomechanics Symposium, 23-26 June, New York City, New York, USA. ARMA-2019-0439.
- Witherspoon, P. A., Wang, J. S., Iwai, K. et al. 1980. Validity of cubic law for fluid flow in a deformable rock fracture. *Water resources research*, 16(6), 1016-1024.
- Wojtanowicz, A.K., Bourgoyne, A.T., Zhou, D. et al. 2000. Strength and Fracture Gradients for Shallow Marine Sediments. *US Department of Interior Mineral Management Service Final Report*.
- Wolterbeek, T. K. T., Cornelissen, E. K., Nolan, S. et al. 2021. Restoration of annular zonal isolation using localized casing expansion (LCE) technology: A proof of concept based on laboratory studies and field trial results. *Journal of Petroleum Science and Engineering*, 108103.
- Won, J., Lee, D., Na, K. et al. 2015. Physical properties of G-class cement for geothermal well cementing in South Korea. *Renewable Energy* 80(August 2015): 123-131. <https://doi.org/10.1016/j.renene.2015.01.067>.

- Xu, Y., Yan, Y., Xu, S. et al. 2020. Numerical Simulation Study on Propagation of Initial Microcracks in Cement Sheath Body during Hydraulic Fracturing Process. *Energies*, 13(5), 1260.
- Yalcinkaya, T., Radonjic, M., Hughes, R. G. et al. 2011. The Effect of CO₂-Saturated Brine on the Conductivity of Wellbore-Cement Fractures. *SPE Drilling & Completion*, 26(03), 332-340. SPE-139713-PA. <https://doi.org/10.2118/139713-PA>.
- Zhang, M. and Bachu, S. 2011. Review of integrity of existing wells in relation to CO₂ geological storage: What do we know?. *International Journal of Greenhouse Gas Control*, 5(4), 826-840.
- Zhang, W., Eckert, A., and Liu, X. 2017. Numerical simulation of micro-annuli generation by thermal cycling. In 51st US Rock Mechanics/Geomechanics Symposium, 25-28 June, San Francisco, California, USA. ARMA-2017-0354.
- Zhang, W., Hilgedick, S., and Eckert, A. 2019. A Novel Approach to Investigate Cement Pore Pressure during Hardening. In 2019 AADE National Technical Conference and Exhibition. American Association of Drilling Engineers, 9-10 April, Denver, CO, USA. AADE-19-NTCE-086.
- Ziashahabi, P., Ravi, K. and Prohaska, M. 2019. Polymer-Based Sealing Materials as Cement Alternative to Restore Wellbore Isolation. Presented at the SPE Gas & Oil Technology Showcase and Conference, Dubai, UAE, 21-23 October. SPE-198584-MS. <https://doi.org/10.2118/198584-MS>.
- Zielonka, M. G., Searles, K. H., Ning, J. et al. 2014. Development and validation of fully-coupled hydraulic fracturing simulation capabilities. In *Proceedings of the SIMULIA community conference, SCC2014* (pp. 19-21).

Appendix A: Basic Rock Mechanics

The theory of elasticity in regards to rock mechanics consists of two major concepts: stress and strain. Stress is defined in Equation A.1 and states that the stress of a material (σ) is equal to the force (F) acting through the cross-sectional area divided by the cross-sectional area (A).

$$\sigma = \frac{F}{A} \tag{A.1}$$

The SI units of stress are Pascal (Pa). The sign convention for stress used in the petroleum industry and this thesis are that compressive stresses are positive while tensile stresses are negative. Two examples of stress are shown in Figure A.1 in which a stress is applied perpendicular to a cylindrical sample, and an example in which stress is applied at an angle.

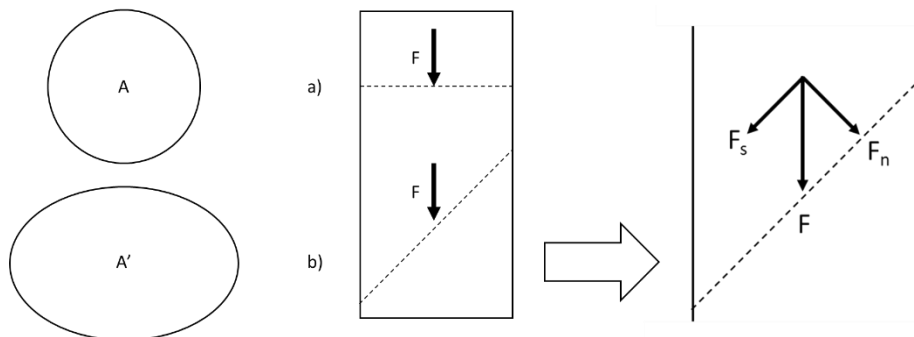


Figure A.1: Two perspectives of stress on a cylindrical sample. A) the cross-sectional area for the two stresses. B) the force applied normal to the sample (a) and at an angle (b). C) the force components for the stress applied at an angle (b).

Stress is considered a tensor in which it is described as a magnitude and direction with reference to the plane (cross-sectional area) it acts across. The magnitude is composed of directional dependent components. If a force is no longer normal to the cross-section, such as in Figure A.1 (C), then the force needs to be broken down into components: normal and shear force. The normal force is perpendicular to the cross-section while the shear force is parallel to the cross-

section. The resulting force components are used in Equation A.1 to determine normal (σ) and shear (τ) stresses. The normal and shear stresses are shown in Equations A.2 and A.3 respectively.

$$\sigma = \frac{F_n}{A} \quad \text{A.2}$$

$$\tau = \frac{F_s}{A} \quad \text{A.3}$$

Using a Cartesian coordinate system, the stress components for a 3D cube will be composed of normal and shear stresses along each axis. The normal stress components are perpendicular to the axis while the shear stress components are parallel to the axis. The 3D stress tensor is composed of nine stress components which are shown in Figure A.2. The 3D stress tensor consists of three normal ($\sigma_x, \sigma_y, \sigma_z$) and six shear ($\tau_{xy}, \tau_{yx}, \tau_{xz}, \tau_{zx}, \tau_{yz}, \tau_{zy}$) stress components.

The 3D stress tensor matrix is shown in Equation A.4.

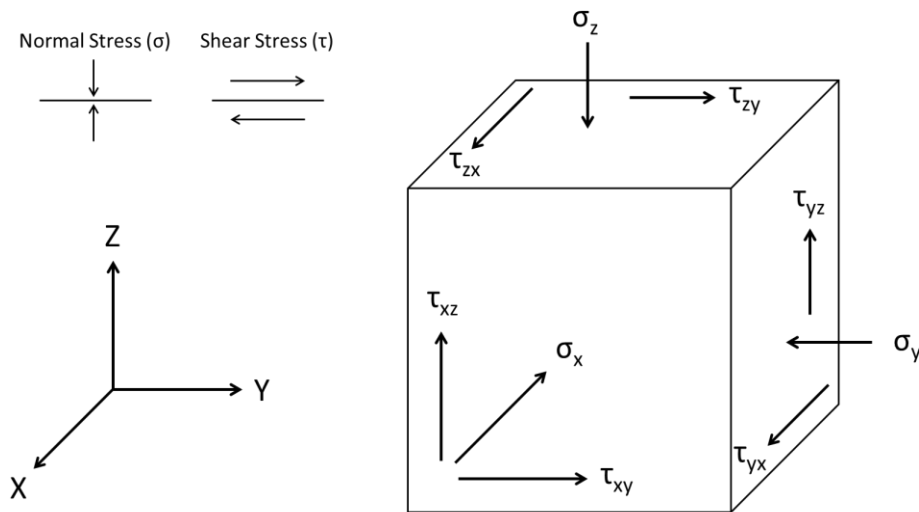


Figure A.2: 3D stresses on a cube with respect to its axis. The normal stress (σ) is perpendicular to the axis plane while the shear stress (τ) is parallel to the axis plane.

$$\begin{bmatrix} \sigma_x & \tau_{xy} & \tau_{xz} \\ \tau_{yx} & \sigma_y & \tau_{yz} \\ \tau_{zx} & \tau_{zy} & \sigma_z \end{bmatrix} \quad \text{A.4}$$

If the rock (body) is considered to be in equilibrium (no translational or rotational forces acting on it), the stress tensor (Equation A.4) simplifies down such that there are still three normal stress components, but the six shear components simplify down to three components since the shear stresses are opposite of one another must be equal in magnitude ($\tau_{xy} = \tau_{yx}$). This stress tensor is shown in Equation A.5. The result of this is that now the stresses of a body in equilibrium can be described using three normal and three shear stresses.

$$\begin{bmatrix} \sigma_x & \tau_{xy} & \tau_{xz} \\ \tau_{yx} & \sigma_y & \tau_{yz} \\ \tau_{zx} & \tau_{zy} & \sigma_z \end{bmatrix} \quad \text{A.5}$$

Which $\tau_{xy} = \tau_{yx}$, $\tau_{xz} = \tau_{zx}$, & $\tau_{yz} = \tau_{zy}$

$$\rightarrow \begin{bmatrix} \sigma_x & \tau_{xy} & \tau_{xz} \\ \tau_{xy} & \sigma_y & \tau_{yz} \\ \tau_{xz} & \tau_{yz} & \sigma_z \end{bmatrix} \quad \text{A.6}$$

Principal Stresses

If the coordinate system is rotated such that the normal stress components of Equation A.6 are equal to the maximum and minimum values resulting in the shear stress components being equal to zero, the normal stresses become re-defined as principal stresses as shown in Equation A.7.

$$[\sigma] = \begin{bmatrix} \sigma_x & \tau_{xy} & \tau_{xz} \\ \tau_{xy} & \sigma_y & \tau_{yz} \\ \tau_{xz} & \tau_{yz} & \sigma_z \end{bmatrix} \rightarrow \begin{bmatrix} \sigma_1 & 0 & 0 \\ 0 & \sigma_2 & 0 \\ 0 & 0 & \sigma_3 \end{bmatrix} = \begin{bmatrix} \sigma_v & 0 & 0 \\ 0 & \sigma_H & 0 \\ 0 & 0 & \sigma_h \end{bmatrix} \quad \text{A.7}$$

Any stress field, in equilibrium, can then be defined with three orthogonal principal stresses where no shear stresses will occur. These stresses will be referred to as the in-situ stresses. Assuming the seafloor as a free even surface not translating any shear stresses, the in-situ stresses

are represented by the overburden stress in the vertical direction (σ_v) and the maximum and minimum horizontal stresses (σ_H and σ_h respectively) which are orthogonal to the overburden. Given the three in-situ stresses, there are three stress regimes related to the magnitude of the in-situ stresses (Anderson, 1951).

- i. Normal Faulting: $\sigma_v > \sigma_H > \sigma_h$
- ii. Strike-Slip Faulting: $\sigma_H > \sigma_v > \sigma_h$
- iii. Reverse Faulting: $\sigma_H > \sigma_h > \sigma_v$

In-Situ Principal Stress Magnitudes

Many different methods can be used to determine the in-situ stresses for a given region depending on the stress regimes. For a normal faulting regime, empirical correlations have been developed and state that if the overburden stress is determined, the maximum and horizontal stresses are ratios of the overburden stress (Finkbeiner et al., 1996). Calculating the overburden stress can be done using the following equation:

$$\sigma_v = \int_0^D \rho(z)g dz \quad \text{A.8}$$

Where σ_v is the overburden stress, $\rho(z)$ is the bulk density of the formation at a depth (z), g is the acceleration due to gravity, and dz is the depth increment. An important note is that for offshore wells, the water density will replace the bulk density in the water column and needs to be included.

To determine the overburden stress with Equation A.8, the exact formation depths and the bulk density of the formations from log data is required.

Effective Stress

Sedimentary rocks encountered in oil and gas fields are porous rocks filled with connate fluids or hydrocarbons. Hardened cement is similar to rocks in that it is also a porous material (Saint-Marc et al., 2008). Porous materials often contain a fluid within the pore spaces thus creating a pore pressure which can offset the in-situ stresses. This new stress is called the effective stress (σ') and is represented in Equation A.9. As shown in Equation A.9, the effective stress is related to the compressional in-situ stresses (σ) and pore pressure (P_p).

$$\sigma' = \sigma - P_p \quad \text{A.9}$$

In the above equation, the pore volume fluid is assumed to have negligible compressibility when compared to the compressibility of the material. The importance of this concept is that an increased pore pressure will shift the effective stresses closer to the tensile range which may be sufficient enough to cause the rock (or cement) to fail (Terzaghi, 1936; Terzaghi, 1951). A more general definition of effective stress includes Biot's coefficient (γ , where $0 \leq \gamma \leq 1$) which takes into consideration for the bulk rock and grain compressibility of the material and is shown in Equation A.10.

$$\sigma' = \sigma - \gamma P_p \quad \text{A.10}$$

Equation A.10 represents the generalized effective stress model. In this work the Biot's coefficient is assumed to be one for both cement and rock materials thus reducing the effective stress model down as given in Equation A.9.

Strain

The strain of a body is related to the resulting displacement caused by the force applied to it. The definition of strain is shown in Equation A.11 and states that the strain (ϵ , unitless) is equal to the change in length (Δu) divided by the original length (u).

$$\epsilon = \frac{u - u'}{u} = -\frac{\Delta u}{u} \quad \text{A.11}$$

Stress and strain are related through the theory of linear elasticity in which the relationship between the applied stresses and the resulting strains in a linear relationship which is shown in Hooke's Law in Equation A.12.

$$\epsilon_x = \frac{1}{E} \sigma_x \quad \text{A.12}$$

The Poisson's ratio is the measure of lateral expansion relative to the longitudinal contraction as shown in Equation A.13.

$$\nu = -\frac{\epsilon_y}{\epsilon_x} \quad \text{A.13}$$

Appendix B: Wellbore Abandonment Requirements

Table B.1: 30 CFR 250, Subpart Q, Decommissioning Activities, Section §250.1715.

Condition	What to do
(1) Zones in open hole	Cement plug(s) set from at least 100 feet below the bottom to 100 feet above the top of oil, gas, and fresh-water zones to isolate fluids in the strata.
(2) Open hole below casing	<ul style="list-style-type: none"> <li data-bbox="824 489 1425 583">(i) A cement plug, set by the displacement method, at least 100 feet above and below deepest casing shoe; <li data-bbox="824 590 1425 783">(ii) A cement retainer with effective back-pressure control set 50 to 100 feet above the casing shoe, and a cement plug that extends at least 100 feet below the casing shoe and at least 50 feet above the retainer; or <li data-bbox="824 789 1425 909">(iii) A bridge plug set 50 feet to 100 feet above the shoe with 50 feet of cement on top of the bridge plug, for expected or known lost circulation conditions.
(3) A perforated zone that is currently open and not previously squeezed or isolated	<ul style="list-style-type: none"> <li data-bbox="824 930 1425 989">(i) A method to squeeze cement to all perforations; <li data-bbox="824 995 1425 1121">(ii) A cement plug set by the displacement method, at least 100 feet above to 100 feet below the perforated interval, or down to a casing plug, whichever is less; or <li data-bbox="824 1127 1425 1890">(iii) If the perforated zones are isolated from the hole below, you may use any of the plugs specified in paragraphs (a)(3)(iii)(A) through (E) of this section instead of those specified in paragraphs (a)(3)(i) and (a)(3)(ii) of this section. <ul style="list-style-type: none"> <li data-bbox="898 1329 1425 1556">a. A cement retainer with effective back-pressure control set 50 to 100 feet above the top of the perforated interval, and a cement plug that extends at least 100 feet below the bottom of the perforated interval with at least 50 feet of cement above the retainer; <li data-bbox="898 1562 1425 1688">b. A casing bridge plug set 50 to 100 feet above the top of the perforated interval and at least 50 feet of cement on top of the bridge plug; <li data-bbox="898 1694 1425 1820">c. A cement plug at least 200 feet in length, set by the displacement method, with the bottom of the plug no more than 100 feet above the perforated interval; <li data-bbox="898 1827 1425 1890">d. A through-tubing basket plug set no more than 100 feet above the perforated

	<p>interval with at least 50 feet of cement on top of the basket plug; or</p> <p>e. A tubing plug set no more than 100 feet above the perforated interval topped with a sufficient volume of cement so as to extend at least 100 feet above the uppermost packer in the wellbore and at least 300 feet of cement in the casing annulus immediately above the packer.</p>
(4) A casing stub where the stub end is within the casing	<p>(i) A cement plug set at least 100 feet above and below the stub end;</p> <p>(ii) A cement retainer or bridge plug set at least 50 to 100 feet above the stub end with at least 50 feet of cement on top of the retainer or bridge plug; or</p> <p>(iii) A cement plug at least 200 feet long with the bottom of the plug set no more than 100 feet above the stub end.</p>
(5) A casing stub where the stub end is below the casing	A plug as specified in paragraph (a)(1) or (a)(2) of this section, as applicable.
(6) An annular space that communicates with open hole and extends to the drilling fluid line	A cement plug at least 200 feet long set in the annular space. For a well completed above the ocean surface, you must pressure test each casing annulus to verify isolation.
(7) A subsea well with unsealed annulus	A cutter to sever the casing, and you must set a stub plug as specified in paragraphs (a)(4) and (a)(5) of this section.
(8) A well with casing	A cement surface plug at least 150 feet long set in the smallest casing that extends to the drilling fluid line with the top of the plug no more than 150 feet below the drilling fluid line.
(9) Fluid left in the hole	A fluid in the intervals between the plugs that is dense enough to exert a hydrostatic pressure that is greater than the formation pressures in the intervals.
(10) Permafrost areas	<p>(i) A fluid to be left in the hole that has a freezing point below the temperature of the permafrost, and a treatment to inhibit corrosion; and</p> <p>(ii) Cement plugs designed to set before freezing and have a low heat of hydration.</p>
(11) Removed the barriers required in §250.420(b)(3) for the well to be completed	Two independent barriers, one of which must be a mechanical barrier, in the center wellbore as described in §250.420(b)(3) once the well is to be placed in a permanent or temporary abandonment.

Appendix C: Parallel Plate Capillary Pressure

The generalized definition of capillary pressure is described in Equation b in which the capillary pressure is equal to the inverse summation of the radii multiplied by the interfacial tension.

$$P_c = \sigma \left(\frac{1}{r_1} + \frac{1}{r_2} \right) \quad \text{C.1}$$

Due to the geometry of parallel plates, the radii of the wetting phase is described in Equations C.2 and C.3.

$$r_1 = \frac{w}{2 \cos \theta} \quad \text{C.2}$$

$$r_2 = \infty \quad \text{C.3}$$

Substituting Equations C.2 and C.3 into Equation C.1 results in Equation C.4 which is simplified into Equation C.5.

$$P_c = \sigma \left(\frac{2 \cos \theta}{w} + \frac{1}{\infty} \right) \quad \text{C.4}$$

$$P_c = \frac{2\sigma \cos \theta}{w} \quad \text{C.5}$$

Appendix D: Case Well Data

Form MMS 123A/123S - Electronic Version

Application for Permit to Drill a New Well

Lease G17199 Area/Block HI A 545 Well Name 002 ST 00 BP 00 Well Exploration
Application Status Approved Operato 01764 Energy Resource Technology, Inc.

General Well Information

API Number	427094116400	Approval Date	11/07/2007	Approved By	Ronald Fowler
Date of Request	10/19/2007	Req Spud	11/07/2007	Kickoff Point	N/A
Water Depth (ft.)	243	Drive Size (in)	30	Mineral Code	Hydrocarbon
RKB Elevation	105	Drive Depth	548	Subsea BOP	No
Verbal Approval	Verbal Approval By				

Proposed Well Location

SURFACE LOCATION

LEASE (OCS)	G17199	Area/Block	HI A 545	Authority	Federal Lease
Entered NAD 27	Calculated NAD 27 Departures		Calculated NAD 27 X-Y		
Lat: 28.04504417	N	7464.0	X	3609715.02251	
Lon: -94.00894056	W	7199.0	Y	111335.995826	
Surface Plan	Plan Lease (OCS) G17199		Area/Block	HI A 545	

BOTTOM LOCATION

LEASE (OCS)	G17199	Area/Block	HI A 545		
Entered NAD 27	Calculated NAD 27 Departures		Calculated NAD 27 X-Y		
Lat: 28.04504417	N	7464.0	X	3609715.02251	
Lon: -94.00894056	W	7199.0	Y	111335.995826	
Bottom Plan	Plan Lease (OCS) G17199		Area/Block	HI A 545	

Approval Comments

O.K as is. Caution avoid shallow channel margin. (The proposed well location will be 100 ft NE of a shallow channel margin.)

Form MMS 123A/123S - Electronic Version

Application for Permit to Drill a New Well

Lease G17199 Area/Block HI A 545 Well Name 002 ST 00 BP 00 Well Exploration
Application Status Approved Operato 01764 Energy Resource Technology, Inc.

Geologic Information

H2S Designation Absent	H2S TVD
Anticipated Geologic Markers	
Name	Top MD
Lentic 1	8131

Rig Information

RIG SPECIFICATIONS		ANCHORS No	
Rig Name	ROWAN LOUISIANA		
Type	JACKUP	ID Number	91307
Function	DRILLING	Constructed	1975
Shipyard	LETOURNEAU	Refurbished	
RATED DEPTHS			
Water Depth	300	Drill Depth	20000
CERTIFICATES			
ABS/DNV	12/03/2011	Coast Guard	12/04/2007
SAFE WELDING AREA			
Approval Date	12/24/2002	District	3.0
Remarks			

Form MMS 123A/123S - Electronic Version

Application for Permit to Drill a New Well

Lease G17199 **Area/Block** HI A 545 **Well Name** 002 **ST** 00 **BP** 00 **Well** Exploration
Application Status Approved **Operato** 01764 Energy Resource Technology, Inc.

Question Information

Number	Question	Resposns	Response Text
1	Will you maintain quantities of mud and mud material (including weight materials and additives) sufficient to raise the entire system mud weight 1/2 ppg or more?	YES	452 sxs of barite and 200 sxs of gel will be maintained on the rig during drilling operations. See Attachment "Barite Sack Calculations?" for deta
2	If hydrocarbon-based drilling fluids were used, is the drilling rig outfitted for zero discharge and will zero discharge procedures be followed?	N/A	
3	If drilling the shallow casings strings riserless, will you maintain kill weight mud on the rig and monitor the wellbore with an ROV to ensure that it is not flowing?	N/A	
4	If requesting a waiver of the conductor casing, have you submitted a log to MMS G&G that is with in 500 feet of the proposed bottom hole location for the proposed surface casing point?	N/A	
5	Will the proposed operation be covered by an EPA Discharge Permit? (please provide permit number in comments for this question)	YES	All drilling mud and cuttings will be discharged in compliance with the NPDES Permit No. GMG 290079. No fluids containing free oil will be discharged. Daily discharge rates will vary over the duration of the drilling process. EPA outfall discharge numbers for HI A545 #2 Lease OCS-G 17199 have been applied for with EPA. See Attachment ?HI A545 #2 EPA NOI? for details.
6	Will all wells in the well bay and related production equipment be shut-in when moving on to or off of an offshore platform, or from well to well on the platform? If not, please explain.	N/A	

Form MMS 123A/123S - Electronic Version

Application for Permit to Drill a New Well

Lease G17199 **Area/Block** HI A 545 **Well Name** 002 **ST** 00 **BP** 00 **Well** Exploration
Application Status Approved **Operato** 01764 Energy Resource Technology, Inc.

Permit Attachments

File Type	File Description	Status
-----------	------------------	--------

Required Attachments

pdf	Proposed Well Location Plat	Attached
pdf	Drilling prognosis and summary of drilling, cementing, and mud processes	Attached
pdf	Directional Program	Attached
pdf	Engineering Calculation	Attached
pdf	Proposed Wellbore Schematic	Attached
pdf	Pore pressure (PP), Mud Weight (MW), and Fracture Gradient (FG) Plot	Attached
pdf	BOP & Diverter Schematics with Operating Procedures	Attached

Optional/Supplemental Attachments

pdf	HI A 545 #2 Compliance Work Sheet NTL 2007 G13	Attached
pdf	HIA 545 #2 OSFR Coverage - Apache	Attached
pdf	HI A545 #2 MMS Form 123S	Attached
pdf	HI A545 #2 EPA NOI	Attached
pdf	HI A545 #2 Barite Sack Calculations	Attached

Form MMS 123A/123S - Electronic Version

Application for Permit to Drill a New Well

Lease G17199 Area/Block HI A 545 Well Name 002 ST 00 BP 00 Well Exploration
Application Status Approved Operato 01764 Energy Resource Technology, Inc.

Well Design Information

Interval Number 1		Type Casing			Name Conductor		
Section Number	Casing Size (in)	Casing Weight (lb/ft)	Casing Grade	Burst Rating	Collapse Rating (psi)	Depth (ft) MD TVD	Pore Pressure (ppg)
1	20.0	94.0	K-55	2110.0	520.0	1000. 1000.	8.5
GENERAL INFORMATION		PREVENTER INFORMATION			TEST INFORMATION		
Hole Size (in)	26.0	Type	Diverter		Annular Test (psi)	0.0	
Mud Weight (ppg)	9.0	Size (in)	30		BOP/Diverter Test	250.0	
Mud Type Code	Water Base	Wellhead Rating	3000		Test Fluid Weight	9.0	
Fracture Gradient	10.6	Annular Rating (psi)	0		Casing/Liner Test	250.0	
Liner Top Depth (ft)	0.0	BOP/Diverter Rating	1000		Formation Test (ppg)	0.0	
Cement Volume (cu)	1988.0						
Interval Number 2		Type Casing			Name Surface		
Section Number	Casing Size (in)	Casing Weight (lb/ft)	Casing Grade	Burst Rating	Collapse Rating (psi)	Depth (ft) MD TVD	Pore Pressure (ppg)
1	13.375	68.0	HCN-80	5020.0	2910.0	3100. 3100.	9.0
GENERAL INFORMATION		PREVENTER INFORMATION			TEST INFORMATION		
Hole Size (in)	17.5	Type	Blowout		Annular Test (psi)	3500.0	
Mud Weight (ppg)	9.5	Size (in)	13.625		BOP/Diverter Test	5000.0	
Mud Type Code	Water Base	Wellhead Rating	5000		Test Fluid Weight	9.5	
Fracture Gradient	14.0	Annular Rating (psi)	5000		Casing/Liner Test	3500.0	
Liner Top Depth (ft)	0.0	BOP/Diverter Rating	10000		Formation Test (ppg)	14.0	
Cement Volume (cu)	2545.0						
Interval Number 3		Type Casing			Name Production		
Section Number	Casing Size (in)	Casing Weight (lb/ft)	Casing Grade	Burst Rating	Collapse Rating (psi)	Depth (ft) MD TVD	Pore Pressure (ppg)
1	9.625	53.5	P-110EC	12390.0	9140.0	6300. 6300.	13.0
GENERAL INFORMATION		PREVENTER INFORMATION			TEST INFORMATION		
Hole Size (in)	12.25	Type	Blowout		Annular Test (psi)	3500.0	
Mud Weight (ppg)	13.5	Size (in)	13.625		BOP/Diverter Test	7500.0	
Mud Type Code	Water Base	Wellhead Rating	10000		Test Fluid Weight	13.5	
Fracture Gradient	17.0	Annular Rating (psi)	5000		Casing/Liner Test	7200.0	
Liner Top Depth (ft)	0.0	BOP/Diverter Rating	10000		Formation Test (ppg)	17.0	
Cement Volume (cu)	1202.0						

Form MMS 123A/123S - Electronic Version

Application for Permit to Drill a New Well

Lease G17199 Area/Block HI A 545 Well Name 002 ST 00 BP 00 Well Exploration
Application Status Approved Operato 01764 Energy Resource Technology, Inc.

Well Design Information

Interval Number 4		Type Liner			Name Production		
Section Number	Casing Size (in)	Casing Weight (lb/ft)	Casing Grade	Burst Rating	Collapse Rating (psi)	Depth (ft) MD TVD	Pore Pressure (ppg)
1	7.625	33.7	HCP-110	10860.0	8800.0	8605. 8605.	16.0
GENERAL INFORMATION		PREVENTER INFORMATION			TEST INFORMATION		
Hole Size (in)	8.5	Type	Blowout		Annular Test (psi)	3500.0	
Mud Weight (ppg)	16.5	Size (in)	13.625		BOP/Diverter Test	7500.0	
Mud Type Code	Water Base	Wellhead Rating	10000		Test Fluid Weight	16.5	
Fracture Gradient	17.8	Annular Rating (psi)	5000		Casing/Liner Test	1000.0	
Liner Top Depth (ft)	5800.0	BOP/Diverter Rating	10000		Formation Test (ppg)	0.0	
Cement Volume (cu)	237.0						

PAPERWORK REDUCTION ACT OF 1995 (PRA) STATEMENT: The PRA (44 U.S.C. 3501 et seq. Requires us to inform you that we collect this information to obtain knowledge of equipment and procedures to be used in drilling operations. MMS uses the information to evaluate and approve or disapprove the adequacy of the equipment and/or procedures to safely perform the proposed drilling operation. Responses are mandatory (43 U.S.C. 1334). Proprietary data are covered under 30 CFR 250.196. An agency may not conduct or sponsor, and a person is not required to respond to, a collection of information unless it displays a currently valid OMB Control Number. Public reporting burden for this form is estimated to average 27 hours per response, including the time for reviewing instructions, gathering and maintaining data, and completing and reviewing the form. Direct comments regarding the burden estimate or any other aspect of this form to the

**High Island A-545
OCS-G 17199
Well #2
Rowan Louisiana
APD DRILLING PROCEDURE**

General: The following general drilling program will be utilized to drill this well. This program is subject to change based on actual drilling operations. All drilling operations will be in compliance with all applicable state and government rules and regulations.

- 1) MOL. RU and drive 30" by 1" drive pipe to +/-548' RKB (+/- 200 BML).
- 2) NU 30" diverter system and function test the assembly.
- 3) Wash out the drive pipe. Drill 26" hole. Survey as required.
- 4) Set 20" conductor casing at +/-1,000' MD/TVD.
- 5) Cement casing back to the surface.
- 6) WOC. ND diverter. Cut casing, Weld on 20" SOW X 20 3/4" 3M casing head. Test weld to 50% collapse.
- 7) NU diverter system and function test the assembly.
- 8) Test casing and diverter to 250 psi with 9.0 ppg mud in hole.
- 9) Drill 17 1/2" hole to 3,100' MD/TVD.
- 10) Set 13 3/8" surface casing.
- 11) Cement casing back to the mud line.
- 12) WOC. ND diverter, install casing head. NU 20 3/4" 3M X 13 5/8" 5M casing head. Test to 50% of collapse.
- 13) NU BOP's. Test rams to 5000 psi / 250 psi and annular to 3500 psi / 250 psi.
- 14) Test casing to 3500 psi with 9.5 ppg mud in hole.
- 15) Drill out and test shoe to maximum of 14.0 ppg FIT or leakoff.
- 16) Drill 12 1/4" hole to +/-6,300' MD / TVD.
- 17) Set 9 5/8" intermediate casing.
- 18) Cement 9 5/8" csg, bringing TOC to 2600'.
- 19) ND BOP , set slips , NU 13 5/8" 5M x 11" 10M wellhead.
- 20) NU 13 5/8" 10M BOP's. Test rams 250 psi / 7,500 psi and annular to 250 psi / 3500 psi.
- 21) Test 9 5/8" casing to 7200 psi with 13.5 ppg mud

High Island A-545

OCS-G 17199

Well #2

Rowan Louisiana

APD DRILLING PROCEDURE

- 22) Drill out and test shoe to maximum of 17.0 ppge or leakoff.
- 23) Drill 8 1/2" hole to +/-8,605' MD/TVD.
- 24) Run 7 5/8" production liner and cement same to +/-5,800' MD (top of liner).
- 25) Test casing and liner top to 1,000 psi with 16.5 ppg mud.
- 26) Complete well under separate APM.

High Island A-545
 OCS-G 17199
 Well #2
 Cementing Program

Drive Pipe Drive 30 inch csg to 548 ft MD. No cement planned.

Conductor Set 20 inch csg at 1000 ft MD and cement same to surface.

Cement Type	TOC	BOC	ftg	yield	wght
Lead Slurry	0	600	600	3.07	11.4
Tail Slurry	600	1000	400	1.10	16.4

Capacities	ft3/ft	bpf
Csg x csg annulus	2.094	0.373
Csg x OH annulus	1.505	0.268
Shoe track	1.995	0.355

Cement Volumes	Cmt	ftg	ft3	sks	Total sks	
Csg x csg annulus	lead	548	1148	374		
Csg x OH annulus	lead	52	78	25	399	lead
Csg x OH annulus	tail	400	602	547		
Shoe track	tail	80	160	145	692	tail
			1988	1092		

Surface Set 13.375 inch csg at 3100 ft MD and cement same to surface.

Cement Type	TOC	BOC	ftg	yield	wght
Lead Slurry	0	2600	2600	3.07	11.4
Tail Slurry	2600	3100	500	1.06	16.4

Capacities	ft3/ft	bpf
Csg x csg annulus	1.019	0.182
Csg x OH annulus	0.695	0.124
Shoe track	0.841	0.150

Cement Volumes	Cmt	ftg	ft3	sks	Total sks	
Csg x csg annulus	lead	1000	1019	332		
Csg x OH annulus	lead	1600	1111	362	694	lead
Csg x OH annulus	tail	500	347	328		
Shoe track	tail	80	67	63	391	tail
			2545	1085		

Intermediate Set 9.625 inch csg at 6300 ft MD and bring TOC to 2600 ft MD.

Cement Type	TOC	BOC	ftg	yield	wght
Lead Slurry	2600	5300	2700	1.39	13.7
Tail Slurry	5300	6300	1000	1.07	16.4

Capacities	ft3/ft	bpf
Csg x csg annulus	0.335	0.060
Csg x OH annulus	0.313	0.056
Shoe track	0.397	0.071

Cement Volumes	Cmt	ftg	ft3	sks	Total sks	
Csg x csg annulus	lead	500	168	121		
Csg x OH annulus	lead	2200	689	496	616	lead
Csg x OH annulus	tail	1000	313	293		
Shoe track	tail	80	32	30	322	tail
			1202	939		

High Island A-545
 OCS-G 17199
 Well #2
 Cementing Program

Prod Liner Set 7.625 inch liner at 8605 ft MD and cement to 5800 ft MD (TOL).

Cement Type	TOC	BOC	ftg	yield	wght
Tail Slurry	5800	8605	2805	1.27	17.0

Capacities	ft3/ft	bpf
Csg x csg annulus	0.080	0.014
Csg x OH annulus	0.077	0.014
Shoe track	0.250	0.044

Cement Volumes	Cmt	ftg	ft3	sks	bbbls
Csg x csg annulus	tail	500	40	32	7.1
Csg x OH annulus	tail	2305	177	140	31.6
Shoe track	tail	80	20	16	3.6
			237	187	42.3

High Island A-545
OCS-G 17199
Well #2
Casing Design

Drive Pipe

Csg OD	Csg ID	Gr	Wght	IYP (psi)	Coll (psi)	Ten (body)	Ten (conn)	Conn	Top (MD)	Top (TVD)	Depth (MD)	Depth (TVD)
30.000	28.000	B	309.7	2042	1364	3189.0	3189.0	Welded	0	0	548	548

Conductor

Csg OD	Csg ID	Gr	Wght	IYP (psi)	Coll (psi)	Ten (body)	Ten (conn)	Conn	Top (MD)	Top (TVD)	Depth (MD)	Depth (TVD)
20.000	19.124	K55	94.0	2110	520	1480.0	1402.0	BTC	0	0	1000	1000
MWe (external MW)		9.00										
FG @ shoe		10.60										
Gas Gradient		0.10										

	Load	SF
Burst Load (psi):	451	4.68
=(FG x TVD x 0.052) - (GG x TVD)		
Collapse Load (psi):	368	1.41
=(MWe x TVD x 0.052) - (GG x TVD)		
Tensile Load (klbs):	94	14.91
=(Csg ppf x MD)/1000		

Surface

Csg OD	Csg ID	Gr	Wght	IYP (psi)	Coll (psi)	Ten (body)	Ten (conn)	Conn	Top (MD)	Top (TVD)	Depth (MD)	Depth (TVD)
13.375	12.415	HCN80	68.0	5020	2910	1556.0	1732.0	BTC	0	0	3100	3100
MWe (external MW)		9.50										
FG @ shoe		14.00										
Gas Gradient		0.10										

	Load	SF
Burst Load (psi):	1947	2.58
=(FG x TVD x 0.052) - (GG x TVD)		
Collapse Load (psi):	1221	2.38
=(MWe x TVD x 0.052) - (GG x TVD)		
Tensile Load (klbs):	211	8.22
=(Csg ppf x MD)/1000		

Intermediate

Csg OD	Csg ID	Gr	Wght	IYP (psi)	Coll (psi)	Ten (body)	Ten (conn)	Conn	Top (MD)	Top (TVD)	Depth (MD)	Depth (TVD)
9.625	8.535	P110EC	53.5	12390	9140	1943.0	1422.0	LTC	0	0	6300	6300
MWe (external MW)		13.50										
FG @ shoe		17.00										
Gas Gradient		0.10										

	Load	SF
Burst Load (psi):	4939	2.51
=(FG x TVD x 0.052) - (GG x TVD)		
Collapse Load (psi):	3793	2.41
=(MWe x TVD x 0.052) - (GG x TVD)		
Tensile Load (klbs):	337	4.22
=(Csg ppf x MD)/1000		

High Island A-545
 OCS-G 17199
 Well #2
 Casing Design

Prod Liner

Csg OD	Csg ID	Gr	Wght	IYP (psi)	Coll (psi)	Ten (body)	Ten (conn)	Conn	Top (MD)	Top (TVD)	Depth (MD)	Depth (TVD)
7.625	6.765	P110 HC	33.7	10860	8800	1069.0	714.0	STL	5900	5900	8605	8605

MWe (external MW)	16.50
PP (at TD)	16.00
TVD	8605
Gas Gradient	0.10

	Load	SF
Burst Load (psi):	6299	1.72
→(PP *TVD x 0.052) - (GG x TVD)		
Collapse Load (psi):	6523	1.35
→(MWe x TVD x 0.052) - (GG x TVD)		
Tensile Load (klbs):	91	7.83
→(Csg ppf x length)/1000		

High Island A-545
 OCS-G 17199
 Well #2

Maximum Anticipated Surface Pressure (MASP)

Drive Pipe	Csg OD	Csg ID	Gr	Wght	IYP (psi)	Coll (psi)	Ten (body)	Ten (conn)	Conn	Top (MD)	Top (TVD)	Depth (MD)
	30.000	28.000	B	309.7	2042	1364	3189.0	3189.0	Welded	0	0	548

No Csg Test

Conductor	Csg OD	Csg ID	Gr	Wght	IYP (psi)	Coll (psi)	Ten (body)	Ten (conn)	Conn	Top (MD)	Top (TVD)	Depth (MD)
	20.000	19.124	K55	94.0	2110	520	1480.0	1402.0	BTC	0	0	1000
FG @ shoe				10.60								
Gas Gradient				0.10								
MWI @ shoe				9.00								

MASP (psi): 451

= (FG x TVD x 0.052) - (GG x TVD)

Selected Csg Test Pressure (psi) 250

Surface	Csg OD	Csg ID	Gr	Wght	IYP (psi)	Coll (psi)	Ten (body)	Ten (conn)	Conn	Top (MD)	Top (TVD)	Depth (MD)
	13.375	12.415	HCN80	68.0	5020	2910	1556.0	1732.0	BTC	0	0	3100
FG @ shoe				14.00								
Gas Gradient				0.10								
MWI @ shoe				9.50								
MWbu (backup)				9.00								
MWoh (OH below shoe)				13.50								
TVDoh				6300								

MASP (psi): 1947

= (FG x TVD x 0.052) - (GG x TVD)

Calculated Csg Test Pressure (psi) 3433

= (0.70 x IYP) - ((MWI - MWbu) x TVD x 0.052)

Selected Csg Test Pressure (psi) 3500

Intermediate	Csg OD	Csg ID	Gr	Wght	IYP (psi)	Coll (psi)	Ten (body)	Ten (conn)	Conn	Top (MD)	Top (TVD)	Depth (MD)
	9.625	8.535	P110EC	53.5	12390	9140	1943.0	1422.0	LTC	0	0	6300
FG @ shoe				17.00								
Gas Gradient				0.10								
MWI @ shoe				13.50								
MWbu (backup)				9.00								
MWoh (OH below shoe)				17.00								
TVDoh				8605								

MASP (psi): 4939

= (FG x TVD x 0.052) - (GG x TVD)

MASP (psi): 2462

= (FG x TVD x 0.052) - 0.667(GG x TVDoh) - 0.333(MWoh x TVDoh x 0.052)

Calculated Csg Test Pressure (psi) 7199

= (0.70 x IYP) - ((MWI - MWbu) x TVD x 0.052)

Selected Csg Test Pressure (psi) 7200

} Use lesser of these for MASP 2462

Prod Liner

Csg OD	Csg ID	Gr	Wght	IYP (psi)	Coll (psi)	Ten (body)	Ten (conn)	Conn	Top (MD)	Top (TVD)	Depth (MD)
7.625	6.765	P110 HC	33.7	10860	8800	1069.0	714.0	STL	5900	5900	8605
PP @ TD			16.00								
FGps (prev. shoe)			17.00								
TVDps (prev. shoe)			6300								
MWI @ shoe			16.50								
MWbu (backup)			9.00								
Gas Gradient			0.10								

MASP (psi):

6299

= (PP * TVD x 0.052) - (GG x TVD)

Calculated Liner lap test pressure (psi)

664

= ((FGps - MWI) x TVDps x 0.052) + 500

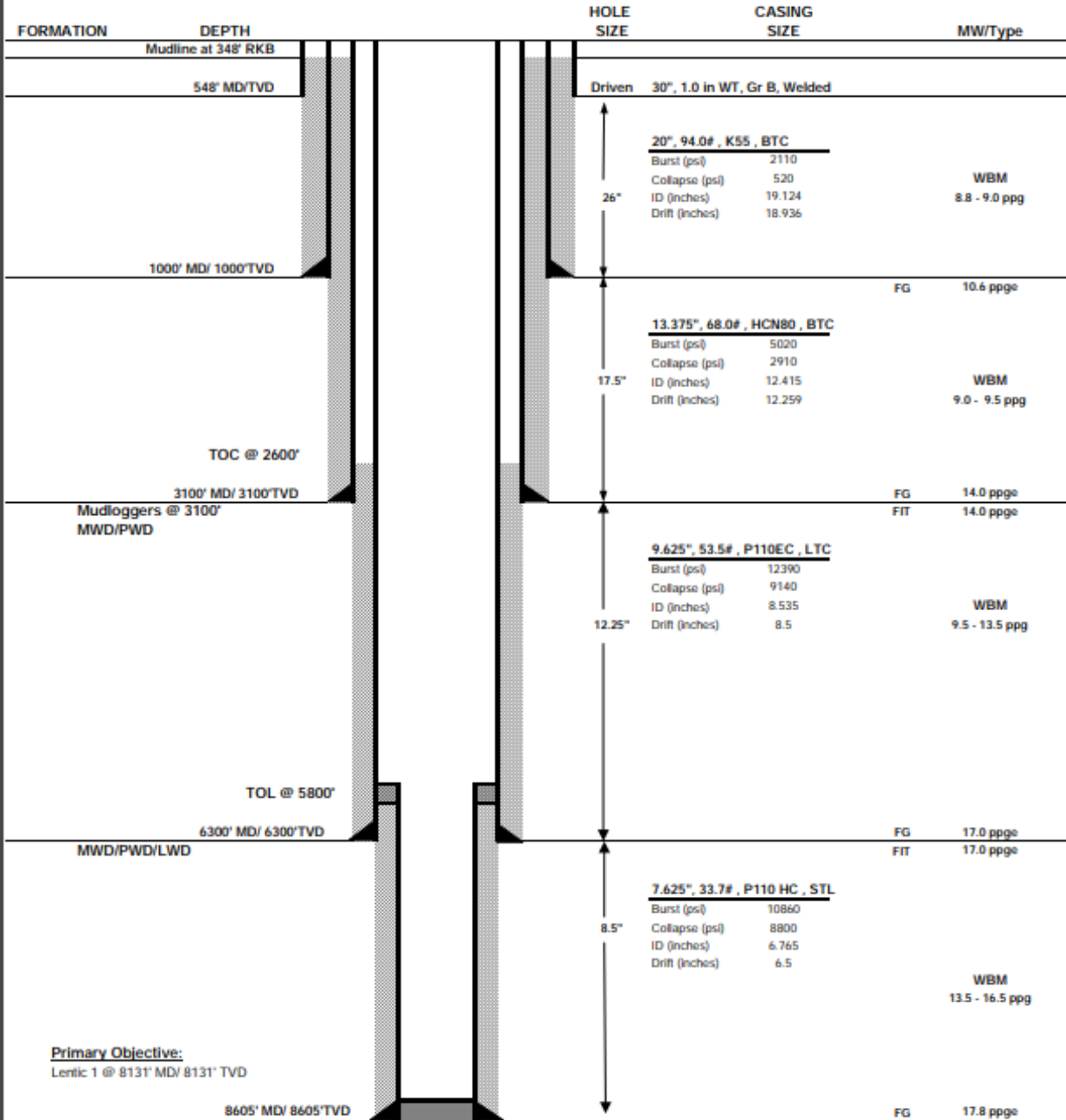
Selected Csg Test Pressure (psi)

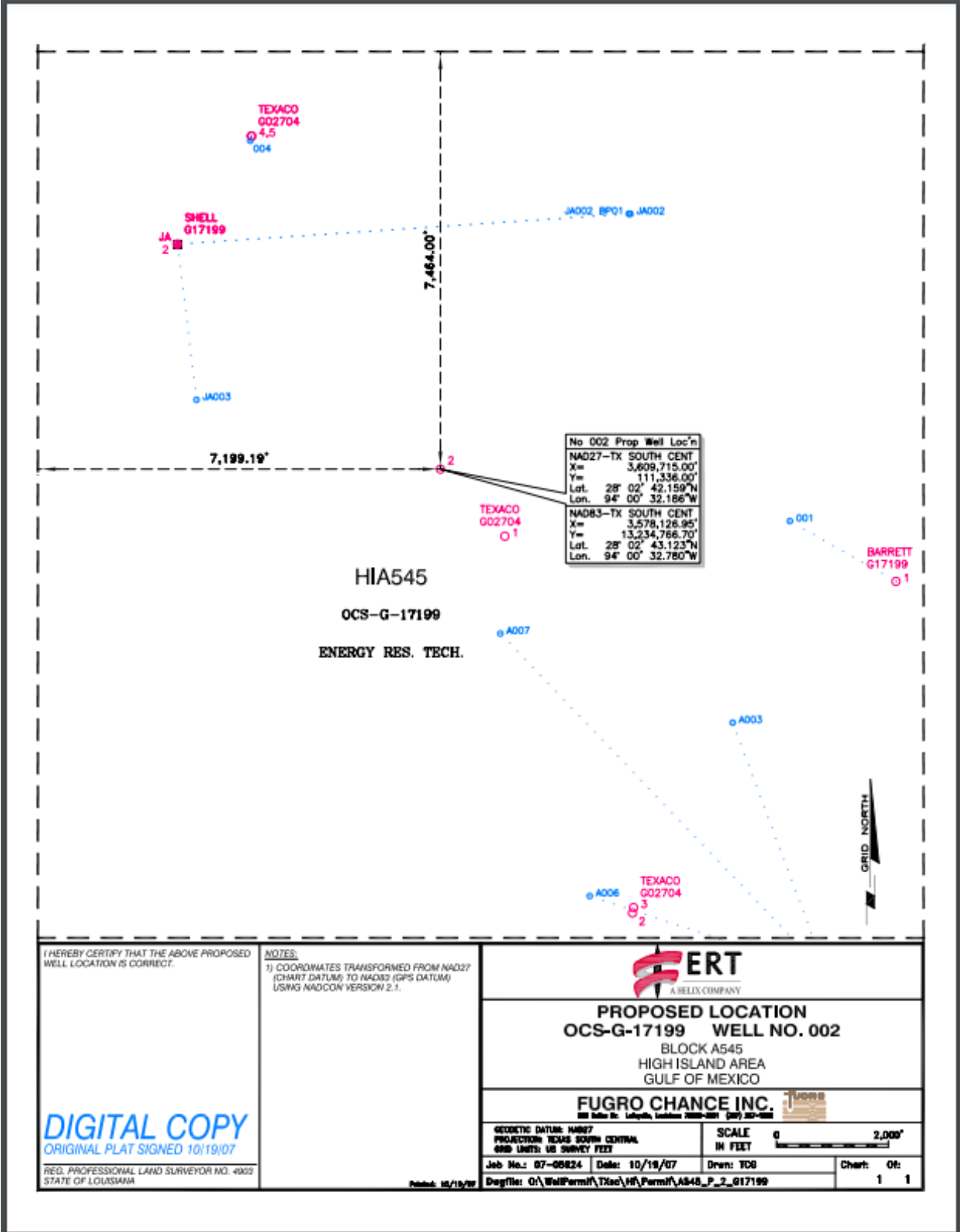
1000

Liner lap

ERT Gulf of Mexico PROPOSED DRILLING SCHEMATIC

OPERATOR:	ERT Gulf of Mexico	DATE:	07/31/07
WELL NAME:	High Island A-545	TD:	8605 MD/ 8605 TVD
FIELD / PROSPECT:	OCS-G 17199 Well #2	RKB:	105
SURFACE LOCATION:	X=3,609,715.00 Y=111,336.00	WD:	243
BOTTOM HOLE LOC:	X=3,609,715.00 Y=111,336.00	RIG:	Rowan Louisiana
			Straight Hole





I HEREBY CERTIFY THAT THE ABOVE PROPOSED WELL LOCATION IS CORRECT.

NOTES:
1) COORDINATES TRANSFORMED FROM NAD27 (CHART DATUM) TO NAD83 (GPS DATUM) USING NADCON VERSION 2.1.

DIGITAL COPY
ORIGINAL PLAT SIGNED 10/19/07

REG. PROFESSIONAL LAND SURVEYOR NO. 49025
STATE OF LOUISIANA

Printed: 10/19/07



PROPOSED LOCATION
OCS-G-17199 WELL NO. 002
BLOCK A545
HIGH ISLAND AREA
GULF OF MEXICO

FUGRO CHANCE INC.

GEODETIC DATUM: NAD83 PROJECTION: TEXAS SOUTH CENTRAL GRID UNITS: US SURVEY FEET	SCALE IN FEET 1" = 2,000'
Job No.: 07-08824 Date: 10/19/07 Drawn: FCG	Chart: 01: 1 1
Drawfile: G:\WellPermit\TX\01\H\Permit\A545_P_2_017199	

ENERGY RESOURCE TECHNOLOGY, INC. (ERT)

HIGH ISLAND BLOCK A-545, OCS-G 17199, WELL NO. 02

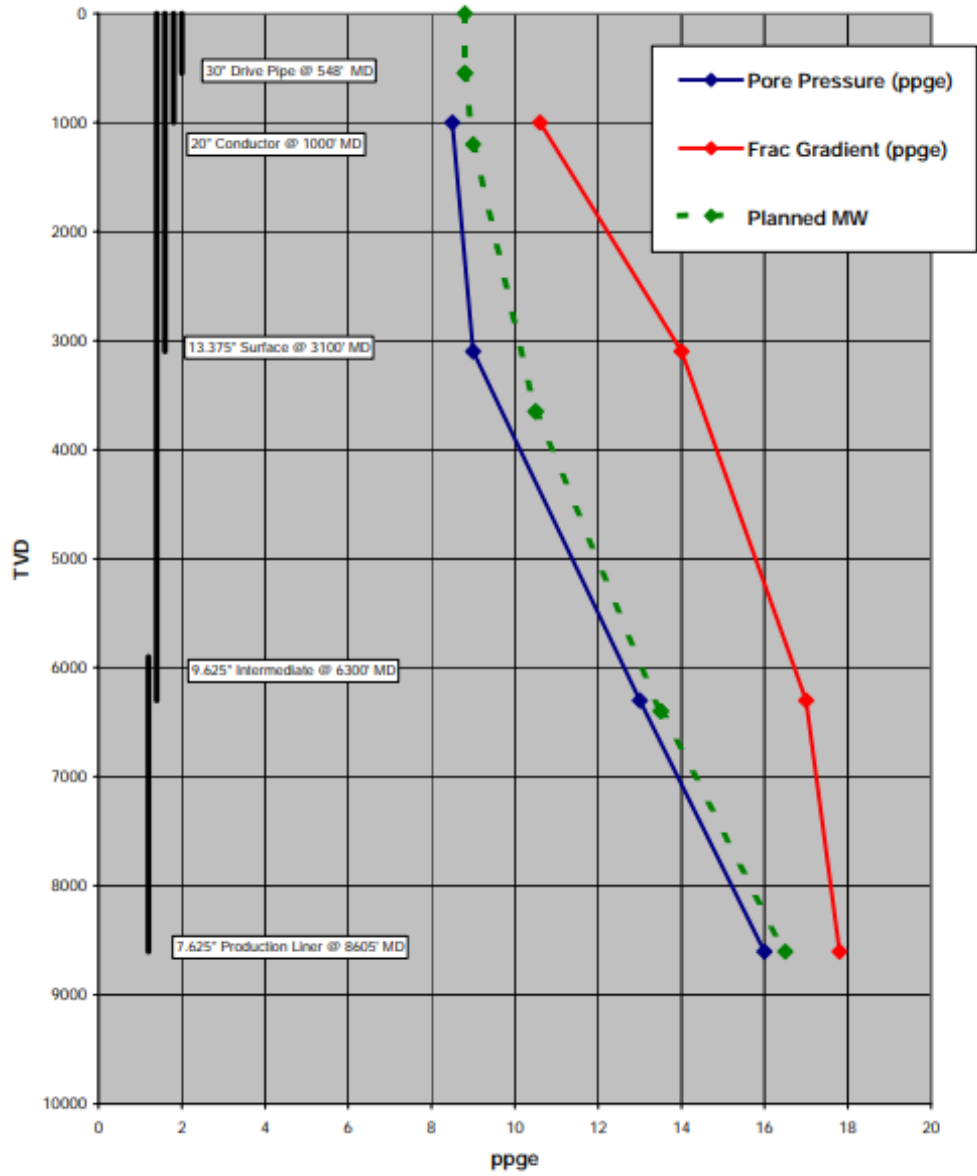
PROPOSED DIRECTIONAL PLAN

NOT APPLICABLE

**WELLBORE WILL BE A VERTICAL HOLE DRILLED TO A PROPOSED
TD OF 8605' MD / TVD**

Csg Program/PPFG

High Island A-545 Well #2



DIVERTER PROCEDURES FOR ROWAN LOUISIANA

While drilling:

1. Pick up pipe above rotary to the closing position.
2. Shut down pumps.
3. Check for flow.
4. If flowing, close diverter system – diverter packer will close and diverter valves will open simultaneously.
5. Circulate seawater at a high rate.

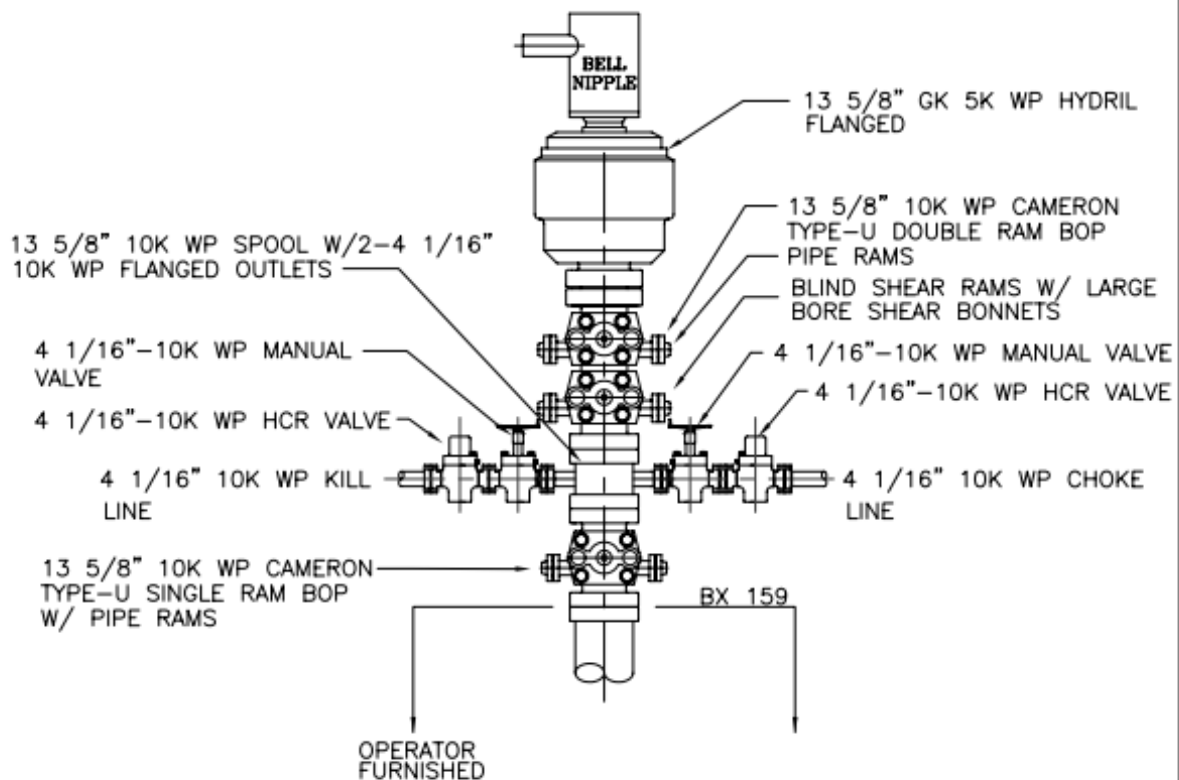
While tripping:


1. Check for flow.
2. If flowing, install full opening safety valve.
3. Close diverter system – diverter packer will close and diverter valves will open simultaneously.
4. Pick up top drive.
5. Circulate seawater at a high rate.

Note: Remington's policy is **not** to shut-in the diverter system after cementing either the conductor or surface casing.

Should the pressure on the annular preventer reach between 2000 – 3000 psi, Remington will then immediately closed the pipe rams to prevent the annular being subject to pressures that would exceed the working pressure of the preventer.

Note: Should both diverter valves open and the wind is strong enough to blow back gas to the rig, the up wind diverter will be closed.



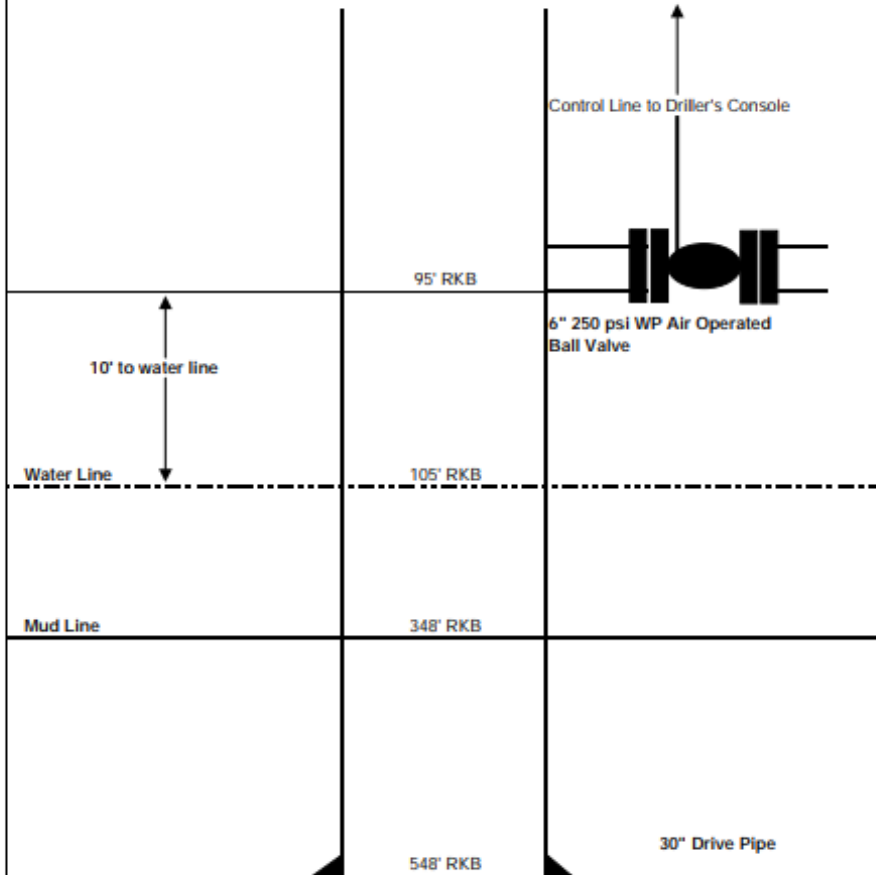
 ROWAN COMPANIES, INC.		HOUSTON, TEXAS	
TITLE ROWAN LOUISIANA-016 3-5/8"-10K STACK ASS. W/WELLHEAD			
DR.	L.G.	RIG 016	DATE 11/6/06
CK.	LARRY G.	DIVISION G.O.M.	DWG. NO. 16BOP
SCALE	NONE		

ERT

High Island A-545
OCS-G 17199
Well #2

Typical 6" (Plus 10') Ball Valve Installation

Valve is used to reduce the mud hydrostatic pressure during the primary cementing of the surface casing. The valve is installed 10' above the water line after the drive pipe is driven to its setting depth. The valve is removed and the outlet in the drive pipe is plugged after the surface casing is cemented back to the surface. The valve will be continuously monitored during drilling operations as noted in the APD information worksheet.



ENERGY RESOURCE TECHNOLOGY, INC. (ERT)
HIGH ISLAND BLOCK A545, OCS-G 17199, WELL NO. 002
BARITE SACK CALCULATIONS TO WIEGHT UP SYSTEM 0.50 PPG

Csg. Ft.	bbls/ft	csg. vol.	Hole Ft.	bbl/ft	hole vol.	pit vol.	total vol
6300.0	0.0707	445.4	2305.0	0.0702	161.8	500.0	1107.3
Initial MW	Final MW	Sxs/bbls	Sacks Required				
16.5	17.0	40.8	452.1				

Depth of Casing Above Prod Csg.	6300.0
Bbbls/ft.	
9 5/8"53.5#/FT	0.0707
From Halliburton Book	
Casing Volume	445.4
Depth of Casing Above Prod Csg.	
bbls/ft	
Hole ft.	2305.0
TD - Last Casing	
bbls/ft	0.0702
Prod Casing Hole size squared divided by 1029	
Open Hole Volume	161.8
bbls/ft x TD - Last Casing	
Pit Volume	500.0
Normally in pit	
Total Volume	1107.3
Pit Volume + Hole Volume + Csg. Volume	
Sacks per Bbl	40.8
$1470 \cdot (15.0 - 14.5) / (35 - 15.0)$	
$1470 \cdot (M_2 - M_1) / (35.0 - M_2)$	
$M_1 = \text{MW @ TD}$	
$M_2 = \text{MW @ TD} - .5$	
Sacks to make 1 bbl of mud	0.4083
Sacks/bbl divided by 100	
Sacks Required	452.1
Sacks to make 1 bbl of mud x Total Volume	



Notice of Intent for the Offshore Subcategory of the Oil and Gas Extraction Point Source Category for the Western Portion of the Outer Continental Shelf of the Gulf of Mexico (GMG290000).

U.S. EPA Region 6
Offshore General Permits
Mail Code 6EN-WC
P.O. Box 50625
Dallas, TX 75250-0625

Submission of this completed Notice of Intent (NOI) constitutes notice that the entity in Section B intends to be authorized to discharge pollutants to Federal waters of the Gulf of Mexico seaward of the outer boundary of the territorial seas offshore of Louisiana and Texas [64 Fed. Reg. No. 74, pp 19156-19177, April 19, 1999, and modified with an effective date of Feb. 16, 2003, www.epa.gov/region6/6en/w/offshore/permit02162002.pdf]. Submission of the NOI also constitutes notice that the party identified in Section B of this form has read, understands, and meets the eligibility conditions in the **Regulated Entities** section of the Final General Permit for the above mentioned permit; agrees to comply with all applicable terms and conditions of the General Permit. In order to be granted coverage, **all information required on this form must be completed** unless designated as optional. Please read and make sure you comply with all permit requirements.

Section A: Permit Selection

Permit Number assigned to your facility under the previous or existing permit: GMG29 0079 Not Assigned

Section B: Facility Legal Name and Address of Operator

1. Operator Name: Energy Resource Technology GOM, Inc.

Contact Name (optional): Wendy Braddock

Phone Number & e-mail (optional): (281) 618-0551 wbraddock@helixesg.com

2. Mailing Address (Street or PO Box): 400 N. Sam Houston Parkway E., Ste. 400

3. City: Houston State: TX Zip Code: 77060

Section C: List of lease areas/block numbers assigned by the Department of Interior or the State, if none, the name commonly assigned to the lease area, state whether non-aqueous based drilling fluids (synthetic based muds (SBM)) will be used (Y=Yes, N=No).

	SBM Y/N	EPA Use		SBM Y/N	EPA Use
High Island A-545	N				

For additional lease area/blocks, please list the names on another page with the certification statement at the bottom, signature of authorized official, and date.

Section D: New Source

NOI must identify any facility which is a New Source and state the date on which the facility's protection from more stringent new source performance standards or technology based limitations ends. That date is the soonest of ten years from the date that construction is completed, ten years from the date the source begins to discharge process or non-construction related wastewater, or the end of the period of depreciation or amortization of the facility for the purposes of section 167 or 169 (or both) of the Internal Revenue Code of 1954. See 58 Fed. Reg. No. 12504 and 61 Fed. Reg. No. 66085 for more information.

New Source: Yes Date: 10/01/2007 No

Section E: Certification

I certify under penalty of law that this document and all attachments were prepared under my direction or supervision in accordance with a system designed to assure that qualified personnel properly gather and evaluate the information submitted. Based on my inquiry of the person or persons who manage the system, or those persons directly responsible for gathering the information, the information submitted is, to the best of my knowledge and belief, true, accurate, and complete. I am aware that there are significant penalties for submitting false information, including the possibility of fine and imprisonment for knowing violations.

Print Name: Johnny Edwards

Signature: _____ Date (mm/dd/yy): 8 / 27 / 07

Title: President

Modified November 2002 by EPA Region 6 for use with the general permit referenced above. Copies of this form may be obtained on the Internet at: <http://www.epa.gov/region6/6en/w/forms.htm> and more information on Offshore permits can be found at <http://www.epa.gov/region6/6en/w/offshore/home.htm>



Notice of Intent for the Offshore Subcategory of the Oil and Gas Extraction Point Source Category for the Western Portion of the Outer Continental Shelf of the Gulf of Mexico (GMG290000).

U.S. EPA Region 6
Offshore General Permits
Mail Code 6EN-WC
P.O. Box 50625
Dallas, TX 75250-0625

Instructions

This form is an optional form prepared to assist applicants in the completion of the Notice of Intent for the EPA Region 6 Western Outer Continental Shelf National Pollutant Discharge Elimination System permit [64 Fed. Reg. No. 74, pp 19156-19177, April 19, 1999, and modified at 66 Fed. Reg. No. 242, p. 65209, December 18, 2001] in accordance with Part I.A.2. of the permit. The permit language can be found on the internet at www.epa.gov/region6/6en/w/offshore/permit02162002.pdf.

When to File the NOI Form:

All NOI's must be submitted at least 14 days prior to the commencement of discharge.

Where to File the NOI Form:

U.S. EPA Region 6
Water Enforcement Branch (6EN-WC)
P.O. Box 50625
Dallas, TX 75250-0625

Completing the NOI Form:

Please ensure all sections and requirements of this NOI form have been completed. Failure to submit a completed NOI will delay coverage as the omitted data will have to be requested and submitted prior to coverage. You will only receive SBM Discharge Monitoring Report forms for those properties you identify as using SBMs.

NOI Certification: Federal statutes provide for severe penalties for submitting false information on this application form. Federal regulations require this application to be signed as follows:

For a corporation: by a responsible corporate officer, which means: (i) president, secretary, treasurer, or vice-president of the corporation in charge of a principal business function, or any other person who performs similar policy or decision making functions, or (ii) the manager of one or more manufacturing, production, or operating facilities employing more than 250 persons or having gross annual sales or expenditures exceeding \$25 million (in second-quarter 1980 dollars), if authority to sign documents has been assigned or delegated to the manager in accordance with corporate procedures;

For a partnership or sole proprietorship: by a general partner or the proprietor; or

For a municipality, state, Federal, or other public facility: by either a principal executive officer or ranking elected official.

Who is Not Authorized Under This General Permit:

Facilities which adversely affect properties listed or eligible for listing in the National Register of Historic Places.

Submit ORIGINAL plus THREE copies with ONE copy marked "Public Information".

U.S. Department of the Interior
Minerals Management Service (MMS)

SUPPLEMENTAL APD INFORMATION SHEET

1. OPERATOR NAME Energy Resource Technology - Gulf of Mexico		5. WELL NAME (Proposed) #2		6. TYPE OF WELL <input checked="" type="checkbox"/> EXPLORATORY <input type="checkbox"/> DEVELOPMENT		11. WATER DEPTH 243		12. ELEVATION AT R/S 105											
2. APD WELL NO. (Proposed) (12 digit) OCS-G 17199		3. BOTTOM LEASE NO. (Proposed) OCS-G 17199		7. SIDETRACK NO. (Proposed) 00		13. H ₂ S DESIGNATION <input type="checkbox"/> KNOWN <input type="checkbox"/> UNKNOWN <input checked="" type="checkbox"/> ABSENT		14. H ₂ S ACTIVATION PLAN DEPTH (TVD) N/A											
4. TOTAL DEPTH (Proposed) TVD 8,605		8. RIG NAME Rowan Louisiana		10. RIG TYPE JU															
15. ENGINEERING DATA																			
Hole Size (Casing & Annulus) (in)	Drive Pipe	Casing Size (in)	Weight (lb/ft)	Neve Rating (psi)	Type of Connection	Safety Factors	Casing Depth (ft)			Well Head Rating (psi)	RSDP Size (in)	Backlog (working Pressure) (psi)	Test Pressures		Casing Shoe (ft)	Casing Shoe (ft)	Drilling Fluid Type (Gel Based, water based, Synthetic)		
							B	C	T				MD	TD				PP	MO
30	B	2110	94	2110	Welded		548	548			30	10000	250	250	N/A	N/A	N/A		
26	Conductor	20	835	520	BTC	4.68 1.41 14.91	1000	8.5	9.0	10.8	3000	N/A	2500	2500	9.0	N/A	1808		
17 1/2	Surface	13 3/8	HC2M0	2910	BTC	2.58 2.38 8.22	3100	9.0	9.5	14.0	5000	5000	5000	5000	9.5	14.0	2545		
12 1/4	Intermediate	9 5/8	P110EC	9140	LTC	2.42 2.51 2.41	6300	11.0	11.5	17.0	10000	5000	7500	7500	11.5	17.0	1202		
8 1/2	Prod Liner	7 5/8	P110HC	8800	STL	1.72 1.35 7.83	8605	16.0	16.5	17.8	10000	5000	3500	3500	16.5	17.8	237		
16. CONTACT NAME J. V. DELCAMPRE										17. CONTACT PHONE NO. 337-952-9428									
18. Will you maintain quantities of mud and mud material (including weight materials and additives) sufficient to raise the entire system mud weight 12 ppg or more? YES										18. CONTACT E-MAIL ADDRESS jvdeltcampre@erdc.com									

19. REMARKS:

Minimum Quantities: A minimum of 817 sacks of barite and 200 sacks of gel will be kept aboard.
Zone Protection Statement: All zones containing hydrocarbons or fresh water will be protected by casing and/or cement per OCS Operating Regulations, 30 CFR 250.54.
Mud Disposal Statement: All drilling mud and cuttings will be discharged in compliance with MPOES General Discharge Permit GMS 290211. No fluids containing free oil will be discharged.
Daily discharge rates will vary over the duration of the drilling process.

Cement Volumes: Cement volumes are calculated without excess and are the minimum volumes that will be pumped.
Additional Requests: A 6" air activated valve will be installed in the drive string 10' above mean sea level.

MMS FORM MMS-1235 (4/1/2003) - Supersedes all previous versions of form MMS-1235 which may not be used.)

U.S. DEPARTMENT OF THE INTERIOR, MINERALS MANAGEMENT SERVICE, 1225 NORTH MICHIGAN AVENUE, SUITE 1000, ANCHORAGE, ALASKA 99501-5008. (907) 261-2000. FAX (907) 261-2001. WWW.MMS.DOI.GOV

J.V. Delcambre

From: wbraddock@helixesg.com
Sent: Thursday, September 06, 2007 3:08 PM
To: jv@regservicesinc.com
Cc: dlogan@helixesg.com
Subject: FW: HI A545
Importance: High

See Apache's agreement below to maintain OSFR coverage over all of HI A-545.

Wendy

*Wendy Braddock
Regulatory Manager
Energy Resource Technology, Inc.
(281) 618-0551 (Direct)
(281) 618-0544 (Fax)
wbraddock@helixesg.com*

From: Fred Deusinger
Sent: Thursday, September 06, 2007 2:37 PM
To: Wendy Braddock
Subject: FW: HI A545

FYI

**W. Fred Deusinger
Shelf Land Manager
Energy Resource Technology, Inc.
Office: 281-618-0531
Fax: 281-618-0544
Mobile: 281-770-1424**

From: Linscomb, Gene [mailto:Gene.Linscomb@usa.apachecorp.com]
Sent: Thursday, September 06, 2007 2:21 PM
To: Fred Deusinger
Subject: RE: HI A545

Apache will continue OSFR coverage.

Gene

-----Original Message-----
From: fdeusinger@helixesg.com [mailto:fdeusinger@helixesg.com]
Sent: Thursday, September 06, 2007 1:38 PM
To: Linscomb, Gene
Cc: wbraddock@helixesg.com
Subject: HI A545

9/11/2007

As we discussed today ERT is seeking a permit to drill and complete a well into the depths below 5,795' in which ERT owns 100% record title interest. As Apache is currently the operator of the only producing well and platform on the Block, Apache has OSFR coverage over the entire Block. As OSFR coverage is necessary to obtain our permit to drill, please confirm that Apache will continue it's OSFR coverage over the entire Block, even during our drilling operations. Thanks---Fred

W. Fred Deusinger
Shelf Land Manager
Energy Resource Technology, Inc.
Office: 281-618-0531
Fax: 281-618-0544
Mobile: 281-770-1424

This e-mail may contain confidential and privileged material for the sole use of the intended recipient. Any review, use, distribution or disclosure by others is strictly prohibited. If you are not the intended recipient (or authorized to receive for the recipient), please contact the sender by reply e-mail and delete all copies of this message.

This e-mail may contain confidential and privileged material for the sole use of the intended recipient. Any review, use, distribution or disclosure by others is strictly prohibited. If you are not the intended recipient (or authorized to receive for the recipient), please contact the sender by reply e-mail and delete all copies of this message.

9/11/2007

Worksheet For NTL 2007-G13 AND API 95J

WELL NAME: High Island A-545 Well #2 RIG NAME: Rowan Louisiana
 LEASE NO.: OCS-G 17199

I. SITE DATA BEFORE RIG ARRIVAL			
A. Location Coordinates	LAT: 28° 02' 42.159 N	LONG: 94° 00' 32.186 W	X: 3,609,715.00 Y: 111,336.00
B. Water Depth	243	Feet	
C. Was Rig Previously on Location	No	If Yes, Dates:	Rig Name:
D. Bottom Survey Supplied to Contractor			
Shallow Hazards Survey:	Yes	Date of Survey: 8-Jul-07	Date of Report: Jul-07
Previous MesoTech	No	Date of Survey:	Comment:
Nearest Pipeline:	16.2' 2100' from Apache 6" S-11841 pipeline	Direction: SE	Block #: HI A-545
Other Nearby Pipelines:	14-6900' from ERT 8" S-11282	Direction: EW	Block #: HI A-545
Nearby Debris:	No	Direction:	Block #:
Nearby Soil Disturbance:	No	Comment:	
Other:	No	Comment:	

II. GEOTECHNICAL DATA	
A. Soil Boring (Supplied By Remington)	
Date Obtained: Max-07	Core Vendor: Fuqua-McClelland Marine Geosciences
Core Depth: 180	Comments:
B. Suitability of Location as Determined By Rig Contractor	
Punch Through Potential: No	Date Obtained:
Mud Slide Potential: No	Date Obtained:
Comments:	Comments: Sealcoat foundation is capable of supporting maximum leg loads

III. MINIMUM AIR GAP PER API 95J	
A. Air Gap From Appendix A of API 95 J:	62 Feet
B. 100-Year Wave Height From Appendix D:	58 Feet
C. Planned Air Gap:	65 Feet

IV. PRELOADING PROCESS FROM CONTRACTOR PROCEDURES	
A. Contractor Preloading Procedures:	Date Obtained: Sep-07
B. Preloading Holding Time From Contractor Procedures:	>1.0 Hours
C. Time Since Last Spudcan Settling From Contractor Procedures:	>1.0 Hours

V. HURRICANE PREPARATIONS	
A. MOM's Procedure Obtained From Contractor:	Date Obtained: Sep-07
B. Storm Packer Depth:	1-200 BML Feet
C. Procedure For Supporting and Securing Well:	Received from contractor
	Set storm packer @ 200' BML. MD BOPE and install DH tree and test to 500 psi. Skid rig in and secure cantilever.
	Ensure leg loads meet storm survival requirements. Secure rig for storm and evacuate personnel.

VI. SATELLITE TRACKING SYSTEM	
A. Installed:	No
B. Operating:	No

Table D.1: 2017atlasOfGulfOfMexicoGasAndOilSandsData.gdb from <https://www.data.boem.gov/Main/GandG.aspx> for API 427094116400. The definition of the acronyms are found at <https://www.data.boem.gov/Main/HtmlPage.aspx?page=2017sands>.

SAND_NAME	0981_HI544A_LF1	OVOL	0
ASSESSED	Y	GTHK	60.47
SDDATE	12/8/2007	GAREA	36
SDYEAR	2007	GVOL	2177
SDDATEH	12/8/2007	DRIVE	PAR
SDYEARH	2007	RESTYP	N
WELLAPI	427094116400	POROSITY	0.31
BOEM_FIELD	HI544A	SW	0.1
FCLASS	PDP	PERMEABILITY	965
FSTAT	A	Pi	6773
FSTRUC	B	TI	178
FTRAP1	D	SDPG	0.834
FTRAP2		SDTG	1.37
FDDATE	9/19/1977	RSI	0
FDYEAR	1977	YIELD	2.096
EIAID	854544	PROP	0
PLAREA	WGM	GOR	476.998
SAND	LF1	SPGR	0.57
PLAY_NUM	0981	API	0
PLAY_NAME	PU_F1	BGI	330.5
POOL_NAME	0981_HI544A	BOI	0
CHRONOZONE	PU	RECO_AF	0
PLAY_TYPE	F1	RECG_AF	570.995
SD_TYPE	G	OIP	0
WDEP	237	GIP	8744238
Original Oil	2606	ORF	0
Original Gas	1243057	ORECO	0
Original BOE	223791	ORECG	0
Cum Oil	2606	ORP	0
Cum Gas	1243057	GRF	0.14
Cum BOE	223791	GRECO	2606
Oil Reserves	0	GRECG	1243057
Gas Reserves	0	GRP	476.998
BOE Reserves	0	NCNT	1
SS	8122	UCNT	0
THK	60.47	SCNT	0
TAREA	36	TCNT	1
TVOL	2177	BHCOMP	1
OTHK	0	LAT	28.04494
OAREA	0	LONG	-94.0089


```
ESEL,S,TYPE,,101  
SFE,ALL,,PRES,1,ARG2  
ALLS
```

```
ESEL,S,TYPE,,102  
SFE,ALL,,PRES,1,ARG2  
ALLS
```

```
ESEL,S,TYPE,,103  
SFE,ALL,,PRES,1,ARG2  
ALLS
```

```
ESEL,S,TYPE,,104  
SFE,ALL,,PRES,1,ARG2  
ALLS
```

Figure E.4: APDL code for the pore pressure at the cement interfaces.

```
ESEL,S,TYPE,,100  
SFE,ALL,,PRES,1,ARG1  
ALLS
```

Figure E.5: APDL code for the production pressure.

Appendix F: Compressibility Factor Method Verification

The Peng-Robinson equation of state is shown in Equation F.1.

$$P = \frac{RT}{v - b} - \frac{a}{v(v + b) + b(v - b)} \quad \text{F.1}$$

Where,

$$a = a_c \cdot \phi(T) \quad \text{F.2}$$

$$\phi(T) = \left[1 + \varphi \left(1 - \sqrt{T/T_c} \right) \right]^2 \quad \text{F.3}$$

$$\varphi = 0.37464 + 1.54226\omega - 0.26992\omega^2 \quad \text{F.4}$$

$$a_c = 0.457235R^2 \frac{T_c^2}{P_c} \quad \text{F.5}$$

$$b = 0.077796R \frac{T_c}{P_c} \quad \text{F.6}$$

Where P , T , P_c , T_c , R , and ω are the pressure (*bar*), temperature (*K*), critical pressure (*bar*), critical temperature (*K*), the universal gas constant ($\frac{\text{m}^3 \cdot \text{Pa}}{\text{K} \cdot \text{mol}}$), and the acentric factor of the pure gas, respectively. Rearranging Equation F.1 into polynomial form, and using the relationship of the real gas law (Equation F.7), results in Equation F.8.

$$z = \frac{PV}{nRT} \quad \text{F.7}$$

$$z^3 + \alpha z^2 + \beta z + \gamma = 0 \quad \text{F.8}$$

$$\alpha = -1 + B \quad \text{F.9}$$

$$\beta = A - 3B^2 - 2B \quad \text{F.10}$$

$$\gamma = -AB + B^2 + B^3 \quad \text{F.11}$$

$$B = \frac{Pb}{RT} \quad \text{F.12}$$

For the Peng-Robinson equation of state to be solved, the roots of the polynomial in Equation F.8 have to be determined. To solve a third degree polynomial, Equation F.13 is used. A limitation of Equation F.13 is that it can result in complex numbers resulting in crashing of the FEA model if used explicitly within it.

$$z = \sqrt[3]{\left(-\frac{\alpha^3}{27} + \frac{\alpha\beta}{6} - \frac{\gamma}{2}\right) + \sqrt{\left(-\frac{\alpha^3}{27} + \frac{\alpha\beta}{6} - \frac{\gamma}{2}\right)^2 + \left(\frac{\beta}{3} - \frac{\alpha^2}{9}\right)^3}} + \sqrt[3]{\left(-\frac{\alpha^3}{27} + \frac{\alpha\beta}{6} - \frac{\gamma}{2}\right) - \sqrt{\left(-\frac{\alpha^3}{27} + \frac{\alpha\beta}{6} - \frac{\gamma}{2}\right)^2 + \left(\frac{\beta}{3} - \frac{\alpha^2}{9}\right)^3}} - \frac{\alpha}{3} \quad \text{F.13}$$

The variables used to compare the Peng-Robinson equation of state with method used in this work (Equation 4.41) are listed in Table F.1, and the results of the z-factor versus depth are shown in Figure F.1. Note that the percent difference from Equation 4.41 to the Peng-Robinson

equation of state are also on the graph. The average percent difference is 1.4%. Therefore, Equation 4.41 is verified for the pressures and temperatures used in the case well study.

Table F.1: Variables used in the Peng-Robinson equation of state and/or Shell empirical formula for methane.

Variable	Value
$R \left(\frac{\text{m}^3 \cdot \text{Pa}}{\text{K} \cdot \text{mol}} \right)$	8.3145
P_c (Pa)	4.60E6
T_c (K)	190.4
ω	0.011

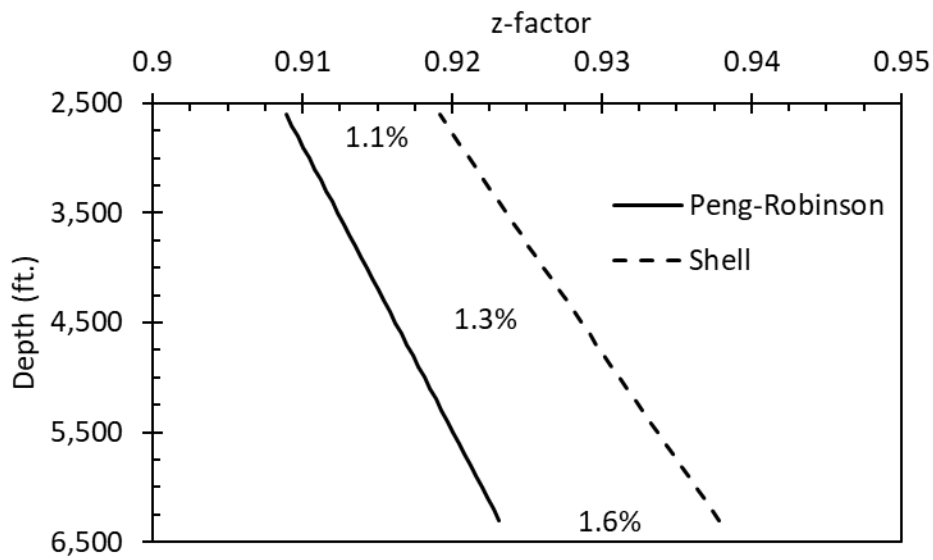


Figure F.1: Results for the comparison between the Peng-Robinson equation of state and the Shell empirical formula (Equation 4.41). The average percent difference is 1.4%.

Appendix G: Riemann Sum Verification

To determine the summation of the fracture volume ($\sum_i \Delta L_i w_i^{-3}$) from the case study well, essentially the total volume is wanted for the microannuli. Since the microannuli gap width is a function of depth ($f(w_i^{-3})$ and L_i respectively), a definite integral of the function can be formulated. But since the integral of the function would be difficult to formulate, the trapezoidal rule (Riemann sum integral) can be used which is a technique for approximating a definite integral. The trapezoidal rule for a definite integral is shown in Equation G.1. This methodology will be referred to as the Riemann sum method in the rest of this work.

$$C \quad \int_a^b f(x) dx = \sum_{i=1}^n f(x_i^*) \Delta x_i \quad \text{G.1}$$

To calculate the total volume from the microannuli determined by the case study well, the following equation, Equation G.2, is used which calculates the total volume given 1 m ($\Delta L = 1$) segments (6,300 ft. – 2,600 ft. = 3,700 ft. \approx 1,127 m).

$$D \quad \int_{TVD}^{TOC} f(w_L^{-3}) dL = \sum_{i=1}^{1127} \frac{f(w_{i+1}^{-3}) + f(w_i^{-3})}{2} \Delta L_i \quad \text{G.2}$$

To verify the Riemann sum methodology, a simple example is presented. For the example, the area between two lines is of question. From Figure G.1, the area between the blue and red curves is wanted.

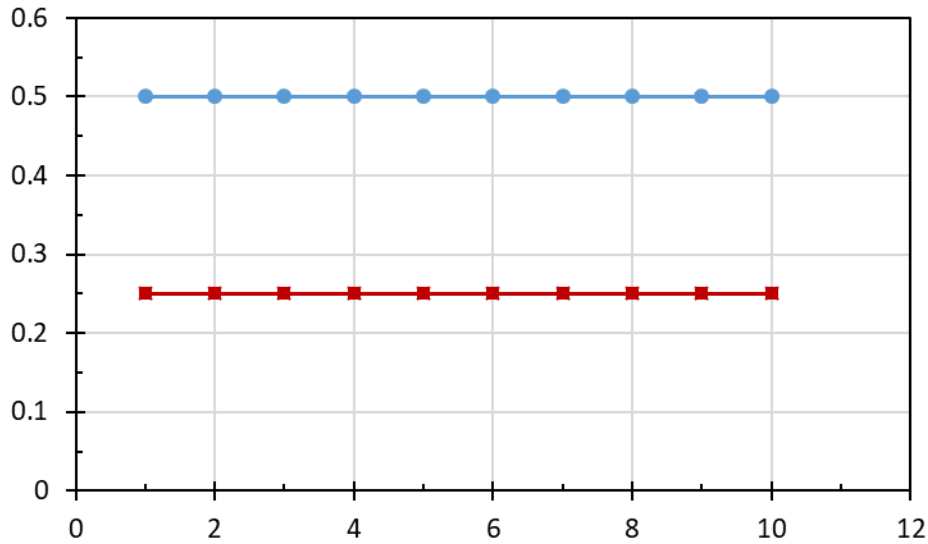


Figure G.1: Graphical representation of the example to verify the Riemann sum methodology.

The integral formula is represented as follows:

$$Area = \int_1^{10} 0.5 \, dx - \int_1^{10} 0.25 \, dx = 4.5 - 2.5 = 2.25 \quad \mathbf{G.3}$$

The geometric formula is represented as follows:

$$Area = (Base \cdot Height)_{blue} - (Base \cdot Height)_{red} \quad \mathbf{G.4}$$

$$Area = (9 \cdot 0.5) - (9 \cdot 0.25) = 2.25 \quad \mathbf{G.5}$$

The Riemann sum using the trapezoidal rule is as follows:

$$Area = \sum_{i=1}^{10} \left[\left(\frac{y_i + y_{i+1}}{2} \right) \cdot (x_{i+1} - x_i) \right]_{blue} - \left[\left(\frac{y_i + y_{i+1}}{2} \right) \cdot (x_{i+1} - x_i) \right]_{red} \quad \mathbf{G.6}$$

Breaking the Riemann sum into 10 segments, results in Table G.1 which each segment equals the area of that segment. Summing the segments results in the total area between the curves which matches the integral and geometric methods.

Table G.1: Riemann sum calculations for the area between the curves for with 10 segments.

Segment	y (blue)	y (red)	Area (blue)	Area (red)	Blue - Red
1	0.5	0.25	0.5	0.25	0.25
2	0.5	0.25	0.5	0.25	0.25
3	0.5	0.25	0.5	0.25	0.25
4	0.5	0.25	0.5	0.25	0.25
5	0.5	0.25	0.5	0.25	0.25
6	0.5	0.25	0.5	0.25	0.25
7	0.5	0.25	0.5	0.25	0.25
8	0.5	0.25	0.5	0.25	0.25
9	0.5	0.25	0.5	0.25	0.25
10	0.5	0.25			
		Sum	4.5	2.25	2.25

Appendix H: Mesh Sensitivity Analysis

The mesh sensitivity analysis for the cement, casing, and rock formation are shown in Figures H.1-3, respectively. The element circumference size, face element size, and height size are all varied to determine the optimum mesh density in terms of percent difference in microannuli size and computational time. The red data points are the original mesh size while the green data point are the updated size.

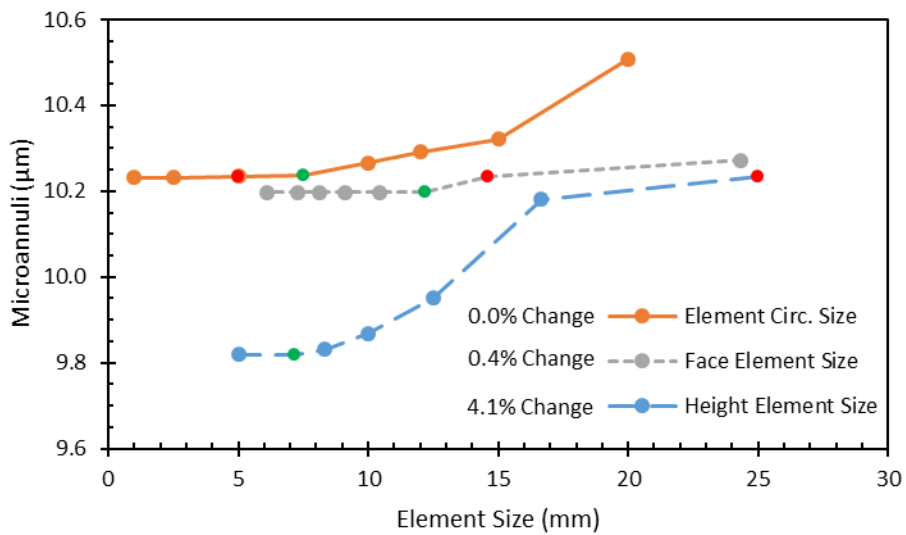


Figure H.1: Mesh size versus microannuli gap width for the cement sheath elements.

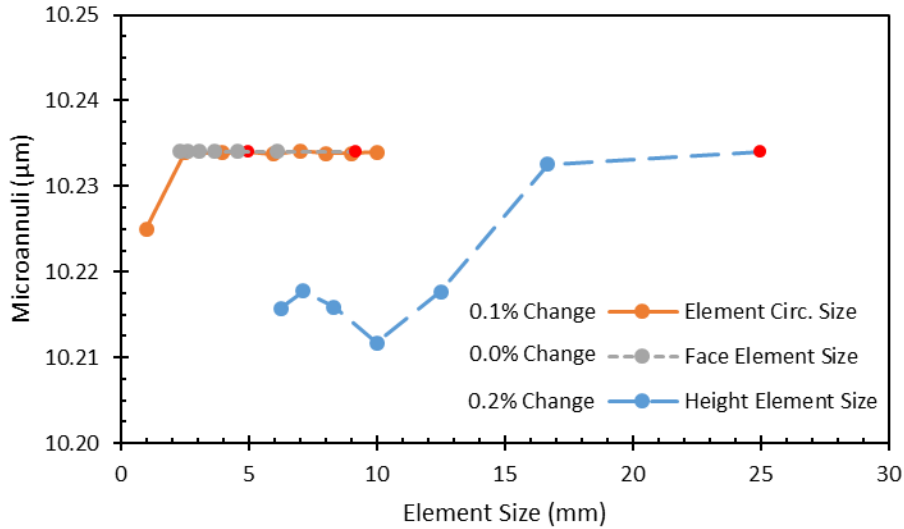


Figure H.2: Mesh size versus microannuli gap width for the casing elements.

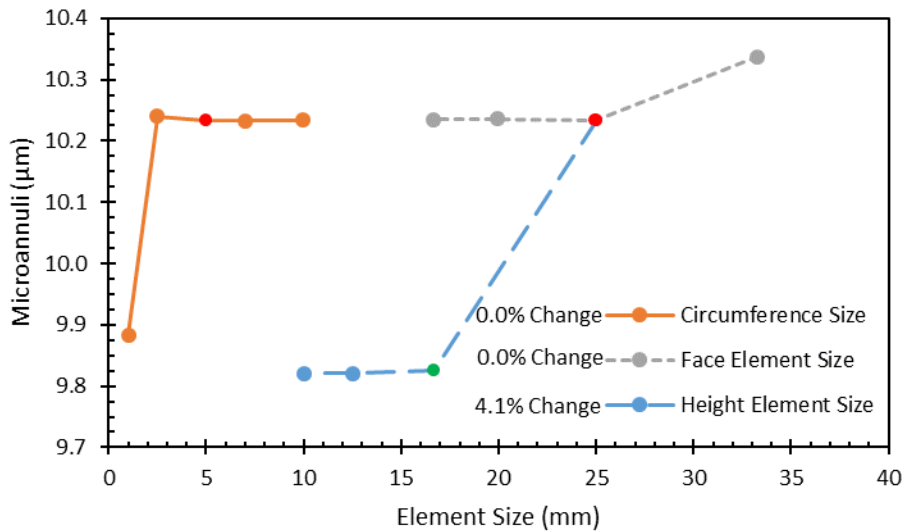


Figure H.3: Mesh size versus microannuli gap width for the rock formation elements.

The results of the mesh sensitivity analysis show that the element circumference and the face element size have little effect (<0.4%) on the microannuli size. However, the cement sheath element height has a 4.1% effect. For the casing elements, all three dimensions have less than 0.2% change in microannuli size. Therefore, the casing elements do not need optimized. For the rock formation, the element circumference and face element size have zero effect on the microannuli size whereas the element height has a 4.1% effect. Since the height of the cement and rock

formation elements has an effect, do both need to be optimized or does it matter? Table H.1 shows the results of optimizing the cement and rock formation elements versus just the cement elements.

Table H.1: Cement and rock formation element optimization versus only the cement element optimization.

	Cement and Rock Formation Elements	Only Cement Elements
Time:	6 min 46 sec	4 min 46 sec
Elements:	14,464	11,304
Before Optimization:	10.23 μm	10.23 μm
After Optimization:	9.85 μm	9.85 μm
% Difference:	3.84%	3.84%

From Table H.1, the optimization of both the cement and rock formation elements resulted in a total microannuli reduction of 3.84%. The optimization of only the cement elements resulted in a total microannuli reduction of 3.84%. However, the cement and rock formation optimization took two minutes longer for the simulation to converge compared to the total run time on only optimizing the cement elements. Therefore, only the cement elements were optimized based on the mesh size versus microannuli gap width.

Appendix I: Staged Poro-Elastic FEA Stress Continuum Model Results

The results from the staged poro-elastic FEA stress model, published in Wise et al. (2019), is shown in three sections. Section 1 contains the results of comparing a staged FEA model versus a not staged model. Section 2 presents the results for the base wellbores, and Section 3 contains the parametric analysis for the three wells.

Staged FEA

Modeling the well cycle requires a staged finite element approach which allows the stress and deformations to be monitored in each loading step. Figure I.1 shows two model wellbores with each depicting the hoop and radial stress throughout the cement sheath. The model on top is a staged model following the load steps described previously while the lower model is not staged and has the far field stresses, cement framework stress, and internal casing pressure applied in a single time step. Figure I.1 shows that when all the load steps and initial conditions are put in a single step, the resulting stress patterns do not accurately depict the stresses at the interfaces for the radial stress. The cement/rock formation interface's radial stresses are not constant throughout the cement and do not match between the interfaces of the casing/cement and the cement/rock formation. The cement sheath along the cement/rock formation interface violates Newton's Third Law as marked on Figure I.1. No external force is applied to the cement or casing, therefore, the radial stress should be equal throughout the cement sheath along both interfaces (Weideman 2014).

Instead, the effective radial stress is less in the marked section of the cement sheath along the casing/cement interface than the cement along the cement/rock interface. The hoop stress in the cement sheath shows a similar pattern for the non-staged model. The hoop stress changes in the cement sheath when it should be constant throughout.

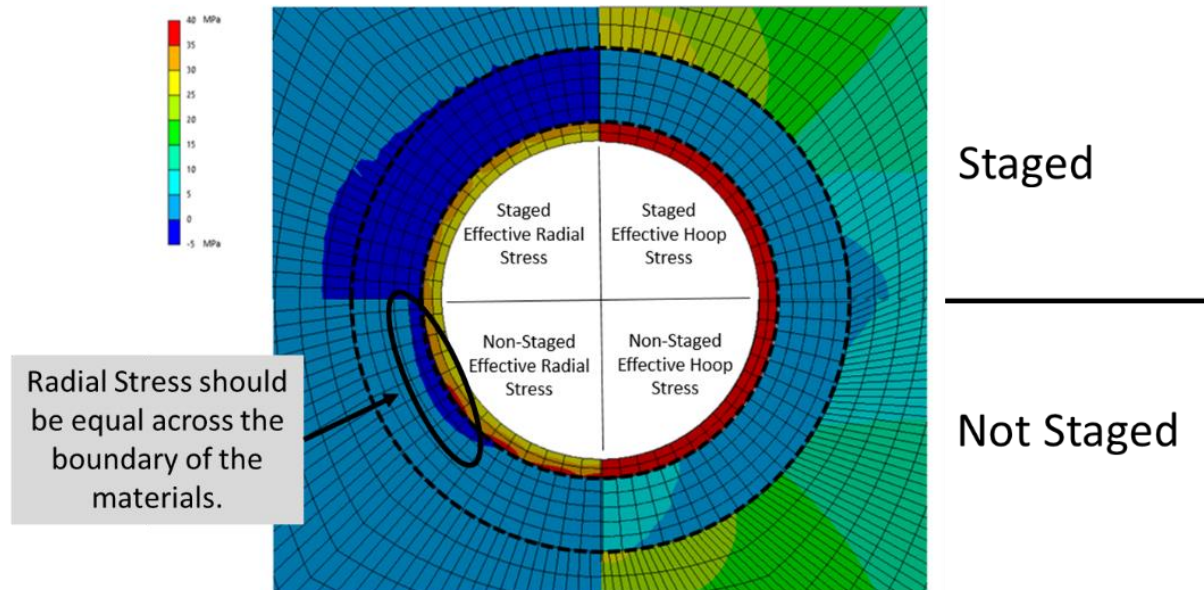


Figure I.1: Staged FEA (top) compared to the non-staged FEA (bottom).

Base Case Wellbores

For the first part of the results analysis regarding potential cement sheath debonding and cement fracturing, three base case wellbores were simulated. The effective stresses (hoop and radial) of the cement sheath is presented for the casing/cement and cement/rock formation interfaces.

The effective stress results for the base case parameters of the three wells are represented in Table I.1. The medium depth well results are considered the standard and the shallow and deep depths are normalized to the medium well. The shadowed coloring indicates tensile stresses while the others are compressive. The base results show that the medium and deep wells are experiencing tensile stresses in the radial directions which indicate debonding. The medium depth well is debonding at both the casing/cement and cement/rock interfaces while the deep well is only debonding at the casing/cement interface. The shallow depth well is not experiencing any tensile stresses, but it should be noted that the effective stresses are close to the tensile range. Disking of

the cement sheath is not a concern for the three wells since the effective vertical stresses are all compressive.

Table I.1: Cement sheath effective stress results for the base case parameters for the three case studies. The shallow and deep well are normalized to the medium well.

Effective Interface Stresses	Well		
	Shallow	Medium MPa	Deep
Hoop Stress Casing/Cement	-84%	5.70	167%
Hoop Stress Cement/Rock	-78%	3.70	242%
Radial Stress Casing/Cement	-121%	-2.75	-59%
Radial Stress Cement/Rock	-174%	-0.84	-390%
Vertical Stress Casing/Cement	-70%	3.03	276%
Vertical Stress Cement/Rock	-71%	3.01	287%

Compressive	Tensile
-------------	---------

To analyze the potential of shear failure, a Mohr-Coulomb graph was used to evaluate whether the shear stresses were in failure as shown in Figure I.2. Figure I.2 shows that all three wells are far from being in shear failure. The deepest well proves closest to shear failure, but the gap between its Mohr circle and the failure envelope is significant. An interesting observation is that the shear stresses in the shallow well are not significant. The stresses are barely visible when compared to the medium and deep wells let alone the failure envelope. Another observation is that Figure I.2 shows that the medium well has tensile stresses at both interfaces and the deep well has tensile stresses at the casing/cement interface as shown by their respective Mohr circles crossing the tensile cutoff.

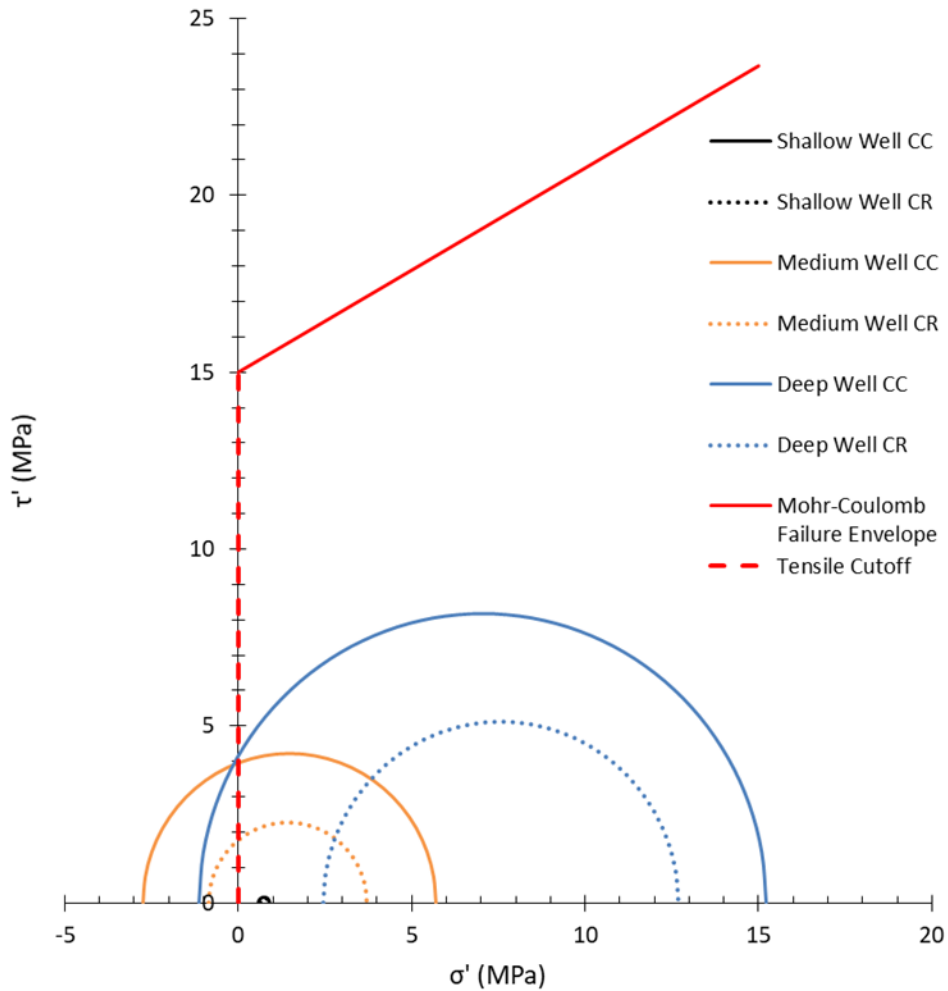


Figure I.2: Shear failure envelope of cement compared to the cement sheath for the three base case wells.

Figure I.3 depicts the graphical results of the base case cement sheaths for the three wells. The effective radial stresses are depicted on the left, and the effective hoop stresses are shown on the right. The inner radius of the sheath is the casing/cement interface while the outer radius is the cement/rock formation interface.

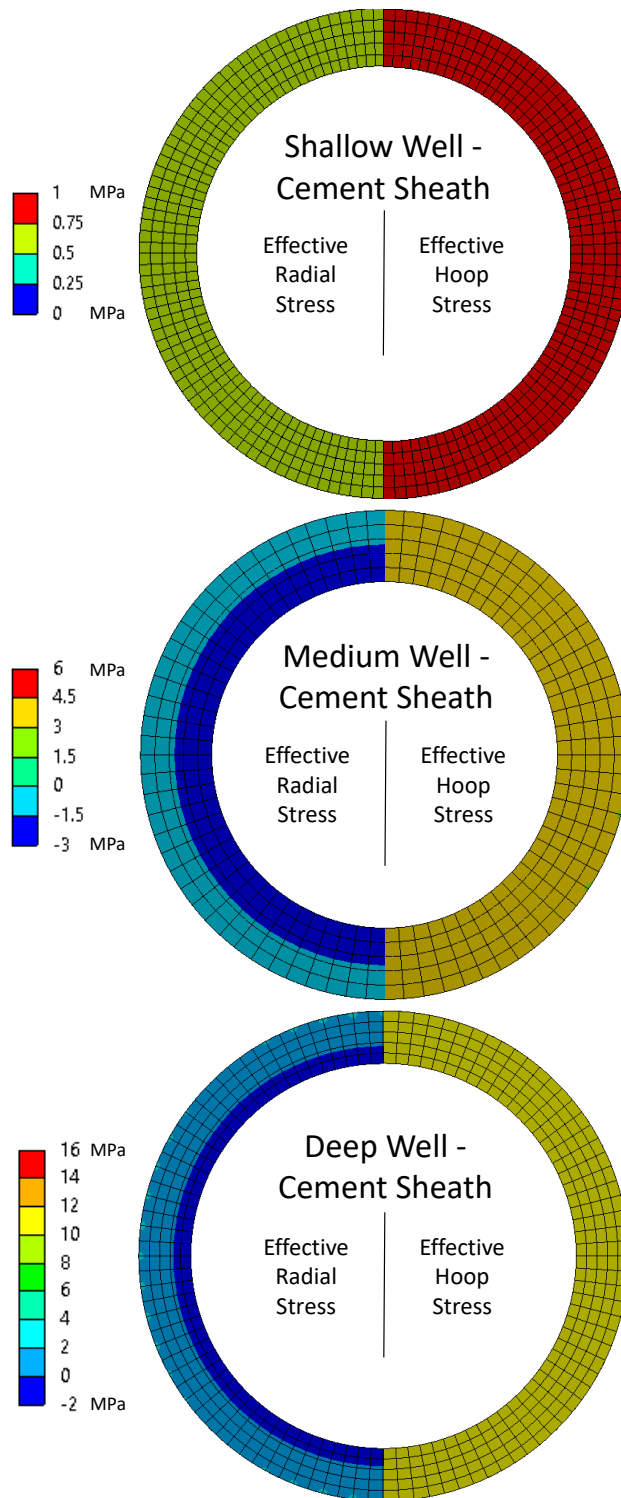


Figure I.3: Graphical results of the base case stress values shown in Table I.1 for the three case studies; shallow, medium, and deep wells.

For the shallow well, the maximum effective stress is 1 MPa and is not experiencing any tensile stresses. The medium well is experiencing tensile radial stress throughout the cement sheath, and the magnitude is higher along the casing/cement interface implying that the resulting debonding gap would be greater than along the cement/rock interface. The deep well is only experiencing debonding along the casing/cement interface as indicated in Table I.1 and Figure I.3. It is important to note that the effective hoop stresses have variances due to the anisotropic in-situ stresses but is masked in Figure I.3 due to the scale resolution. The effective hoop stresses for the medium and deep wells are not close to the tensile range, (therefore not resulting in radial cracks) and consequently not of interest to this discussion.

The results of the medium and deep well base case simulations are in agreement with an analysis from the literature. These two wells experienced debonding after the production step when the mud weight pressure inside the casing changed to a production pressure. Previous studies have documented that changes in thermal cycling can cause cement sheath debonding (Lavrov et al., 2015; Zhang et al., 2017) while Nygaard et al. (2014) concluded that debonding at the casing/cement interface occurs as a result of thermal and pressure changes. It should be noted that Zhang et al. (2017) observed debonding as a result of thermal cycling of cooling fluid at the cement/rock interface whereas the results shown here conclude that debonding is occurring at the casing/cement interface.

Parametric Analysis

The second part of this study is the parametric study of the base case wells to rank the stress contributing factors. The interpretation of the results are shown in Figures I.4-I.6 for the shallow, medium, and deep well respectively. The maximum and minimum normalized effective stress

values from the three wells are shown. The parameters are ranked from largest to smallest percent change with respect to the effective radial stress at the cement/rock formation interface. Due to the large variation of the parameters, log scales were used for the x-axis. The solid bars represent a positive percent change while the checkered bars represent a negative percent change.

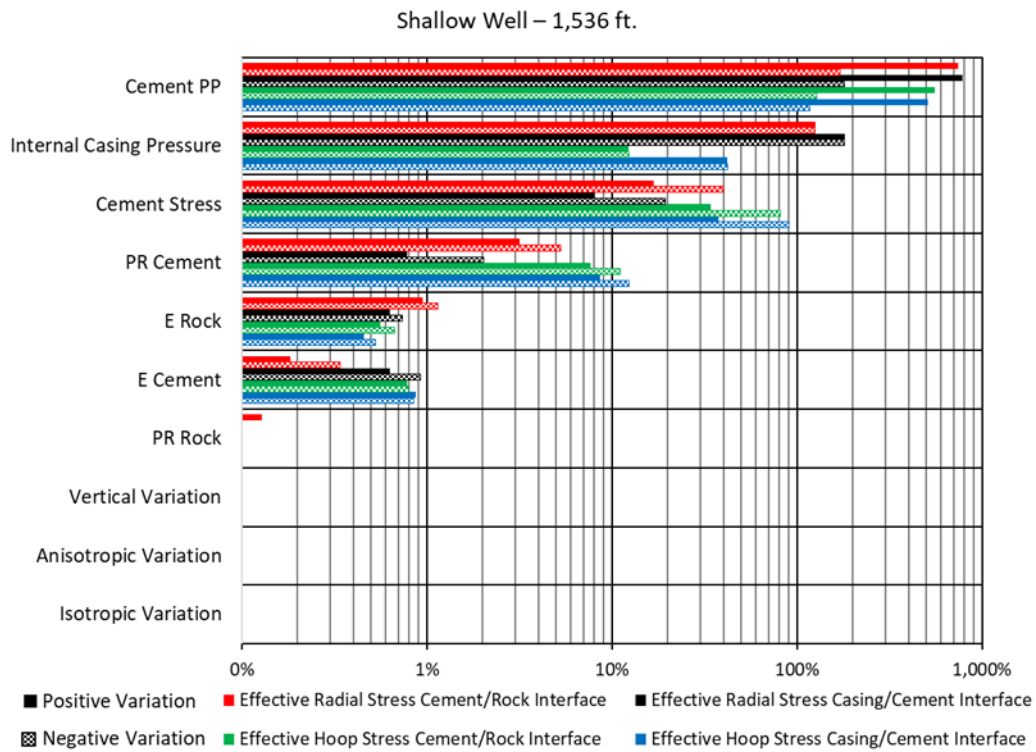


Figure I.4: Results of the parametric study ranking the parameters with the largest impact on stress development for the shallow well in the Eugene Island OPD.

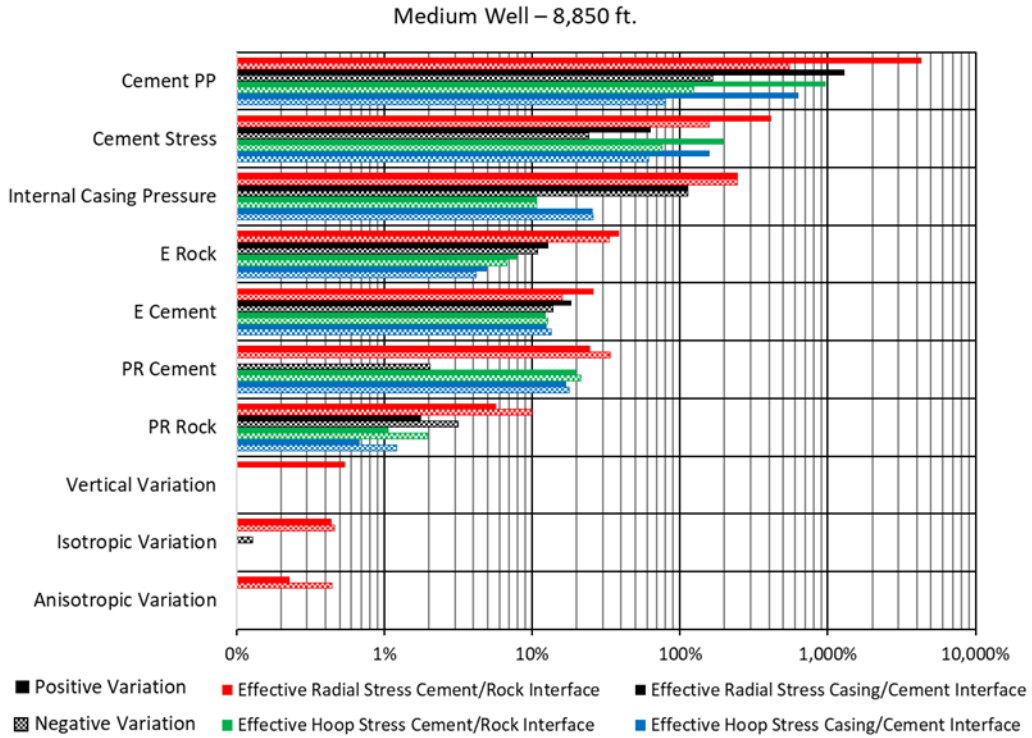


Figure I.5: Results of the parametric study ranking the parameters with the largest impact on stress development for the medium well in the Eugene Island OPD.

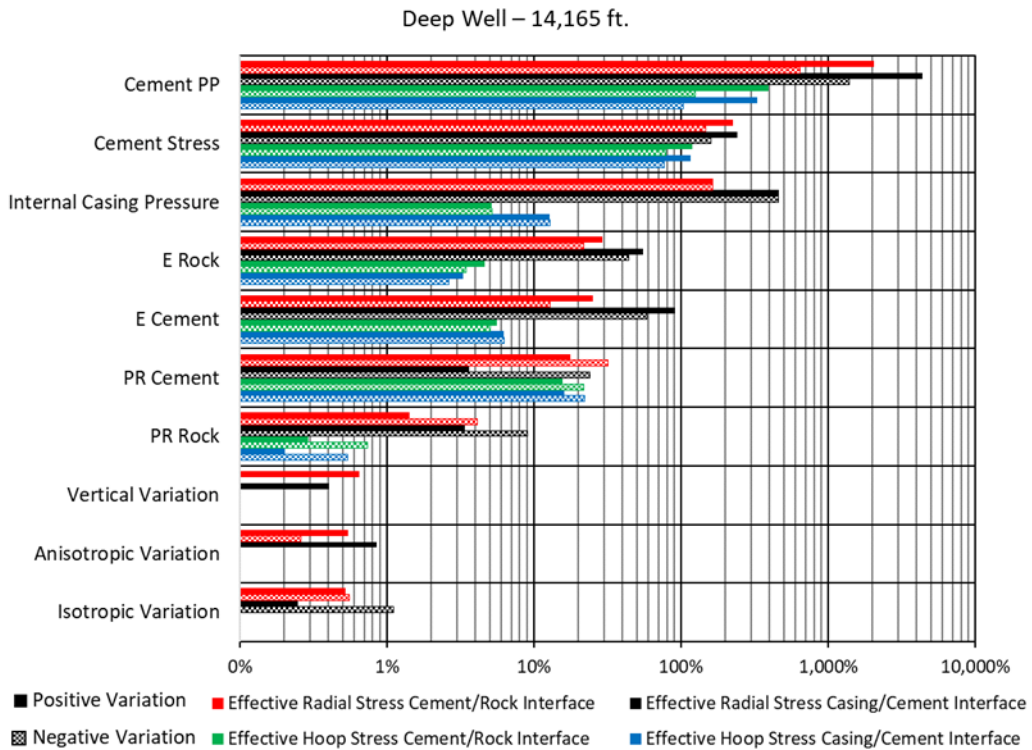


Figure I.6: Results of the parametric study ranking the parameters with the largest impact on stress development for the deep well in the Eugene Island OPD

Figures I.4-I.6 show that the ranking of the parameters are not the same for all three wells. All three wells have cement P_p listed as the most important contributing factor, but the ranking of the parameters after that change. The medium and deep well are the most similar; both have the same order of parameters until the in-situ stresses. For the shallow well, the setting stress of the cement is more critical than the internal casing pressure, and the mechanical properties of the surrounding rock formation and cement are different from the other two wells. Overall, the general interpretation of the three figures (Figures I.4-I.6) are similar for all three wells: the cement hydration parameters and the internal casing pressure are the most critical parameters in the stress development of the cement sheath, followed by the mechanical properties of the rock and cement, and lastly, the in-situ stresses have little impact on the stress development in the sheath. Another observation is that the radial stresses are more sensitive to parameter changes than the hoop stresses which indicates that variation of parameters are more likely to lead to tensile debonding than radial cracks.

The results of this study are in agreement with Bois et al. (2011) in which the authors state that the two most critical aspects of cement sheath integrity are the cement hydration parameters and changes in pressure in the wellbore. The changes in internal casing pressure have already been proven in the literature to be a major cause of cement sheath debonding and will not be discussed further, yet the cement hydration parameters (setting stress and pore pressure development) have not been studied as intensely. Simulating the setting stress from the maximum possible value (P_{Frac}) to the lowest possible scenario (zero effective stress) significantly affects the cement sheath stress by 100% in both the radial and hoop stresses. The change in effective stresses is significant enough to take the cement sheath from compressive to tensile and vice versa. The cement P_p acts the same way. A maximum P_p (equal to the setting stress resulting in an effective stress of zero)

and a minimum P_p (zero P_p) affects the cement stress from 100% to greater than 1,000% in some instances. Both of these parameters are critical in the development of the hydration of cement, but they are not well understood. The upper and lower ranges for both parameters presented in this paper are realistic, but the variation has dramatic results. Therefore, cement hydration should be investigated further to develop a better understanding of how the cement setting stress and P_p develop during cement hydration.

When designing a cementing job to complete a well, many factors go into it. The cement density is arguably the most critical factor, but the structural properties of hardened cement should also be considered. The only changeable parameters for the cement job are the cement composition which directly affects the mechanical properties, such as E, PR, UCS, and bonding strength. From the results of this study, the mechanical parameters have less effect on cement sheath integrity. The effective radial and hoop stresses were less sensitive to changes in the mechanical properties of cement. The maximum change in one of said parameters is approximately 20% (except for a few instances with the deep well) which will not change any of the baseline effective stresses results in Table I.1 from being in compressive to tensile or vice versa. Therefore, changing cement compositions to develop enhanced structural properties is not dominant in cement sheath integrity in terms of radial cracks, diskings, or tensile debonding. This result is not in agreement with Fleckenstein et al. (2001) in which they concluded that ductile cements (high PR & low E) would “significantly” reduce tangential (hoop) tensile stresses, but the authors did not take into account pore pressure of the cement. The results of this paper do appear to agree with Nygaard et al. (2014) in which the mechanical properties of the intact cement do not affect the radial stresses dramatically.

Another trend seen for all three wells is that changing the in-situ stresses have less than 1% effect on the stress development in the cement sheath. This indicates that the geologic location of the well has little impact regarding the potential failure of the cement sheath in vertical wells for normal faulting stress regimes although the changes of in-situ stresses due to compaction and subsidence, which was not addressed in this study, have been shown to play a factor in casing shear as described by Dusseault et al. (2001).

A final result, that is not as obvious and is not explicitly shown from the parametric study, is how the depth of the well affects cement sheath stress. The shallow well is not experiencing debonding at either interface, but both the medium and deep wells are experiencing at least one interface debonding. The medium well is experiencing debonding at both interfaces while the deep well is only debonding at one interface implying that there is a depth in which the cement sheath will be at a higher risk to develop gaps. This depth versus risk of debonding curve may look similar to a bell curve as seen with the three wells presented in this paper. There may be an “optimum” depth that puts wells at a higher risk for debonding, but above and below that depth have less prime conditions. This reasoning would explain why the medium depth well appears to be debonding at both interfaces, but the deep well is only debonding at one interface. This phenomenon was described by Gray et al. (2009) in which they concluded that debonding does not always occur at the deepest locations within a wellbore.

Appendix J: Rock Formation Failure Mechanism

Drilling fluid weight is used when drilling wells for multiple reasons including stability issues. The drilling fluid weight is used to balance the stresses in the borehole between compressive (or shear) failure and tensile failure. Compressive or shear failure occurs when the drilling fluid weight pressure is too low and results in breakouts. Tensile failure from collapsing (too low of drilling fluid weight), and from fracturing (too high of drilling fluid weight).

The most common shear failure criteria for rocks is Mohr-Coulomb. This theory states that the failure of material is due to the combination of normal and shear stresses. The normal and shear stresses are determined by only the minimum (σ_3) and maximum (σ_1) principal stresses. The failure line is given by Equation J.1 where τ_f is the shear strength, τ_o is the rock cohesion, ϕ is the internal friction angle, μ is the coefficient of internal friction, and σ' is the effective normal stress.

$$\tau_f = \tau_o + \sigma' \tan(\phi) = \tau_o + \sigma' \mu \quad \text{J.1}$$

The normal and shear effective stresses that cause the failure within the rock are given by Equations J.2 and J.3, respectively, and illustrated in Figure J.1.

$$\sigma' = \frac{1}{2}(\sigma'_1 + \sigma'_3) + \frac{1}{2}(\sigma'_1 - \sigma'_3)\cos 2\beta \quad \text{J.2}$$

$$\tau' = \frac{1}{2}(\sigma'_1 - \sigma'_3)\sin 2\beta \quad \text{J.3}$$

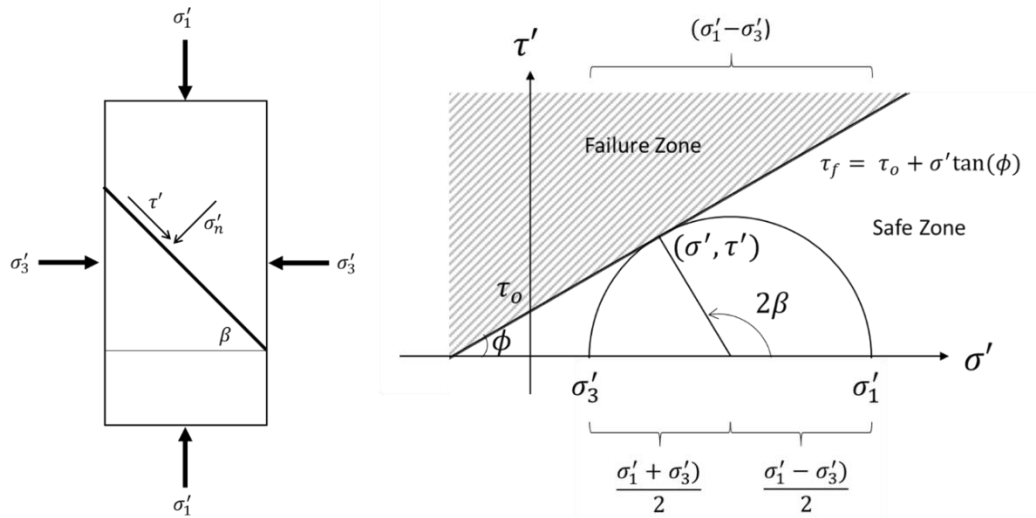


Figure J.1: A) Mohr-Coulomb failure criteria of a cylindrical sample. B) Mohr circle depicting the failure criteria.

The rock is in shear failure if (σ', τ') touches or crosses the failure line, τ_f . The rock is in tensile failure if (σ', τ') touches or crosses the shear (τ') axis. The concept of shear and tensile failure is illustrated in Figure J.2.

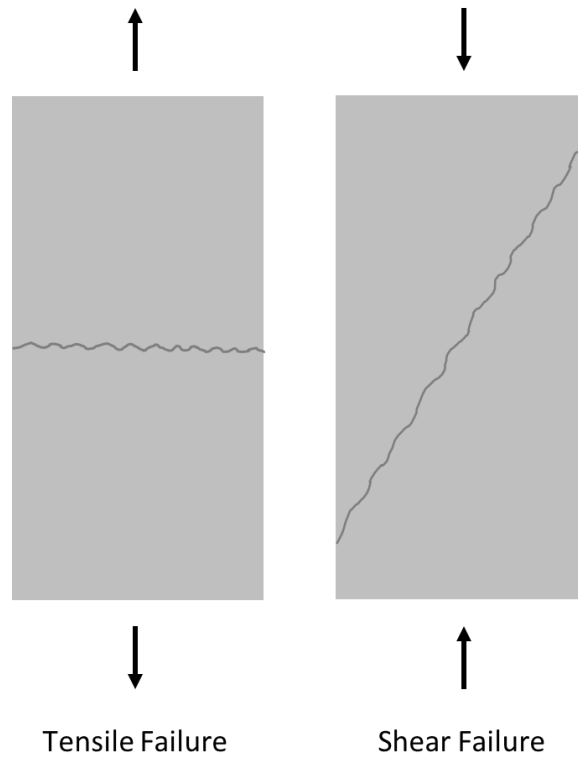


Figure J.2: Illustration showing tensile and shear failure.

Appendix K: Finite Element Model Theory

Finite element modeling is defined as the “Process of finding the responses of a problem domain subject to some environmental conditions” (Lee 2017). In which the domain are the bodies being modeled (solids, surfaces, or lines), the environmental conditions are the boundary conditions (loads and supports), and the responses are the displacements, stresses, or strains. Fundamental discussion and the relationship between displacements, stresses, and strains is discussed in Appendix A.

For a body in finite element modeling, there are 15 variables that describe a body: 3 displacements, 6 stresses, and 6 strains. For the 15 variables, 15 governing equations exist: 3 equilibrium (displacement) relations, 6 strain-displacement relations, and 6 stress-strain relations.

The equilibrium equations sum down to a general form shown in Equation K.1 in which the sum of all forces equals zero in all three directions.

$$\sum F_x = 0, \sum F_y = 0, \sum F_z = 0 \quad \mathbf{K.1}$$

The expanded form of the equilibrium equations is shown in Equations K.2-K.7. Note that there are only 3 equilibrium equations. The first 3 (Equations K.2, K.3, and K.4) apply if the forces are inside the structural body. If surface forces are on the body, Equations K.5, K.6, and K.7 apply.

Structural Internal Equilibrium Equations:

$$\frac{\delta\sigma_x}{\delta x} + \frac{\delta\tau_{xy}}{\delta y} + \frac{\delta\tau_{xz}}{\delta z} + b_x = 0 \quad \mathbf{K.2}$$

$$\frac{\delta\tau_{yx}}{\delta x} + \frac{\delta\sigma_y}{\delta y} + \frac{\delta\tau_{yz}}{\delta z} + b_y = 0 \quad \mathbf{K.3}$$

$$\frac{\delta\tau_{zx}}{\delta x} + \frac{\delta\tau_{zy}}{\delta y} + \frac{\delta\sigma_z}{\delta z} + b_z = 0 \quad \mathbf{K.4}$$

Where b are components of body forces.

Structural Surface Equilibrium Equations:

$$\sigma_x n_x + \tau_{xy} n_y + \tau_{xz} n_z + S_x = 0 \quad \mathbf{K.5}$$

$$\tau_{yx} n_x + \sigma_y n_y + \tau_{yz} n_z + S_y = 0 \quad \mathbf{K.6}$$

$$\tau_{zx} n_x + \tau_{zy} n_y + \sigma_z n_z + S_z = 0 \quad \mathbf{K.7}$$

Where S and n are components of surface forces and unit normal vectors, respectively.

The strain-displacement relations are shown in Equations K.8-K.13. These relationships are assumed to be linear when small deformations are applied.

$$\epsilon_x = \frac{\delta u_x}{\delta x} \quad \mathbf{K.8}$$

$$\epsilon_y = \frac{\delta u_y}{\delta y} \quad \mathbf{K.9}$$

$$\epsilon_z = \frac{\delta u_z}{\delta z} \quad \mathbf{K.10}$$

$$\gamma_{xy} = \frac{\delta u_x}{\delta y} + \frac{\delta u_y}{\delta x} \quad \mathbf{K.11}$$

$$\gamma_{yz} = \frac{\delta u_y}{\delta z} + \frac{\delta u_z}{\delta y} \quad \mathbf{K.12}$$

$$\gamma_{zx} = \frac{\delta u_z}{\delta x} + \frac{\delta u_x}{\delta z} \quad \mathbf{K.13}$$

The stress-strain equations (Equations K.14-K.19) stem from Hooke's law which states that the relationship between stress and strain is linear with when small strains (i.e. displacements) are applied.

$$\epsilon_x = \frac{\sigma_x}{E} - \nu \frac{\sigma_y}{E} - \nu \frac{\sigma_z}{E} \quad \mathbf{K.14}$$

$$\epsilon_y = \frac{\sigma_y}{E} - \nu \frac{\sigma_z}{E} - \nu \frac{\sigma_x}{E} \quad \mathbf{K.15}$$

$$\epsilon_z = \frac{\sigma_z}{E} - \nu \frac{\sigma_x}{E} - \nu \frac{\sigma_y}{E} \quad \mathbf{K.16}$$

$$\gamma_{xy} = \frac{\tau_{xy}}{G} \quad \mathbf{K.17}$$

$$\gamma_{yz} = \frac{\tau_{yz}}{G} \quad \mathbf{K.18}$$

$$\gamma_{zx} = \frac{\tau_{zx}}{G} \quad \mathbf{K.19}$$

From Equations K.17, K.18, and K.19, G is the shear modulus and is shown in Equation K.20.

$$G = \frac{E}{2(1 + \nu)} \quad \mathbf{K.20}$$

Therefore there are 15 equations with 15 variables in which all linear elastic materials only need the material properties of E and ν .

Appendix L: Fanning Friction Factor from Bernoulli's Equation

To account for realistic fluids, a common method investigates fluid flow through Bernoulli's equation. In Bernoulli's equation, a friction term (\mathfrak{F}) is included as shown in Equation L.1 (de Nevers 2005; Bird et al. 2007; White 2011; Kleinstreuer 2010).

$$\Delta \left(\frac{P}{\rho} + gz + \frac{V^2}{2} \right) = \frac{dW_{n.f.}}{dm} - \mathfrak{F} \quad \text{L.1}$$

Equation L.1 reduces down to Equation L.2 for a zero velocity flow in which the work input $\left(\frac{dW_{n.f.}}{dm} \right)$ is equal to the change in potential energy (Δgz). Therefore, the friction loss term (\mathfrak{F}) is equal to the change in pressure (ΔP) with respect to density (ρ).

$$\mathfrak{F} = \left(-\frac{\Delta P}{\rho} \right)_{friction} \quad \text{L.2}$$

From Chapter 2.4, the velocity profile is known to be parabolic. Since the velocity goes from zero at the pipe wall to the average velocity near the center, the velocity gradient is a function of the average velocity and the diameter of the pipe which is proportional to the friction loss term.

$$\mathfrak{F} \propto \frac{V_{avg}^2}{D} \quad \text{L.3}$$

Assuming the flow is within the pipe, the frictional loss term is also proportional to the length of the pipe (Δx).

$$\mathfrak{F} \propto \frac{\Delta x V_{avg}^2}{D} \quad \text{L.4}$$

To account for the frictional loss in the pipe, a friction factor (f) is introduced which is equal to half the proportionality constant in Equation L.4. Dropping the average subscript from the velocity, the frictional loss of a pipe is defined as:

$$\mathfrak{F} = 2f \frac{\Delta x V^2}{D} = 4f \frac{\Delta x V^2}{2D} \quad \text{L.5}$$

Rearrangement of Equation L.5 in terms of f results in Equation L.6.

$$f = \frac{\mathfrak{F}}{4 \left(\frac{\Delta x}{D}\right) \left(\frac{V^2}{2}\right)} \quad \text{L.6}$$

It is important to note that there are two versions of f : the fanning friction factor (used in chemical engineering) and the Darcy-Weisbach friction factor (used in mechanical and civil engineering). The relationship between the two friction factors is four times as shown in Equation L.7.

$$f_{D.W.} = \frac{\mathfrak{F}}{\left(\frac{\Delta x}{D}\right) \left(\frac{V^2}{2}\right)} = 4f_{Fanning} \quad \text{L.7}$$

Now that f is defined, what does it mean? f should be dependent upon the roughness of the surface per the definition of surface friction. As shown by the Moody diagram (Moody 1944), f is a function of the relative roughness (ϵ/D , in which ϵ is the roughness of the surface and D is the diameter of the pipe) and the Reynold's number (Re). The Moody diagram is shown in Figure L.1.

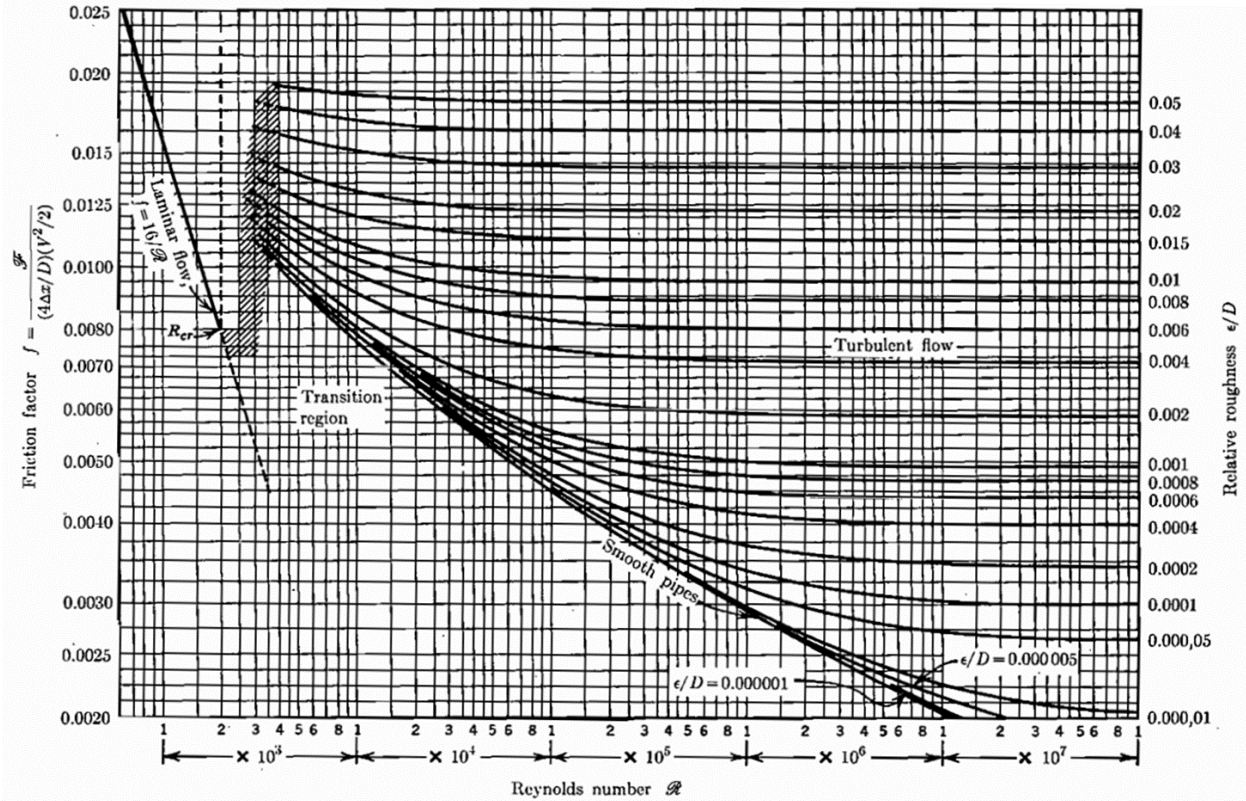


Figure L.1: Moody diagram showing the relationship between the fanning friction factor (f), Reynolds number (N_{Re}), and relative roughness (ϵ/D). Figure modified from de Nevers (2005).

The laminar flow on the Moody diagram is expressed by Equation L.8 whereas the turbulent flow curves are represented by the Colebrook equation (Colebrook 1939) in Equation L.9.

$$f_{Fanning} = \frac{16}{Re} \quad \text{L.8}$$

$$\frac{1}{\sqrt{f}} = -2 \log \left(\frac{\epsilon}{3.7D} + \frac{2.51}{Re\sqrt{f}} \right) \quad \text{L.9}$$

For both laminar and turbulent flow, the Reynold's number (N_{Re}) is defined in Equation L.10.

$$N_{Re} = \frac{DV\rho}{\mu} \quad \text{L.10}$$

Therefore, the fluid friction factor for laminar flow is linear and independent on relative roughness of the pipe. For turbulent flow, either the Moody diagram is used or the Colebrook equation (Equation L.9) is used.

Appendix M: Biography

Jarrett Wise was born on December 27, 1991. He received his Bachelor's degree in physics from Hastings College in Hastings, Nebraska (2014). Before starting his Master's at Oklahoma State University, he worked as a product compounder at Platte Valley Energetics in Alda, Nebraska. He finished his Master's degree in petroleum engineering from Oklahoma State University in 2019. In August 2019, he began his PhD program in petroleum engineering at the University of Oklahoma.